

Conservative LES-CMC Modelling for Turbulent Jet Flames

von der
Fakultät Energie-, Verfahrens- und Biotechnik
der Universität Stuttgart
zur Erlangung der Würde eines
Doktors der Ingenieurwissenschaften
(Dr.-Ing) genehmigte Abhandlung

vorgelegt von
Papakorn Siwaborworn
aus Bangkok, Thailand

Hauptberichter: Prof. Dr. Andreas Kronenburg
Mitberichter: Apl. Prof. PD Dr.-Ing. Uwe Schnell
Tag der mündlichen Prüfung: 16 Juli 2013

Institut für Technische Verbrennung
der Universität Stuttgart

2013

Acknowledgements

This thesis would not have been possible without the encouragement and support from many people around me. First of all, I am heartily thankful to my supervisor, Prof. Andreas Kronenburg, for not only offering me a work opportunity but also for his close guidance, support and encouragement throughout this project. His work pattern and methods to analyse problems have demonstrated to me that any complicated outcome can always be explained by the fundamental theories. My knowledge over the last three years is directly attributed to his coaching.

I would like to especially acknowledge the help and support of Dr. Oliver Stein. His ways of explanation make it easy to understand the more comprehensive issues. Moreover his proofreading and wonderful suggestions of this thesis are values that I will always admire.

I am indebted to my colleagues at University of Stuttgart for a fantastic work atmosphere in our group. I would like to thank Konstantina Vogiatzaki, my first colleague, not only for her kindness and friendship but also for her substantial helps and ideas corresponding to my work. I am grateful to the next generation, Niko Seubert, Gizem Inci and Gregor Olenik for the great time that we have had together. I also would like to thank the next BOFFIN generation Christian Eberle, Satoshi Ukai and Jung Choi for all fruitful discussions of coding. They show me how worthwhile teamwork is.

A special thanks goes to the High Performance Computing Center Stuttgart (HLRS), which supported me with leading edge supercomputing technology, including D-Grid resources.

No gratitude is ever enough to repay the ceaseless love, supports, perpetual encouragements and understandings of my parents and brothers for always being there by my side along all the journeys I have been taking since my first unsteady steps. Last

IV

but certainly not least, I would like to thank Ralf Stolte who is always by my side for his optimism and patience.

Contents

Table of Contents	V
Nomenclature	XI
Kurzfassung	XVII
Abstract	XIX
1 Introduction	1
1.1 Motivation	2
1.2 Thesis Outline	4
2 Background	7
2.1 Fluid Mechanics	7
2.1.1 Governing Equations	7
2.1.1.1 Conservation of Mass	8
2.1.1.2 Conservation of Momentum	8
2.1.1.3 Conservation of Scalar Quantities	9
2.1.2 Fundamentals of Turbulence	11
2.1.2.1 Definition of Turbulence	11
2.1.2.2 Length Scales in Turbulent Flows	12
2.1.3 Numerical Modelling of Turbulent Flows	15
2.1.3.1 Direct Numerical Simulation, DNS	15
2.1.3.2 Large Eddy Simulation, LES	16
2.1.3.3 Reynolds Averaged Navier Stokes Equations, RANS	16
2.2 Non-Premixed Combustion	17

2.2.1	Chemical Reaction Kinetics	17
2.2.2	Mixture Fraction	19
2.2.3	Model Overview	20
2.2.3.1	Fast Chemistry Combustion Models	21
2.2.3.2	Finite Rate Chemistry Combustion Models	22
3	The LES Method	25
3.1	Spatial Filtering	25
3.2	Filtered Governing Equations	28
3.2.1	Filtered Continuity Equation	28
3.2.2	Filtered Momentum Equation	28
3.2.3	Filtered Species Transport Equation	29
3.3	Subgrid-scale Modelling	29
3.3.1	Subgrid-scale Reynolds Stress Models	29
3.3.1.1	Smagorinsky Model	29
3.3.1.2	Dynamic Model	31
3.3.2	Subgrid-scale Scalar Flux Model	32
3.4	Other Models	33
3.4.1	Variance of Mixture Fraction Model	33
3.4.2	Scalar Dissipation Model	34
4	The CMC Model	35
4.1	Conditional Filtering	36
4.2	Non-Conservative CMC Formulation	37
4.3	Conservative CMC Formulation	39
4.4	Closure	40
4.4.1	Filtered Density Function	40
4.4.2	First Order Closure of the Reaction Source Term	42
4.4.3	Conditionally Filtered Scalar Dissipation	42
4.4.4	Conditionally Filtered Velocity	43
4.4.5	Conditional Turbulent Diffusivity	43
4.5	Implementation of the CMC Model	44
4.5.1	Conditionally Filtered Equations on the CMC Resolution	44

4.5.2	Relations between LES and CMC Codes	50
5	Numerical Methods	53
5.1	Spatial Discretisation	54
5.1.1	Approximation of Diffusive Fluxes	58
5.1.2	Approximation of Convective Terms	59
5.2	Temporal Discretisation	63
5.3	Pressure Correction	66
5.4	Numerical Aspects	66
5.4.1	CMC Formulations	66
5.4.2	Flux Approximations	67
5.4.3	Conditionally Filtered Turbulent Diffusivity Models	68
5.5	Boundary Conditions	68
5.5.1	Inflow Boundary Condition	69
5.5.2	Outflow Boundary Condition	70
5.5.3	Lateral Boundary Condition	70
6	LES-CMC of the Sandia Flame series	71
6.1	Introduction	71
6.2	Experimental Setup	72
6.3	Computational Setup	73
6.4	Parametric Studies	76
6.4.1	Parametric Studies of Flow and mixing Field	76
6.4.2	Parametric Studies of the Combustion Model	77
6.4.3	Parametric Study of CMC Grid Resolution	78
6.5	Results of Sandia Flame D	80
6.5.1	Parametric Studies of Flow and mixing Field	80
6.5.2	Parametric Studies of Combustion Model	85
6.5.2.1	Flow and Mixing Field	85
6.5.2.2	Preliminary Studies	89
6.5.2.3	Conditionally Filtered Reactive Scalars	96
6.5.2.4	Unconditionally Filtered Reactive Scalars	101
6.5.3	Parametric Study of CMC Grid Resolution	105

6.5.3.1	Conditionally Filtered Reactive Scalars	105
6.5.3.2	Unconditionally Filtered Reactive Scalars	107
6.6	Results of Sandia Flame E	109
6.6.1	Parametric Studies of Combustion Model	110
6.6.1.1	Flow and Mixing Field	110
6.6.1.2	Preliminary Studies	113
6.6.1.3	Conditionally Filtered Reactive Scalars	116
6.6.1.4	Unconditionally Filtered Reactive Scalars	121
6.6.2	Parametric Study of CMC Grid Resolution	125
6.6.2.1	Conditionally Filtered Reactive Scalars	125
6.6.2.2	Unconditionally Filtered Reactive Scalars	127
6.7	Results of Sandia Flame F	129
6.7.1	Parametric Studies of Combustion Model	130
6.7.1.1	Flow and Mixing Field	130
6.7.1.2	Preliminary Studies	133
6.7.1.3	Conditionally Filtered Reactive Scalars	136
6.7.1.4	Unconditionally Filtered Reactive Scalars	140
6.7.2	Parametric Study of CMC Grid Resolution	142
6.7.2.1	Conditionally Filtered Reactive Scalars	142
6.7.2.2	Unconditionally Filtered Reactive Scalars	144
6.8	Summary	146
7	Conclusions and Future Work	149
7.1	Overview	149
7.2	Conclusions	149
7.3	Suggestions for Future Work	152
	Appendix	155
	A Derivation of CMC Conservative Form	155
	B Details of Pressure Correction	159
	Bibliography	161

CONTENTS

IX

Lebenslauf

171

Nomenclature

Roman Symbols

a_e, a_w, a_n, a_s	spatial flux coefficients	[1/s]
a_+, a_-	reference space flux coefficients	[1/s]
A	area	[m ²]
A_{fi}	pre-exponential factor	[1/s]
B	β -function parameter	
c	Courant number	[-]
c_α	species concentration	[kmol/m ³]
C_s	Smagorinsky constant	[-]
C_p	mixture specific heat capacity	[J/kg-K]
D	molecular diffusivity (equal for all species)	[m ² /s]
Da	Damköhler number	[-]
D_t	turbulent diffusivity	[m ² /s]
e	internal energy	[J/kg]
$E_{a,i}$	activation energy in reaction i	[J/kmol]
f	a scalar	
\bar{f}	conventional filtering of scalar f or resolved component of scalar f	
\tilde{f}	Favre filtering of scalar f or resolved component of scalar f using Favre averages	
f'	subgrid (unresolved) component of scalar f	

F	fuel stream	
F_e, F_w, F_n, F_s	specific mass flows across faces of control volume	[1/s]
g_i	gravity in x_i direction	[m/s ²]
G	filter kernel	
h	specific enthalpy	[J/kg]
J_α	diffusion of species α	[kg/m ² -s]
J_j^{sgs}	subgrid-scale scalar flux	[kg/m ² -s]
k_c	cut-off wave number	[1/m]
k_{fi}	rate coefficients of forward reaction	[1/s]
k_{ri}	rate coefficients of reverse reaction	[1/s]
K	Kelvin	
ℓ_0	integral length scale or turbulence macroscale	[m]
ℓ_λ	Taylor microscale	[m]
ℓ_K	Kolmogorov (micro)scale	[m]
Le	Lewis number (= Sc/Pr)	[-]
L_{ij}	Germano identity	[N/m ²]
L	characteristic width of the flow or macroscale	[m]
n	total number of species	
N	scalar dissipation	[1/s]
\tilde{N}	filtered scalar dissipation	[1/s]
\tilde{N}_{mean}	resolved-scale scalar dissipation	[1/s]
\tilde{N}_{sgs}	subgrid-scale scalar dissipation	[1/s]
\tilde{N}_η	conditionally filtered scalar dissipation	[1/s]
N_{DNS}	number of grid points for DNS	
O	oxidizer stream	
p	pressure	[Pa]
P	products stream	
\tilde{P}	probability	
Pe	Peclet number	[-]
Pr	Prandtl number	[-]
q_j	heat flux vector	[J/kg]

q_j^c	heat transfer due to conduction	$[J/kg]$
q_j^d	heat transfer due to inter-diffusion of heat between species	$[J/kg]$
q_R	heat transfer due to radiation	$[J/kg]$
q_ϕ	production/destruction of scalar	
Q_α	conditionally filtered mass fraction of species α	$[-]$
Q_h	conditional enthalpy	$[J]$
Re	Reynolds number	$[-]$
\mathfrak{R}_i	reaction rate for the i th elementary reaction	$[kmol/m^3-s]$
R_x	correlation coefficient	$[-]$
R_u	universal gas constant	$[J/kmol-K]$
S_{ij}	strain rate tensor	$[1/s]$
Sc	Schmidt number	$[-]$
$\ \tilde{S}\ $	Frobenius norm of the resolved strain rate tensor	$[1/s]$
t	time	$[s]$
t_K	Kolmogorov time scale	$[s]$
T	temperature	$[K]$
T_{ij}^{sgs}	subtest-scale stress	$[N/m^2]$
u'	velocity fluctuation	$[m/s]$
u_0	integral velocity scale	$[m/s]$
u_K	Kolmogorov velocity scale	$[m/s]$
u_i	velocity vector (u_i, u_j, u_k)	$[m/s]$
\tilde{u}_j	resolved velocity in the j direction	$[m/s]$
\tilde{u}_η	conditionally filtered velocity	$[m/s]$
V or ΔV	volume	$[m^3]$
w_α	reaction source term of species α	$[kg/m^3-s]$
$\tilde{w}_{\alpha,\eta}$	conditionally filtered reaction source term	$[1/s]$
$\tilde{w}_{R,\eta}$	conditionally filtered radiation term	$[J/s]$
W_α	molecular weight of species α	$[kg/kmol]$
x_i	cartesian coordinate vector (x_i, x_j, x_k)	
Y_α	mass fraction of species α	$[-]$
Z_i	element mass fraction of an atom i	$[-]$

Greek Symbols

α	species	
γ	product of density and FDF ($\bar{\rho}\tilde{P}(\eta)$)	$[kg/m^3]$
Γ	Gamma function, diffusion coefficient	
δ	Dirac delta function	
Δ	filter width	$[m]$
$\hat{\Delta}$	test filter width	$[m]$
ε	dissipation rate of the kinetic energy per unit mass	$[m^2/s^3]$
η	mixture fraction sample space	
$\Theta(\phi)$	joint effects of diffusion, convection and source/sink terms	
κ	thermal conductivity of mixture	$[W/m-K]$
λ	interpolation factor	$[-]$
μ	dynamic viscosity	$[Pa-s]$
μ_t	eddy viscosity	$[Pa-s]$
ν	kinematic viscosity	$[m^2/s]$
ν_t	turbulent kinematic viscosity	$[m^2/s]$
ξ	mixture fraction	$[-]$
$\tilde{\xi}$	filter mixture fraction	$[-]$
ξ_{st}	stoichiometric mixture fraction	$[-]$
$\widetilde{\xi_{sgs}''^2}$	subgrid-scale variance of mixture fraction	$[-]$
ρ	density	$[kg/m^3]$
τ_{ij}	viscous stress tensor	$[N/m^2]$
τ_{ij}^{sgs}	subgrid-scale Reynolds stress	$[N/m^2]$
ν_F	moles of fuel	
ν_O	moles of oxidizer	
ν_P	moles of products	
$\nu'_{\alpha i}$	stoichiometric coefficients of reactants side	
$\nu''_{\alpha i}$	stoichiometric coefficients of products side	
ϕ, Φ	scalar quantity	
ψ_η	fine-grained PDF	
Ω	entire flow domain	

Superscripts

$\langle \ \rangle$	expectation or average
—	filtered procedure
\sim	Favre (density-weighted) filtered average
'	unconditional fluctuation
''	conditional fluctuation
$\widetilde{(\cdot)}^*$	Favre filtered property evaluated on a CMC cell

Shorthands

<i>atm</i>	atmospheres
BOFFIN	BOundary Fitted Flow INtegrator
CFD	computational fluid dynamics
CFL	Courant-Friedrichs-Lewy
CDS	central differencing scheme
CMC	conditional moment closure
CV	control volume
DNS	direct numerical simulation
EDM	eddy dissipation model
FDF	filtered probability density function
FVM	finite volume method
GRI	Gas Research Institute
IEA	International Energy Agency
IEO	International Energy Outlook
LES	large eddy simulation

LFM	laminar flamelet model
LHS	left hand side of an equation
PDE	partial differential equation
PDF	probability density function
RANS	Reynolds averaged Navier Stokes/simulation
RHS	right hand side of an equation
RMS	root mean square
R&D	Research and Development
SIMPLE	Semi-Implicit Method for Pressure-Linked Equations
SLFM	stationary laminar flamelet model
TV	total variation
TVD	total variation diminishing
UDS	upwind differencing scheme

Kurzfassung

Das Ziel der vorliegenden Arbeit ist die Analyse turbulenter, nicht-vorgemischter Flammen mittels einer kombinierten Large Eddy Simulation - Conditional Moment Closure (LES-CMC) Methode. LES beruht auf räumlicher Filterung und löst die großen turbulenten Skalen auf, wohingegen die kleinen turbulenten Strukturen durch ein Feinstrukturmodell beschrieben werden, in diesem Fall durch das Smagorinsky-Modell. CMC basiert auf einer skalaren Erhaltungsgröße, dem Mischungsbruch, und es wird angenommen, dass die Fluktuationen der reaktiven Skalare mit den Fluktuationen des Mischungsbruchs korrelieren. Deshalb wird CMC mit Konditionierung auf den Mischungsbruch in dieser Arbeit eingesetzt, um turbulente Flammen vorherzusagen. Im letzten Jahrzehnt hat eine Reihe an Simulationen basierend auf der nicht-konservativen LES-CMC Formulierung zu guten Vorhersagen der chemischen Spezies in unterschiedlichen Flammen geführt. Ungenaue Vorhersagen ergeben sich allerdings in CMC-Zellen, die starke zeitliche Schwankungen des Mischungsbruchfelds aufweisen. Ein wichtiger Grund für diese schwachen Vorhersagen liegt im Fehlen einer Gewichtung des konvektiven Terms mit dem Verhältnis der filtered density functions (FDFs) in den nicht-konservativen CMC-Gleichungen. Im Gegensatz zur nicht-konservativen LES-CMC erhält die hier vorgestellte konservative Formulierung streng die Masse. Die Gewichtung des konvektiven Terms mit dem FDF-Verhältnis wird berücksichtigt, so dass verbesserte Vorhersagen der lokalen, konditionierten Skalare erzielt werden können.

Simulationen turbulenter Strahlflammen (Sandia Flammen D, E und F) mittels der konservativen LES-CMC Methode werden durchgeführt. Flamme D wird als ein erster Testfall zur Validierung der numerischen Ergebnisse anhand etablierter experimenteller Daten verwendet. Eine Studie des Strömungs- und Mischungsfeldes der Flamme D dient zur Festlegung der relevanten Parameter für die Flammen E und F. Die Studie ergibt

optimale Werte für die laminare und turbulente Schmidt-Zahl von 0,7 und 0,4. Ein geeigneter Wert für die Konstante im Modell für die Feinstruktur-Varianz ergibt sich zu 0,2. Eine Sensitivitätsstudie des Varianzlevels am Einstromrand zeigt, dass Varianzwerte von $\frac{2}{3}$, $\frac{1}{3}$ und $\frac{2}{9}$ der gemessenen Geschwindigkeitsvarianz bei $z/D = 0,14$ geeignete Einstrom-Randbedingungen für die Flammen D, E und F darstellen.

Nachfolgend wird eine Studie der Parameter des Verbrennungsmodells für alle Testfälle durchgeführt. Der Vergleich der Skalarvorhersagen mit Messungen zeigt, dass LES kombiniert mit der konservativen CMC-Formulierung bessere Ergebnisse erzielt, als auf Basis der nicht-konservativen Gleichungen. Allerdings ergeben sich ähnliche Vorhersagen beim Vergleich zweier Approximationsmodelle für den konvektiven Fluss in CMC (Berechnung der konvektiven CMC-Flüsse basierend auf den LES-Zellen am CMC-Zellrand oder basierend auf dem Wert am CMC-Zellmittelpunkt). Eine Parameterstudie der CMC-Gitterauflösung zeigt, dass $8 \times 8 \times 80$ Zellen in x -, y - und z -Richtung akzeptable Vorhersagen innerhalb einer vertretbaren Rechenzeit ergeben. Die Simulationsergebnisse der Flammen E und F zeigen, dass die vorliegenden CMC-Simulationen lokales Verlöschen und Wiederentzündungen nicht ausreichend abbilden. Dies liegt zum Teil am Mittelungseffekt der großen CMC-Zellen auf die konditionierte Dissipation. Wesentlich kleinere CMC-Zellen in der Größenordnung der LES-Filterweite könnten Extremwerte hoher Dissipation deutlich besser abbilden und somit zu genaueren Vorhersagen des lokalen Verlöschens führen. Eine Parameterstudie der CMC-Gitterauflösung für die Flammen E und F ergibt etwas bessere Ergebnisse auf einem feineren CMC-Gitter ($16 \times 16 \times 80$) im Vergleich zum Referenzgitter ($8 \times 8 \times 80$), wobei diese Vorhersagen immer noch verbesserungswürdig sind. Das Problem liegt möglicherweise in der Genauigkeit der Beschreibung des chemischen Quellterms. Aus diesem Grund werden mögliche Vorschläge für zukünftige Arbeiten gemacht, wie eine Schließung zweiter Ordnung und zweifach-konditionierte chemische Quellterme.

Abstract

The objective of the present study is to analyze turbulent non-premixed flames by utilizing a combined large eddy simulation - conditional moment closure (LES-CMC) method. LES is based on spatial filtering, and it resolves large scales of turbulent motion while modelling the small turbulent structures using a subgrid model, here the Smagorinsky model. CMC is a conserved scalar method where fluctuations of the reactive scalar variables can be associated with fluctuations of the mixture fraction. Therefore, CMC is applied to turbulent combustion modelling in this work using mixture fraction as the conditioning variable. In the last decade, computations using a non-conservative LES-CMC formulation have provided good predictions of major and minor species for different flames. However, inaccurate predictions occur in CMC cells which have large temporal variations of the mixture fraction field. A lack of weighting the convective term by a filtered density function (FDF) ratio in non-conservative CMC is believed to be a major reason for these inaccurate predictions. In contrast to non-conservative LES-CMC, the present conservative formulation is inherently mass conserving. It considers weighting the convective term by an FDF ratio so that improved predictions of local conditional scalars can be obtained.

Investigations of turbulent jet flames (Sandia Flames D, E and F) are performed using the conservative LES-CMC approach. Flame D is used as the first test case to validate the numerical results in comparison with well-established experimental data. A study of the flow and mixing parameters is carried out first to establish the parameters for Flames E and F. Results from these studies show that the optimal values of Schmidt number, Sc , and turbulent Schmidt number, Sc_t are 0.7 and 0.4, respectively. The appropriate value of the subgrid-scale variance modelling constant is 0.2. A sensitivity analysis of the results demonstrates that inflow velocity variance levels corresponding to $\frac{2}{3}$, $\frac{1}{3}$ and $\frac{2}{9}$ of

the measured variances at $z/D = 0.14$ are suitable inflow conditions for Flames D, E and F, respectively.

Subsequently, parametric studies of the combustion model are performed for all test cases. The statistical predictions of scalars compared with measurements show that the LES with the conservative CMC formulation is better than the one based on non-conservative equations. However, similar predictions are obtained from two different flux approximation methods (computing the CMC convective fluxes based on the LES cells located at the CMC faces or based on the CMC cell centres). A parametric study of the CMC grid resolution shows that a resolution of $8 \times 8 \times 80$ cells in x -, y - and z -directions yields appropriate predictions within a reasonable computational time. Simulation results of Flames E and F show that the CMC simulations presented here cannot capture local extinction and re-ignition accurately. This is partially due to the averaging effect of the large CMC cells on the modelled conditional dissipation. Much finer CMC cells of the order of the LES cell size will capture more of the fluctuation of scalar dissipation rates and may lead to a more accurate prediction of the local extinction events. The parametric study of CMC grid resolution for Flames E and F shows that a finer CMC grid ($16 \times 16 \times 80$) predicts slightly better results than the reference grid ($8 \times 8 \times 80$), but predictions could still be improved. It is possible that the problem is associated with the accuracy of the chemical source term. Hence, some possible solutions, such as second-order closure and doubly conditional reaction source terms, are suggested for future works.

CHAPTER 1

Introduction

Combustion, known as the important technology of mankind, is used for energy production. It provides more than 90% of energy consumption (e.g. in heating, traffic, electrical power generation) in the world [108]. As stated in the International Energy Outlook (IEO2010) by the International Energy Agency (IEA) [24], the total world consumption of marketed energy has increased during the past ten years and will increase steeply in the projection. More than 80% of the world marketed energy originated from fossil fuels, composed of petroleum, natural gas and coal. Even if the prospects of renewable energy resources improve due to the increase of oil price and the awareness of environmental impacts of fossil fuels, fossil fuels will remain the major energy source for at least the next twenty years.

The benefits of combustion can be realized as living comfort and world economy development. However, the drawbacks of combustion are not only its production of carbon dioxide (CO_2), one of the greenhouse gases, but also pollutants as by-products. The major pollutants from combustion are unburned hydrocarbons, nitrogen oxides (NO and NO_2), carbon monoxide, sulphur oxides (SO_2 and SO_3), volatile organic compounds and particulate matter. These affect the environment in both the long and short terms. "Air pollution is a significant reason for not only acid rain, global warming, smog and the depletion of the ozone layer, but it is so vital for human health risk (i.e. serious respiratory and other illnesses)" [1]. Therefore, there are many programs for reducing, limiting and monitoring CO_2 emission and pollutant formation. The European emission standard is one of the examples of a regulation to limit pollutant emissions for the registration and sale of new

types of vehicles for European countries. These strict regulations force manufacturers to carry out further research for technologies in order to reduce CO₂ emission and pollutant formation from their products. However, investment costs have increased by carrying out the regulatory experiment.

Computational fluid dynamics (CFD) is an alternative approach for R&D. In general, this approach uses numerical techniques to achieve discrete solutions to the governing equations of combustion processes.

1.1 Motivation

Recently, CFD simulations coupled with detailed modelling of chemical reactions are becoming increasingly important for the design of industrial combustors. They can be used to predict combustor performance and pollutant emissions, such as particulate matter, unburned hydrocarbons, sulphur oxides (SO₂ and SO₃) and oxides of nitrogen (NO_x). This accurate prediction of pollutants has played an important role for environmentally friendly machine design in recent years. CFD approaches based on Reynolds averaging of the Navier-Stokes equations (RANS) have been partially successful in predicting reacting turbulent flows but often struggled in cases where strong streamline curvature, intermittency and non-gradient transport were present [12]. Large eddy simulation (LES) can overcome these RANS deficiencies. However, a high computational cost is required for LES.

Since Deardoff [21] applied LES to a turbulent channel flow in 1970, LES has been applied to many non-reacting flow configurations and also recently to turbulent reacting flows. In the LES methodology, the mean (known as large scale) flow and mixing fields are solved directly while the small scales are modelled. However, neither LES nor RANS can describe species transport without further modelling assumptions. The reaction length and time scales are much smaller than the smallest scale of turbulence, the Kolmogorov scale. Therefore, a combustion model is needed to deal with this task.

In recent years, many different combustion models have been applied to turbulent reacting flows. They give different results which vary in the capability of minor and major species predictions as well as in terms of accuracy. The most studied models, suitable for non-premixed combustion, are the steady laminar flamelet model (SLFM)

[39, 72], the transport of the joint probability density function (PDF) [81, 87, 60] and conditional moment closure (CMC) [47, 43, 49]. While SLFM is the least demanding of these approaches, it is based on the assumption of high chemical reaction rates compared with the flow time scales (high Damköhler assumption) and not suitable for the prediction of important combustion phenomena like extinction, re-ignition and pollutant formation. In contrast, in transported PDF methods the chemical source term appears in closed form, allowing for an accurate prediction of such phenomena. However, the PDF transport equation requires non-trivial closure of the mixing term and the typically used Monte-Carlo based solution methods are expensive due to their requirement of large numbers of stochastic particles. The CMC method offers an accurate prediction of all relevant combustion phenomena, while being computationally less expensive than transported PDF methods. In theory, CMC states the fundamental hypothesis that the mean reaction rates in a turbulent flow can be more accurately modelled by conditioning on a conserved scalar, such as mixture fraction (ξ). This reaction model has been proved to successfully predict major and minor species in jet flames and also in elliptic flows such as bluff-body flames [16].

The possibility of coupling LES and CMC was first mentioned by Klimenko and Bilger [47]. The typical CMC is introduced as a non-conservative formulation which means there is no PDF-weighted flux across the cell faces in the convective term. This leads to an equal importance of convective fluxes in all three directions (x -, y - and z -directions). The non-conservative LES-CMC was initially implemented by Navarro *et al.* [68, 65, 66], who applied it to simulate Sandia Flame D, bluff-body and lifted methane flames. Their simulation results show a very good accordance with the experimental data only for the simple flames, such as Sandia Flame D. However, for more complicated flames, for example the bluff-body flames, there are overpredictions of temperature and product species in the location closest to the nozzle, even though the simulation accurately captures the mixing field in the entire domain [65]. These overpredictions are likely attributed to the combustion sub-model. The traditional CMC cannot deal with that position, where there are two distinct temperature branches in the experiment, which can be seen more clearly on the right of Fig. 1.1. The mixing branch corresponds to a recirculation flow of hot products plus cold oxidizer having a lower temperature. The burning branch corresponds to a fully burning mixture. The lack of PDF-weighted fluxes in CMC non-conservative

form is believed to be one reason for this result. Therefore, a new conservative CMC formulation is implemented in this study.

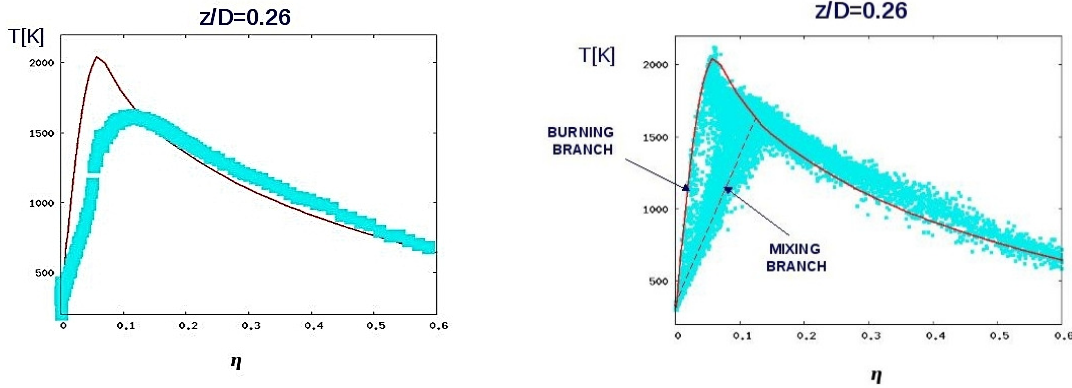


Figure 1.1: The average over the cross-section of the conditional temperature, T , vs. mixture fraction, η , at downstream location $z/D = 0.26$ of the bluff-body flame [65]. The left figure shows the comparison between results of non-conservative LES-CMC (red line) and the conditionally averaged experimental data (symbols) from [20]. The right figure shows the results of non-conservative LES-CMC (red line) and instantaneous values (dots) indicating a large scatter about the conditional average and the existence of two main branches.

1.2 Thesis Outline

The main focus of this research is the investigation of the performance of conservative LES-CMC compared with the non-conservative approach. Therefore, LES coupling with CMC in conservative form is used here instead of the traditional one. The conservative CMC form was derived by Cleary [16] having conditional moments dependent on the three spatial dimensions and time. In this study, Cleary's formulation is applied to Sandia Flames in order to validate the conservative LES-CMC approach. Due to their simple geometry and wealth of experimental validation data, Flames D, E and F are ideally suited as a validation target group in this work. Note that the bluff-body flames are not the ideal test cases for development since they require a large domain for simulation and thus they are computationally expensive. The results of parameter analyses from Sandia Flame D with the new code are used for further research, i.e. Flames E and F. Moreover, the ability of first-order CMC in conservative form to predict extinction and re-ignition of flames (Flames E and F) is investigated. The structure of the document is as follows:

In Chapter 2, the principal theories for non-premixed flames are introduced. The fundamentals and governing equations of turbulent reacting flow are also given. Computational methods for turbulent reacting flow will be briefly discussed. Subsequently, the fundamental theories of non-premixed combustion and different combustion models based on different assumptions on the chemical and mixing states are explained.

Chapter 3 provides the basis of LES methodology. Spatial filtering is applied to the governing equations, and the models required for unclosed terms are addressed.

In Chapter 4, the CMC methodology is introduced, in particular its conservative form. The treatment of unclosed terms is discussed. This chapter closes with the implementation details of the CMC model.

In Chapter 5, the numerical treatments are provided. Spatial and time discretisation schemes of the employed simulation program are described. Subsequently, pressure correction and different numerical methods for each parametric study within the combustion model are discussed. Finally, initial and boundary conditions which are used in this research are outlined.

In Chapter 6, the experimental data is provided. The computational set-up will be addressed and all parametric studies are described. Subsequently, the simulation results of the Sandia flames are presented under various conditions. The performances of all cases in each parametric study are discussed and compared with the relevant experiments. This chapter closes with a summary of all investigations.

In Chapter 7, the conclusions of the research are detailed and recommendations for future work are made.

CHAPTER 2

Background

In this chapter, basic theories of fluid mechanics, turbulence and non-premixed combustion will be presented. Firstly, the governing equations, Navier-Stokes and conservation of scalar quantity equations, are given in their instantaneous form. Secondly, the principles of turbulence will be addressed, followed by the discussion of flow and mixing models. Then, theories related to non-premixed combustion, which are used in this approach, are discussed. Finally, the chapter closes with an overview of some commonly used combustion models in turbulent reacting flames.

2.1 Fluid Mechanics

In continuum mechanics, a fluid is regarded as a continuous substance which can be transferred by the action of externally applied forces known as driving forces. These forces can be classified as surface forces (e.g. shear forces, surface tension and pressure differences) and body forces (e.g. gravity and forces induced by rotation). The spatio-temporal evolution of a given flow field, which is represented by the governing equations of fluid motion will be presented in the next section.

2.1.1 Governing Equations

The flow of an isothermal compressible fluid is accurately described by the conservation equations of mass and momentum (Navier-Stokes equations). Additionally for premixed laminar and nonpremixed turbulent reacting flows, the conservation of scalar quantities,

composed of enthalpy, species mass fraction and mixture fraction, are necessary. In the following subsections, the governing equations are given in Cartesian tensor notation for simplicity.

2.1.1.1 Conservation of Mass

In the differential form, the mass conservation or continuity equation is written as

$$\frac{\partial \rho}{\partial t} + \frac{\partial}{\partial x_j}(\rho u_j) = 0. \quad (2.1)$$

In Eq. (2.1) ρ denotes density and u_j is the velocity component in x_j direction.

2.1.1.2 Conservation of Momentum

Based on Newton's second law (i.e. the acceleration of an object results from the net force acting on it), the momentum equation is given in differential form by

$$\frac{\partial}{\partial t}(\rho u_i) + \frac{\partial}{\partial x_j}(\rho u_i u_j) = \frac{\partial \tau_{ij}}{\partial x_j} - \frac{\partial p}{\partial x_i} + \rho g_i, \quad (2.2)$$

where on the LHS, the first term represents the temporal change and the second term represents convection. All terms on the RHS are the forces which may act on the fluid, such as surface forces and body forces. If the body force concerns only gravity, g , the surface forces will be expressed by pressure, p , and the viscous stress, τ_{ij} . With the assumption of a Newtonian fluid, a fluid whose stress versus strain rate curve is linear and passes through the origin [6], τ_{ij} can be expressed as a function of the strain rate tensor, S_{ij} ,

$$\tau_{ij} = \mu \left[2S_{ij} - \frac{2}{3}\delta_{ij} \frac{\partial u_k}{\partial x_k} \right], \quad (2.3)$$

where μ is the dynamic viscosity, a function of the composition and temperature of the fluid. The δ_{ij} denotes the Kronecker symbol ($\delta_{ij} = 1$ if $i = j$ and $\delta_{ij} = 0$ otherwise). The strain rate tensor is calculated as

$$S_{ij} = \frac{1}{2} \left(\frac{\partial u_i}{\partial x_j} + \frac{\partial u_j}{\partial x_i} \right). \quad (2.4)$$

Substituting Eqs. (2.3) and (2.4) into Eq. (2.2), the final equation of momentum conservation reads

$$\frac{\partial}{\partial t}(\rho u_i) + \frac{\partial}{\partial x_j}(\rho u_i u_j) = \frac{\partial}{\partial x_j} \left[\mu \left(\frac{\partial u_i}{\partial x_j} + \frac{\partial u_j}{\partial x_i} \right) - \frac{2}{3} \mu \delta_{ij} \frac{\partial u_k}{\partial x_k} \right] - \frac{\partial p}{\partial x_i} + \rho g_i. \quad (2.5)$$

2.1.1.3 Conservation of Scalar Quantities

In the differential form, the generic conservation of a scalar quantity, ϕ , is

$$\frac{\partial}{\partial t}(\rho \phi) + \frac{\partial}{\partial x_j}(\rho u_j \phi) = -\frac{\partial J_{\phi,j}}{\partial x_j} + q_\phi, \quad (2.6)$$

with the terms from left to right representing temporal change, convection, diffusive transport and the production/destruction of scalar, q_ϕ . In turbulent reacting flow, scalars of interest comprise reactive species and enthalpy.

Conservation of Species

In the species transport equation, the term $J_{\phi,j}$ may include diffusion due to concentration (Fickian), pressure and temperature gradients. However, most of these effects are assumed to be negligible at high Reynolds number Re (Eq. (2.14)), since turbulent diffusion (mixing) is dominant and only Fickian diffusion is retained. For the species α the diffusion, $J_{\alpha,j}$, can be described by Fick's law as

$$J_{\alpha,j} = -\rho D_\alpha \frac{\partial Y_\alpha}{\partial x_j}, \quad (2.7)$$

where D_α is the molecular diffusivity of species α which is related to viscosity through the Schmidt number $Sc_\alpha = \mu/\rho D_\alpha$. From the definition, the Schmidt number can be seen as a non-dimensional quantity, representing the ratio of the rate of momentum transfer to the rate of mass transfer. Here, D_α is assumed to be equal for all species, $D_\alpha = D$. As a

result, the conservation of mass fraction for species α can be written as

$$\frac{\partial}{\partial t}(\rho Y_\alpha) + \frac{\partial}{\partial x_j}(\rho u_j Y_\alpha) = \frac{\partial}{\partial x_j} \left(\rho D \frac{\partial Y_\alpha}{\partial x_j} \right) + w_\alpha, \quad (2.8)$$

where Y_α is the mass fraction of species α and w_α presents the reaction source term of species α .

Conservation of Energy

An energy transport equation can be expressed in terms of enthalpy h (i.e. $h \equiv u + \frac{p}{\rho}$, where u is the internal energy) as

$$\frac{\partial}{\partial t}(\rho h) + \frac{\partial}{\partial x_j}(\rho u_j h) = \frac{Dp}{Dt} - \frac{\partial q_j}{\partial x_j} + \tau_{ij} \frac{\partial u_i}{\partial x_j} + q_R. \quad (2.9)$$

For incompressible flows, low-speed flows are assumed so that acoustic interactions are negligible. The first term on the RHS denotes the convective derivative of pressure, $\frac{Dp}{Dt} = \frac{\partial p}{\partial t} + u_j \frac{\partial p}{\partial x_j}$. The second term on the RHS is the gradient of heat flux vector. The third term on the RHS is the viscous heating which is generally smaller than other terms and has thus been neglected. The last term on the RHS, q_R , denotes the radiative thermal flux. Subsequently, the conservation equation for the enthalpy becomes

$$\frac{\partial}{\partial t}(\rho h) + \frac{\partial}{\partial x_j}(\rho u_j h) = \frac{Dp}{Dt} - \frac{\partial q_j}{\partial x_j} + q_R, \quad (2.10)$$

In a multi-component system, the heat flux vector, q_j , is expressed in terms of heat conduction, q_j^c and inter-diffusion of heat between species, q_j^d .

$$q_j = q_j^c + q_j^d = -\kappa \frac{\partial T}{\partial x_j} - \frac{\mu}{Sc} \sum_{\alpha} h_{\alpha} \frac{Y_{\alpha}}{x_j}, \quad (2.11)$$

where κ is the thermal conductivity of the mixture, Sc is the Schmidt number ($Sc = \mu/\rho D$) and h_{α} is the absolute enthalpy of species α (i.e. the sensible enthalpy plus standard enthalpy of formation [14]). When the temperature gradient is converted to an enthalpy gradient ($\frac{\partial h}{\partial x_j} = C_p \frac{\partial T}{\partial x_j} + \sum_{\alpha} h_{\alpha} \frac{Y_{\alpha}}{x_j}$, where C_p is the mixture specific heat capacity), the heat flux vector is

$$q_j = -\frac{\mu}{Pr} \frac{\partial h}{\partial x_j} - \mu \left(\frac{1}{Sc} - \frac{1}{Pr} \right) \sum_{\alpha} h_{\alpha} \frac{Y_{\alpha}}{x_j}, \quad (2.12)$$

where Pr is the Prandtl number, representing the ratio of the rate of momentum transfer to the rate of thermal energy transfer $Pr = C_p \mu / \kappa$. Substituting Eq. (2.12) into Eq. (2.10), the energy transport equation can be expressed as

$$\frac{\partial}{\partial t}(\rho h) + \frac{\partial}{\partial x_j}(\rho u_j h) = \frac{Dp}{Dt} + \frac{\partial}{\partial x_j} \left(\frac{\mu}{Pr} \frac{\partial h}{\partial x_j} \right) - \frac{\partial}{\partial x_j} \left(\mu \left(\frac{1}{Pr} - \frac{1}{Sc} \right) \sum_{\alpha} h_{\alpha} \frac{Y_{\alpha}}{x_j} \right) + q_R. \quad (2.13)$$

Within this study, the domain is open to the atmosphere and thus, pressure can be considered as constant. Consequently, the term $\frac{Dp}{Dt}$ is neglected. If the Lewis number, $Le = Sc/Pr$, is assumed to be unity ($\kappa/C_p = \rho D$), all species and energy are assumed to diffuse at the same rate. Therefore, the third term on the right-hand side of Eq. (2.13) can be omitted.

2.1.2 Fundamentals of Turbulence

The governing equations introduced in section 2.1.1 are known to be valid for both laminar and turbulent fluid flows. In reality, the flow in most practical combustion devices is turbulent [103]. This section introduces some basic concepts of turbulent flows.

2.1.2.1 Definition of Turbulence

The nature of turbulence is characterised by irregularity, diffusivity, vorticity fluctuations, dissipation and large Reynolds numbers [97]. Turbulence has an important influence on the transport and fluid mixing which are much more effective than in a laminar flow [82]. In his pipe-flow experiments (dye is steadily injected on the centerline of a long pipe in which water is flowing), Osborne Reynolds (1883) characterized the flow by a dimensionless parameter, known as Reynolds number Re . The number is defined as

$$Re = \frac{UL}{\nu}, \quad (2.14)$$

where U and L are the characteristic velocity and length scales of the flow and ν is the kinematic viscosity, $\nu = \mu/\rho$. At large Re , turbulence is generated from the instabilities of laminar flows. During experiments, a pipe flow is turbulent if its Re is more than 2300 (for a pipe flow, U is an average velocity over the pipe cross section and L is the diameter of the pipe).

According to its random unsteadiness associated with the flow properties, a turbulent flowfield can be characterized in terms of mean and fluctuating quantities [103]

$$\phi(t) = \bar{\phi} + \phi'(t), \quad (2.15)$$

where ϕ is any flow property, such as velocity or pressure in Eq. (2.15). $\bar{\phi}$ is a mean property defined by taking a time-average of the flow properties over a sufficiently large time interval. The fluctuation $\phi'(t)$ is the difference between instantaneous and mean value of that property. This method is known as the Reynolds decomposition and forms the basis of the Reynolds averaged Navier Stokes (RANS) approaches described in section 2.1.3.3. Moreover, in large eddy simulation (LES), this mean value can be defined as a spatial average, outlined in Chapter 3. To understand the structure of turbulent flows, some important length scales are introduced in the following sub-section.

2.1.2.2 Length Scales in Turbulent Flows

Four principal length scales characterising turbulent flows can be defined. In decreasing order of magnitude, these are the characteristic width of the flow or macroscale L , integral scale or turbulence macroscale ℓ_0 , Taylor microscale ℓ_λ and Kolmogorov (micro)scale ℓ_K . Since L is used to define Re based on mean flow velocity as Eq. (2.14), it rather represents the geometry of the actual device than the turbulent structures. The Taylor microscale may be used to characterise homogeneous isotropic turbulence, but is less relevant for the focus of this thesis. The integral and Kolmogorov scales, ℓ_0 and ℓ_K , are however fundamental to LES modelling which will be described in the following paragraphs.

Integral scale, ℓ_0 : The physical definition of the integral scale is the mean size of the large eddies in turbulent flows. Even though they are the same order of size, ℓ_0 is always smaller than L . ℓ_0 can be defined as the spacing between narrow vortex tubes [96]. For

isotropic turbulence, the integral scale is given by

$$\ell_0 = \int_0^{\infty} R_x(r) dr, \quad (2.16)$$

where $R_x(r)$ is the correlation coefficient which is a normalized value of velocity fluctuation between two points having coherent structures (vortices). $R_x(r)$ takes values between -1 and 1 and describes the average relation of the velocity between two positions, having distance r [14]. $R_x(r)$ is given by

$$R_x(r) \equiv \frac{\overline{u'_x(0)u'_x(r)}}{\overline{u'^2}}, \quad (2.17)$$

where u' is the velocity fluctuation and $\overline{u'^2}$ does not change with time for stationary turbulence. If u_0 is the integral velocity scale, u_0 can be defined in terms of the value of the velocity fluctuation around the mean for a three-dimensional velocity field as

$$\begin{aligned} \frac{3}{2}u_0^2 &= \frac{1}{2}(\overline{u_1'^2} + \overline{u_2'^2} + \overline{u_3'^2}) \\ u_0 &= \sqrt{\frac{2k}{3}}, \end{aligned} \quad (2.18)$$

where k is the turbulent kinetic energy.

Energy cascade: The concept of the energy cascade is attributed to Richardson [85]. His notion is that the large scales of turbulent motion are unstable and subsequently break up to form ever smaller vortices. Therefore, energy of the large scales is transferred to smaller scales, until the energy is dissipated into heat at the smallest scales as schematically seen in Fig. 2.1. The energy transfer (or dissipation) rate is independent of viscosity and can be defined as:

$$\varepsilon \equiv \frac{u_0^3}{\ell_0}. \quad (2.19)$$

The energy cascade is best illustrated by a plot of turbulence energy as a function of wave number (an inverse measure of length scale) as in Fig. 2.2.

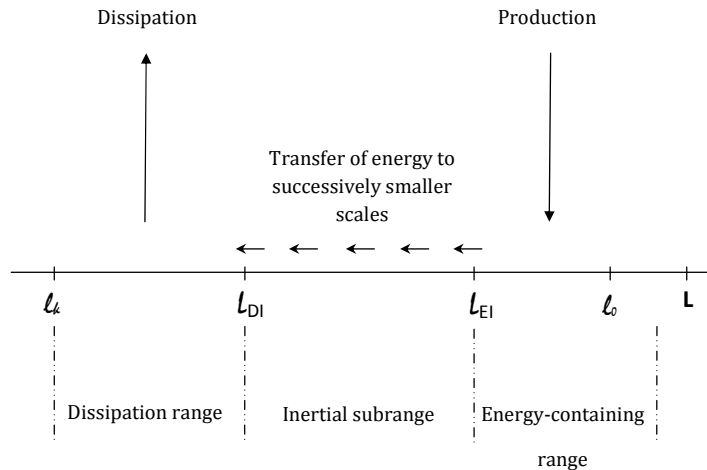


Figure 2.1: A schematic diagram [82] of energy cascade with eddy sizes ℓ (on a logarithmic scale) at very high Reynolds number, illustrating various length scales and ranges. $\ell_{DI} \approx 60\ell_K$ and $\ell_{EI} = \frac{1}{6}\ell_0$.

Kolmogorov Scale, ℓ_K : The Kolmogorov scale is the smallest length scale of turbulent flow. It represents the dimension at which the kinetic energy dissipates into internal energy (heat) by viscosity. The Kolmogorov scale, ℓ_K can be presented by the rate of dissipation of kinetic energy per unit mass, ε as

$$\ell_K \equiv \left(\frac{\nu^3}{\varepsilon} \right)^{\frac{1}{4}}, \quad (2.20)$$

where ν is the molecular kinematic viscosity.

The Kolmogorov velocity and time scales, for the smallest velocity and time, can be defined as

$$u_K \equiv (\nu\varepsilon)^{\frac{1}{4}}. \quad (2.21)$$

$$t_K = \frac{\ell_K}{u_K} \equiv \left(\frac{\nu}{\varepsilon} \right)^{\frac{1}{2}}. \quad (2.22)$$

2.1.3 Numerical Modelling of Turbulent Flows

According to Bardina *et al.* (1980), the dominant approaches for the modelling of turbulent flows can be classified into six categories [26]. However, three major simulation approaches are DNS, LES and RANS. Fundamentals of these methods are introduced briefly in this section. A more detailed description of LES, used in this research, will be presented in Chapter 3.

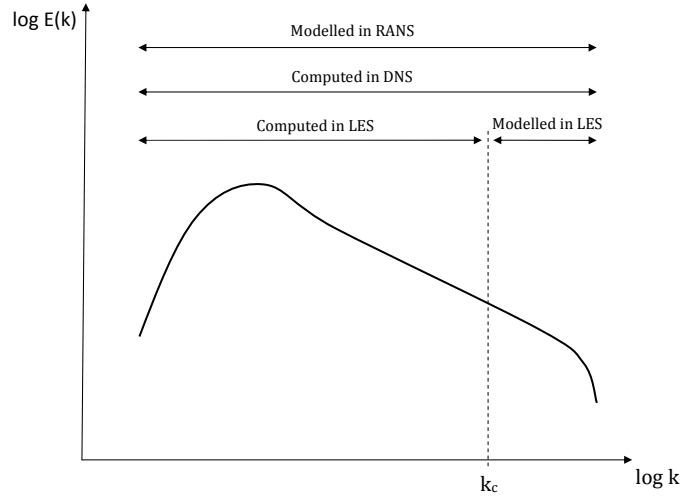


Figure 2.2: A turbulence energy spectrum plotted as a function of wave number [80]. The ranges of wave numbers (inversely proportional to the length scales) relevant for RANS, LES and DNS are indicated. k_c is the cut-off wave number used in LES.

2.1.3.1 Direct Numerical Simulation, DNS

DNS is the most accurate approach for turbulence simulation. The Navier-Stokes equations are discretized and solved directly without involving any modelling (as indicated in Fig. 2.2). However, since DNS requires the resolution of all relevant flow scales down to the Kolmogorov scale, very fine grids and time steps are necessary. According to Eqs. (2.19) and (2.20), the number of grid points for DNS, N_{DNS} , can be estimated as

$$N_{DNS} \sim \left(\frac{\ell_0}{\ell_K}\right)^3 \approx \left(\frac{\ell_0^3 \varepsilon^{\frac{3}{4}}}{\nu^{\frac{9}{4}}}\right) \approx \left(\frac{\ell_0^{\frac{9}{4}} u_0^{\frac{9}{4}}}{\nu^{\frac{9}{4}}}\right) = Re_0^{\frac{9}{4}}, \quad (2.23)$$

where Re_0 is the integral scale Reynolds number. As N_{DNS} scales with $Re_0^{\frac{9}{4}}$, the high processing speed machines which have enough storage are required for DNS. Therefore, DNS is currently limited to moderate Reynolds number flows. Even though the results of a DNS provide more detailed information than other methods, it is too expensive to use as a design methodology. For this reason, DNS is currently restricted to research environments.

2.1.3.2 Large Eddy Simulation, LES

In section 2.1.2.2, the concept of turbulent flows, comprising a range of different length and time scales, was introduced. In turbulent flows, the large scale (integral) turbulent motions, which depend on the nature of the flow and its boundaries, contain the major contribution to the statistics of mass, momentum, mixture fraction and species concentration. Based on this concept, the large scales are treated explicitly by applying a low-pass filter to the Navier-Stokes equation, while the effect of small scales are modelled in the LES approach as shown in Fig. 2.2. Therefore, computational costs are reduced using LES instead of DNS methods. Compared with other simulation methods, LES is an appropriate intermediate approach between DNS and RANS in terms of computational costs and the accuracy of simulation results. Since the LES method resolves large scales of turbulent motion, it provides more accurate results than RANS. Moreover, the computational power at the present time makes LES more attractive than DNS methodologies. Because of these reasons, LES is hoped to be applicable as a standard industry tool in the near future.

2.1.3.3 Reynolds Averaged Navier Stokes Equations, RANS

The oldest computational approach, which is still widely used today, is named in honor of Osborne Reynolds who first derived the decomposition method as shown in Eq. (2.15). In the RANS methodology, turbulent flows are defined in terms of temporal mean and statistical fluctuation using a decomposition method, as already discussed in the pre-

vious section. Consequently, the averaged conservation equations represent the mean properties and contain an unclosed term, the so-called Reynolds stress tensor which requires turbulence modelling for closure. One of the most common closure models is the $k - \varepsilon$ model, developed by Jones and Launder, 1972 [35]. This means the whole turbulent spectrum in RANS needs to be modelled. Therefore, the simulation results from RANS contain much less detail than DNS. However, this method is suitable for a simulation approach in industry, since results are produced with the lowest computational demand compared with other comparative techniques.

2.2 Non-Premixed Combustion

In non-premixed combustion, fuel and oxidizer are injected separately. Turbulent mixing (turbulent diffusion) and molecular diffusion transport reacting species into the flame front where they can react. Therefore, this type of flame is also known as diffusion flame. The flame front of non-premixed flames is located where fuel and oxidizer form a near-stoichiometric mixture. In order to understand this flame, a fundamental concept of chemical reaction kinetics will be explained first in this section. Subsequently, the concept of a conserved scalar (mixture fraction) will be introduced to solve the problem of mixing and turbulence chemistry interaction. Finally, an overview of turbulent combustion models will be discussed.

2.2.1 Chemical Reaction Kinetics

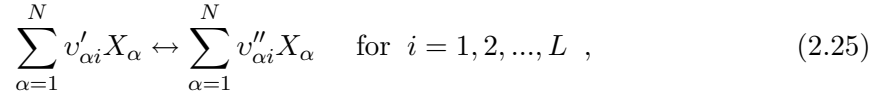
Consider a global reaction mechanism where the reaction of v_F moles of fuel (F) and v_O moles of oxidizer (O) produces v_P moles of products (P):



In reality, the global reaction (Eq. (2.24)) does not occur but rather a sequence of elementary reactions, which can be classified into four types of radical chain reactions. According to [108], these four types are:

1. chain initiation reaction (reactive species, radicals, are produced by stable species)
2. chain propagation (radicals react with stable species to form other radicals)
3. chain branching (radicals react with stable species to form more radicals)
4. chain termination (radicals react to stable species).

The collection of elementary reactions, so called detailed reaction mechanism, is necessary to accurately describe the combustion process. The elementary reactions can be written in their general form as



where $v'_{\alpha i}$ and $v''_{\alpha i}$ are stoichiometric coefficients of reactant and products, respectively. i denotes the number of chemical reactions for species α . The reaction rate, \mathfrak{R}_i , for the i th elementary reaction is

$$\mathfrak{R}_i = k_{fi} \prod_{\alpha} [c_{\alpha}]^{v'_{\alpha i}} - k_{ri} \prod_{\alpha} [c_{\alpha}]^{v''_{\alpha i}}, \quad (2.26)$$

where k_{fi} and k_{ri} represent the rate coefficients of forward and reverse reactions. The species concentration, c_{α} , can be calculated from $c_{\alpha} = \frac{\rho Y_{\alpha}}{W_{\alpha}}$, where W_{α} is the molecular weight. If the temperature range of interest is not too wide, the rate coefficient is expressed by the Arrhenius law as

$$k_{fi} = A_{fi} T^{\beta} \exp\left(\frac{-E_{a,i}}{R_u T}\right). \quad (2.27)$$

A denotes the pre-exponential factor, β is the empirical parameter, $E_{a,i}$ is the activation energy and R_u is the universal gas constant ($8.314 \frac{J}{Kmol}$). Using previous equations, the reaction source term, w_{α} , from Eq. (2.8) can be written as

$$w_{\alpha} = W_{\alpha} \sum_{i=1}^L (v''_{\alpha i} - v'_{\alpha i}) \mathfrak{R}_i. \quad (2.28)$$

However, even RANS or LES cannot solve for the mean or filtered species transport

equation since the average reaction source term is non-linear. This can be seen by considering the Zel'dovich NO ($N_2 + O = NO + N$) reaction. The reaction source term can be written as

$$w \propto AT^\beta \exp\left(\frac{-E_a}{R_u T}\right) Y_{N_2} Y_O. \quad (2.29)$$

Applying the decomposition method, Eq. (2.15), to temperature and species in Eq. (2.29), and using a Taylor expansion, the average source term in second-order terms is given by

$$\begin{aligned} \bar{w} \propto A\bar{T}^\beta \exp\left(\frac{-T_a}{\bar{T}}\right) \bar{Y}_{N_2} \bar{Y}_O \left\{ 1 + \frac{\overline{Y'_{N_2} Y'_O}}{\bar{Y}_{N_2} \bar{Y}_O} + \left(\beta + \frac{T_a}{\bar{T}}\right) \left(\frac{\overline{Y'_{N_2} T'}}{\bar{Y}_{N_2} \bar{T}} + \frac{\overline{Y'_O T'}}{\bar{Y}_O \bar{T}}\right) \right. \\ \left. + \frac{1}{2} \left[\beta(\beta - 1) + \frac{2(\beta - 1)T_a}{\bar{T}} + \frac{T_a^2}{\bar{T}^2} \right] \frac{\overline{T'^2}}{\bar{T}^2} + \dots \right\}, \quad (2.30) \end{aligned}$$

where $T_a = E_a/R_u$. Equation (2.30) shows that the turbulent correlation terms are unclosed. Moreover, the fluctuating quantities can become as large as a term including only the average quantities [47]. These errors cannot be ignored. Hence, a combustion model is required for turbulent reacting flows.

2.2.2 Mixture Fraction

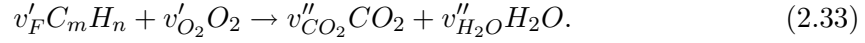
Mixture fraction is an important quantity in turbulent non-premixed combustion modelling. If equal diffusivity is assumed for all species, the non-premixed combustion problem can be reduced to a pure mixing problem. Mixing of fuel and oxidizer can be described by a conserved scalar called mixture fraction which is defined as

$$\xi = \frac{\text{mass of material having origin in the fuel stream}}{\text{mass of mixture}} \quad (2.31)$$

For two stream mixing, ξ is unity in the fuel stream and zero in the oxidizer stream. Within the flow field, the mixture fraction of element i ($i = \text{H, C or O}$) is given as the normalized mass fraction of this element,

$$\xi_i = \frac{Z_i - Z_{i,2}}{Z_{i,1} - Z_{i,2}}, \quad (2.32)$$

where Z_i is an element mass fraction of an element i , which denotes the ratio of the mass of an element i to the total mass. Subscripts 1 and 2 are applied for the species concentrations in the fuel and oxidizer respectively. For a general case of hydrocarbon fuel C_mH_n with air (where nitrogen is assumed as an inert gas), the global reaction can be written as



Mixture fraction of Eq. (2.33) is defined according to Bilger [7] as

$$\xi = \frac{\frac{Z_C}{mW_C} + \frac{Z_H}{nW_H} + 2\frac{Y_{O_2,2} - Z_O}{v'_{O_2} W_{O_2}}}{\frac{Z_{C,1}}{mW_C} + \frac{Z_{H,1}}{nW_H} + 2\frac{Y_{O_2,2}}{v'_{O_2} W_{O_2}}}, \quad (2.34)$$

where W_i is the molecular weight of an element i .

Since it is assumed that diffusivities are equal, the mixture fraction is independent on the choice of species i . The conservation equation of mixture fraction does not contain a reaction source term and is written as

$$\frac{\partial}{\partial t}(\rho\xi) + \frac{\partial}{\partial x_j}(\rho U_j \xi) = \frac{\partial}{\partial x_j} \left(\rho D \frac{\partial \xi}{\partial x_j} \right), \quad (2.35)$$

where D is the molecular diffusivity, which is assumed equal for all species.

2.2.3 Model Overview

For non-premixed flames, combustion normally occurs at length and time scales smaller than the Kolmogorov scales in which, given the computational capabilities of modern computers, cannot be resolved for high Re and practical devices. Thus, an averaging process is commonly applied to the governing equations in order to generate an equivalent set of equations that is governed by fewer scales. Then combustion modelling is required

for the closure of the averaged reaction rate that appears as an unclosed term in the averaged equations. Combustion models can be grouped into two main categories, fast chemistry and finite rate chemistry, depending on the assumptions of the relation between chemical and turbulent time scales. For the fast chemistry model, the chemical time scales are assumed to be shorter than all other flow characteristic times. Therefore, the reaction rate is associated directly to the turbulent mixing rate. Since fast chemistry is simple and convenient for numerical calculations, many combustion models are based on it, for instance, the equilibrium model and the eddy dissipation model (EDM) [58]. However, in many combustion phenomena, turbulent time scales vary considerably and can be shorter than the chemical time scales. Thus, the former assumption has become invalid. The finite rate chemistry models are introduced to overcome this deficiency. In the next section, some key features of both groups of chemistry models will be addressed (more details can be found in Peters [73] and Warnatz [108]).

2.2.3.1 Fast Chemistry Combustion Models

Burke-Schumann Analysis

One of the first modelling approaches for non-premixed combustion is the Burke-Schumann flame-sheet approach [13]. This is based on an irreversible one step global reaction (i.e. intermediates are not considered). Since this model is based on infinitely fast chemistry, fuel and oxidizer cannot be found together. An infinitely-thin flame sheet can be found at the stoichiometric mixture fraction, ξ_{st} , where reaction takes place (products reach their maximum value and there is no fuel or oxidizer). Outside of this thin sheet, the species mass fractions, temperature and fluid properties are piecewise linear functions of mixture fraction.

Equilibrium Chemistry Approach

The equilibrium model is an extension of the Burke-Schumann approach which allows reversible reactions to occur. Therefore, fuel, oxidizer and products can be co-existing. Species concentrations and temperature at equilibrium are calculated a priori and stored as a function of mixture fraction which is calculated by a moment solver. More details of this approach can be found in Warnatz *et al.* [108] (theory) and Forkel [27, 38] presents some successful applications of LES with this model.

The equilibrium solution is a suitable approach if predictions are required with minimum computational time. However, with real flames, the influence of fluid mechanics, such as fluid strain, needs to be considered because the fluid strain may cause flame extinction, which cannot be predicted by the equilibrium model. Furthermore, soot (existing in non-equilibrium state) cannot be predicted and other pollutants may be predicted incorrectly. Therefore, even under conditions where the temperature is close to the equilibrium, finite rate chemistry may govern pollutant concentration and has to be considered in the modelling process.

2.2.3.2 Finite Rate Chemistry Combustion Models

In reality, non-premixed flames can be predicted by the equilibrium model but some species are not in the equilibrium state. Some chemical reactions might occur in non-equilibrium state, e.g. close to the burner nozzle. Moreover, flame stretch, resulting from fluid strain, needs to be considered especially for non-premixed combustion where the mixing time scale can be shorter than the chemical reaction time scale. Three main combustion models based on finite rate chemistry are the laminar flamelet model (LFM), the conditional moment closure (CMC) model and the transported probability density function (PDF) method. The first two models are based on the additional assumption that fluctuations of the species can be associated with the fluctuations of mixture fraction (see section 2.2.2). For this reason, LFM and CMC models are also known as conserved scalar approaches. Brief descriptions of the LFM model and the PDF method are given in the following paragraphs, while the CMC model will be separately explained in Chapter 4.

Laminar Flamelet Model

The laminar flamelet model is based on the assumption that a turbulent flame can be described as an ensemble of stretched laminar flames, which are called flamelets. If the chemical time scales are assumed to be short enough ($Da \gg 1$, where Damköhler number, Da , is the ratio of flow times to chemical times), reactions occur in a thin surface near the stoichiometric mixture fraction, $\xi = \xi_{st}$, at a scale smaller than the smallest scales of turbulence (Kolmogorov scales). Turbulent eddies do not enter into this thin area (only controlling the flame at a large scale) and then the instantaneous structure of the reacting zone can be considered as laminar.

Proposed by Peters [72], the laminar flamelet equation is given for unity Lewis number as

$$\rho \frac{\partial Y_\alpha}{\partial t} = \rho N \frac{\partial^2 Y_\alpha}{\partial \xi^2} + w_\alpha. \quad (2.36)$$

The fluid strain is included in the model through the term known as the scalar dissipation rate, N . This scalar dissipation rate is equal to $D|\nabla\xi|^2$, where D is the molecular diffusivity ($D = \mu/\rho Sc$). It can be seen from the form of the above equation that the scalar dissipation rate represent the effects of diffusivity and fluid strain on the mixture fraction field [73]. If the scalar dissipation rate is high, a thin flame will be found due to stretching by turbulent strain. On the other hand, the thicker flame can be found for lower scalar dissipation rates. Therefore, the effect of finite rate chemistry is considered via this parameter. For steady flames, the transient term can be omitted and the stationary laminar flamelet model (SLFM) equation is expressed as

$$\rho N \frac{\partial^2 Y_\alpha}{\partial \xi^2} + w_\alpha = 0. \quad (2.37)$$

Normally, a library of species mass fractions Y_α can be pre-calculated and stored as a function of ξ and N so that $Y_\alpha = Y_\alpha(\xi, N)$. The average mass fraction in physical space of each species can be obtained by convolution of $Y_\alpha(\xi, N)$ with the joint PDF of ξ and N (the joint PDF and its shape will be outlined in section 4.4.1) as

$$\widetilde{Y}_\alpha = \int_0^1 \int_0^\infty Y_\alpha(\xi, N) \widetilde{P}(\xi, N) dN d\xi, \quad (2.38)$$

where $\widetilde{P}(\xi, N)$ is the joint PDF of ξ and N . Using a precomputed library makes the laminar flamelet model (LFM) a computationally efficient and attractive model that has been widely implemented for the computation of different turbulent diffusion flames [14].

In spite of the relative success of this methodology, issues arise in cases where the reaction zones are not thin [8]. For the prediction of pollutants formation, where the scalar dissipation is low, transient flamelet modelling is required.

Transported PDF Method

In the transported PDF approach, the turbulence-chemistry interaction is modelled by a transport equation for the joint PDF of the velocity and the reactive scalars. The chemical source term is closed but since the PDF represents only one-point statistics, models for the dissipation rate of scalars, the conditional velocity and the molecular mixing term are required [14].

A transport equation of the joint PDF can be derived from the instantaneous conservation equations of mass, momentum and scalars presented by Pope [82, 81]. The major attraction of the transported PDF method is that chemistry (reaction source term) can be treated exactly. Furthermore, the PDF transport equation is universally valid for all types of turbulent combustion (premixed, non-premixed and partially premixed combustion).

Due to its high dimensionality, the PDF transport equation is not solved directly, but via a Monte-Carlo particle method (i.e. PDF is represented by a large number of stochastic particles [108]). However, the numerical solution is computationally expensive since large numbers of particles are necessary in order to reduce statistical errors [14]. Recently, a stochastic field method which approximates the PDF by solving an Eulerian transport equations for stochastic entities (fields) becomes more popular (Valino [104], Soularda [91], Garmory [30] and Mustata [64]).

CHAPTER 3

The LES Method

Pioneering simulations on LES were introduced by Smagorinsky [90] and Lilly [55]) with motivation of meteorological applications. Later on LES was applied to turbulent channel flow by Deardorff [21], Schumann [89], Moin and Kim [63] and Piomelli [75] over the last two decades [82]. Nowadays, LES approaches have been extended to a wide variety of flow types. As explained in the previous chapter, the turbulent flow fields are separated into large scales, containing most of the energy and controlling the dynamics of the turbulence, and small scales. The large scales, which are larger than the computational mesh size, are solved directly by applying spatial filters to the Navier-Stokes equations, whereas the effects of small scales are modelled. In this chapter, spatial filtering and the governing equations of large scales using Favre averaging will be addressed. Then the modelling of the effects of the small scales will be discussed.

3.1 Spatial Filtering

Attributed to Leonard [53], the filtered value of any scalar $f(x, t)$ is defined explicitly as its convolution with a filter kernel G , according to

$$\bar{f}(\mathbf{x}, t) = \int_{\Omega} G(\mathbf{x} - \mathbf{x}'; \Delta) f(\mathbf{x}', t) d\mathbf{x}', \quad (3.1)$$

where $\mathbf{x} - \mathbf{x}'$ is the distance between two points and Δ is the filter width, which may vary with the position. The integration is carried out over the entire flow domain Ω . The filter

kernel G is a localized function which satisfies the normalization condition

$$\int_{\Omega} G(\mathbf{x} - \mathbf{x}'; \Delta) d\mathbf{x}' = 1. \quad (3.2)$$

Here, a box (or top-hat) filter has been employed which is defined in physical space as

$$G(\mathbf{x}) = G(x_1, x_2, x_3) = \begin{cases} 1/\Delta^3 & ; |x_i| \leq \Delta/2, i = 1, 2, 3 \\ 0 & ; \textit{otherwise}. \end{cases} \quad (3.3)$$

In practical applications, filtering occurs implicitly by using the finite volume method (FVM) as a discretisation technique for governing equations. The concept of FVM, dividing the domain into a number of cells, where the variables are located at the center point of each cell, also completes the task of low-pass filtering. Therefore, the discretised governing equations correspond to spatial filtering using an average grid size as a filter width, $\Delta = (\Delta_X \Delta_Y \Delta_Z)^{1/3}$. Based on the application of a spatial filter, the instantaneous variable $f(x, t)$ can be decomposed into its resolved $\bar{f}(x, t)$ and subgrid (unresolved) component $f'(x, t)$ as:

$$f(x, t) = \bar{f}(x, t) + f'(x, t). \quad (3.4)$$

The convolution of the instantaneous variable $f(x, t)$ with a filter conforms to the following rules:

$$\overline{af} = a\bar{f}, \quad (3.5)$$

$$\overline{f_1 + f_2} = \bar{f}_1 + \bar{f}_2, \quad (3.6)$$

where a is a constant. Contrary to RANS simulation methods, the LES perturbation leads to

$$\overline{f'} \neq 0, \quad (3.7)$$

$$\overline{\overline{f}} \neq \overline{f}, \quad (3.8)$$

$$\overline{\overline{f_1 \cdot f_2}} \neq \overline{f_1} \cdot \overline{f_2}, \quad (3.9)$$

where Eq. (3.8) is valid in general cases. However, filtered and doubly filtered are equal when a cut-off filter in the spectral space is used.

In turbulent flow, large density fluctuations may occur which cannot be neglected. Using density-weighted or "Favre" averages is a method to overcome this problem. The Favre filtering is defined as

$$\tilde{f}(x, t) = \frac{\overline{\rho(x, t)f(x, t)}}{\overline{\rho(x, t)}}. \quad (3.10)$$

Using Favre averages in the filtering equation (Eq. (3.1)), a mass-weighted Favre filtering is

$$\bar{\rho}\tilde{f}(\mathbf{x}, t) = \int_{\Omega} G(\mathbf{x} - \mathbf{x}'; \Delta)\rho f(\mathbf{x}', t)d\mathbf{x}'. \quad (3.11)$$

Using Favre filtering, a flow variable f can be decomposed into

$$f(x, t) = \tilde{f}(x, t) + f'(x, t), \quad (3.12)$$

where $\tilde{f}(x, t)$ represents the resolved filtered mean and $f'(x, t)$ also denotes the unresolved component for a density-weighted filter.

3.2 Filtered Governing Equations

3.2.1 Filtered Continuity Equation

Application of the Favre filtering operation to the mass conservation equation (Eq. (2.1)) leads to

$$\frac{\partial \bar{\rho}}{\partial t} + \frac{\partial}{\partial x_j} (\bar{\rho} \tilde{u}_j) = 0, \quad (3.13)$$

where \tilde{u}_j is the resolved velocity in the j direction.

3.2.2 Filtered Momentum Equation

The result of filtering of the conservation of momentum (Eq. (2.5)) yields

$$\frac{\partial}{\partial t} (\bar{\rho} \tilde{u}_i) + \frac{\partial}{\partial x_j} (\bar{\rho} \tilde{u}_i \tilde{u}_j) = \frac{\partial}{\partial x_j} \left[\mu \left(\frac{\partial \tilde{u}_i}{\partial x_j} + \frac{\partial \tilde{u}_j}{\partial x_i} \right) - \frac{2}{3} \mu \delta_{ij} \frac{\partial \tilde{u}_k}{\partial x_k} \right] - \frac{\partial \bar{p}}{\partial x_i} + \bar{\rho} g_i, \quad (3.14)$$

where \bar{p} is the filtered pressure. Since the convective term is non-linear ($\widetilde{u_i u_j} \neq \tilde{u}_i \tilde{u}_j$), the filtering result of this term is closed by the addition of an unknown term called subgrid-scale Reynolds stress, τ_{ij}^{sgs}

$$\bar{\rho} \widetilde{u_i u_j} = \bar{\rho} \tilde{u}_i \tilde{u}_j + \tau_{ij}^{sgs}. \quad (3.15)$$

With the resolved rate of strain $\frac{1}{2} \left(\frac{\partial \tilde{u}_i}{\partial x_j} + \frac{\partial \tilde{u}_j}{\partial x_i} \right) = \widetilde{S}_{ij}$, the filtered momentum equation can be rewritten as

$$\frac{\partial}{\partial t} (\bar{\rho} \tilde{u}_i) + \frac{\partial}{\partial x_j} (\bar{\rho} \tilde{u}_i \tilde{u}_j) = \frac{\partial}{\partial x_j} \left[\overbrace{2\mu \widetilde{S}_{ij} - \frac{2}{3} \mu \delta_{ij} \widetilde{S}_{kk}}^{\widetilde{\tau}_{ij}} \right] - \frac{\partial \tau_{ij}^{sgs}}{\partial x_j} - \frac{\partial \bar{p}}{\partial x_i} + \bar{\rho} g_i, \quad (3.16)$$

where the first term on the RHS denotes the resolved stress tensor, $\widetilde{\tau}_{ij}$. In this equation, the subgrid-scale Reynolds stress (also known as unresolved Reynolds stress), τ_{ij}^{sgs} is unclosed

and therefore, needs to be modelled, which will be discussed in section 3.3.

3.2.3 Filtered Species Transport Equation

For the LES of non-premixed combustion using the conserved scalar approach, an additional transport equation for mixture fraction (as discussed in section 2.2.2) needs to be solved. The filtered transport equation for mixture fraction reads

$$\frac{\partial}{\partial t}(\bar{\rho}\tilde{\xi}) + \frac{\partial}{\partial x_j}(\bar{\rho}\tilde{u}_j\tilde{\xi}) = \frac{\partial}{\partial x_j}\left(\bar{\rho}D\frac{\partial\tilde{\xi}}{\partial x_j}\right). \quad (3.17)$$

Applying the same method as for the filtered momentum equation, here the unknown mixture fraction-velocity correlation, so called subgrid-scale scalar flux, J_j^{sgs} , is given by

$$\bar{\rho}\tilde{u}_j\tilde{\xi} = \bar{\rho}\tilde{u}_j\tilde{\xi} + J_j^{sgs}. \quad (3.18)$$

Consequently Eq. (3.17) can be rewritten as

$$\frac{\partial}{\partial t}(\bar{\rho}\tilde{\xi}) + \frac{\partial}{\partial x_j}(\bar{\rho}\tilde{u}_j\tilde{\xi}) = \frac{\partial}{\partial x_j}\left(\bar{\rho}D\frac{\partial\tilde{\xi}}{\partial x_j}\right) - \frac{\partial J_j^{sgs}}{\partial x_j}, \quad (3.19)$$

where the subgrid-scale scalar flux appears in unclosed form and requires modelling.

3.3 Subgrid-scale Modelling

According to Fig. 2.2, the main part of the turbulent energy spectrum is resolved in LES approach. However, the remaining subgrid-scale contribution needs to be modelled. There are two models being addressed in this section to apply for subgrid-scale Reynolds stress and subgrid-scale scalar flux.

3.3.1 Subgrid-scale Reynolds Stress Models

3.3.1.1 Smagorinsky Model

The most commonly used LES subgrid model was proposed by Smagorinsky [90]. This is widely applied by researchers due to its simple formulation. This model uses the

Boussinesq assumption (viscous, or Reynolds, stress is proportional to the strain rate tensor as in Eq. (2.3)) which is classified into eddy viscosity models. The Smagorinsky model is based on the idea that transport and dissipation are increased by the effects of the subgrid-scale Reynolds stress. Since these phenomena are analogous to the effect of viscosity in laminar flow [26], the Smagorinsky model represents the subgrid-scale stress through the eddy viscosity, μ_t .

$$\tau_{ij}^{sgs} - \frac{1}{3}\delta_{ij}\tau_{kk}^{sgs} = -2\mu_t(\tilde{S}_{ij} - \frac{1}{3}\delta_{ij}\tilde{S}_{kk}), \quad (3.20)$$

$$\mu_t = \bar{\rho}(C_s\Delta)^2 \|\tilde{S}\|, \quad (3.21)$$

where C_s denotes the Smagorinsky constant. $\|\tilde{S}\|$ is the Frobenius norm of the resolved strain rate tensor $\sqrt{2\tilde{S}_{ij}\tilde{S}_{ij}}$. Using the Smagorinsky model (Eq. (3.20)), the closed form of the filtered momentum equation is

$$\frac{\partial}{\partial t}(\bar{\rho}\tilde{u}_i) + \frac{\partial}{\partial x_j}(\bar{\rho}\tilde{u}_i\tilde{u}_j) = 2\frac{\partial}{\partial x_j}\left[(\mu + \mu_t)\left(\tilde{S}_{ij} - \frac{1}{3}\delta_{ij}\tilde{S}_{kk}\right)\right] - \frac{\partial\bar{p}}{\partial x_i} + \bar{\rho}g_i, \quad (3.22)$$

The range of possible values for the Smagorinsky constant C_s is between 0.0065 and 0.2 [26] depending on the flow configuration. However, "the Smagorinsky model has obviously dissipative nature and it cannot account for the reverse energy transfer from the small scales to the large scales" [22], so called backscatter at near-wall locations. Moreover, the Smagorinsky model can produce a non-zero eddy viscosity, regardless of the flow type (laminar or turbulent flow). To overcome these difficulties in the Smagorinsky model, a dynamic model has been proposed in order to determine an appropriate local value of the Smagorinsky coefficient. Following [82] and [80], the dynamic model will be explained briefly in the next section.

3.3.1.2 Dynamic Model

First proposed by Germano *et al.* [31], the dynamic model was further modified by Lilly [56] and Piomelli and Liu [76] to estimate appropriate values for this constant, which is applied in this work. The concept of the dynamic model is based on the scale similarity assumption (i.e. the information contained in the smallest resolved scale motions may be used for the largest subgrid-scale modelling). In the dynamic model, a test filter (denoted by an over-hat) having a size $\widehat{\Delta}$ larger than the LES filter width Δ is introduced. It was found that $\widehat{\Delta} = 2\Delta$ is an optimum value [31]. The subgrid-scale Reynolds stress, τ_{ij}^{sgs} , based on an LES filtering operation is written as

$$\tau_{ij}^{sgs} = \bar{\rho}(\widehat{u_i u_j} - \widetilde{u_i u_j}). \quad (3.23)$$

The subtest-scale stress, T_{ij}^{sgs} , based on a test filtering operation for conservation of momentum is

$$T_{ij}^{sgs} = \widehat{\bar{\rho}}(\widehat{\widehat{u_i u_j}} - \widehat{\widetilde{u_i u_j}}). \quad (3.24)$$

From the Smagorinsky model, both stress tensors, τ_{ij}^{sgs} and T_{ij}^{sgs} can be estimated as

$$\tau_{ij}^{sgs} - \frac{1}{3}\delta_{ij}\tau_{kk}^{sgs} = -2\bar{\rho}(C_s\Delta)^2 \|\tilde{S}\| (\tilde{S}_{ij} - \frac{1}{3}\delta_{ij}\tilde{S}_{kk}) = -2C_s^2\beta_{ij}, \quad (3.25)$$

$$T_{ij}^{sgs} - \frac{1}{3}\delta_{ij}T_{kk}^{sgs} = -2\widehat{\bar{\rho}}(C_s\widehat{\Delta})^2 \|\widehat{S}\| (\widehat{S}_{ij} - \frac{1}{3}\delta_{ij}\widehat{S}_{kk}) = -2C_s^2\alpha_{ij}, \quad (3.26)$$

where β and α are introduced to simplify the notation. Applying a test filter to Eq. (3.23) and subtracting the result from Eq. (3.24), the Germano identity, L_{ij} , is

$$L_{ij} = \widehat{\bar{\rho}}(\widehat{\widetilde{u_i u_j}} - \widehat{\widetilde{u_i u_j}}) = T_{ij}^{sgs} - \widehat{\tau_{ij}^{sgs}}. \quad (3.27)$$

Inserting Eqs. (3.25) and (3.26) into Eq. (3.27), the Germano identity can be rewritten as

$$L_{ij} - \frac{1}{3}\delta_{ij}L_{kk}^{sgs} = 2(\widehat{C_s^2\beta_{ij}} - C_s^2\alpha_{ij}), \quad (3.28)$$

where the deviatoric part of L_{ij} is $L_{ij}^d \equiv L_{ij} - \frac{1}{3}\delta_{ij}L_{kk}^{sgs}$ and therefore the following expression leads to

$$L_{ij}^d = 2(\widehat{C_s^{*2}\beta_{ij}} - C_s^2\alpha_{ij}), \quad (3.29)$$

where the coefficient C_s^{*2} is assumed to be known (this value can be estimated from various methods, such as an extrapolated constant, C_s^2 , coming from a previous time step). In the localized dynamic approach of Piomelli and Liu [76], the parameter C_s^2 is a function of space and time. Applying the least square sense for Eq. (3.29) to minimize the residual as suggested by Piomelli and Liu [76], the parameter C_s^2 determined by

$$C_s^2(x, t) = -\frac{1}{2} \frac{(L_{ij}^d - 2\widehat{C_s^{*2}\beta_{ij}})\alpha_{ij}}{\alpha_{mn}^2}, \quad (3.30)$$

where $\alpha_{mn}\alpha_{mn}$ is in wall-bounded flows which becomes small only where the numerator vanishes. In order to avoid negative and very large C_s values (which may lead to instability), clipping of the model parameter is applied in this work as $C_s^2 = \max(\min(C_s^2, 1.5), 0.0)$.

3.3.2 Subgrid-scale Scalar Flux Model

The subgrid-scale scalar flux in Eq. (3.18) can be modelled by a gradient diffusion assumption and written as

$$J_j^{sgs} = -\rho D_t \frac{\partial \tilde{\xi}}{\partial x_j}, \quad (3.31)$$

where D_t is a turbulent diffusivity which can be expressed in a similar way as the molecular diffusivity by using the turbulent viscosity, ν_t , and a turbulent Schmidt number, Sc_t ,

$$D_t = \frac{\nu_t}{Sc_t}, \quad (3.32)$$

where the modelling of $\nu_t = \mu_t/\rho$ can come from the Smagorinsky or dynamic model. For gases, the Schmidt number is commonly assumed to be 0.7 and the turbulent Schmidt number is recommended as 0.4 for LES [79]. However, the justification of both values is included in parametric studies of this work and these results can be found in Chapter 6. Inserting Eq. (3.31) into Eq. (3.19), the closed form of filtered transport equation for mixture fraction can be obtained

$$\frac{\partial}{\partial t}(\bar{\rho}\tilde{\xi}) + \frac{\partial}{\partial x_j}(\bar{\rho}\tilde{U}_j\tilde{\xi}) = \frac{\partial}{\partial x_j}\left(\bar{\rho}(D + D_t)\frac{\partial\tilde{\xi}}{\partial x_j}\right). \quad (3.33)$$

3.4 Other Models

In order to perform CMC computations for combustion, some variables have to be estimated or modelled from the LES variables. These variables are the subgrid-scale variance, $\widetilde{\xi''^2_{sgs}}$ (used to presume the filtered probability density function (FDF)) and the filtered scalar dissipation (\tilde{N}).

3.4.1 Variance of Mixture Fraction Model

To determine the presumed FDF for CMC (detailed in section 4.4.1), the filtered mixture fraction and the subgrid-scale variance, $\widetilde{\xi''^2_{sgs}}$, are required. The subgrid variance can be expressed by a gradient-type model as proposed by Pierce and Moin [74], based on the assumption that the subgrid scale is in equilibrium and thus the production rate of $\widetilde{\xi''^2_{sgs}}$ should be equal to the subgrid-scale scalar dissipation rate, \tilde{N}_{sgs} , as $\tilde{N}_{sgs} \sim \widetilde{\xi''^2_{sgs}} \|\tilde{S}\|$.

$$\widetilde{\xi''^2_{sgs}} = C_\xi \Delta^2 \left(\frac{\partial\tilde{\xi}}{\partial x_j} \frac{\partial\tilde{\xi}}{\partial x_j} \right), \quad (3.34)$$

where C_ξ is a constant. Even though there is a calculation and calibration method [11], a constant value of 0.2 (contributed to the procedure suggested by Branley [11]), is adopted to be used in a parametric study of this work.

3.4.2 Scalar Dissipation Model

Another variable required for CMC is the filtered scalar dissipation, \tilde{N} , which is composed of two terms and modelled, as proposed by Pierce and Moin [74]

$$\begin{aligned}
 \tilde{N} &= \tilde{N}_{resolved} + \tilde{N}_{sgs} \\
 &= \left(\frac{\nu}{Sc} + \frac{\nu_t}{Sc_t} \right) \frac{\partial \tilde{\xi}}{\partial x_j} \frac{\partial \tilde{\xi}}{\partial x_j} \\
 &= \left(\frac{\nu}{Sc} \right) \frac{\partial \tilde{\xi}}{\partial x_j} \frac{\partial \tilde{\xi}}{\partial x_j} + \left(\frac{\nu_t}{Sc_t} \frac{c_d}{\Delta^2} \right) \widetilde{\xi_{sgs}''^2}, \tag{3.35}
 \end{aligned}$$

where c_d is a constant number for the subgrid-scale scalar dissipation modelling and a value of 11 is applied in this work. The turbulent viscosity, ν_t , can be obtained from the Smagorinsky or the dynamic model as explained in the previous section.

CHAPTER 4

The CMC Model

The conditional moment closure (CMC) model will be described in more detail since it is the combustion model of choice in this study. The CMC method was initially developed independently by Klimenko [45] and Bilger [10] and later reviewed by them in a joint paper [47]. Extensive studies have shown encouraging results when the method is coupled with a RANS approach [16, 25, 86]. More recently, the CMC approach has been presented in the LES framework as well. To the present day, the LES-CMC approach has been applied to study Sandia Flame D [68], Sandia Flame F [29], bluff-body flames [65, 101, 102], lifted flames [66, 67, 92, 93] and forced (or spark-) ignition [100]. Moreover, it has been validated by DNS results for turbulent non-premixed combustion [41] and premixed compressible flames [99].

The basic idea of the CMC model for non-premixed flames is the strong relation between reactive species and the mixture fraction and thus fluctuations of the reactive species in physical space can be connected to fluctuations of the same species in the mixture fraction space [23]. Based on this approach, Q_α denotes the conditionally filtered species mass fraction, \widetilde{Y}_α , conditioned on mixture fraction ξ within sample space η defined as

$$Q_\alpha = (\widetilde{Y_\alpha | \xi = \eta}) \equiv \widetilde{Y_\alpha | \eta}. \quad (4.1)$$

In this chapter, the conditional filtering is introduced first, followed by conditionally filtered species transport equations (in both conservative and non-conservative formula-

tions). The comparisons between both formulations and how the unclosed terms of the equations are treated in the formulations will be discussed. Afterwards, the coupling of the CMC model with the LES solver will be explained.

4.1 Conditional Filtering

Unlike RANS-CMC, which was derived by Bilger [47] using the decomposition method, the LES-CMC derivation is based on the idea of a suitably-defined conditional filter in order to ensure the consistency between the CMC equations and the filtered Navier-Stokes equations solved in LES. Based on fine-grained PDF, ψ_η , which is a generalized function [54], the conditional filtering procedure can be defined. The fine-grained PDF [28] is

$$\psi_\eta = \delta[\eta - \xi(x, t)], \quad (4.2)$$

where δ denotes a Dirac delta function and η is the sample space of mixture fraction ξ . The properties of ψ_η can be defined by the convolution with a continuous function $F(\eta)$ which has to be smooth and decay to zero when $\eta \rightarrow \pm\infty$ [68].

Using this ψ_η , the conditional filtering procedure for a scalar Φ was introduced by Steiner and Bushe [94] as

$$\overline{\Phi | \eta} \equiv \frac{\int_{\mathbf{V}} \Phi \psi_\eta G(\mathbf{x} - \mathbf{x}'; \Delta) d\mathbf{V}'}{\overline{P}(\eta)}, \quad (4.3)$$

where the filtered probability density function (FDF) $\overline{P}(\eta)$ is given by [68]

$$\overline{P}(\eta) \equiv \int_{\mathbf{V}} \psi_\eta G(\mathbf{x} - \mathbf{x}'; \Delta) d\mathbf{V}'. \quad (4.4)$$

In the above equations the filtering process is performed through the G function, Eq. (3.1), over a filter width Δ . V is the volume of the whole computational domain.

The relation between the unconditionally filtered and conditionally filtered scalar can be defined by using $\overline{P}(\eta)$ as

$$\bar{\Phi} = \int_0^1 \overline{\Phi | \eta} \bar{P}(\eta) d\eta. \quad (4.5)$$

For variable density flows, the Favre filtered probability density function is defined by

$$\tilde{P}(\eta) \equiv \frac{1}{\bar{\rho}} \int_{\mathbf{V}} \rho \psi_{\eta} G(\mathbf{x} - \mathbf{x}'; \Delta) d\mathbf{V}'. \quad (4.6)$$

Furthermore, the application of Favre filtering for the scalar (i.e. $\bar{\rho}_{\eta} \tilde{\Phi}_{\eta} = \overline{\rho \Phi | \eta}$, where tilde presents Favre filtering) is required so that the Favre conditional filtering procedure for the scalar Φ (in any LES grid) can be rewritten as [18]

$$\widetilde{\Phi | \eta} \equiv \frac{\int_{\mathbf{V}} \rho \Phi \psi_{\eta} G(\mathbf{x} - \mathbf{x}'; \Delta) d\mathbf{V}'}{\int_{\mathbf{V}} \rho \psi_{\eta} G(\mathbf{x} - \mathbf{x}'; \Delta) d\mathbf{V}'}. \quad (4.7)$$

The unconditional Favre filtered value of the scalar Φ can be calculated as

$$\tilde{\Phi} = \int_0^1 \widetilde{\Phi}_{\eta} \tilde{P}(\eta) d\eta, \quad (4.8)$$

where $\widetilde{\Phi}_{\eta} \equiv \widetilde{\Phi | \eta}$.

4.2 Non-Conservative CMC Formulation

According to Navarro *et al.* [68], three assumptions for deriving the LES-CMC equations are required which are:

1. High Reynolds number assumptions that are consistent with the primary closure assumption in the LES context (details in [68, 47])
2. Unity Lewis numbers (that guarantee equal diffusivities)
3. Brownian motion of diffusion in scalar space.

The traditional equations of CMC appear in non-conservative form then the non-conservative CMC species transport equation originated from the transport equation for fine-grained PDF and for ψY_i [68] can be written as

$$\gamma \frac{\partial Q_\alpha}{\partial t} + \gamma \tilde{u}_{j,\eta} \frac{\partial Q_\alpha}{\partial x_j} = \gamma \tilde{w}_{\alpha,\eta} + \gamma \tilde{N}_\eta \frac{\partial^2 Q_\alpha}{\partial \eta^2} + \gamma e_y, \quad (4.9)$$

or as

$$\frac{\partial Q_\alpha}{\partial t} + \tilde{u}_{j,\eta} \frac{\partial Q_\alpha}{\partial x_j} = \tilde{w}_{\alpha,\eta} + \tilde{N}_\eta \frac{\partial^2 Q_\alpha}{\partial \eta^2} + e_y, \quad (4.10)$$

where γ denotes $\bar{\rho}_\eta \tilde{P}(\eta)$ and $\tilde{P}(\eta)$ is detailed in section 4.4.1. $Q_\alpha = \widetilde{Y_\alpha | \eta}$ is the conditionally filtered species mass fraction. \tilde{u}_η is the conditionally filtered velocity, $\tilde{w}_{\alpha,\eta}$ is the conditionally filtered reaction source term and \tilde{N}_η is the conditionally filtered scalar dissipation rate. The term e_y accounts for the fluctuations around the conditional mean of the convective part and thus it is given as

$$e_y = -\frac{1}{\gamma} \frac{\partial}{\partial x_j} \left[\gamma \left(\widetilde{(u_j Y_\alpha) | \eta} - \tilde{u}_{j,\eta} Q_\alpha \right) \right], \quad (4.11)$$

where e_y is the sub-grid scale conditional flux. The non-conservative conditional enthalpy equation is

$$\frac{\partial Q_h}{\partial t} + \tilde{u}_{j,\eta} \frac{\partial Q_h}{\partial x_j} = \tilde{w}_{R,\eta} + \tilde{N}_\eta \frac{\partial^2 Q_h}{\partial \eta^2} + e_h, \quad (4.12)$$

where $Q_h = \widetilde{h | \eta}$ is the conditional enthalpy and $\tilde{w}_{R,\eta}$ is the conditionally filtered radiation term (heat loss due to radiation). The sub-grid scale conditional flux of enthalpy e_h is

$$e_h = -\frac{1}{\gamma} \frac{\partial}{\partial x_j} \left[\gamma \left(\widetilde{(u_j h) | \eta} - \tilde{u}_{j,\eta} Q_h \right) \right]. \quad (4.13)$$

The sub-grid scale conditional fluxes of both CMC formulations (e_y and e_h from Eqs. (4.10) and (4.12)) are modelled by a gradient type approach which gives

$$e_y = \frac{1}{\gamma} \frac{\partial}{\partial x_j} \left(\gamma D_\eta \frac{\partial Q_\alpha}{\partial x_j} \right), \quad (4.14)$$

and

$$e_h = \frac{1}{\gamma} \frac{\partial}{\partial x_j} \left(\gamma D_\eta \frac{\partial Q_h}{\partial x_j} \right), \quad (4.15)$$

where D_η is a conditional turbulent diffusivity (details in section 4.4.5) which is assumed to be equal for all species.

4.3 Conservative CMC Formulation

The idea of the conservative conditional species transport equations was suggested by Cleary [16], and details regarding the derivation of the conservative CMC equation can be found in appendix A. This originated by combining the FDF transport equation and the conditional species transport equation. The conditionally filtered species transport equation reads:

$$\gamma \frac{\partial Q_\alpha}{\partial t} + \frac{\partial}{\partial x_j} (\gamma \tilde{u}_{j,\eta} Q_\alpha) = \gamma \tilde{w}_{\alpha,\eta} + \gamma \tilde{N}_\eta \frac{\partial^2 Q_\alpha}{\partial \eta^2} + Q_\alpha \frac{\partial}{\partial x_j} (\gamma \tilde{u}_{j,\eta}) + \gamma e_y. \quad (4.16)$$

The first term on the LHS describes temporal changes of the conditionally filtered species mass fraction Q_α . The second term on the LHS and the third term on the RHS represent convection of Q_α . The other terms on the RHS account for the chemical reaction and diffusion in mixture fraction space.

Using the same procedure, Klimenko and Bilger [47] suggested that the conditional enthalpy equation can be expressed as

$$\gamma \frac{\partial Q_h}{\partial t} + \frac{\partial}{\partial x_j} (\gamma \tilde{u}_{j,\eta} Q_h) = \gamma \tilde{w}_{R,\eta} + \gamma \tilde{N}_\eta \frac{\partial^2 Q_h}{\partial \eta^2} + Q_h \frac{\partial}{\partial x_j} (\gamma \tilde{u}_{j,\eta}) + \gamma e_h, \quad (4.17)$$

The difference of this form over a non-conservative example is the convective terms (second term on the LHS and the third term on the RHS) in Eqs. (4.16) and (4.17) which appear inside the divergence (i.e. convective terms are conserved). This leads to the usage of FDF information, Eq. (4.18), to calculate the convective flux in each direction when

the finite volume method (FVM) is applied for the spatial discretisation (section 5.1). For example, if the fluid flow from a cell having high FDF to the adjacent cell having low FDF, a high value of convective flux in the flow direction is calculated in the cell having a low FDF value for the CMC conservative form. Consequently, the conservative formulation requires a shorter time period to convect conditionally filtered mass fraction of scalar quantities in that direction compared with the non-conservative formulation. The opposite results will happen if the FDF ratio is smaller than one.

4.4 Closure

In the CMC context of the Filtered Density Function (FDF), the conditional reaction source term (\tilde{w}_η), the conditionally filtered scalar dissipation (\tilde{N}_η), the conditionally filtered velocity ($\tilde{u}_{j,\eta}$), and the conditional turbulent diffusivity (D_η) requires further modelling, which will be described within this section.

4.4.1 Filtered Density Function

The unconditionally filtered values of the reactive scalars can be calculated by convolution of the conditional averages with the FDF (see Eq. (4.8)) of mixture fraction. The FDF can be either calculated from the solution of an extra transport equation for the FDF or, as it is common practice in the CMC methodology, to presume its shape using two parameters: the filtered mixture fraction, $\tilde{\xi}$, and modelling the subgrid-scale variance of mixture fraction, $\tilde{\xi}_{sgs}''^2$. According to Cook and Peters [19, 73], the shape of the subgrid-scale PDF is close to a beta function. Thus, for the presumed FDF, the beta function (β -function) is often applied and defined as

$$\tilde{P}(\eta) = \frac{\eta^{\alpha-1}(1-\eta)^{\beta-1}}{B(\alpha, \beta)}, \quad (4.18)$$

where B is beta-function which can be defined in terms of Gamma function, Γ , [48] as

$$B(\alpha, \beta) = \frac{\Gamma(\alpha)\Gamma(\beta)}{\Gamma(\alpha + \beta)}, \quad (4.19)$$

and Γ is

$$\Gamma(x) = \int_0^{+\infty} e^{-\eta} \eta^{x-1} d\eta = (x-1)!. \quad (4.20)$$

The FDF parameters α and β are

$$\begin{aligned} \alpha &= \tilde{\xi} \left(\frac{\tilde{\xi}(1-\tilde{\xi})}{\xi_{sgs}''^2} - 1 \right) \\ \beta &= \frac{\alpha}{\tilde{\xi}} - \alpha. \end{aligned} \quad (4.21)$$

The shapes of the β -PDF which depend on two parameters α and β are illustrated in Fig. 4.1, where x denotes the sample space of mixture fraction. The β -function is defined only for $0 < \eta < 1$ which is appropriate for the CMC methodology since it represents the FDF of mixture fraction. Both boundaries are either zero or asymptotic to infinity.

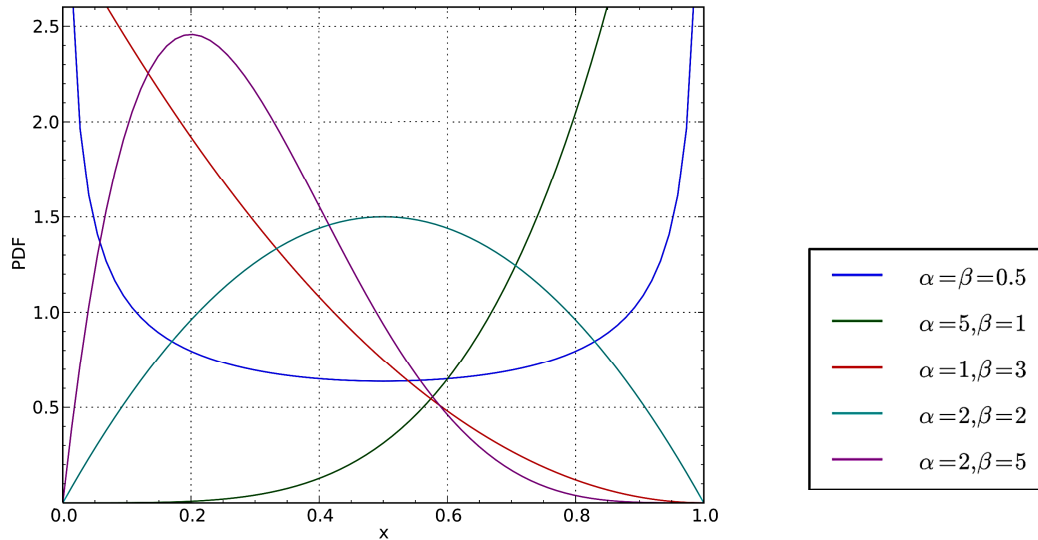


Figure 4.1: Behaviour of the β -function for different sets of parameter α and β [109].

4.4.2 First Order Closure of the Reaction Source Term

In general, the reaction source term is a function of the species mass fractions, Y_1, Y_2, \dots, Y_n and enthalpy, h , which can be written as $w_\alpha = w_\alpha(\mathbf{Y}, h)$, where $\mathbf{Y} \equiv (Y_1, Y_2, \dots, Y_n)$. However, the relationship is non-linear and thus the filtered values of w_α are not functions of the filtered mass fractions and filtered enthalpy, i.e. $\widetilde{w}_\alpha(\mathbf{Y}, h) \neq w_\alpha(\widetilde{\mathbf{Y}}, \widetilde{h})$.

Nevertheless in the CMC model, the conditionally filtered mass fraction, $Q_\alpha \equiv \widetilde{Y}_\alpha|_\eta$, provides more detailed characteristics of the reactive species than the unconditional filtered value, \widetilde{Y}_α . The conditional fluctuations (i.e. $Y'_\alpha = Y_\alpha - Q_\alpha$) in the conditional reaction source term may be neglected because these values are small (smaller than the unconditional fluctuations, i.e. $Y'_\alpha = Y_\alpha - \widetilde{Y}_\alpha$). From Eq. (2.29), the second-order accuracy of the conditionally filtered reaction source term can be written as

$$\begin{aligned} \widetilde{w}|_\eta &\propto A Q_T^\beta \exp\left(\frac{-T_a}{T}\right) Q_{N_2} Q_O \left\{ 1 + \frac{\langle Y''_{N_2} Y''_O | \eta \rangle}{Q_{N_2} Q_O} + \left(\beta + \frac{T_a}{Q_T} \right) \right. \\ &\quad * \left. \left(\frac{\langle Y''_{N_2} T'' | \eta \rangle}{Q_{N_2} Q_T} + \frac{\langle Y''_O T'' | \eta \rangle}{Q_O Q_T} \right) + \frac{1}{2} \left[\beta(\beta - 1) + \frac{2(\beta - 1)T_a}{Q_T} + \frac{T_a^2}{Q_T^2} \right] \frac{\langle T''^2 | \eta \rangle}{Q_T^2} \right\}, \end{aligned} \quad (4.22)$$

where $Q_T \equiv \widetilde{T}|_\eta$. It can be seen from Eq. (4.22) that a first-order closure can be applied if the conditional fluctuations of species mass fractions and temperature are small relative to the square of their conditional means [47]. Thus, the first-order conditional chemical source term can be calculated from the conditional averages of the scalars

$$\widetilde{w}_{\alpha, \eta} = \widetilde{w}_\alpha|_\eta = w_\alpha(Q_1, Q_2, \dots, Q_n, Q_h), \quad (4.23)$$

and the terms involving the conditional fluctuations are neglected.

4.4.3 Conditionally Filtered Scalar Dissipation

According to Navarro *et al.* [68], conditional scalar dissipation can be obtained by conditioning the filtered scalar dissipation on the mixture fraction such as,

$$\tilde{N}_\eta = \tilde{N} \mid \eta \approx \tilde{N}, \quad (4.24)$$

where the term \tilde{N} is modelled by using Eq. (3.35) and the conditionally filtered scalar dissipation of a LES cell \tilde{N}_η is considered to be equal to the unconditional value for the whole mixture fraction space.

4.4.4 Conditionally Filtered Velocity

For RANS, Klimenko and Bilger [47] introduced a linear approximation for the conditional expectation of velocity, which is given by

$$\langle u_j \mid \eta \rangle = u_j + \frac{\langle u'_j \xi' \rangle}{\langle \xi'^2 \rangle} (\eta - \langle \xi \rangle), \quad (4.25)$$

where the brackets $\langle \rangle$ denote ensemble averaging. $\langle u'_j \xi' \rangle$ denotes the unconditional covariance of turbulent flux in the j direction. However, this model has not been validated for LES [100]. Following the ideas of section 4.4.3, a direct model for the conditional velocity is not applied. Alternatively, the filtered values of the velocity from the LES grid are used by conditioning the corresponding filtered value on the mixture fraction. This method proposed by Navarro *et al.* [68] has been applied in this study as

$$\tilde{u}_{j,\eta} = \tilde{u}_j \mid \eta \approx \tilde{u}_j. \quad (4.26)$$

4.4.5 Conditional Turbulent Diffusivity

The conditional turbulent diffusivity, D_η , can be modelled using the turbulent diffusivity value from LES. Cleary [17] has proposed the modelling of this term which considers turbulent diffusivity to be the same value for the whole mixture fraction space as

$$D_\eta = D_t \mid \eta = D_t, \quad (4.27)$$

where D_t is the turbulent diffusivity (as explained in section 3.3.2) and Eq. (4.27) is used throughout this work.

4.5 Implementation of the CMC Model

As discussed in Chapter 3, the in-house code LES-BOFFIN is used as the flow solver (solving for mass, momentum and mixture fraction equations), whereas the CMC code solves for the reacting species and enthalpy. Based on Klimenko's research [46], the gradients of conditional scalars vary weakly in turbulent shear flows. The conditional scalars have a weaker dependence on a coordinate in physical space (especially on the coordinate perpendicular to the flow direction) than the unconditional scalars since the turbulence-chemistry interactions are resolved in mixture fraction space [100]. Therefore, CMC grids can be coarser than LES grids, $\Delta_{CMC}^3 \gg \Delta_{LES}^3$, and homogeneity (i.e. uniform quantities) of conditional moments in a CMC cell is assumed. Since the CMC equations in sections 4.2 and 4.3 are defined for the LES resolution, the CMC equations and conditional values based on the CMC resolution are required.

4.5.1 Conditionally Filtered Equations on the CMC Resolution

A value of any fluid property (e.g. in sections 4.4.3, 4.4.4 and 4.4.5) in a CMC cell, $\widetilde{\Phi|\eta}^*$, can be calculated from the integration of conditionally filtered average of the random property $\widetilde{\Phi|\eta}$ over the volume V_{CMC} of a CMC cell as

$$\widetilde{\Phi|\eta}^* = \frac{\int_{V_{CMC}} \widetilde{\Phi|\eta} \widetilde{P}(\eta) dV'}{\int_{V_{CMC}} \widetilde{P}(\eta) dV'}, \quad (4.28)$$

where $(\cdot)^*$ indicates a Favre filtered property evaluated on a CMC cell and the volume integrals are integrals over a CMC cell. $\widetilde{P}(\eta)$ is the FDF of any η bin. Note that $\widetilde{\Phi|\eta}^*$ is calculated by the CMC code at the CMC resolution, while $\widetilde{\Phi|\eta}$ and $\widetilde{P}(\eta)$ are available at the LES resolution. The FDF for the CMC resolution is computed as a volume average of the FDF from LES cells within a CMC cell,

$$\widetilde{P}^*(\eta) = \frac{\int_{V_{CMC}} \widetilde{P}(\eta) dV'}{\int_{V_{CMC}} dV'}. \quad (4.29)$$

Non-Conservative CMC Formulation

The non-conservative CMC equation for the conditionally filtered species mass fraction on the CMC resolution is

$$\frac{\partial Q_\alpha^*}{\partial t} + \tilde{u}_{j,\eta}^* \frac{\partial Q_\alpha^*}{\partial x_j} = \tilde{w}_{\alpha,\eta}^* + \tilde{N}_\eta^* \frac{\partial^2 Q_\alpha^*}{\partial \eta^2} + e_y^*, \quad (4.30)$$

where reaction rates $\tilde{w}_{\alpha,\eta}^*$ are closed due to the first order CMC assumption (section 4.4.2). The modelling of e_y^* is given as

$$e_y^* = \frac{1}{\gamma^*} \frac{\partial}{\partial x_j} \left(\gamma^* D_\eta^* \frac{\partial Q_\alpha^*}{\partial x_j} \right). \quad (4.31)$$

The term γ^* in Eq. (4.31) denotes $\bar{\rho}_\eta^* \tilde{P}^*(\eta)$ which is calculated as follows:

$$\bar{\rho}_\eta^* \tilde{P}^*(\eta) = \frac{\int_{V_{CMC}} \bar{\rho}_\eta \tilde{P}(\eta) dV'}{\int_{V_{CMC}} dV'}, \quad (4.32)$$

where $\bar{\rho}_\eta = \bar{\rho}|\eta$. The non-conservative CMC equation for the conditional enthalpy on the CMC resolution is given in the same manner as

$$\frac{\partial Q_h^*}{\partial t} + \tilde{u}_{j,\eta}^* \frac{\partial Q_h^*}{\partial x_j} = \tilde{w}_{R,\eta}^* + \tilde{N}_\eta^* \frac{\partial^2 Q_h^*}{\partial \eta^2} + e_h^*, \quad (4.33)$$

where e_h^* can be modelled as

$$e_h^* = \frac{1}{\gamma^*} \frac{\partial}{\partial x_j} \left(\gamma^* D_\eta^* \frac{\partial Q_h^*}{\partial x_j} \right). \quad (4.34)$$

Conservative CMC Formulation

The same concept of volume integration over the CMC cell, Eq. (4.28), is applied to the conservative CMC formulation. Therefore, the conditionally filtered species transport equation in conservative formulation solved on the CMC resolution reads:

$$\gamma^* \frac{\partial Q_\alpha^*}{\partial t} + \frac{\partial}{\partial x_j} (\gamma^* \tilde{u}_{j,\eta}^* Q_\alpha^*) = \gamma^* \tilde{w}_{\alpha,\eta}^* + \gamma^* \tilde{N}_\eta^* \frac{\partial^2 Q_\alpha^*}{\partial \eta^2} + Q_\alpha^* \frac{\partial}{\partial x_j} (\gamma^* \tilde{u}_{j,\eta}^*) + \gamma^* e_y^*. \quad (4.35)$$

Subsequently, the conservative CMC formulation for conditionally filtered enthalpy solved on the CMC resolution is

$$\gamma^* \frac{\partial Q_h^*}{\partial t} + \frac{\partial}{\partial x_j} (\gamma^* \tilde{u}_{j,\eta}^* Q_h^*) = \gamma^* \tilde{w}_{R,\eta}^* + \gamma^* \tilde{N}_\eta^* \frac{\partial^2 Q_h^*}{\partial \eta^2} + Q_h^* \frac{\partial}{\partial x_j} (\gamma^* \tilde{u}_{j,\eta}^*) + \gamma^* e_h^*. \quad (4.36)$$

The comparisons of both CMC formulations (conservative and non-conservative formulations, Eqs. (4.35) and (4.30)) are illustrated by OH concentrations in Fig. 4.2.

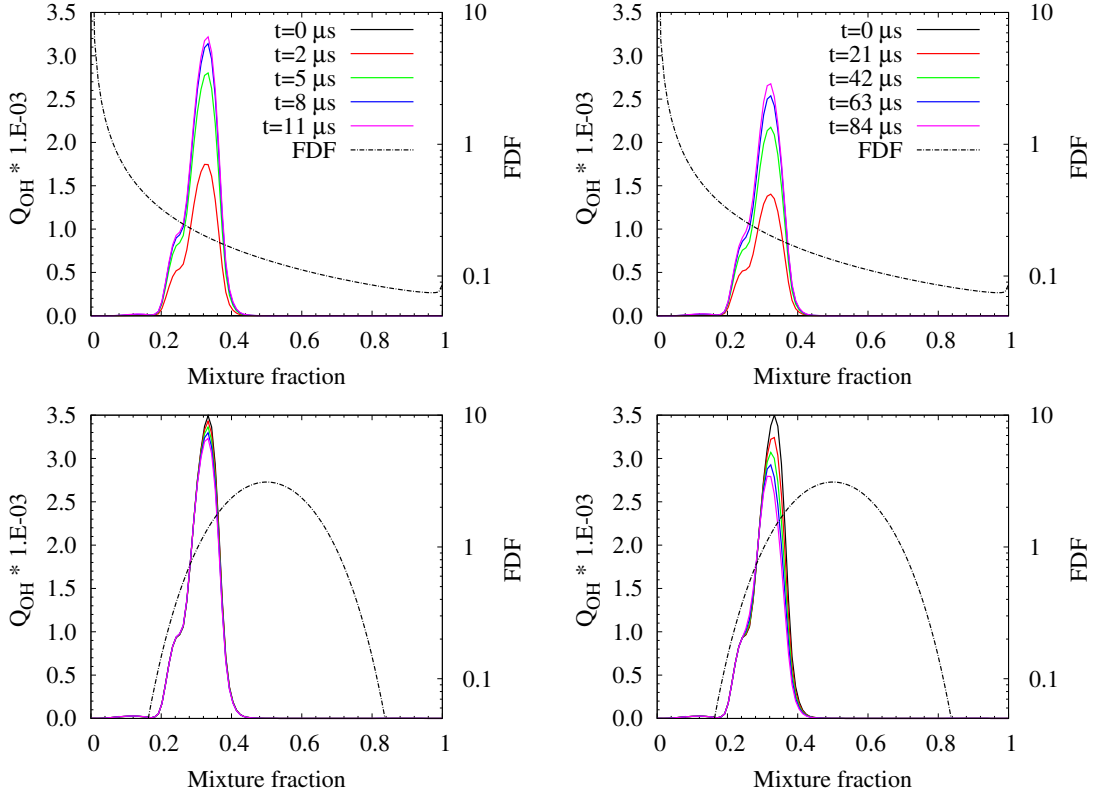


Figure 4.2: Comparison of two different CMC implementations. LHS and RHS pictures denote conservative and non-conservative CMC formulations, respectively. Lower and upper pictures denote lower and upper cells nearby each other and the fluid flows from lower to upper cells.

In this figure, only one direction of the convection is considered, since fluid flows from lower to upper CMC cells. Other physical aspects (diffusion and reaction) are neglected. The lower CMC cell contains non-zero OH concentrations, while the upper CMC cell is initialized with a zero OH distribution at the first time step. It should be noted that the FDF of both cells are constructed to provide an example for possible differences between the two implementations. Due to the large differences of the FDF between the lower and upper cells, the high values of convective fluxes in the upper cell of CMC conservative form are computed (Eqs. (5.19) and (5.28)) in every time step. Therefore, the conservative term takes only 11 μs to convect the conditional scalar from the lower to the upper cells. On the other hand, the non-conservative formulation (which does not use FDF information to calculate convective flux) takes 84 μs for the convection of the conditional scalar from the lower to the upper cells. Thus, the conservative formulation is considered to have a dynamic response of the conditionally filtered reactive scalars to turbulent fluctuations.

Conditionally Filtered Scalar Dissipation on the CMC Resolution

To obtain the conditionally filtered scalar dissipation for a CMC cell \tilde{N}_η^* , the integration process in Eq. (4.28) of \tilde{N}_η from each LES cell (Eq. (4.24)) located in a CMC cell is given as

$$\begin{aligned}\tilde{N}_\eta^* &= \frac{\int_{V_{CMC}} \widetilde{N}|\eta\tilde{P}(\eta)dV'}{\int_{V_{CMC}} \tilde{P}(\eta)dV'}, \\ &= \frac{\int_{V_{CMC}} \tilde{N}\tilde{P}(\eta)dV'}{\int_{V_{CMC}} \tilde{P}(\eta)dV'}.\end{aligned}\tag{4.37}$$

Conditionally Filtered Velocity on the CMC Resolution

As prescribed in section 4.4.4, the conditionally filtered velocity of each LES cell is considered to be constant in the mixture fraction space. Inserting Eq. (4.26) into Eq. (4.28), the integration of the velocity for a single CMC cell is written as

$$\begin{aligned}
\tilde{u}_{j,\eta}^* &= \frac{\int_{V_{CMC}} \widetilde{u_j} \tilde{P}(\eta) dV'}{\int_{V_{CMC}} \tilde{P}(\eta) dV'}, \\
&= \frac{\int_{V_{CMC}} \tilde{u}_j \tilde{P}(\eta) dV'}{\int_{V_{CMC}} \tilde{P}(\eta) dV'}.
\end{aligned} \tag{4.38}$$

Conditionally Filtered Turbulent Diffusivity on the CMC Resolution

In this work, there are three methods used to model the conditionally filtered turbulent diffusivity on the CMC resolution, D_η^* . However, all of them are based on the Smagorinsky model.

In the first method, D_η^* is calculated based entirely on quantities from CMC cell (named $D_{\eta,1}^*$). $D_{\eta,1}^*$ is given by

$$D_{\eta,1}^* = \nu_t^* / Sc_t, \tag{4.39}$$

where ν_t^* is the ‘CMC level’ viscosity [100]. This value is calculated using the Smagorinsky model in the CMC resolution. The equation of ν_t^* is

$$\nu_t^* = (C_s \Delta^*)^2 \| \tilde{S}^* \|, \tag{4.40}$$

where C_s is the Smagorinsky constant ($C_s = 0.1$) and Δ^* is a filter width of the CMC grid which is equal to an average CMC grid size. The Frobenius norm of the integrated characteristic strain rate for any CMC cell is written as

$$\| \tilde{S}^* \| = \left(2 \tilde{S}_{ij}^* \tilde{S}_{ij}^* \right)^{1/2}. \tag{4.41}$$

From the previous equation, the filtered rate-of-strain tensor of CMC resolution \tilde{S}_{ij}^* is

defined as

$$\tilde{S}_{ij}^* = \frac{1}{2} \left(\frac{\partial \tilde{u}_{i,\eta}^*}{\partial x_{j,CMC}} + \frac{\partial \tilde{u}_{j,\eta}^*}{\partial x_{i,CMC}} \right), \quad (4.42)$$

where, the integrated velocity fields for the CMC resolution, $\tilde{u}_{i,\eta}^*$ and $\tilde{u}_{j,\eta}^*$ are given by Eq. (4.38).

In the second method, $D_{\eta,2}^*$ is calculated based on D_t from every LES cell (Eq. (4.27)) which is located inside a CMC cell. The ensemble averaging over a CMC cell can be computed by weighting with the FDF from Eq. (4.28). Thus, the numerical modelling of this method is written as

$$\begin{aligned} D_{\eta,2}^* &= \frac{\int_{V_{CMC}} D_t |\eta \tilde{P}(\eta) dV'}{\int_{V_{CMC}} \tilde{P}(\eta) dV'}, \\ &= \frac{\int_{V_{CMC}} D_t \tilde{P}(\eta) dV'}{\int_{V_{CMC}} \tilde{P}(\eta) dV'}. \end{aligned} \quad (4.43)$$

In the third method $D_{\eta,3}^*$, the ratio of the size of a CMC cell to any LES cell is included into the second method in order to adjust the length scale during modelling the D_{η}^* value. This additional value is expected to provide higher accuracy for D_{η}^* since the D_{η}^* model should be based on the filter width of the CMC cell rather than on the filter width of the LES cell. The modelling of this method is

$$D_{\eta,3}^* = \frac{\int_{V_{CMC}} \Delta_{ratio} D_t \tilde{P}(\eta) dV'}{\int_{V_{CMC}} \tilde{P}(\eta) dV'}, \quad (4.44)$$

where Δ_{ratio} is the ratio of filter widths between a CMC cell to each LES cell located inside.

Reaction models

In this study, the chemical kinetics library, CHEMKIN-II, mechanism interpreter (version 3.1) and library (version 4.9) has been utilized as a software package for solving complex chemical kinetics problems. The mechanism employed in this study is composed of 4 elements, 29 species and 141 reactions [62]. Therefore, 35 equations need to be solved. This is composed of 3 momentum equations, 1 pressure equation and 1 mixture fraction equation on the LES grid and 29 species, as well as an enthalpy equation on the coarse CMC grid (compared with LES grid size). The radiation model for conditionally filtered enthalpy equations follows the thin flames radiation model from the TNF workshop [2].

Transfer of scalars to the LES Resolution

The unconditionally filtered property on the fine LES grid can be computed from the interpolation of conditionally filtered property on the CMC grid and then integrated following the process

$$\tilde{\Phi} = \int_0^1 \widetilde{\Phi|\eta} \tilde{P}(\eta) d\eta. \quad (4.45)$$

4.5.2 Relations between LES and CMC Codes

In order to couple both solvers, some variables are needed to be exchanged between them. The communication procedure of the two codes is schematically presented in Fig. 4.3 in which a loop over a time step can be separated into four parts.

The first part is an LES solver. The information of the flow and mixing field such as velocity, scalar dissipation rate, turbulent diffusivity, mixture fraction and subgrid-scale variance of mixture fraction are calculated in this part. The subgrid-scale variance, $\widetilde{\xi_{sgs}''^2}$, is modelled based on the assumption that the subgrid scale is in 'equilibrium' and thus the production rate of $\widetilde{\xi_{sgs}''^2}$ should be equal to the subgrid-scale scalar dissipation rate, \tilde{N}_{sgs} , Eq. (3.35). These quantities are solved (or modelled as in the case of subgrid-scale variance, Eq. (3.34)) on the fine spatial LES grid (four dimensions in total accounting for the three spatial coordinates and time), and then passed onto the second part which is the intermediate part between the LES and the CMC solvers.

In the second part, the conditionally filtered values of scalar dissipation, velocity

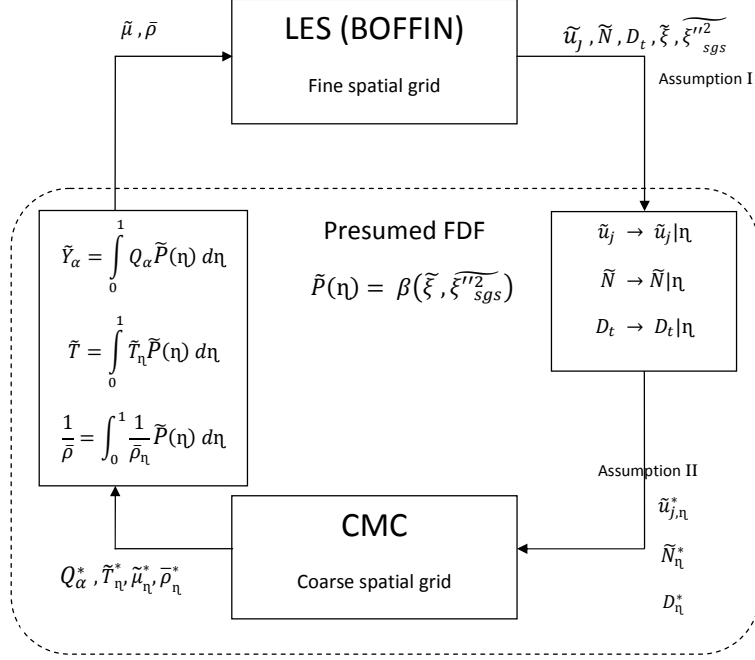


Figure 4.3: Schematic of the coupling of the LES and CMC codes.

and turbulent diffusivity are modelled as described in Eqs. (4.24), (4.26) and (4.27), respectively.

The third part denotes a CMC solver. In this part, the assumption of homogeneity of the conditional moments in a CMC cell allows any conditional property of each CMC cell to be calculated from the averaging of that conditionally filtered property from LES cells inside a CMC cell, Eq. (4.28). The presumed filtered density function (FDF) of any LES cell, $\tilde{P}(\eta)$, is calculated with the assumption of a β -function for the shape of the FDF and calculation of α and β parameters based on the resolved mixture fraction and subgrid-scale variance, Eq. (4.21). The value of the FDF on the CMC resolution is calculated as a volume average of $\tilde{P}(\eta)$ from the LES cells inside a CMC cell, Eq. (4.29). The conditionally filtered properties on the CMC resolution are modelled using Eqs. (4.37), (4.38) and (4.39) - (4.44) for the conditionally filtered scalar dissipation, velocity and turbulent diffusivity, respectively. Moreover, an FDF table which contains the relations of FDF values, mixture fractions and subgrid-scale variances using Eq. (4.18) is created and stored at the first CMC iteration to reduce the computation time for the fourth part. In the CMC procedure, five dimensions (three spatial coordinates, time and mixture fraction)

are considered. As a result, the conditionally filtered species mass fractions and enthalpy are computed. The conditionally filtered temperature is computed from the conditionally filtered enthalpy, i.e. $Q_h^* = \int_{T_0}^{\tilde{T}_\eta^*} C_{p,mix} dT_\eta + \sum_\alpha \Delta h_{f,\alpha}^\circ Q_\alpha^*$, where $\Delta h_{f,\alpha}^\circ$ is the standard enthalpy of formation of species α . Consequently, conditional temperature, viscosity and density are updated. Note that the conditional density is computed from the conditional temperature through the ideal gas equation of the state, i.e. $\bar{\rho}_\eta^* = P \widetilde{M^*}(\eta) / R_u \tilde{T}_\eta^*$, where M is the mixture molecular weight and R_u is the universal gas constant.

Finally for the fourth part, the CMC results (Q_α^* , \tilde{T}_η^* and $\bar{\rho}_\eta^*$) are interpolated to each LES cell and this conditional results (Q_α , \tilde{T}_η and $\bar{\rho}_\eta$) need to be integrated with the presumed FDF (from the FDF table) over η -space in order to calculate the unconditionally filtered values (Eq. (4.45)), which are fed back to the LES solver. Furthermore, the updated quantities of unconditionally filtered viscosity and density from the CMC solver, using Eq. (4.45), are used in the LES solver in the next time step.

CHAPTER 5

Numerical Methods

The LES program, BOundary Fitted Flow INtegrator (BOFFIN), is used throughout to solve the filtered Navier-Stokes equations. BOFFIN was originally created as a RANS solver by Jones [33] and further developed for the LES methodology by Jones *et al.* [34] in FORTRAN77 at Imperial College, London. The LES-BOFFIN code implements a parallelization procedure which was implemented by Marquis and Wille in 2008 [59]. In this research, BOFFIN is coupled with CMC in which the species and enthalpy transport equations are solved explicitly. The CMC part was developed by A. Kronenburg at the University of Stuttgart in FORTRAN90.

The purpose of this chapter is to report the numerical treatment exercised in this study. Firstly a spatial discretisation using the finite volume method (FVM) for the governing equations will be given in section 5.1. This section also includes the approximation of diffusive and convective fluxes. Subsequently, the temporal discretisation schemes, which are used in both LES and CMC, are provided in section 5.2. In section 5.3, the solution procedure of the pressure and the velocity field is outlined. The different numerical methods which are used in parametric studies of the combustion model are explained in the later section. At the end, this chapter is completed with the discussion of initial and boundary conditions in section 5.5.

5.1 Spatial Discretisation

In this section, a brief introduction of a coordinate transformation approach is provided first as one of the numerical methods applied in the LES-CMC code. Further, the discretisation of the computational domain for the finite volume method is discussed. For those who are interested in this topic, they are referred to [26] and [106] for further reading.

According to Thompson [98], the coordinate transformation was introduced. In this approach, the finite difference equations are formulated in a transformed curvilinear coordinate system that coincides with the boundaries of the flow domain [34]. This approach is implemented in this study in order to map the physical flow domain, which might have a complex shape, onto a simple rectangular computational domain. The explanations of coordinate transformation can be found in Tannehill *et al.* [95]. The alternative description can also be found in [11] and LES-BOFFIN user's guide [34].

In Chapters 3 and 4, the governing equations of LES and CMC are expressed in differential forms. These partial differential equations (PDEs) are discretised to yield algebraic equations which can be solved numerically. The finite volume method (FVM) is exercised in this study, as the solution domain is subdivided into a number of control volumes (CVs) and the governing equations are applied to each CV [26].

In the finite volume method, the equations are integrated over the computational cell and the volume integrals over the convection and diffusion terms are rewritten as fluxes over the cell boundaries using Gauss' divergence theorem as depicted in Fig. 5.1 for a 2-D computational domain.

A 2-D collocated computational grid arrangement is illustrated in Figure 5.1, where all variables are stored at the centre of each cell. The normal vector of the west and east sides are aligned with the x_1 direction, while north and south sides correspond to the x_2 direction. Variables having a subscript P are stored at the centre of the computational cell. The other variables having subscripts n , s , e and w denote the locations at the cell surfaces at north, south, east and west sides respectively, while the subscripts N , S , E and W refer to values at the neighbouring centres of north, south, east and west cells, respectively.

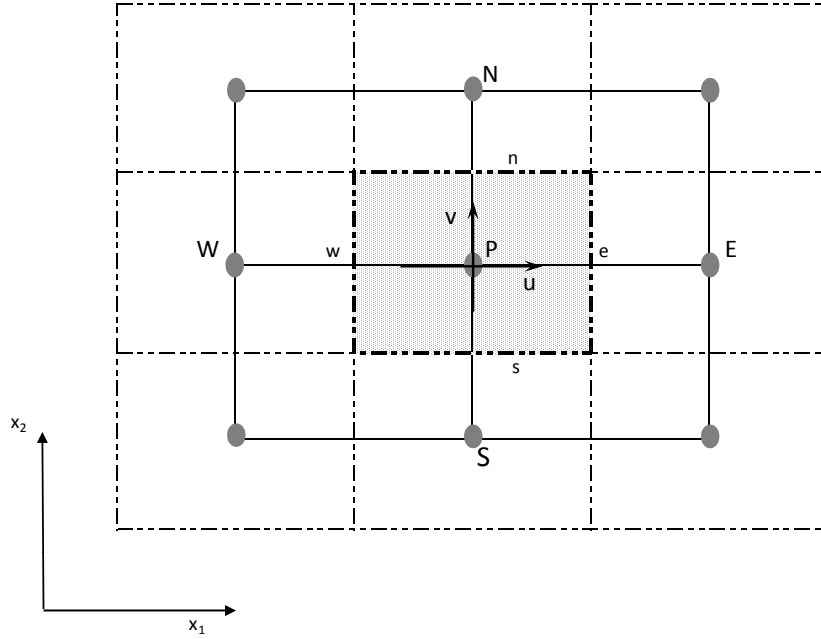


Figure 5.1: A control volume in two-dimensional computational space having the notation of grid points and surfaces.

To illustrate the FVM concept, the transport equation for an arbitrary scalar property ϕ is introduced as

$$\frac{\partial(\rho\phi)}{\partial t} + \frac{\partial}{\partial x_j}(\rho\phi u_j) = \frac{\partial}{\partial x_j}(\Gamma \frac{\partial\phi}{\partial x_j}) + S_\phi, \quad (5.1)$$

where on the LHS, the first term denotes the temporal change term and the second term presents the convective term, while on the RHS, the diffusive term with Γ as a diffusion coefficient is placed first, followed by the source term. Applying the finite volume method to Eq. (5.1) yields

$$\int_{\Delta V} \frac{\partial(\rho\phi)}{\partial t} dV + \int_{\Delta V} \frac{\partial}{\partial x_j}(\rho\phi u_j) dV = \int_{\Delta V} \frac{\partial}{\partial x_j}(\Gamma \frac{\partial\phi}{\partial x_j}) dV + \int_{\Delta V} S_\phi dV, \quad (5.2)$$

where $\int_{\Delta V}$ means integration over a finite volume. The Gauss' divergence theorem equates the volume integral of the divergence to the surface integral across the volume boundary. For a vector \mathbf{a} , this theorem reads

$$\int_{\Delta V} \frac{\partial \mathbf{a}}{\partial x_j} dV = \int_{\Delta A} \mathbf{a} \cdot \mathbf{n} dA, \quad (5.3)$$

where $\mathbf{a} \cdot \mathbf{n}$ is the component of the vector \mathbf{a} in the outward direction of the unit vector \mathbf{n} normal to the surface element dA . Applying the Gauss' divergence theorem, Eq. (5.2) can be written as

$$\frac{\partial}{\partial t} \int_{\Delta V} (\rho\phi) dV + \int_{\Delta A} (\rho\phi u_j) \cdot \mathbf{n} dA = \int_{\Delta A} \left(\Gamma \frac{\partial \phi}{\partial x_j} \right) \cdot \mathbf{n} dA + \int_{\Delta V} S_\phi dV, \quad (5.4)$$

where the time derivative of the first term on the LHS can be taken outside of the volume integral. A common approximation for the volume integral (e.g. the second term on the RHS) is the product of the cell volume, ΔV , and the value of the variable at the centre of the cell, P . Therefore, the source term of Eq. (5.4) becomes

$$\int_{\Delta V} S_\phi dV \approx S_{\phi,P} V. \quad (5.5)$$

Similarly, the surface integral is approximated by the sum of values of the variable at the cell surface multiplied by the area of that cell surface, A , and the face normal unit vector, \mathbf{n} . Therefore, the convective term on the RHS of Eq. (5.4) is rewritten as

$$\int_{\Delta A} (\rho\phi u_j) \cdot \mathbf{n} dA \approx \sum_f (\rho\phi u)_f \cdot \mathbf{n}_f A_f, \quad (5.6)$$

where \mathbf{n}_f is the normal unit vector pointing outward of any surface A_f and u_f represents the velocity pointing outward of a cell face. Applying the approximation of volume integral and surface integral to Eq. (5.4), the finite volume approximation of the generic transport equation reads

$$\frac{\partial}{\partial t}((\rho\phi)_P V) + \sum_f (\rho\phi u)_{f \cdot \mathbf{n}_f} A_f = \sum_f \mathbf{F}_f \cdot \mathbf{n}_f A_f + S_{\phi, P} V. \quad (5.7)$$

where \mathbf{F}_f is $(\Gamma \frac{\partial \phi}{\partial x_j})_f$ evaluated at the cell face centre in each direction.

In this section, only the principle of the finite volume method for the conservative CMC species transport equation is discussed while the finite volume method of the LES-BOFFIN code can be found in [11] and the LES-BOFFIN user's guide [34]. The application of FVM to the conservative CMC species transport equation was firstly introduced by Cleary [16]. Following Fig 5.1, two dimensions are considered in this discussion for clarity.

Applying the FVM, the conditionally filtered species transport equation for the CMC resolution (Eqs. (4.35) and (4.31)) yields

$$\begin{aligned} \frac{\partial}{\partial t}((\gamma^* Q_\alpha^*)_P V) + \sum_f (\gamma^* \tilde{u}_\eta^* Q_\alpha^*)_{f \cdot \mathbf{n}_f} A_f &= \gamma^* V (\tilde{w}_{\alpha, \eta} + \tilde{N}_\eta^* \frac{\partial^2 Q_\alpha^*}{\partial \eta^2})_P \\ &+ Q_{\alpha, P}^* \sum_f (\gamma^* \tilde{u}_\eta^*)_{f \cdot \mathbf{n}_f} A_f + \sum_f (\gamma^* D_\eta^* \frac{\partial Q_\alpha^*}{\partial x_j})_{f \cdot \mathbf{n}_f} A_f, \\ \frac{\partial}{\partial t}((\gamma^* Q_\alpha^*)_P V) + \sum_f (\gamma^* \tilde{u}_\eta^* Q_\alpha^* - \gamma^* D_\eta^* \frac{\partial Q_\alpha^*}{\partial x_j})_{f \cdot \mathbf{n}_f} A_f &= \gamma^* V (\tilde{w}_{\alpha, \eta} + \tilde{N}_\eta^* \frac{\partial^2 Q_\alpha^*}{\partial \eta^2})_P \\ &+ Q_{\alpha, P}^* \sum_f (\gamma^* \tilde{u}_\eta^*)_{f \cdot \mathbf{n}_f} A_f, \end{aligned} \quad (5.8)$$

which can be rearranged (written in 2-D for clarity) relating to Fig 5.1 as

$$\begin{aligned} \frac{\partial}{\partial t}((\gamma^* Q_\alpha^*)_P V) + \gamma_e^* A_e \left(\tilde{u}_\eta^* Q_\alpha^* - D_\eta^* \frac{\partial Q_\alpha^*}{\partial x_1} \right)_e - \gamma_w^* A_w \left(\tilde{u}_\eta^* Q_\alpha^* - D_\eta^* \frac{\partial Q_\alpha^*}{\partial x_1} \right)_w \\ + \gamma_n^* A_n \left(\tilde{v}_\eta^* Q_\alpha^* - D_\eta^* \frac{\partial Q_\alpha^*}{\partial x_2} \right)_n - \gamma_s^* A_s \left(\tilde{v}_\eta^* Q_\alpha^* - D_\eta^* \frac{\partial Q_\alpha^*}{\partial x_2} \right)_s &= \gamma^* V \left(\tilde{w}_{\alpha, \eta} + \tilde{N}_\eta^* \frac{\partial^2 Q_\alpha^*}{\partial \eta^2} \right)_P \\ + Q_{\alpha, P}^* ((\gamma^* \tilde{u}_\eta^* A)_e - (\gamma^* \tilde{u}_\eta^* A)_w + (\gamma^* \tilde{v}_\eta^* A)_n - (\gamma^* \tilde{v}_\eta^* A)_s). \end{aligned} \quad (5.9)$$

5.1.1 Approximation of Diffusive Fluxes

According to Eq. (5.7), approximations are required for the property ϕ at the centre point of each cell face which is denoted by subscript f . Fluid properties such as density and viscosity are determined by linear interpolation. Using the central differencing scheme (CDS), the assumption of a linear profile between centres P and E approximates the gradient as

$$\left(\frac{\partial\phi}{\partial x_1}\right)_e \approx \frac{\phi_E - \phi_P}{x_{1,E} - x_{1,P}}. \quad (5.10)$$

Employing Eq. (5.10) with the assumption of an orthogonal grid, the diffusive flux of Eq. (5.7) over the east face is given as

$$\left(\Gamma \frac{\partial\phi}{\partial x_1}\right)_e \cdot \mathbf{n}_e A_e \approx \Gamma_e \frac{\phi_E - \phi_P}{x_{1,E} - x_{1,P}} A_e. \quad (5.11)$$

Adopting the central differencing scheme, the sub-grid scale conditional flux at the east face of Eq. (5.9) can be written as

$$\begin{aligned} -\gamma_e^* A_e \left(D_\eta^* \frac{\partial Q_\alpha^*}{\partial x_1} \right)_e &\approx -\gamma_e^* A_e D_{\eta,e}^* \left(\frac{Q_{\alpha,E}^* - Q_{\alpha,P}^*}{x_{1,E} - x_{1,P}} \right), \\ &\approx -\gamma_e^* A_e \left(\frac{D_\eta^*}{\Delta x} \right)_e (Q_{\alpha,E}^* - Q_{\alpha,P}^*). \end{aligned} \quad (5.12)$$

The mixture fraction space is divided into a CMC grid with boundaries at $\eta = 0$ and 1. A derivative of the diffusive flux in mixture fraction space (from Eq. (5.9)) is expressed using a CDS as

$$\left(\tilde{N}_\eta^* \frac{\partial^2 Q_\alpha^*}{\partial \eta^2} \right)_P \approx \frac{\tilde{N}_{\eta,P}^*}{\Delta\eta\Delta\eta_+} (Q_{\alpha,++}^* - Q_\alpha^*) - \frac{\tilde{N}_{\eta,P}^*}{\Delta\eta\Delta\eta_-} (Q_\alpha^* - Q_{\alpha,--}^*), \quad (5.13)$$

where

$$\Delta\eta = \frac{1}{2}(\eta_{++} - \eta_{--}), \quad \Delta\eta_+ = \eta_{++} - \eta \quad \text{and} \quad \Delta\eta_- = \eta - \eta_{--}. \quad (5.14)$$

Subscripts (+) and (-) are used to denote the positive and negative directions in mixture fraction space. The single subscript shows values at the boundary between adjacent η bins (discrete points in the mixture fraction space), while double subscripts are used for the values at the bin centres.

5.1.2 Approximation of Convective Terms

In principle, the approximation of convective flux over the cell surface is similar as in section 5.1.1. The approximation of the convective flux for an orthogonal grid arrangement in Fig 5.1 is illustrated by the east cell face ($-_e$) as

$$(\rho\phi u)_e A_e \approx \rho_e (\lambda_e \phi_E + (1 - \lambda_e) \phi_P) (uA)_e. \quad (5.15)$$

One of the convective terms in the east face (second term on the LHS) of Eq. (5.9) can be written as,

$$\gamma_e^* A_e (\tilde{u}_\eta^* Q_\alpha^*)_e \approx \gamma_e^* A_e \tilde{u}_{\eta,e}^* (\lambda_e Q_{\alpha,E}^* + (1 - \lambda_e) Q_{\alpha,P}^*), \quad (5.16)$$

where λ_e is a linear interpolation factor (weighting factor) which is normally defined as

$$\lambda_e = \frac{x_{1,e} - x_{1,P}}{x_{1,E} - x_{1,P}}, \quad (5.17)$$

where λ_e is 0.5 corresponding to the central differencing scheme (CDS). Therefore, the property at the cell face ϕ_e is written as

$$\phi_e = \frac{\phi_P + \phi_E}{2} \quad (5.18)$$

Using Taylor series expansion of ϕ_e regarding the point P , CDS can be shown to be of second-order accuracy [26]. Within the scope of this study, CDS is adopted for the convective term in the momentum equation in LES-BOFFIN.

Applying the approximation of diffusive and convective fluxes (Eqs. (5.12) to (5.14) and (5.16)) to the conditionally filtered species transport equation (Eq. (5.9)), this equation can be rewritten as

$$\begin{aligned} \frac{\partial}{\partial t} ((\gamma^* Q_\alpha^*)_P V) + (a_e(Q_{\alpha,P}^* - Q_{\alpha,E}^*) + F_e Q_{\alpha,P}^*) &- (a_w(Q_{\alpha,W}^* - Q_{\alpha,P}^*) + F_w Q_{\alpha,P}^*) \\ + (a_n(Q_{\alpha,P}^* - Q_{\alpha,N}^*) + F_n Q_{\alpha,P}^*) &- (a_s(Q_{\alpha,S}^* - Q_{\alpha,P}^*) + F_s Q_{\alpha,P}^*) = (\tilde{w}_{\alpha,\eta}^*)_P \\ + (a_+(Q_{\alpha,++}^* - Q_\alpha^*) - a_-(Q_\alpha^* - Q_{\alpha,--}^*)) &+ Q_{\alpha,P}^*(F_e - F_w + F_n - F_s), \end{aligned} \quad (5.19)$$

where F denotes the specific mass flows (s^{-1}) across the four cell surfaces as

$$\begin{aligned} F_e &= \frac{(\gamma^* A \tilde{u}_\eta^*)_e}{\gamma^* V}, & F_w &= \frac{(\gamma^* A \tilde{u}_\eta^*)_w}{\gamma^* V} \\ F_n &= \frac{(\gamma^* A \tilde{v}_\eta^*)_n}{\gamma^* V}, & F_s &= \frac{(\gamma^* A \tilde{v}_\eta^*)_s}{\gamma^* V}, \end{aligned} \quad (5.20)$$

and the coefficients, a , are defined by

$$\begin{aligned} a_e &= \frac{\gamma_e^* A_e}{\gamma^* V} \left(-\lambda \tilde{u}_\eta^* + \frac{D_\eta^*}{\Delta x} \right)_e, & a_w &= \frac{\gamma_w^* A_w}{\gamma^* V} \left(\lambda \tilde{u}_\eta^* + \frac{D_\eta^*}{\Delta x} \right)_w \\ a_n &= \frac{\gamma_n^* A_n}{\gamma^* V} \left(-\lambda \tilde{v}_\eta^* + \frac{D_\eta^*}{\Delta x} \right)_n, & a_s &= \frac{\gamma_s^* A_s}{\gamma^* V} \left(\lambda \tilde{v}_\eta^* + \frac{D_\eta^*}{\Delta x} \right)_s \\ a_+ &= \frac{\tilde{N}_{\eta,P}^*}{\Delta \eta \Delta \eta_+}, & a_- &= \frac{\tilde{N}_{\eta,P}^*}{\Delta \eta \Delta \eta_-}. \end{aligned} \quad (5.21)$$

However, the nature of CDS can create spatial oscillations which may result in negative

values for positively defined or physically bounded quantities such as mixture fraction (required to be bounded between 0 and 1) [34]. Furthermore, these oscillating solutions may lead to numerical instability. It was shown by Patankar [69] that the oscillations and instability of this approximation do not occur if the cell Peclet number, a measure of the relative strengths of convection and diffusion ($Pe = \frac{u\Delta x}{\Gamma}$), is less than or equal to two. Therefore, two other types of approximation schemes which preserve monotonicity (i.e. a stable, non-oscillatory and higher-order scheme) are adopted for the filtered transport equation for mixture fraction in LES and conditional species transport equation in CMC.

For the LES part, a sophisticated scheme is preferred for the scalar equation based on the idea that the total variation of the property at any surface of a cell is reduced. This is known as the total variation diminishing (TVD) scheme in which the undesirable oscillation is counteracted by adding a weighting towards the upstream contribution [106]. Considering the discrete data set in Fig 5.2, the total variation (TV) in i -direction for the set of data is defined as

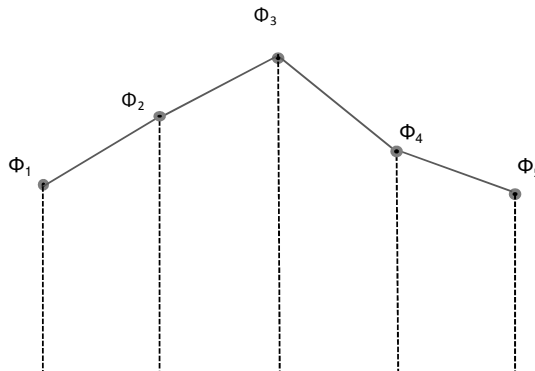


Figure 5.2: An example of a discrete data set for the total variance scheme [106].

$$TV(\phi) = \sum_i |\phi_{i+1} - \phi_i|, \quad (5.22)$$

which is equal to

$$\begin{aligned}
TV(\phi) &= |\phi_2 - \phi_1| + |\phi_3 - \phi_2| + |\phi_4 - \phi_3| + |\phi_5 - \phi_4| \\
&= |\phi_3 - \phi_1| + |\phi_5 - \phi_3|.
\end{aligned} \tag{5.23}$$

For a monotonicity-preserving scheme, the discrete solution of a property that is approximated by the TV scheme should diminish in the further time steps. A numerical scheme is called total variation diminishing, if

$$TV(\phi^{n+1}) \leq TV(\phi^n), \tag{5.24}$$

where n and $n + 1$ refer to consecutive time steps. If the fluid flows directly through the positive x_i direction and ϕ_W, ϕ_P and ϕ_E refer to the values of a property at west cell, central cell and east cell centres, respectively (Fig. 5.1), the value of ϕ_e using the TVD scheme is written as

$$\phi_e = \phi_P + \frac{1}{2}\mathbb{B}(r)(\phi_E - \phi_P), \tag{5.25}$$

where r is the local ratio of the upstream gradient to the downstream gradient and thus $r = \left(\frac{\phi_P - \phi_W}{\phi_E - \phi_P}\right)$. In LES-BOFFIN, the method proposed by Van Leer [52] is adopted for the limiter function $\mathbb{B}(r)$ which can be defined as

$$\mathbb{B}(r) = \frac{r + |r|}{1 + r} = \frac{\left(\frac{\phi_P - \phi_W}{\phi_E - \phi_P}\right) + \left|\frac{\phi_P - \phi_W}{\phi_E - \phi_P}\right|}{1 + \left(\frac{\phi_P - \phi_W}{\phi_E - \phi_P}\right)}. \tag{5.26}$$

For the CMC part, the power-law interpolation scheme [69] is adopted. In principle, this hybrid scheme switches from CDS to upwind differencing scheme (UDS) at high Pe numbers ($Pe > 2$). Using UDS, the numerical scheme is stable and without undesirable oscillation, albeit of lower accuracy. Considering the east cell face, the power-law interpolation factor λ_e (in Eq. (5.21)) can be expressed as

$$\lambda_e = \frac{1}{Pe_e} - \frac{(1 - 0.1 | Pe_e |)^5}{Pe_e}, \quad (5.27)$$

where $Pe = \frac{\tilde{u}_\eta^* \Delta x}{D_\eta^*}$ (in the CMC section).

Using the power-law scheme (Eq. (5.27)), the coefficients at cell faces from Eq. (5.21) are rewritten as

$$\begin{aligned} a_e &= \frac{\gamma_e^* A_e}{\gamma^* V} \left(\| -\tilde{u}_\eta^*, 0 \| + A(Pe) \frac{D_\eta^*}{\Delta x} \right)_e, & a_w &= \frac{\gamma_w^* A_w}{\gamma^* V} \left(\| \tilde{u}_\eta^*, 0 \| + A(Pe) \frac{D_\eta^*}{\Delta x} \right)_w \\ a_n &= \frac{\gamma_n^* A_n}{\gamma^* V} \left(\| -\tilde{v}_\eta^*, 0 \| + A(Pe) \frac{D_\eta^*}{\Delta x} \right)_n, & a_s &= \frac{\gamma_s^* A_s}{\gamma^* V} \left(\| \tilde{v}_\eta^*, 0 \| + A(Pe) \frac{D_\eta^*}{\Delta x} \right)_s, \end{aligned} \quad (5.28)$$

where $\| a, b \|$ is equal to the maximum value between a and b and $A(Pe) = (1 - 0.1 | Pe |)^5$.

5.2 Temporal Discretisation

In unsteady flow computations, time is considered to be a coordinate direction as the space coordinates. Therefore, the time derivative of the governing equations (e.g. term $\frac{\partial \phi}{\partial t}$ in Eq. (5.7)) has to be approximated. In the LES-CMC code, a two-level method is adopted as time discretisation. Three principal procedures of the discretisation methods related to this study are explicit method, implicit method and the Crank-Nicolson method. The time derivative term in Eq. (5.7) can be simply expressed first as

$$\frac{\partial \phi_P}{\partial t} = \frac{1}{(\rho V)_P} \left(\sum_f (\mathbf{F}_f - (\rho \phi u)_f) \cdot \mathbf{n}_f A_f \right) + \frac{S_{\phi,P}}{\rho} = \Theta(\phi), \quad (5.29)$$

where $\Theta(\phi)$ represents the joint effects of diffusion, convection and source/sink terms. Subsequently, the concepts of three different methods are given in the next section.

Explicit Method

This method evaluates all fluxes and sources at the new time level ϕ^{n+1} using the known values ϕ^n at time step n only. The simplest form of this method is the explicit Euler method which is written as

$$\phi^{n+1} \approx \phi^n + \Theta(\phi^n)\Delta t. \quad (5.30)$$

The advantage of this method is its simplicity since the known values at the time step n are available and no iterative solver is required. However, this method is known as first order accurate which requires small step sizes in time to ensure its accuracy and stability [26]. For flows which are dominated by convection, a restriction on the information propagation rate is required by limiting the convective time step by the Courant number, c , or CFL number which is defined as

$$c = \frac{u\Delta t}{\Delta x}, \quad (5.31)$$

where the dimensionless c should be less than unity which means the fluid element cannot move further than one grid cell length in a time step [26]. For flows which are dominated by diffusion, the equivalent criterion reads

$$d = \frac{\Gamma\Delta t}{\rho(\Delta x)^2}, \quad (5.32)$$

where the parameter d is the ratio of time step to the characteristic diffusion time. However, when both convection and diffusion are present, the stability criterion becomes more complicated and most people prefer their individual criterion [26].

Implicit Method

An alternative time discretisation method evaluates all fluxes and sources of the new time level ϕ^{n+1} using the unknown value ϕ^{n+1} . The basic form of the implicit method is known as the implicit Euler method which is expressed as

$$\phi^{n+1} \approx \phi^n + \Theta(\phi^{n+1})\Delta t. \quad (5.33)$$

Even though this method offers the advantage of stability, the complexity of the implicit method would increase the computational cost. This is because the equations of the unknown values at the next time step need to be solved leading to the calculation of a large coupled set of equations at each time step.

Crank–Nicolson Method

A second order accuracy based on the trapezoid rule method (one of the approximation methods using straight line interpolation between initial and final points [26]) is known as the Crank-Nicolson method. This semi-implicit method is a weighted combination of first order explicit and implicit Euler methods (fluxes and sources of the new time level are a function of the values at time step n and $n + 1$). The Crank-Nicolson method is simply written as

$$\phi^{n+1} \approx \phi^n + \frac{1}{2}[\Theta(\phi^n) + \Theta(\phi^{n+1})]\Delta t. \quad (5.34)$$

As a result of this equation, using this method would require less computational effort per step than the first order implicit Euler method [26]. Furthermore, Gustafsson *et al.* [32] proved the advantage of this method in which the Crank-Nicolson scheme is stable when the Dirichlet and Neumann boundary conditions are used (both conditions are also applied into this work, as detailed in section 5.5).

In the BOFFIN code, two different time discretisation methods are employed. The Crank-Nicolson method is adopted in LES time integration whereas the explicit Euler scheme is applied for time integration in CMC for moderate computational costs. A time step width which is controlled by the finer LES grid, during the simulation is proved and adjusted to be small to obtain the CFL numbers in a range between 0.15 and 0.25.

5.3 Pressure Correction

When the momentum equations are discretised, the velocity field will not satisfy the continuity equations. Therefore, the pressure correction (e.g. the SIMPLE algorithm [70] as applied in this code) is required to ensure mass conservation at each time step. Consequently, a second order accuracy for time discretisation is maintained by using a predictor-corrector projection scheme (as detailed in appendix B). The mathematic solution algorithm for the pressure increment is managed by using the conjugate gradient method with incomplete Cholesky preconditioning (ICCG) [40], [61] and [105]).

Since a collocated grid arrangement is employed in LES-BOFFIN, a pressure smoothing method, which was created by Rhie and Chow [84] is applied to prevent an oscillatory pressure field which is decoupled from the velocity at grid nodes [71]. The details of the implementation of this method in LES-BOFFIN can be found in LES-BOFFIN user's guide [34] or in the Ph.D. thesis of [11] and [110] and will not be repeated here.

5.4 Numerical Aspects

One of the key concerns in a parametric study within the combustion model is that different numerical methods can be used for any numerical aspects. Three numerical aspects that will be considered within this thesis are:

- the CMC formulation
- the approximation of the CMC convective fluxes
- the model for the conditionally filtered turbulent diffusivity.

5.4.1 CMC Formulations

The difference between the two CMC forms (the non-conservative form in Eq. (4.30) and the conservative form in Eq. (4.35)) is the inclusion of the FDF information into the transport equation, in particular into the convective term of the conservative CMC formulation as previously discussed in section 4.5.1. Based on the finite volume method (section 5.1), both conditional species transport equations can be applied to each CV of the computational domain. It is believed that including the FDF information in the

convective flux will make the CMC conservative form more precise than the traditional (non-conservative) formulation [65]. Therefore, the study of two different formulations of the combustion model is performed to verify the assumption.

5.4.2 Flux Approximations

Since each CMC cell comprises of a number of LES cells (e.g. 784 LES cells for a reference case of Table 6.5), two methods can be applied to approximate the convective flux between CMC cells.

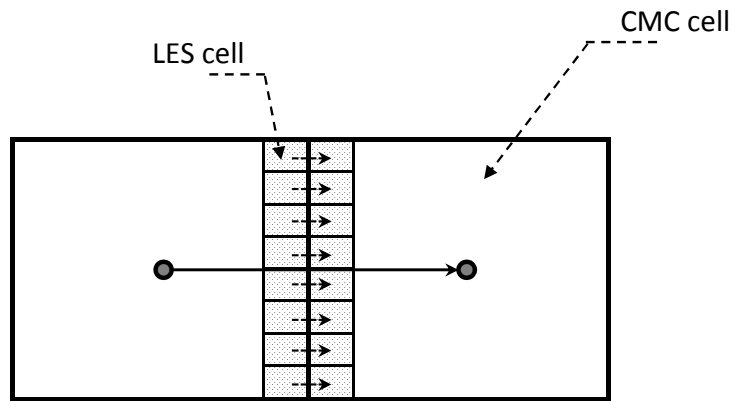


Figure 5.3: A schematic of the two approximations of the CMC convective flux.

In the first method (later called flux-1), a small convective flux between two LES cells which is located on the CMC cell face is calculated from the average values of densities, velocities and turbulent diffusivities from both LES cells. These properties in each LES cell are modelled to be conditional values on the mixture fraction by using $\bar{\rho}_\eta$ from the conditional moments, Eqs. (4.26) and (4.27) for a conditional density, a conditional velocity and a conditional turbulent diffusivity, respectively. The set of FDF values is calculated from averages of mixture fraction and of subgrid-scale variance from both LES cells. The convective flux over the CMC cell face is a sum of every small convective flux of LES cells adjacent to the CMC cell face. The convective flux from this method is shown as the sum of the small arrows in Fig. 5.3.

In the second method (later called flux-2), fluid properties in a CMC cell are considered to be equal throughout the CMC cell. Firstly, all properties are calculated from LES cells located in a CMC cell. Density, velocity and turbulent diffusivity of each LES cell inside a CMC cell are integrated to values of a CMC cell using Eq. (4.28). Subsequently, a convective flux between two CMC cells can be calculated from the average values of both adjacent CMC cells. The convective flux from this method is illustrated by the big arrow in Fig. 5.3.

5.4.3 Conditionally Filtered Turbulent Diffusivity Models

Based on the Smagorinsky model, three different models of conditionally filtered turbulent diffusivity, D_η^* , are defined in section 4.5.1. In the first model, the turbulent diffusivity (named $D_{\eta,1}^*$) is computed based entirely on the CMC cell using Eq. (4.39), while the calculation of the same value in the second method is based on the LES cells within a CMC cell (named $D_{\eta,2}^*$) using Eq. (4.43). The modelling of D_η^* in the third method is based on the second method which includes the ratio of the size of CMC cell to the size of the LES cell following Eq. (4.44). As one of the parametric studies, the effects of each model will be discussed for more details in the next chapter.

5.5 Boundary Conditions

Up to now, the governing equations have been discretised to obtain a numeric system of equations for every CV. However, fluxes through CV faces occurring at domain boundaries still require special treatment [26]. The appropriate boundary conditions must be provided for the momentum and scalar transport equations. In the pressure correction, the momentum equations supply the natural Neumann conditions on the boundaries [110]. Therefore, this section will describe the boundary conditions applied in this study.

For the CMC equations, the boundary conditions are also required, albeit they remain constant in time. Considering mixture fraction space (η), $\eta = 0$ states pure air, while $\eta = 1$ states pure fuel.

5.5.1 Inflow Boundary Condition

In LES-BOFFIN, the Dirichlet condition is implemented as an inflow boundary condition. In this method, the mean inflow velocity at the inlet boundary, $\tilde{u}_i(\mathbf{x}, t)$, is given as the known value of data (e.g. experimental data, $\tilde{u}_i(\mathbf{x}, t) \Big|_{\text{experiment}}$), so that

$$\tilde{u}_i(\mathbf{x}, t) \Big|_{\Gamma} = \tilde{u}_i(\mathbf{x}, t) \Big|_{\text{experiment}}. \quad (5.35)$$

In order to generate inflow conditions, a two-feed mixing profile is defined at the inlet using the measured value of co-flow (air), pilot and main jet (fuel) for the mixture fraction field, while the experimental mean and fluctuation of the velocity profile [3] are used for the velocity field. To prescribe the oscillation of the velocity field, an artificial turbulent inflow generator has been implemented in LES-BOFFIN.

The artificial turbulent inflow generator is based on digital filtering and was proposed by Klein *et al.* [44], where pseudo-turbulent velocity data are generated with a prescribed length scale and Reynolds stress tensor. Firstly, a series of random signals (r_m) is generated for a digital filter with $\overline{r_m} = 0$ and $\overline{r_m r_m} = 1$ based on the observation that filtering increases the spatial correlation of a random field. The digital filter using a random signal field for one dimension is given as

$$u_m = \sum_{n=-N}^N b_n r_{m+n}, \quad (5.36)$$

where b_n are the filter coefficients and $2N + 1$ denotes the filter width. In order to extend this procedure to three-dimensional filtering, the convolution with three one-dimensional filters is calculated as

$$b_{ijk} = b_i \cdot b_j \cdot b_k, \quad (5.37)$$

where i, j and k is the direction of each dimension. Then the filtered fields are renormalized to a mean value of zero and a variance of one in order to keep the effects of turbulence, which are reduced by filtering. The filtering and renormalization procedures are repeated until the prescribed length scale is reached. Finally, the cross-correlations are easily set to

the three-dimensional independent velocity fields by using a procedure suggested by Lund *et al.* [57] to have a turbulent field for the prescribed Reynolds stress tensor which can be used further as the initial conditions.

5.5.2 Outflow Boundary Condition

Since the disturbances of the flow originated at the outlet of the domain are expected to be convected out of the domain without being propagated upstream [34], the Neumann (zero gradient) condition is commonly applied on the outflow boundary, so that

$$\left. \frac{\partial \tilde{u}_i}{\partial n} \right|_{\Gamma} = 0, \quad (5.38)$$

where \tilde{u}_i denotes the mean flow, n represents the outward normal to the boundary surface and Γ refers to the position of the boundary.

For mixture fraction space, a zero gradient outflow boundary condition is applied for conditional scalars.

5.5.3 Lateral Boundary Condition

To minimise the effects of the boundary on the predicted flow, free-slip (symmetry) boundary condition allows the flow tangent to the boundary to slide along a frictionless surface. The wall-normal velocity component, \tilde{u}_n , is assumed to vanish. This means zero wall-normal velocity component and a Neumann (zero gradient) condition on the velocity component parallel to any boundary are imposed at the surface so that

$$\tilde{u}_n|_{\Gamma} = 0 \quad \text{and} \quad \left. \frac{\partial \tilde{u}_{i,t}}{\partial n} \right|_{\Gamma} = 0, \quad (5.39)$$

where $\tilde{u}_{i,t}$ is a tangential velocity component. In this work, the free-slip boundary condition is employed for all lateral boundaries.

CHAPTER 6

LES-CMC of the Sandia Flame series

6.1 Introduction

In this chapter, the test cases of the Sandia Flame series are investigated by using the LES-CMC approach. The Sandia Flame series is composed of flames D, E and F which are piloted methane/air flames with the same geometric set-up. Due to a rich condition in central jet beyond the flammability limit, these flames burn as diffusion flames with a single reaction zone near the stoichiometric mixture fraction in the mixing zone (shear layer) [4].

Since the velocities of the jet and the pilot are increased from Flames D to F, the probability of localized extinction and re-ignition is small in Flame D and is increased for Flames E and F, respectively. These phenomena can be explained by the comparison between mixing and chemical time scales. For non-premixed turbulent flames where an infinitely fast chemistry assumption is considered, the mixing time scales are larger than the chemical time scales. Therefore, the flames exist for any condition and local extinction cannot occur. On the other hand, if a finite rate chemistry assumption is considered, the turbulent time scales can be smaller than the chemical time scales. The heat release from chemical reaction may not balance the heat loss. Consequently, local extinction will occur if the scalar dissipation rates are sufficiently high [78]. Therefore, in order to simulate these phenomena, a combustion model based on the finite rate chemistry assumption should be

considered. As one of a number of combustion models using this assumption, CMC is believed to capture these occurrences.

The Sandia Flame series provides a large set of well-established experimental data and has been used as a target for a large number of CFD modelling studies for turbulence-chemistry interactions. Sandia Flame D has been used as a validation test case in a number of LES studies combined with different combustion models (like flamelet model, CMC and PDF) [37, 79, 77, 68, 107] because of its simplicity. Furthermore, Flames E and F have been used to study the extinction and re-ignition phenomena in [50, 51, 29, 83].

In the next section, the experimental and the computational setups are described, followed by the details of parametric CMC studies in section 6.4. Section 6.5 presents the simulation results for Sandia Flame D, which is carried out as the first test case in order to validate the LES-CMC simulation models as a reference. Subsequently, the examinations of Flames E and F are presented in section 6.6 and section 6.7 to compare the sensitivity of each CMC case to the extinction and re-ignition. The chapter closes with a discussion and conclusions about the performance of various CMC model parameters in section 6.8.

6.2 Experimental Setup

The measurements of the Sandia Flame series were investigated by two major research groups. The Rayleigh measurement is employed for the temperature, Raman scattering and laser induced fluorescence (LIF) techniques are used to measure mixture fraction and species concentrations by Barlow and Frank [4, 3], while the laser-Doppler velocimetry (LDV) technique is applied to measure velocities by Schneider *et al.* [88]. Moreover, the 3D estimation of scalar dissipation of Flames D and E are proposed by Karpetsis and Barlow [36] and used as a validation data set of the scalar dissipation modelling. A close-up of Flame D stabilized on the Sandia burner and the details of the burner geometry are presented in Fig. 6.1. The Sandia Flame series has a fuel composition of 25% methane and 75% dry air by volume. The fuel is injected through the main jet which has 7.2 mm as the inner diameter, D . The bulk velocities of the jet are set to 49.6, 74.4 and 99.2 m/s for Flames D, E and F. Surrounding the main jet, the annular pilot composed of an unstrained premixed CH_4/air flame ($\phi = 0.77$) is set in order to stabilize the flames. With an outer annulus diameter of 18.2 mm, this pilot velocity is set to 11.4, 17.1 and 22.8 m/s

in Flames D, E and F respectively. The burner also has a co-flow velocity of 0.9 m/s for all flames. The temperatures of main jet, pilot and co-flow are 294, 1880 and 291 K at 0.993 atm for Flames D, E and F respectively. The stoichiometric mixture fraction of the given fuel is 0.351 and the pilot has a mixture fraction of 0.27. Note that the calculation of all measured mixture fraction values in the experiments are defined following Bilger (Eq. (2.34)) with the dropping of the oxygen terms in order to have less sensitivity to experimental noise and interference from laser-excited fluorescence [4]. The equation can be written as

$$\xi = \frac{\frac{2(Z_C - Z_{C,2})}{W_C} + \frac{(Z_H - Z_{H,2})}{2W_H}}{\frac{2(Z_{C,1} - Z_{C,2})}{W_C} + \frac{(Z_{H,1} - Z_{H,2})}{2W_H}}, \quad (6.1)$$

where Z 's are elemental mass fractions of carbon and hydrogen; W 's are atomic weights; and the subscripts 1 and 2 refer to the fuel and co-flowing air streams, respectively. The summary of the governing parameters of test cases is shown in Table 6.1.

Table 6.1: Conditions of flow and scalars of the Sandia Flame Series.

Condition	Flame D	Flame E	Flame F
Reynolds number	22400	33600	44800
Main jet (bulk) velocity [m/s]	49.6	74.4	99.2
Pilot velocity [m/s]	11.4	17.1	22.8
Co-flow velocity [m/s]	0.9	0.9	0.9
Stoichiometric mixture fraction	0.351	0.351	0.351
Mixture fraction of the pilot	0.27	0.27	0.27
Fuel equivalence ratio of the pilot (ϕ)	0.77	0.77	0.77

6.3 Computational Setup

The computational grid is generated with dimensions of $80D$ in axial direction and $8D$ in x - and y -directions at the flame base increasing to $60D$ at the outlet of the domain. This grid is generated to have the finest resolutions in the main jet and pilot area. By applying smooth transition and refinement [95], cells are increasingly stretched outwards in the radial and axial directions (as in Fig. 6.2) for the purpose of capturing high gradient

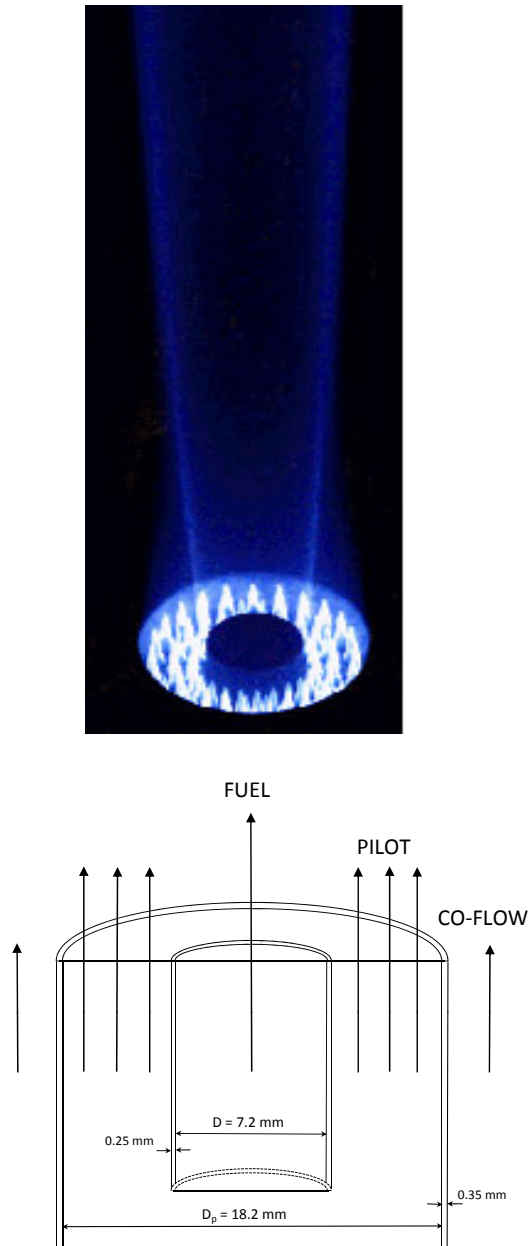


Figure 6.1: Close-up of a piloted flame stabilized on the Sandia burner (top) and details of the burner geometry (bottom).

regions with fine grids. The grid consists of $112 \times 112 \times 320$ LES cells in x -, y - and z -directions, respectively. The regions above the jet and pilot are captured by 784 and 3840 LES cells, respectively. Due to grid independence studies by Navarro *et al.* [68], the number of computational cells achieves a condition that the largest fraction of the energy spectrum is resolved after the initial break-up of the jet. A summary of the particular

details of the computational grid is shown in Table 6.2. Initially, the statistical studies of Flame D are performed by a narrow domain which has the dimension of $30D$ at the outlet of the domain. The initial domain contains $96 \times 96 \times 320$ LES cells in x -, y - and z -directions, respectively. Since the initial domain has a problem of recirculation (more details in section 6.5.2.1), most of the studies are performed by using the current domain (Table 6.2). However, the recirculation effects do not contaminate the statistical predictions of the interesting regions of Flame D. Therefore, rerunning simulations with the wider domain is not necessary for the statistical predictions of parametric studies for Sandia Flame D.

The CMC grid has 100 nodes in mixture fraction space which has refinements at η equal to 0 and 1. In physical space, the reference CMC grid resolution is $8 \times 8 \times 80$ cells, and it is used as a reference case in this study.

Table 6.2: Details of computational grid.

Condition	domain
Inlet dimension	$8D \times 8D$
Outlet dimension	$60D \times 60D$
Dimension in z -direction	$80D$
Computational cells (x -, y - and z -directions)	$112 \times 112 \times 320$

The free-slip boundary condition is applied to all side boundaries, while Dirichlet and Neumann boundary conditions are used at the inlet and outlet, respectively. The inlet velocity profiles are adopted from the experiment by Schneider *et al.* [88] at $z/D \approx 0.14$ for the beginning position of the grid ($z/D = 0$). For mixture fraction space, co-flow, which has pure air conditions, is defined as $\eta = 0$, while the pure fuel from jet is applied at $\eta = 1$. A bi-linear profile in mixture fraction space is adopted at the inlet in physical space.

The computational studies are performed on an IBM BladeCenter HS21XM (Dual core Intel Xeon E5440 2.83 GHz) using 80 cores of the HLRS DGRID/BW-Grid Cluster platform, and the statistics of flow, mixing field and species mass fractions have been calculated over 10,000 samples for the initial domain and 30,000 samples for the wider domain.

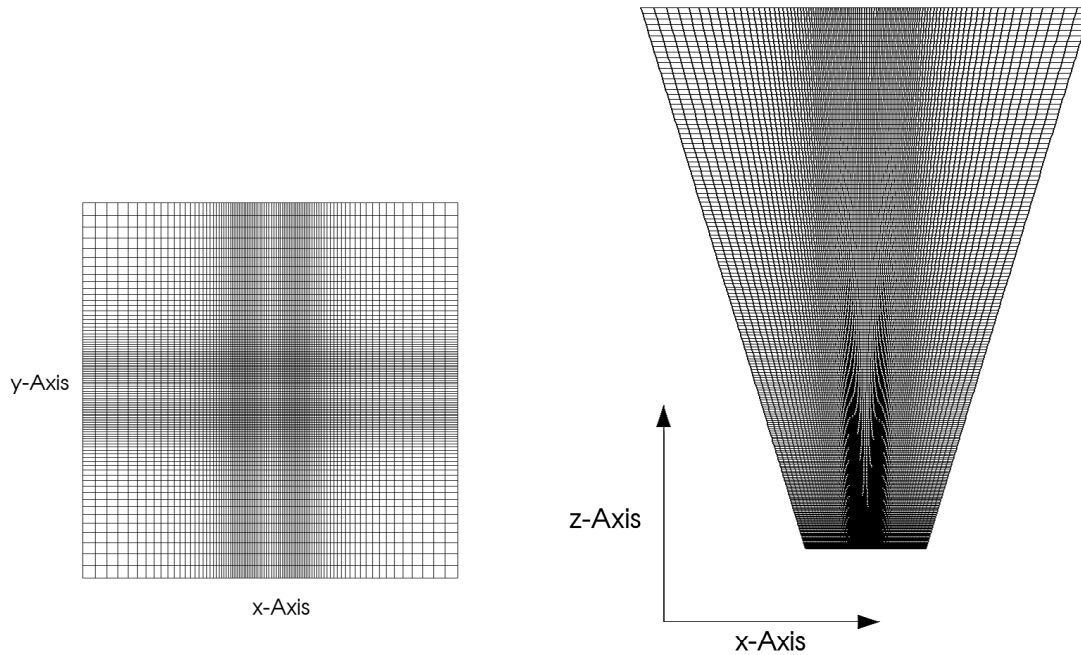


Figure 6.2: Cross sections of computational mesh.

6.4 Parametric Studies

Parametric studies of the flow and mixing fields, combustion model and CMC grid resolution are simulated using LES-CMC modelling to examine the effects of each parameter. Details of the simulation results can be found in the following sections.

6.4.1 Parametric Studies of Flow and mixing Field

The parametric studies of the flow and mixing fields refer to the inflow velocity variances in the turbulent inflow generator, the Schmidt number (Sc), the turbulent Schmidt number (Sc_t), and the variance of mixture fraction ($\widetilde{\xi''^2_{sgs}}$). The Schmidt number is a fluid property which is actually not allowed to be changed. However, the Sc values are varied to test the sensitivity of the flow and mixing fields. Sandia Flame D is used as a reference case and thus the effects of these parameters on simulation results are detailed in section 6.5.

- Effects of Velocity Variance in Turbulent Inflow Generator

A turbulent inflow generator [44] is required to generate pseudo-turbulent structures with a given length scale and Reynolds stress tensor. However, there is no exact

measurement of the velocity profiles inside the jet and pilot pipes and the measurements of velocity profiles at $z/D = 0.14$ are applied as the experimental inlet data for the inflow generator. Therefore, some adjustments of the velocity variances of the inlet data are allowed in order to match the results with the measurement data.

- Effects of Schmidt Number

As previously discussed in section 2.1.1.3, the Schmidt number, Sc denotes the ratio of the rate of momentum transfer to the rate of mass transfer ($D = \frac{\nu}{Sc}$). Therefore, Sc determines the molecular diffusion rate in the filtered transport equation for the mixture fraction, Eq. (3.19). Moreover, since Sc is used for modelling the filtered scalar dissipation (as in Eq. (3.35)), a lower value of Sc leads to a higher value of total scalar dissipation which directly affects the prediction of species in the combustion model.

- Effects of Turbulent Schmidt Number

Similarly, the turbulent Schmidt number, Sc_t , affects both the turbulent diffusion rate (section 5.4.3) and the scalar dissipation rate at subgrid scale, Eq. (3.35).

- Effects of Subgrid-scale Variance of Mixture Fraction, $\widetilde{\xi''^2_{sgs}}$

As previously explained in Chapter 3, C_ξ is a constant used in the modelling of the subgrid-scale variance, $\widetilde{\xi''^2_{sgs}}$ (Eq. (3.34)). Normally, $\widetilde{\xi''^2_{sgs}}$ is used to presume the shape of the FDF (section 4.4.1) of ξ . Moreover, it is directly required for the modelling of subgrid-scalar dissipation rate in this project. Hence, the number of C_ξ affects directly the subgrid-scalar dissipation rate (\widetilde{N}_{sgs} in Eq. (3.35)), which is an important variable in the CMC methodology.

6.4.2 Parametric Studies of the Combustion Model

The evaluation of the LES-CMC combustion model is the focus of this research project. The parametric studies concerning the combustion model carried out here comprise the evaluation of the CMC formulation, the approximation of the CMC convective fluxes and the model for the conditionally filtered turbulent diffusivity for the CMC resolution. The

details of the numerical methods for each numerical aspect can be found in sections 4.5.1 and 5.4.

6.4.3 Parametric Study of CMC Grid Resolution

Another key parametric study for all Sandia Flame series is the CMC grid resolution. For a simple and stable flame, this parameter might not reveal any effect. However, it is believed that a high number of CMC cells may capture the extinction and re-ignition phenomena in Flames E and F due to the better intermittency and less averaging out of peaks of scalar dissipation. Thus, three CMC grid resolutions are performed in this study topic. These are $4 \times 4 \times 80$, $8 \times 8 \times 80$ and $16 \times 16 \times 80$ CMC cells for the same LES resolution.

To summarize, all parametric studies are shown in Table 6.3. All parameters in Table 6.3 were varied for Flame D and the values resulting in the best agreement between simulation and experiments were chosen for further simulations of Flames E and F.

Table 6.3: Summary of parametric studies.

Quantity	Name	values or methods
Variances of inflow generator	variance-1	$u'u', v'v'$ and $w'w'$ [88]
	variance-2	$\frac{2}{3}u'u', \frac{2}{3}v'v'$ and $\frac{2}{3}w'w'$
Schmidt number, $Sc = \mu/\rho D$	Sc_1	0.4
	Sc_2	0.7
	Sc_3	1.0
Turbulent Schmidt number, Eq. (3.32)	$Sc_{t,1}$	0.4
	$Sc_{t,2}$	0.7
Variance of mixture fraction, Eq. (3.34)	$C_{\xi,1}$	0.2
	$C_{\xi,2}$	0.3
CMC formulation	CMC-1	Conservative CMC, Eq. (4.35)
	CMC-2	Non-conservative CMC, Eq. (4.30)
Convective flux	flux-1	Computing fluxes based on LES cells at CMC faces
	flux-2	Computing fluxes based on CMC cell centres
Conditionally filtered turbulent diffusivity	$D_{\eta,1}^*$	Modelling D_{η}^* based on CMC cells, Eqs. (4.39) - (4.42)
	$D_{\eta,2}^*$	Modelling D_{η}^* based on LES cells, Eq. (4.43)
	$D_{\eta,3}^*$	Modelling D_{η}^* with adjusting the length scale, Eq. (4.44)
Number of CMC cells	$4 \times 4 \times 80$	4 CMC cells in x - and y -directions with 80 CMC cells in z -direction
	$8 \times 8 \times 80$	8 CMC cells in x - and y -directions with 80 CMC cells in z -direction
	$16 \times 16 \times 80$	16 CMC cells in x - and y -directions with 80 CMC cells in z -direction

6.5 Results of Sandia Flame D

The results from the parametric studies summarized in Table 6.3 are represented by Flame D as a reference case. At first, the statistics of flow and mixing fields with varying parameters are discussed, followed by the effects of different combustion model parameters. The influence of the CMC grid resolution is also discussed.

6.5.1 Parametric Studies of Flow and mixing Field

It should be noted that the Schmidt number is actually not allowed to change since it is a fluid property. However, the parametric study of the Sc is investigated to test a sensitivity of the flow and mixing fields.

- Effects of Velocity Variance in Turbulent Inflow Generator

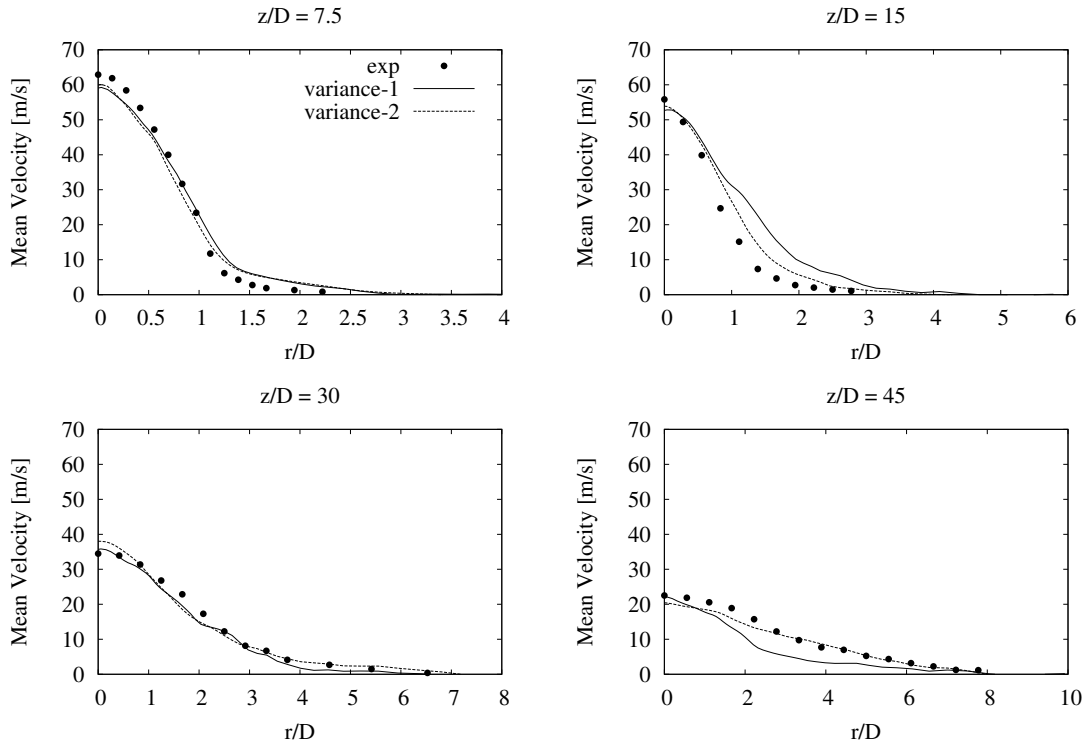


Figure 6.3: Radial profiles of mean axial velocity at four downstream locations. Symbols denote experimental values [88]. Solid and dashed lines indicate LES-CMC simulation with the different values of inflow variance.

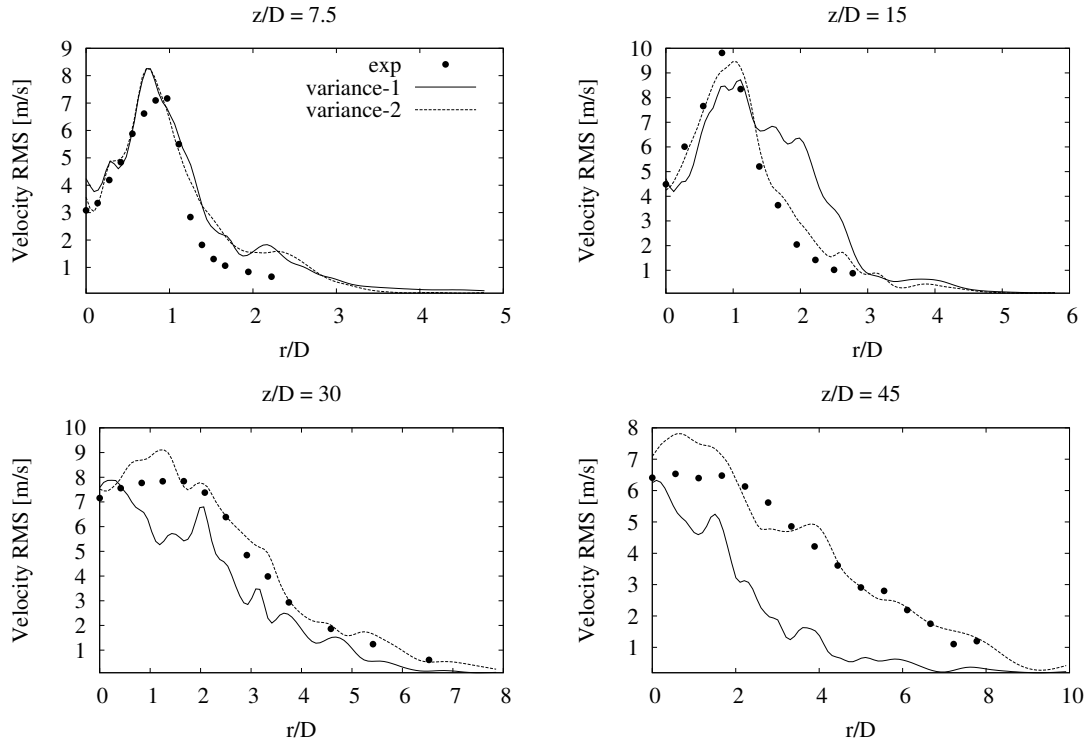


Figure 6.4: Radial profiles of RMS axial velocity at four downstream locations. Symbols denote experimental values [88]. Solid and dashed lines indicate LES-CMC simulation with the different values of velocity variance of inflow generator.

Figures 6.3 and 6.4 show the effects of the velocity variance levels (turbulence levels) of the inflow generator on the statistical mean and RMS of the axial velocity at four different downstream positions. The position x/D is labeled as r/D as in the experiment in order to avoid the confusion. Different results between both velocity variance levels can come from another quantity which affects the velocity profile at $z/D = 15$. The predictions of mean velocity of the higher inflow turbulent level (variance-1) are greater than the experiment (as can be seen from Fig. 6.3 for $r/D > 1$ at $z/D = 15$) and lower mean velocity at the centerline ($r/D = 0$ at $z/D = 15$) compared with the experiment. Moreover, the values of RMS velocity downstream of the higher inflow turbulent level ($z/D = 30$ and 45) are lower than the experiment. On the other hand, variance-2 having a lower inflow turbulence level generates thinner shape of mean velocity upstream profiles which correspond to the experiment, as can be seen from Fig. 6.3 at $z/D = 15$. Furthermore, this case provides good agreement with the experiment for statistical RMS values (Fig. 6.4).

Therefore, the values of the turbulence level from variance-2 ($2/3$ of measured variances at $z/D = 0.14$) are chosen as for the remainder of the simulations.

- Effects of Schmidt number

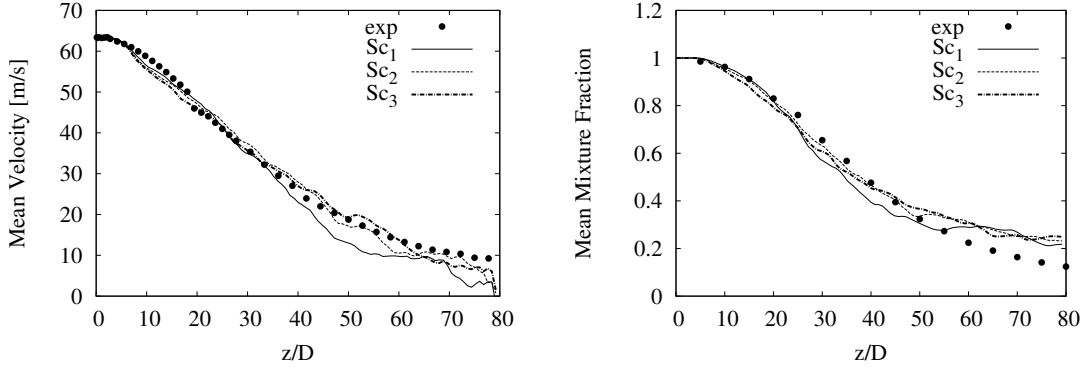


Figure 6.5: Axial profiles of mean axial velocity and mixture fraction. Symbols denote experimental values [4, 88]. Solid and dashed lines indicate LES-CMC simulation with the different Schmidt numbers.

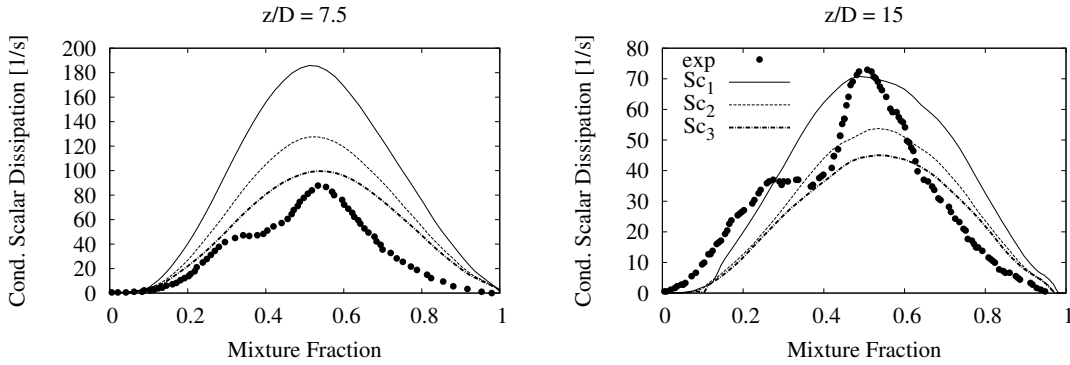


Figure 6.6: Conditional averages of mean scalar dissipation in mixture fraction space at two downstream locations. Symbols are experimental data [36], while the solid and dashed lines are LES-CMC results for various Schmidt numbers.

The influences of different values of Schmidt number on the mean flow and mixing field are shown in Fig. 6.5. In every simulation, the Sc_t is set to be 0.7 and only Sc has been varied (as in Table 6.3). In principle, all values of the Schmidt number provide similar results. However, the results from Sc_2 and Sc_3 seem to correspond with the experiment better than Sc_1 , which results in an under-prediction of the downstream mean axial velocity and mixture fraction. Moreover, the conditional

scalar dissipation (resolved and sub-grid scale) at $z/D = 7.5$ and 15 over mixture fraction space in Fig. 6.6 demonstrates that the low value of Schmidt number in Sc_1 generates extreme over-prediction of conditional scalar dissipation rates compared with the experiment. Since there is high dissipation at $z/D = 7.5$ and 15 with Sc_1 , the updated density values in the rich zone are low. These updated values of density affect the filtered momentum equation and the velocities directly in the next time step. Therefore, the axial velocities which are calculated using updated densities from Sc_1 in the filtered momentum equation are changed to be small in the axial profiles. These results can be seen in the mean axial velocity profile (Fig. 6.5) for the range $20 < z/D < 50$. Since the mixture fraction field is calculated from the velocity field and diffusion model ($D = \nu/Sc$), the same effect can be found on the mean mixture fraction profile. On the other hand, the high value of Schmidt number in Sc_3 results in a relatively low conditional scalar dissipation rate, compared with the experimental data at $z/D = 15$. Having the same value as fluid property, Sc_2 ($Sc = 0.7$) shows good agreement with experiments for the mean axial velocity and mixture fraction, whereas the results of conditional scalar dissipation prediction are acceptable. Therefore, Sc_2 is chosen for all further studies.

- Effects of Turbulent Schmidt number

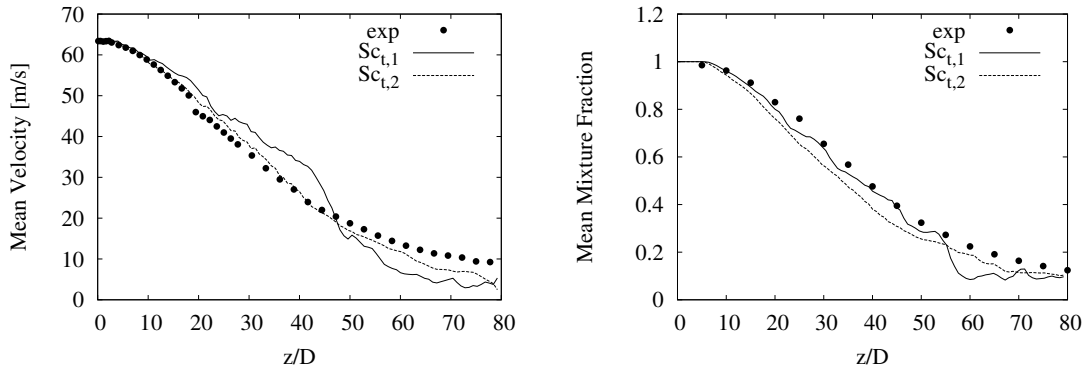


Figure 6.7: Axial profiles of mean axial velocity and mixture fraction. Symbols denote experimental values [4, 88]. Solid and dashed lines indicate LES-CMC simulation with the different turbulent Schmidt numbers.

Similar to Sc , the value of Sc_t also affects both velocity and mixture fraction fields. However, Sc_t describes momentum and mass transfer at the subgrid scale which

is related to the reaction field. The changing of Sc_t is performed to improve the mixture fraction field with some effects on the flow field. Figure 6.7 shows the influence of two different values of Sc_t (0.4 and 0.7). Here, $Sc_{t,1} = 0.4$ increases the mean mixture fraction (right) and yields the better agreement with the experiment, while there are some effects on the mean axial velocity profile (left). Even though some over-predictions can be observed from the velocity profile of $Sc_{t,1}$ from Fig 6.7, the tendency of this velocity prediction seems to correspond with the experimental data. Therefore, the value of the turbulent Schmidt number from $Sc_{t,1}$ is specified for further studies.

- Effects of Variance of mixture fraction

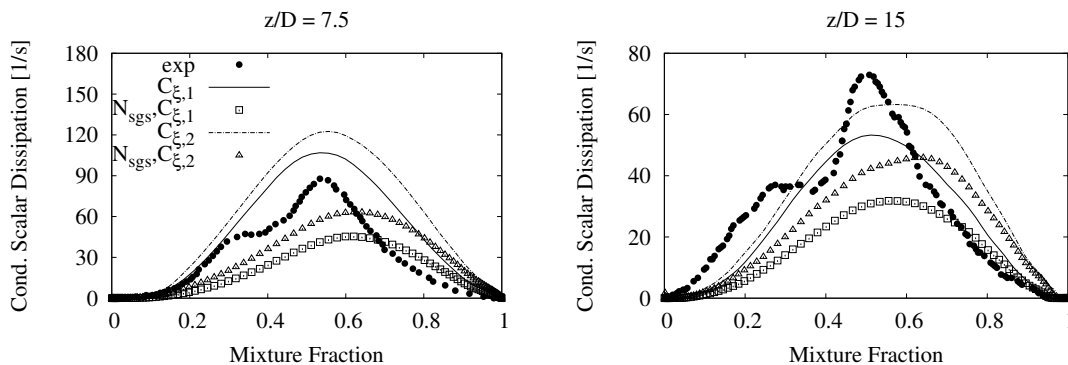


Figure 6.8: Conditional averages of mean scalar dissipation in mixture fraction space at two downstream locations. Circles are 3-D experimental data [36], while the solid lines, dashed lines, squares and triangles are LES-CMC model in various C_ξ cases.

As described in the previous section, C_ξ is known as an independent constant in the subgrid-scale variance modelling which is further employed in the subgrid-scale scalar dissipation, N_{sgs} , modelling. Thus, the larger C_ξ is, the higher subgrid-scale conditional scalar dissipation (squares and triangles in above figure) will be, in accordance with Eqs. (3.34) and (3.35). Figure 6.8 shows the effect of two different values of C_ξ on the conditional scalar dissipation and subgrid-scale conditional scalar dissipation at two downstream locations. $C_{\xi,1}$ ($C_\xi = 0.20$) produces more appropriate conditional scalar dissipations compared with the experiment. Therefore, this value is selected to be applied for further studies.

6.5.2 Parametric Studies of Combustion Model

As demonstrated in Table 6.4, five case studies are performed to show the effects of each case in the CMC model. All cases are based on the optimal conditions from parametric studies of flow and mixing field (variance-2, Sc_2 , $Sc_{t,1}$ and $C_{\xi,1}$) and use $8 \times 8 \times 80$ CMC cells. A reference case (case-1) includes the models CMC-1, flux-1 and $D_{\eta,2}^*$, while the other cases have at least one varied parameter compared with the reference case.

Table 6.4: Summary of different parameters in combustion model study. The meaning of each numerical method can be found in Table 6.3.

Name	Combustion Model	Flow and Mixing Field	CMC Grid Resolution
case-1 (reference case)	CMC-1, flux-1, $D_{\eta,2}^*$	variance-2 $Sc_2, Sc_{t,1}$ $C_{\xi,1}$	$8 \times 8 \times 80$
case-2	CMC-2, flux-1, $D_{\eta,2}^*$		
case-3	CMC-1, flux-2, $D_{\eta,2}^*$		
case-4	CMC-1, flux-2, $D_{\eta,1}^*$		
case-5	CMC-1, flux-1, $D_{\eta,3}^*$		

6.5.2.1 Flow and Mixing Field

In this section, all snapshots and simulation results stem from the reference case (case-1 from Table 6.4) to show an overview of the flow and mixing fields.

Figure 6.9 shows a snapshot of the instantaneous temperature field along a 2D plane through the burner centerline for the entire computational domain (left) and an enlarged area of the upstream region (right). The black lines identify the isoline of stoichiometric mixture fraction. A high level of turbulence which comes from the turbulent inflow generator at the inlet can be observed from the temperature profile (Fig. 6.9 (right)). Moreover, the local extinction, which would be characterized by the discontinuous red colour of the temperature along the isoline of stoichiometric mixture fraction, hardly occurs in Flame D, in accordance with the experimental findings.

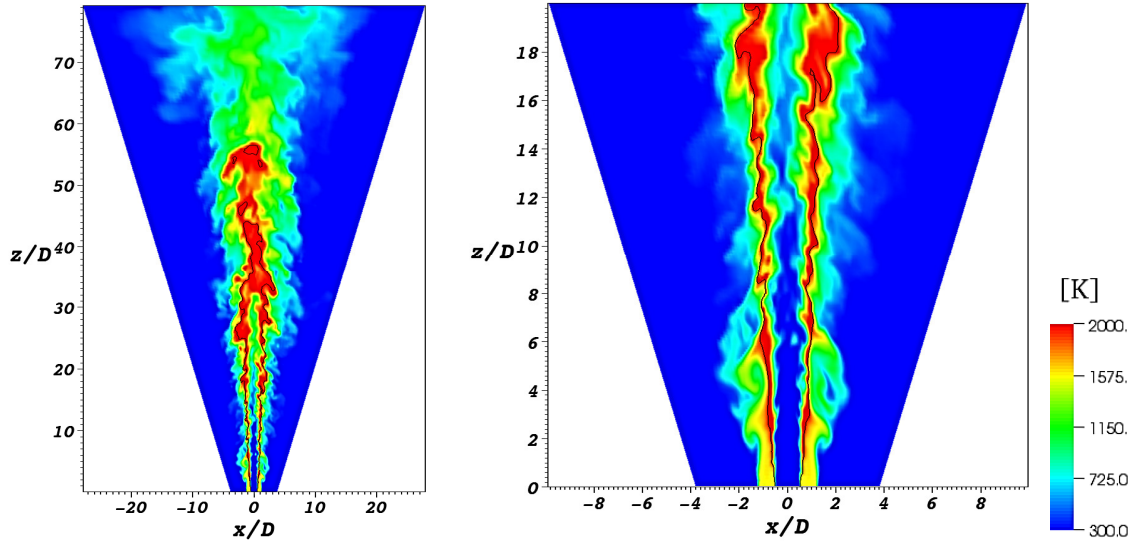


Figure 6.9: Snapshots of the temperature field in the total computational domain (left) and in the upstream region (right) for Sandia Flame D which are rerun using large domain (Table 6.2). The iso-contour of stoichiometric mixture fraction is represented by the black lines.

At the start of the study, the simulations have been performed using another computational domain which is narrower than the current domain. All statistics of Flame D are collected for the parametric studies using this narrow domain. The details of this initial computational domain are explained in section 6.3. However, there is unphysical recirculation along the lateral boundaries which can be observed from the enlarged snapshots of the velocity vectors in Fig. 6.10. This recirculation is a result of the narrow computational domain combined with the symmetry boundary condition at the lateral boundaries. Although there is an evidence of the recirculation, these recirculation effects are irrelevant for the analysis presented here and do not contaminate the simulation results in the region of interest for Flame D. Therefore, the statistics are acceptable and the parametric studies can be performed using data from the narrow domain.

The consideration of interesting positions of experimental data is determined by using Flame E, since the extinction and re-ignition are obviously detected in that flame. As a result of the discussion about this topic in section 6.6, the interesting positions are $z/D = 3, 7.5$ and 15 .

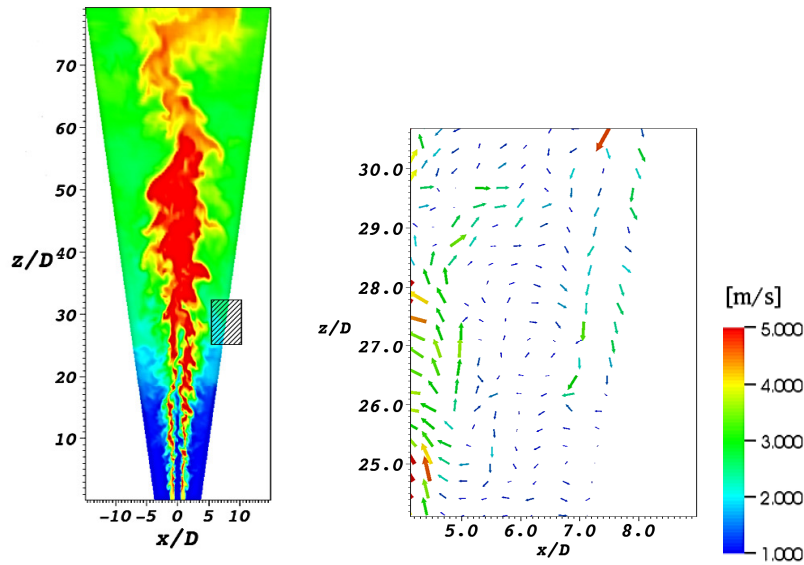


Figure 6.10: Snapshot of the velocity vectors at the lateral bound of domain for Sandia Flame D (right), evaluated in the box marked (left). A colour legend shows the velocity magnitude.

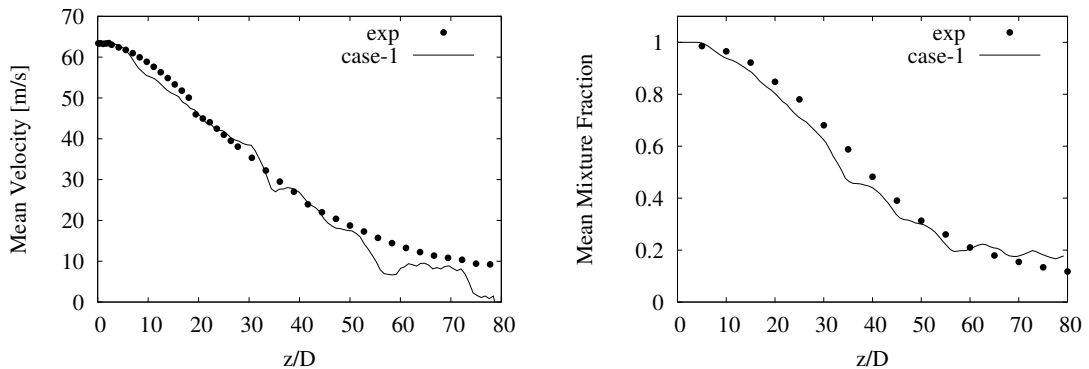


Figure 6.11: Axial profiles of mean axial velocity and mixture fraction along the centerline for Flame D. Symbols denote experimental data [88, 4], while the solid lines present the mean results of LES-CMC (reference case of Table 6.4).

Figure 6.11 shows a good agreement of the axial distributions of mean axial velocity and mixture fraction for the reference case (case-1) of the combustion model with experiments [4, 88]. Radial profiles of mean and RMS axial velocity and mixture fraction at three downstream locations are shown in Fig. 6.12. Both mean and RMS of the axial velocity and the mixture fraction correspond well with the experiments [88, 4], since the effects of inflow are previously checked and adjusted in section 6.5.1. Moreover, it can be seen

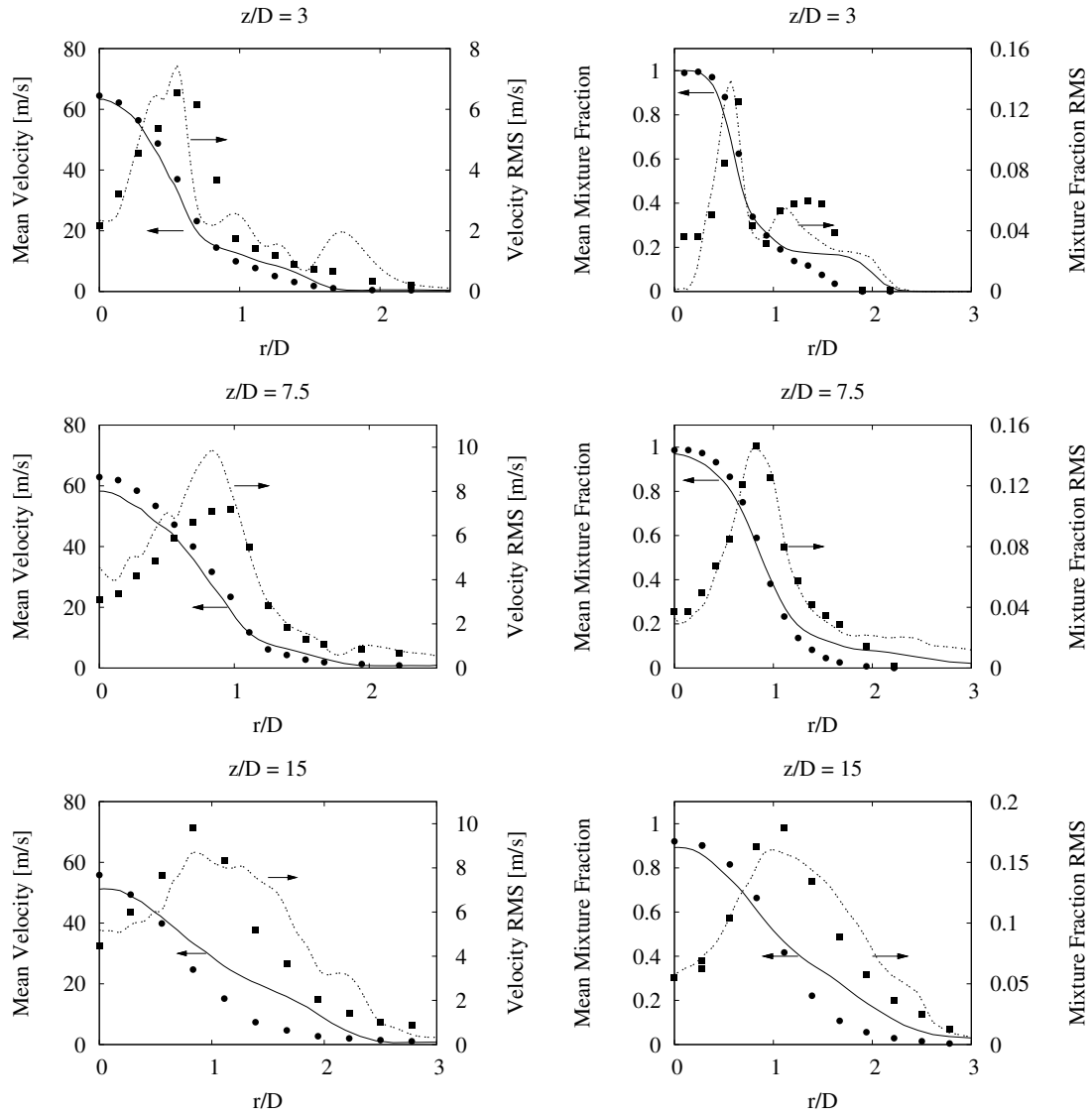


Figure 6.12: Radial profiles of mean and RMS axial velocity and mixture fraction at three downstream locations for Flame D. Symbols denote experimental values [88, 4], while the solid and dotted lines represent the mean and RMS results of LES-CMC (reference case of Table 6.4).

from Fig. 6.12 that the jet spreading is well captured. Small over-predictions of the mean mixture fraction in the range of $1.2 < r/D < 2$ at position $z/D = 3$ may come from some effects of the pilot which remain in these positions due to less turbulence of Flame D. Small over-predictions of the mean axial velocity and mixture fraction can be observed around $1 < r/D < 2$ at position $z/D = 15$. However, the current predictions provide a good basis for the parametric studies of the combustion model.

6.5.2.2 Preliminary Studies

The computational time for parametric studies of a combustion model can be reduced by preliminary studies. These investigations are performed to indicate the cases which have different convective flux predictions compared with the reference case (case-1 from table 6.4). Subsequently, all indicated and the reference cases will be further examined for statistical predictions in the proceeding sections.

In order to understand the processes taking place in this section, the explanations of the conservative CMC species transport equation (Eq. (5.9)) are necessary. Equation (5.9) is rearranged in a 3-D finite volume formulation as

$$\begin{aligned}
& \frac{\partial Q_{\alpha,P}^*}{\partial t} + \\
& \underbrace{\frac{\gamma_e^* A_e}{\gamma_P^* V} \left[\tilde{u}_{\eta,e}^* (Q_{\alpha,e}^* - Q_{\alpha,P}^*) - \left(D_{\eta}^* \frac{\partial Q_{\alpha}^*}{\partial x_1} \right)_e \right]}_I - \underbrace{\frac{\gamma_w^* A_w}{\gamma_P^* V} \left[\tilde{u}_{\eta,w}^* (Q_{\alpha,w}^* - Q_{\alpha,P}^*) - \left(D_{\eta}^* \frac{\partial Q_{\alpha}^*}{\partial x_1} \right)_w \right]}_{II} \\
& + \underbrace{\frac{\gamma_n^* A_n}{\gamma_P^* V} \left[\tilde{v}_{\eta,n}^* (Q_{\alpha,n}^* - Q_{\alpha,P}^*) - \left(D_{\eta}^* \frac{\partial Q_{\alpha}^*}{\partial x_2} \right)_n \right]}_{III} - \underbrace{\frac{\gamma_s^* A_s}{\gamma_P^* V} \left[\tilde{v}_{\eta,s}^* (Q_{\alpha,s}^* - Q_{\alpha,P}^*) - \left(D_{\eta}^* \frac{\partial Q_{\alpha}^*}{\partial x_2} \right)_s \right]}_{IV} \\
& + \underbrace{\frac{\gamma_r^* A_r}{\gamma_P^* V} \left[\tilde{v}_{\eta,r}^* (Q_{\alpha,r}^* - Q_{\alpha,P}^*) - \left(D_{\eta}^* \frac{\partial Q_{\alpha}^*}{\partial x_3} \right)_r \right]}_V - \underbrace{\frac{\gamma_l^* A_l}{\gamma_P^* V} \left[\tilde{v}_{\eta,l}^* (Q_{\alpha,l}^* - Q_{\alpha,P}^*) - \left(D_{\eta}^* \frac{\partial Q_{\alpha}^*}{\partial x_3} \right)_l \right]}_{VI} \\
& = \underbrace{(w_{\alpha,\eta})_P^*}_{VII} + \underbrace{\left(\tilde{N}_{\eta}^* \frac{\partial^2 Q_{\alpha}}{\partial \eta^2} \right)_P}_{VIII}, \quad (6.2)
\end{aligned}$$

where the coefficients, such as $\frac{\gamma_e}{\gamma_P}$, denote the density-FDF ratios between the boundaries and the centre of the cells ($\gamma = \bar{\rho} \tilde{P}(\eta)$). Terms *I* to *VI* represent convection at the CMC

cell face in east, west, north, south, right and left, respectively. Terms *VII* and *VIII* denote the chemical reaction and the diffusion terms, respectively.

Terms *I* to *VIII* in Eq. (6.2) can be shown as conditionally averaged values, Fig. 6.13, for any CMC cell. As an example, Fig. 6.13 shows the comparison of the instantaneous magnitudes between a convective flux in each direction, diffusion and chemistry of CO_2 in mixture fraction space. The simulation is performed using the reference case (case-1). Comparing Eq. (6.2) and Fig. 6.13, the convective flux in x -direction (X-conv) is the term *I* – *II*, the convective flux in y -direction (Y-conv) is the term *III* – *IV*, and the convective flux in z -direction (Z-conv) is the term *V* – *VI*.

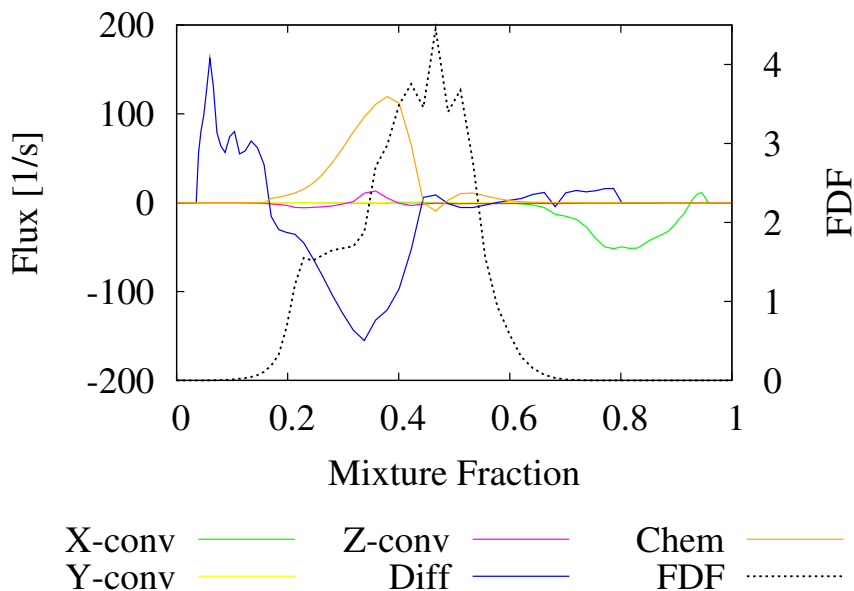


Figure 6.13: Convective fluxes in three directions of CO_2 for a time step at $r/D = 1$ and $z/D = 7.5$ compared with diffusion and chemistry terms of the reference case.

It can be observed from Fig. 6.13 that the diffusion (blue line) is the strongest term balancing the chemical reaction (orange line) term. Small convection occurs only in the z -direction. These similar predictions (as in Fig. 6.13) can be found for every species. A consideration of the FDF profile is required, since it is applied to transfer the values from a mixture fraction space to a physical space. A low value of FDF means only a small influence of any property can appear in physical space. Consequently, the large values of the convective flux in x -direction at $\eta > 0.6$ are not considered because there are low FDF values in this range. On the other hand, a large value of FDF means a large influence of

any property can appear in physical space. Therefore, all convective fluxes in the large values of FDF at $0.2 < \eta < 0.6$ are considered. The convective flux in z -direction, which has the largest value compared with the other direction, indicates most of the effects of convection on every scalar mass fraction. Thus, only the convective fluxes in z -direction will be investigated for the analyses of convective fluxes in further studies.

In order to focus on the effects of each case study that is different from the reference case, one possible method is the investigation of the convective fluxes in z -direction of all cases. This is because all numerical methods for the implementation of the CMC equation directly affect the spatial flux terms. To ensure that the solutions are correlated with the same LES results, the procedures of investigation begin by letting all case studies (Table 6.4) run only one time step from the same iteration. Since the fluxes and other terms of Eq. (6.2) in each case can change immediately, the differences of fluxes between each case can be detected. The examination of CH_4 fluxes in z -direction for all cases is performed at different CMC cells in axial and radial positions. The axial positions (Fig. 6.14) are varied from upstream ($z/D = 7.5$) to downstream positions ($z/D = 15$ and 30) along the centerline while the radial positions (Fig. 6.15) are varied, especially the positions comprising the shear layer ($r/D = 0, 1$ and 2) at the position $z/D = 7.5$.

Considering the results of the two directions from Figs. 6.14 and 6.15, it is found that the comparisons of the convective fluxes between different cases can be investigated in radial positions better than in axial positions. This consideration includes the effect of the FDF profiles at each position in order to compare the results in the real physical space as previously discussed in this section. Therefore, the comparison of fluxes in the radial direction is chosen to discuss in the further studies.

The results from Fig. 6.15 show that the convective flux predictions of case-1 and case-5 are similar, while the convective flux predictions of case-3 and case-4 are similar. The reason of these similar fluxes predictions is due to the small effects of different D_η models on the convective term (more details of $D_{\eta,1}^*$, $D_{\eta,2}^*$ and $D_{\eta,3}^*$ can be found in section 5.4.3). Since the similar flux predictions can be observed in case-3 and case-4, one of them is selected for the further studies. In this study, case-3 is chosen because it has only the method of flux approximation that is different from reference case. Therefore, case-1, case-2 and case-3 will be discussed below.

The predictions of convective fluxes from case-1 and case-2 at radial positions

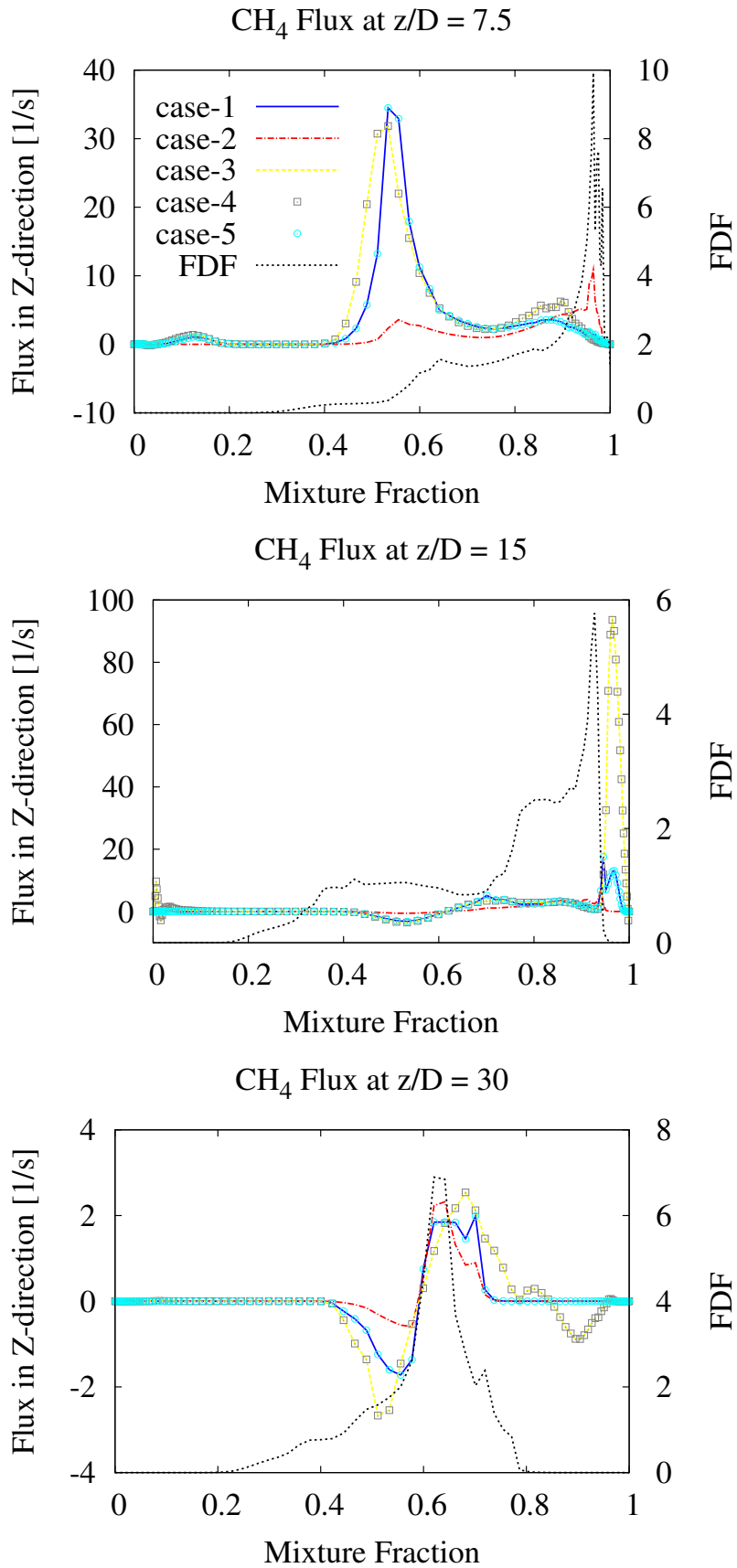


Figure 6.14: Convective fluxes of CH₄ in z-direction for a time step at three different axial positions with the same radial position, $r/D = 0$, for Flame D.

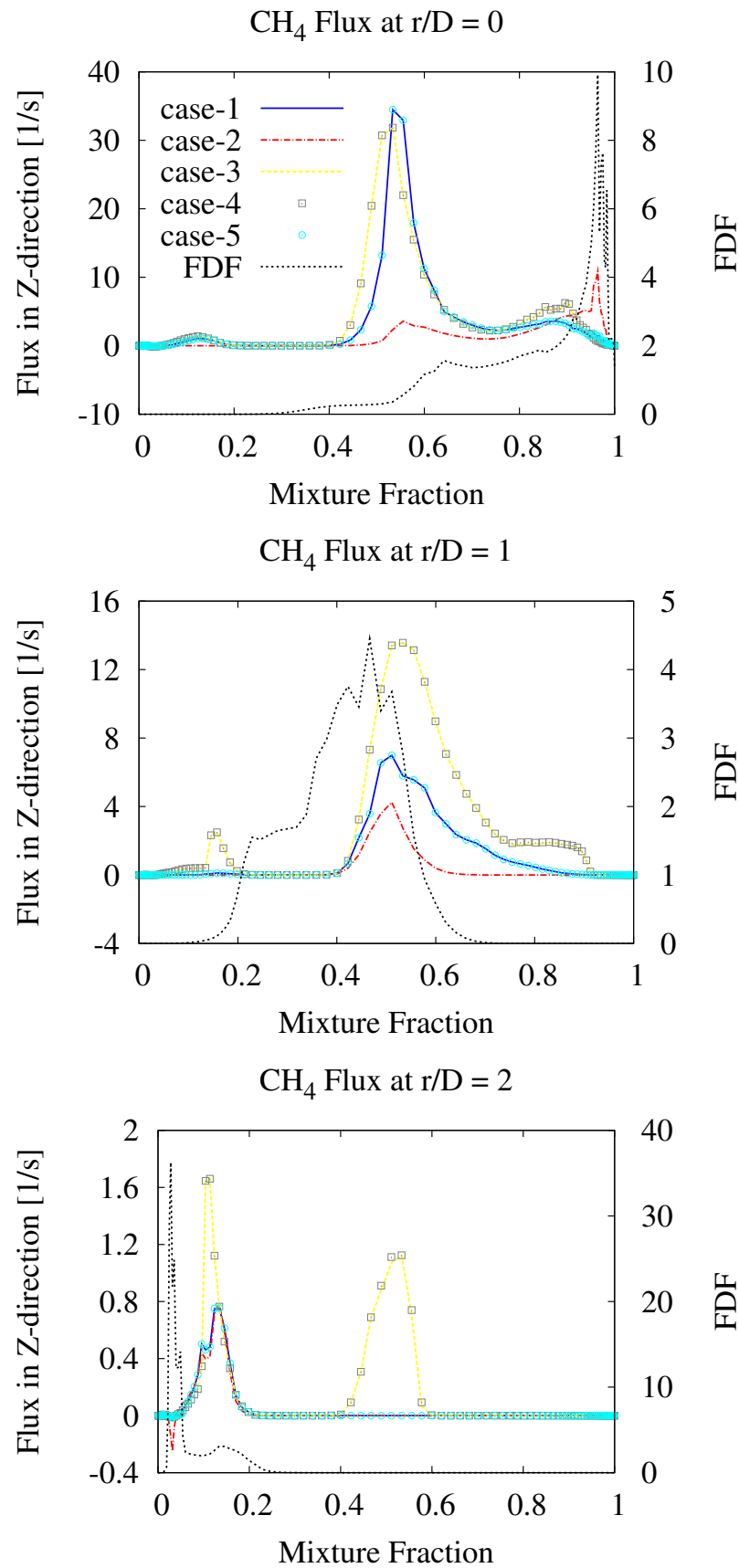


Figure 6.15: Convective fluxes of CH_4 in z -direction for a time step at three different radial positions with the same axial position, $z/D = 7.5$, for Flame D.

(Fig. 6.15) show that the convective flux predictions from the conservative form (case-1) differ from the predictions from the non-conservative form (case-2). The reason of these predictions is the difference between the convective flux calculations in the two different CMC formulations. As discussed in section 4.3, the conservative form has a weighting by the FDF ratio for the convective flux calculation. If the FDF values of two neighbouring CMC cells in z -direction are completely different, a high weighting factor ($\frac{\gamma_{face}^*}{\gamma_P^*}$) is calculated in z -direction, and it leads to a high convective flux for this direction. In general, the weighting factor for the z -direction can be more, less or equal to the one of other directions. These values depend on the ratio of the mixture fraction and the subgrid-scale of mixture fraction of the cell faces to the cell centre. As another numerical method, the non-conservative formulation has no weighting by FDF ratio in the convective flux calculation. This means it weights a flux in each direction equally. Therefore, the different predictions of case-1 and case-2 can be explained by the influences of weighting by FDF ratio in conservative CMC formulation.

The predictions of the convective fluxes from case-1 and case-3 at different radial positions (Fig. 6.15) show that fluxes from both cases are similar at position $r/D = 0$ and have the same tendency at positions $r/D = 1$ and 2. The additional flux of case-3 for $0.4 < \eta < 0.6$ at position $r/D = 2$ has almost no effect in physical space, since the FDF value is very low. The reason of similar flux predictions from both cases can be explained by the conservative CMC formulation used in case-1 and case-3. All convective fluxes are calculated by weighting with the FDF ratios and thus, they are similar. However, some different fluxes from both cases can be found at positions $r/D = 1$ and 2, since the different flux approximation methods influence the flux calculation especially at locations with high turbulence.

The investigations of different flux predictions are performed further for many species (e.g. OH, CH₂O, H₂O, CO₂ etc.) to ensure the decision of dominant cases which have different simulation results to each other. Case-1, case-2 and case-3 are initially considered as relevant cases, since they have different flux predictions at any position for all investigated species. Subsequently, the flux investigation at another starting point is observed by using the same procedures to have time-independent relations of flux predictions from variant case studies. It can be determined from the results of two different starting points that the different instantaneous flux predictions are also found in case-1, case-2 and case-

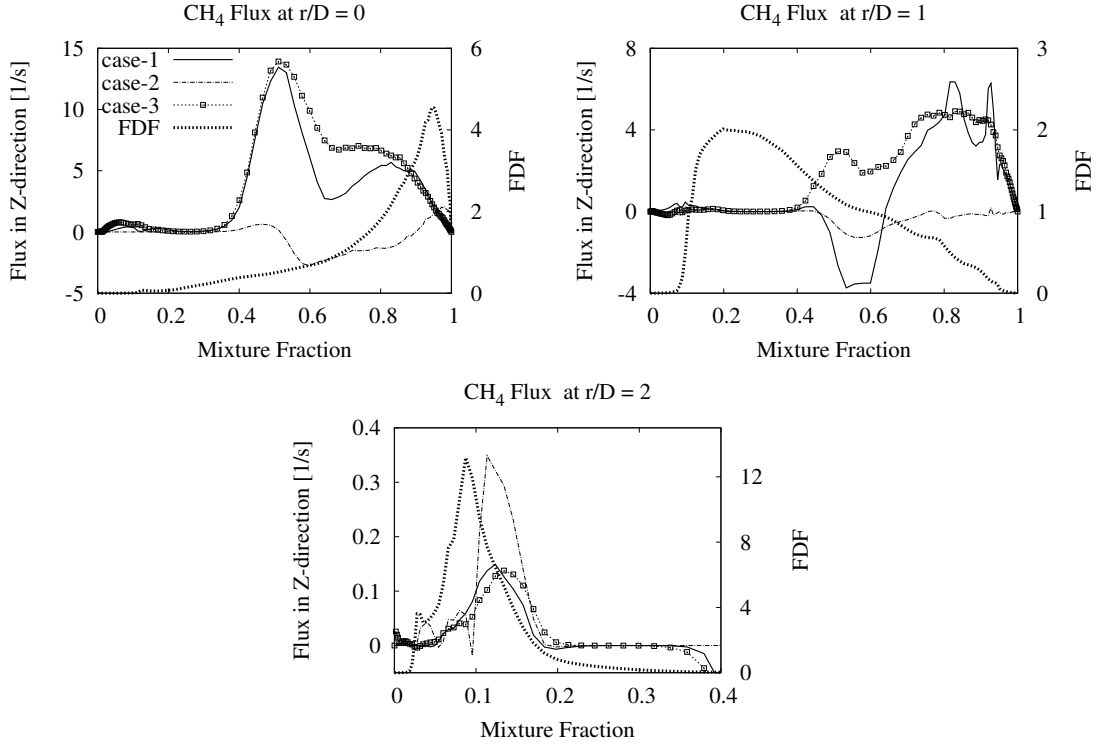


Figure 6.16: Mean convective fluxes of CH_4 in z -direction at three different radial positions with the same axial position, $z/D = 7.5$ (Sandia Flame D). The solid, dashed and square-dotted lines represent the results of LES-CMC in different cases and FDF (reference case) in combustion model (Table 6.4).

3. When the instantaneous fluxes of any case study differ from the reference case, it can imply that the statistical flux predictions will differ. These differences directly influence the conditional and unconditional profiles of each species. The statistical flux predictions which are sampled over 10,000 time steps from the three selected cases can be observed in Fig. 6.16. At position $r/D = 2$, the mixture fraction is shown only in the range of $\eta \leq 0.4$. This is because there are very low FDF values where $\eta > 0.4$, and so that the mean convection in physical space are very small in this range.

In the following sections, statistical temperature and species of these three cases are sampled for 7.6 ms (physical time, i.e. over 10,000 time steps) to validate by comparison with experimental data and to investigate the different effects of the statistical results from three case studies in the combustion model. Note that the reference time which is required for the fluid particle to travel from inlet to outlet of the computational domain is defined as $t_{ref} \equiv 80D/U_j$, where U_j is the mean jet (bulk) velocity. Thus, the t_{ref}

of Sandia Flame D is 11.61 *ms*. Although the physical time which is considered in this project is less than t_{ref} of Sandia Flame D, it provides enough data for collecting statistics at the interesting positions ($z/D = 3, 7.5$ and 15).

6.5.2.3 Conditionally Filtered Reactive Scalars

The performance of each case of the combustion model can be directly considered in mixture fraction space. All statistics of measurement data in this section are available only in cross-sectionally averaged values and thus all conditional simulation results in this section are presented in the same type as the measurements.

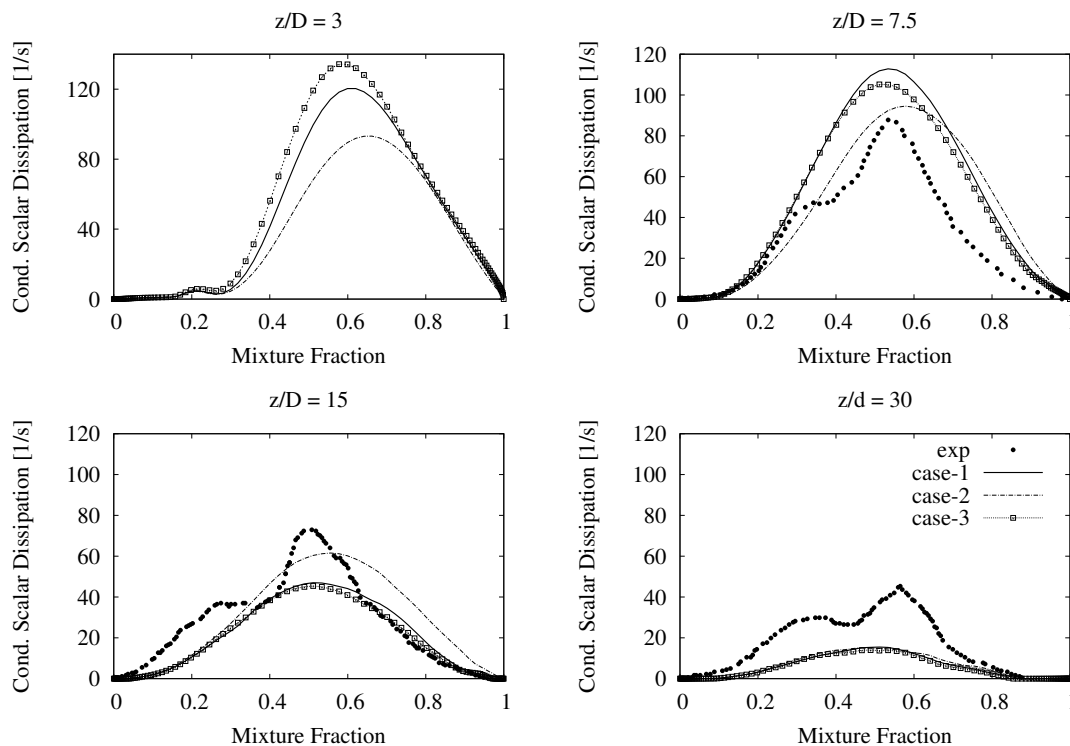


Figure 6.17: Conditional averages of mean scalar dissipation in mixture fraction space at four downstream locations for Flame D. Circles are 3-D experimental data [36], while the solid, dashed and square-dotted lines represent the results of LES-CMC in different cases of combustion model (Table 6.4).

The comparison between experiments and simulation results (case-1, case-2 and case-3 from Table 6.4) of the conditional scalar dissipation, Eq. (4.37), at four different downstream locations is presented in Fig. 6.17. For a short explanation, case-1 is the conservative CMC with a flux approximation based on LES cells at CMC faces, case-2 is

the non-conservative CMC with the same flux approximation as case-1 and case-3 is the conservative CMC with a flux approximation based on CMC cell centres.

A local minimum of experiments at mixture fraction values around 0.4 may be associated with differential molecular diffusion [36]. The differences of statistically conditional scalar dissipation between each case study should come from the differences of instantaneous convective fluxes (discussed in section 6.5.2.2). Species and densities, which are outcomes of the combustion model, vary between each case. Consequently, different mixture fraction in the same LES cell of each case is computed from these updated densities in the next time step. The conditional scalar dissipation rates for all cases are computed based on the gradient of mixture fraction, Eq. (3.35). Thus, different values of the instantaneous conditional scalar dissipation in each case are calculated. Since statistical values are the averages of the instantaneous value, predictions of the statistically conditional scalar dissipation in each case are different. These facts can be observed in Fig. 6.17.

From this figure, some over-predictions of this value occur in upstream locations ($z/D = 7.5$). However, the agreement of the predictions and experiments at $z/D = 15$ is very good, especially for case-1. The over-prediction of the upstream location comes from the configured constant value of the filtered scalar dissipation model (Eq. (3.35)) so that the predictions of the downstream location match with the relevant experiments. It should be noted that uncertainty estimates are not provided for the measurement [68]. More details of an analysis of uncertainties from experimental noise and spatial averaging can be found in [5].

A good agreement of case studies with experiments is shown in Figs. 6.18 and 6.19 for the conditional mean temperature and the conditional mean mass fraction of CO, CH₄ and H₂. Note that the error bars indicate the conditional RMS and they are only plotted to illustrate the conditional turbulent fluctuations of each scalar. Under-predictions of conditional temperature distribution on the lean side ($\eta < 0.35$) at position $z/D = 3$ (Fig. 6.18) may belong to the effect of CMC initial conditions (from the SLFM solution).

Since there are gaps of experimental data on the rich side of mixture fraction space ($0.38 \leq \eta \leq 0.65$) for Flame D at the position $z/D = 3$ (Figs. 6.18 and 6.19), it should be better to investigate and validate the predictions at this position by using Flame E. The reason of the gaps is quoted in [4] that CO-Raman measurement, are strongly affected

by hydrocarbon fluorescence interferences. Consequently, imperfect corrections of these interferences cause errors in the conditional means in the region of high interference on the rich side ($\eta > 0.35$) of the reaction zone.

Figures 6.18 and 6.19 demonstrate that case-1 (conservative CMC) gives generally more accurate results than the others at the positions $z/D = 7.5$ and 15. Moreover, both sets of figures show that case-2 (non-conservative CMC) is usually over-predicted on the rich side of mixture fraction in temperature and intermediate products, while the under-predictions occur at the same positions in the fuel (CH_4).

It can also be observed from the Figs. 6.18 and 6.19 that the cross-sectionally averaged simulation results from case-1 and case-3 are close, even though the convective fluxes of any cell of both cases (Fig. 6.16) are different from each other. This is caused by FDF value of each CMC cell in the same cross section, whose value is employed to calculate the cross-sectional averages. If the conditional predictions between two cases of any CMC cell have a difference where the low FDF is calculated, the conditional predictions in cross-sectional averages will be similar. This aspect of FDF values can be seen in Fig. 6.20.

Figure 6.20 shows the conditional temperature predictions at the radial positions $r/D = 0, 1$ and 2 which are computed from the fifth, sixth and seventh CMC cells, respectively. Note that at position $r/D = 2$, mixture fraction space is shown only in the range of $\eta \leq 0.32$, since the numerical problem in postprocessing (statistical calculation) makes statistical temperature do not exist outside this range. The numerical problem originates from very small FDF values where $\eta > 0.32$. These small FDF values make the statistics of the conditional temperature, whose values are calculated by weighting with instantaneous FDF and a time step of every iteration, do not exist. Thus, the range of $\eta > 0.32$ at $r/D = 2$ is not shown here. The different FDFs can be observed in Fig. 6.20. The conditional mean temperatures of case-1 and case-2 differ from each other especially at $r/D = 0$ and 1. The reason for different predictions between case-1 and case-2 on the rich side ($\eta > 0.35$) is due to two different sets of convective fluxes which are calculated from the two CMC formulations. Because of the lack of FDF-weighting function in convective term, the different convective fluxes on the rich side of case-2 (non-conservative CMC) are generated in the upstream positions. The same tendency can be observed at position $z/D = 7.5$ in Figs. 6.15 and 6.16.

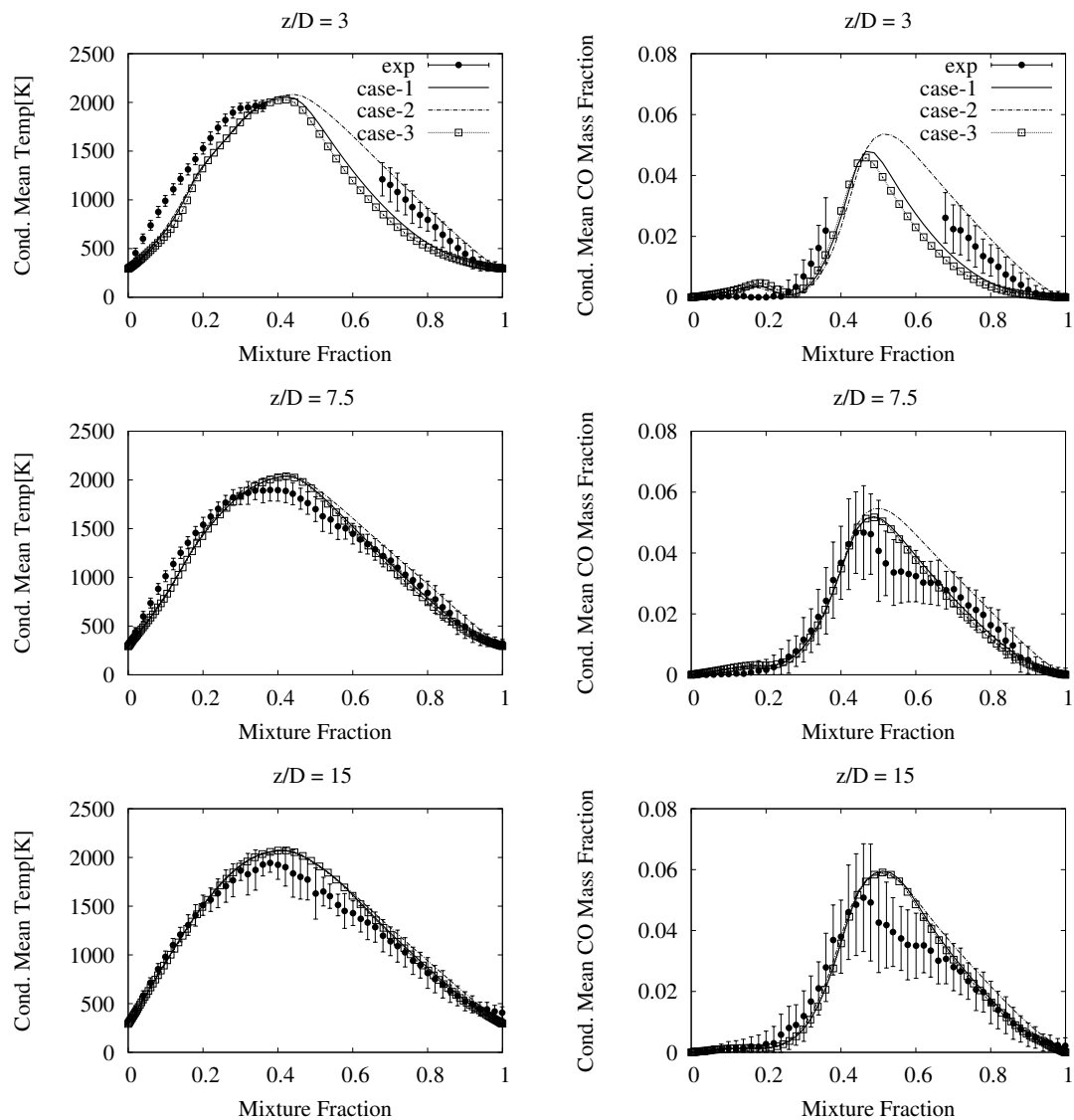


Figure 6.18: Conditional profiles of cross-sectionally averaged temperature and CO at three different downstream positions in mixture fraction space for Flame D. Circles are experimental data [4], while the solid, dashed and square-dotted lines represent the results of LES-CMC in different cases in combustion model (Table 6.4).

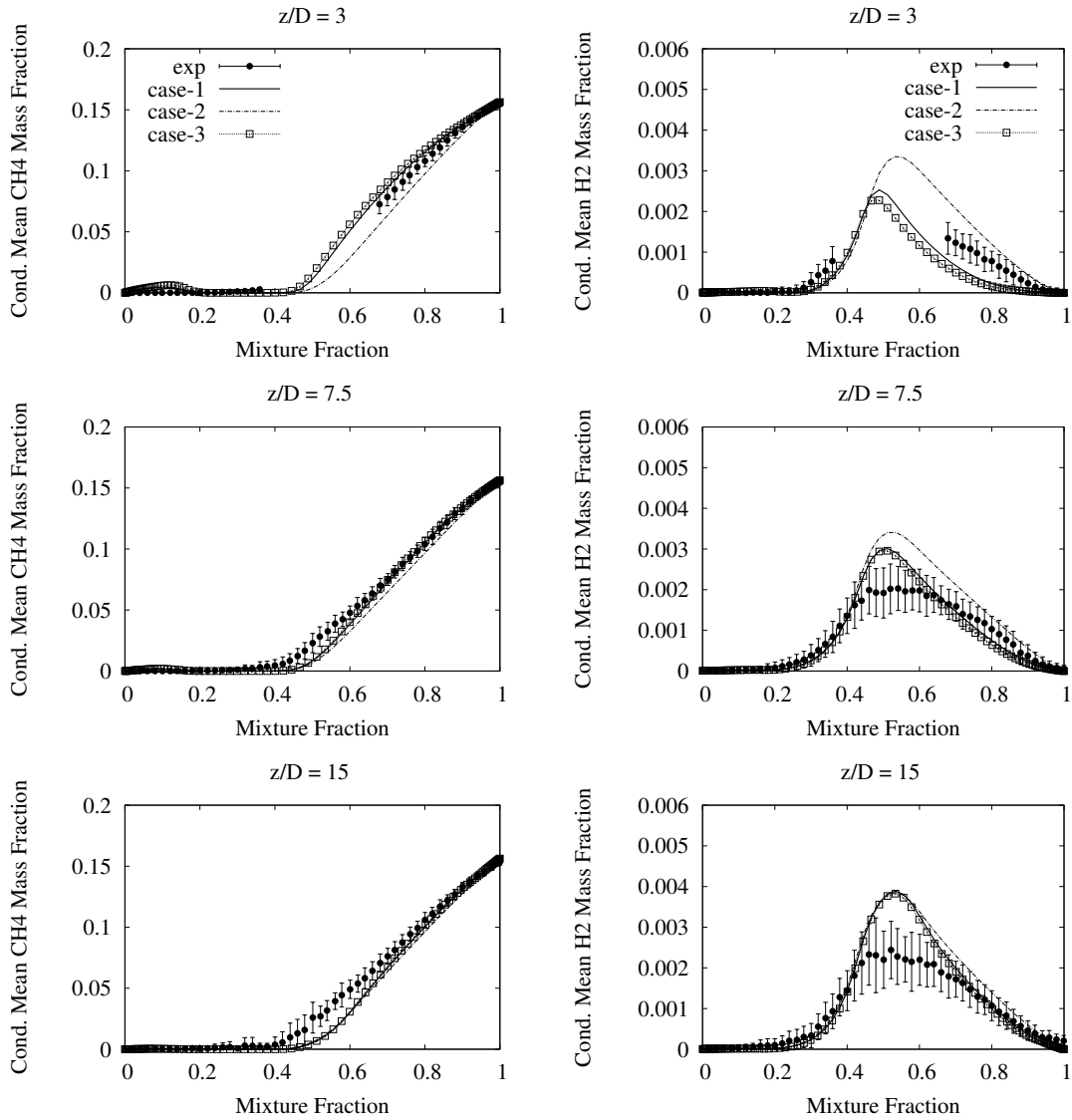


Figure 6.19: Conditional profiles of cross-sectionally averaged CH₄ and H₂ at three different downstream positions in mixture fraction space for Flame D. Circles are experimental data [4], while the solid, dashed and square-dotted lines represent the results of LES-CMC in different cases in combustion model (Table 6.4).

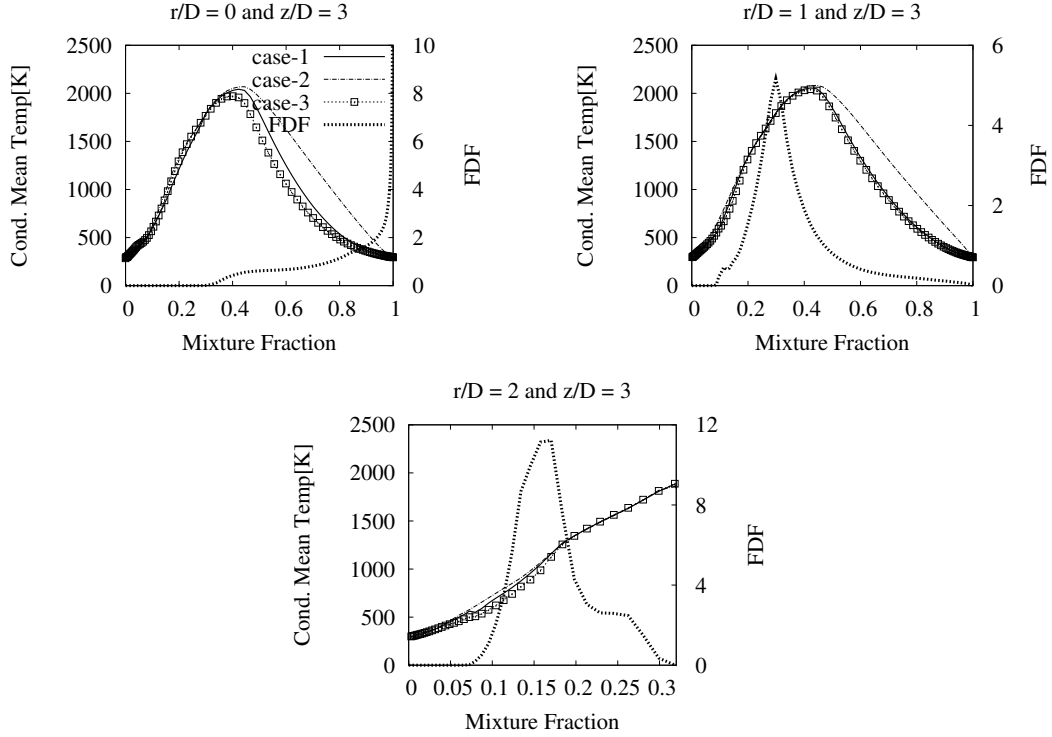


Figure 6.20: Conditional profiles of averaged temperature at three different radial positions of $z/D = 3$ in mixture fraction space for Flame D. The solid, dashed and square-dotted lines represent the results of LES-CMC in different cases and FDF (reference case) in combustion model (Table 6.4).

6.5.2.4 Unconditionally Filtered Reactive Scalars

Generally, an agreement is observed throughout the simulation results of radial distributions of unconditional temperature and reactive species from three implementations of the combustion model in Figs. 6.21 and 6.22. From the predictions of CO and H₂ at positions $z/D = 3$ and 7.5 (Figs. 6.21 and 6.22 (right)), it can be seen that the simulation results of case-2 agree well with the experimental data only around the centre (axial) regions. On the other hand, over-predictions in radial profiles of these species around $r/D = 0.4 - 0.8$ are observed, whereas the under-predictions in the same positions can be found in the radial profiles of fuel (CH₄ in Fig. 6.22 (left)). In general, these unconditional results exactly follow the conditional results from section 6.5.2.3. However, over-predictions of all cases for temperature at position $z/D = 3$ where $r/D > 1.2$ are caused by the over-predictions from radial distributions of mixture fraction at the same position (Fig. 6.23).

Additionally, over-predictions of the radial predictions of CO and H₂ in case-1 and case-3 around $r/D = 1.0 - 1.4$ at position $z/D = 7.5$ and for all range at position $z/D = 15$ can be attributed to the over-predictions of mixture fraction which can be seen from Fig. 6.23. Note that mixture fraction is employed to transfer the conditional value to the unconditional value via an FDF table (discussed in section 4.5).

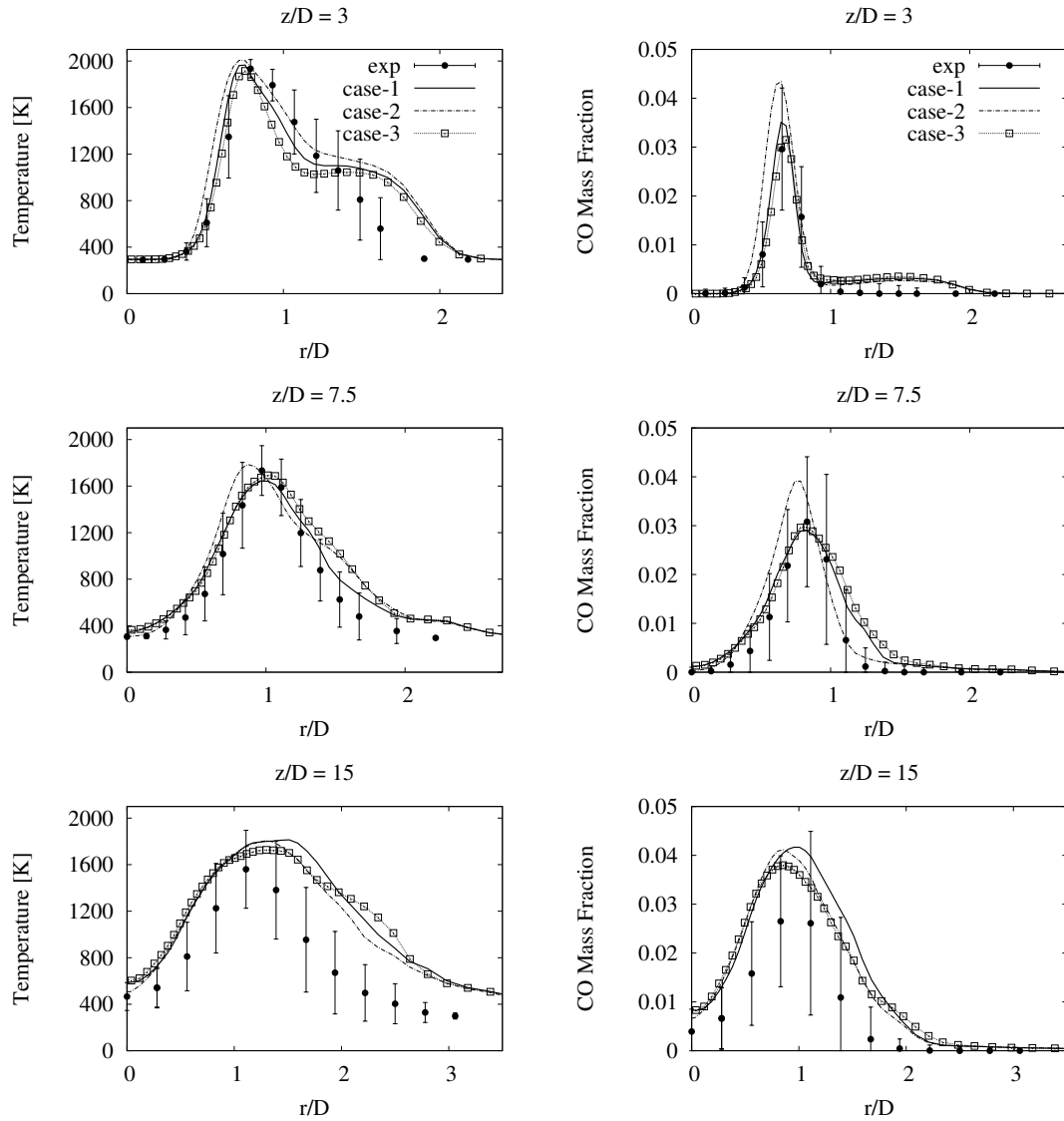


Figure 6.21: Radial profiles of mean temperature and CO for Flame D. Circles are experimental data [4], while the solid, dashed and square-dotted lines represent the results of LES-CMC in different cases in combustion model (Table 6.4).

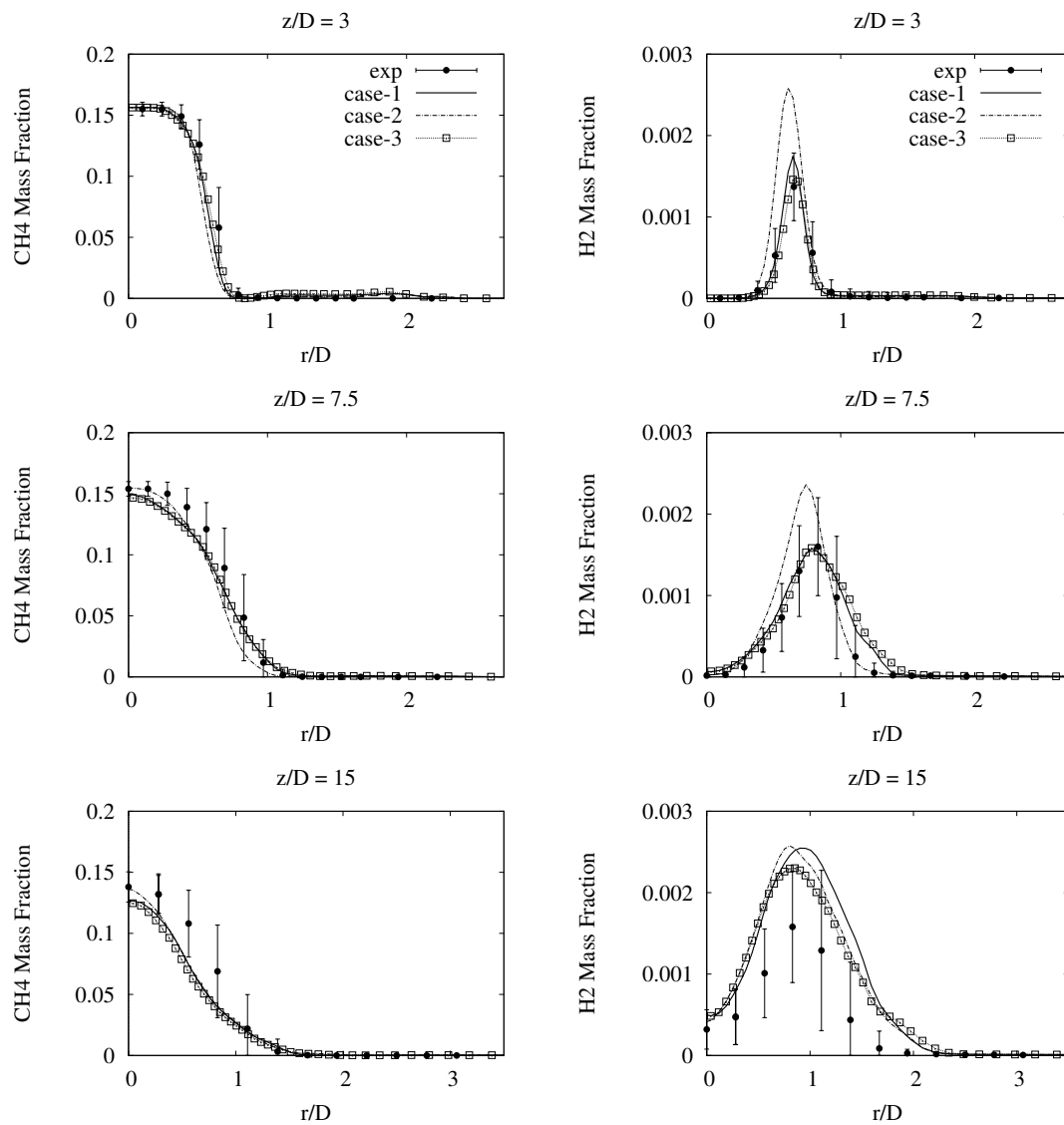


Figure 6.22: Radial profiles of mean CH_4 and H_2 for Flame D. Circles are experimental data [4], while the solid, dashed and square-dotted lines represent the results of LES-CMC in different cases in combustion model (Table 6.4).

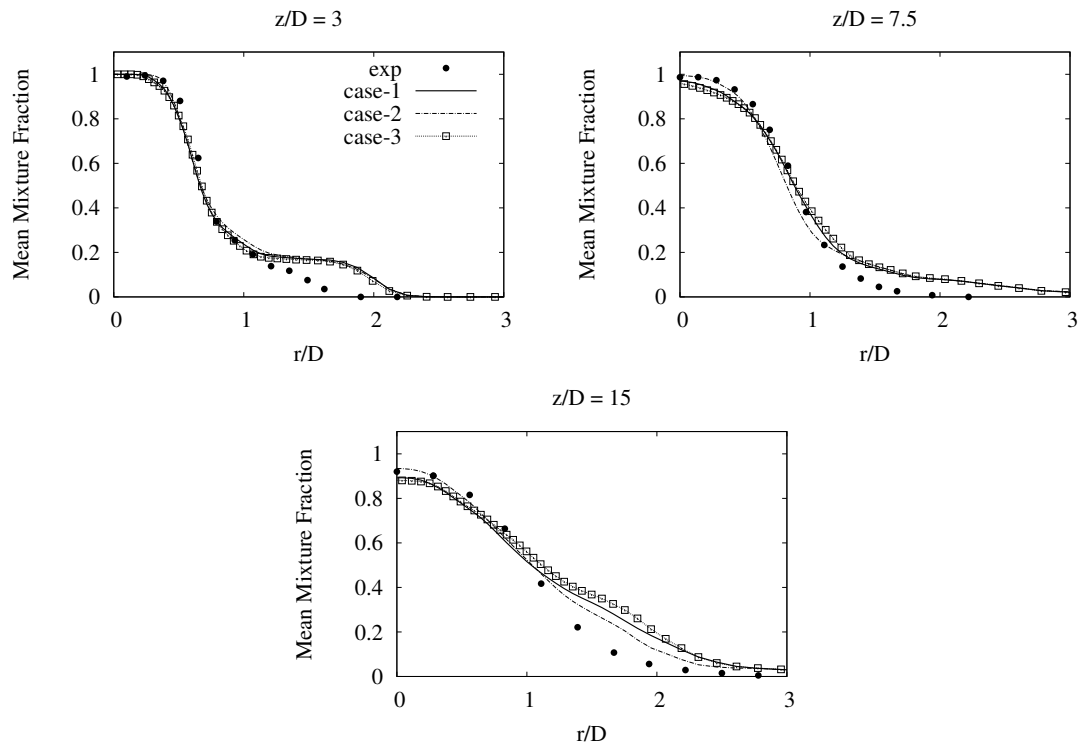


Figure 6.23: Radial profiles of mean mixture fraction for Flame D. Circles are experimental data [4], while the solid, dashed and square-dotted lines represent the results of LES-CMC in different cases in combustion model (Table 6.4).

6.5.3 Parametric Study of CMC Grid Resolution

As described in Table 6.3, three cases of the CMC grid resolution are varied, while the same conditions of the flow and mixing fields (variance-2, Sc_2 , $Sc_{t,1}$ and $C_{\xi,1}$) and CMC combustion model (CMC-1, flux-1 and $D_{\eta,2}^*$) are set up. The variations of the CMC cells in each x - and y -direction are 4 cells for res-1, 8 cells for res-2 (reference case) and 16 cells for res-3 with the same 80 CMC cells in z -direction, as summarized in Table 6.5. Note that flow and mixing fields of the reference case will not be shown in this section since a reference case has same conditions as the one in the parametric studies of the combustion model (section 6.5.2.1).

Table 6.5: Summary of different cases in CMC grid resolution study.

Name	CMC Grid Resolution	Flow and Mixing Fields	Combustion Model
res-1	$4 \times 4 \times 80$	variance-2	CMC-1, flux-1 $D_{\eta,2}^*$
res-2 (reference case)	$8 \times 8 \times 80$	$Sc_2, Sc_{t,1}$	
res-3	$16 \times 16 \times 80$	$C_{\xi,1}$	

6.5.3.1 Conditionally Filtered Reactive Scalars

Since the CMC resolution varies in the radial direction for three case studies, the radial positions of conditional value should show more prominent features. Therefore, the radial positions of mean scalar are investigated at axial positions $z/D = 7.5$ and 15. A reason behind the examination of both axial positions is caused by a high variation of turbulence, and thus the small size of CMC cells (res-3) is believed to capture specific details of combustion, especially in the regions above the jet and mixing zone. However, predictions at position $z/D = 15$ are not provided here since they show the same trends as the predictions at position $z/D = 7.5$.

Conditional mean predictions of temperature and CO at position $z/D = 7.5$ are shown in Fig. 6.24. Colours of lines and symbols in Fig. 6.24 denote different radial positions, where green, red and black lines are positions $r/D = 0, 1$ and 2, respectively.

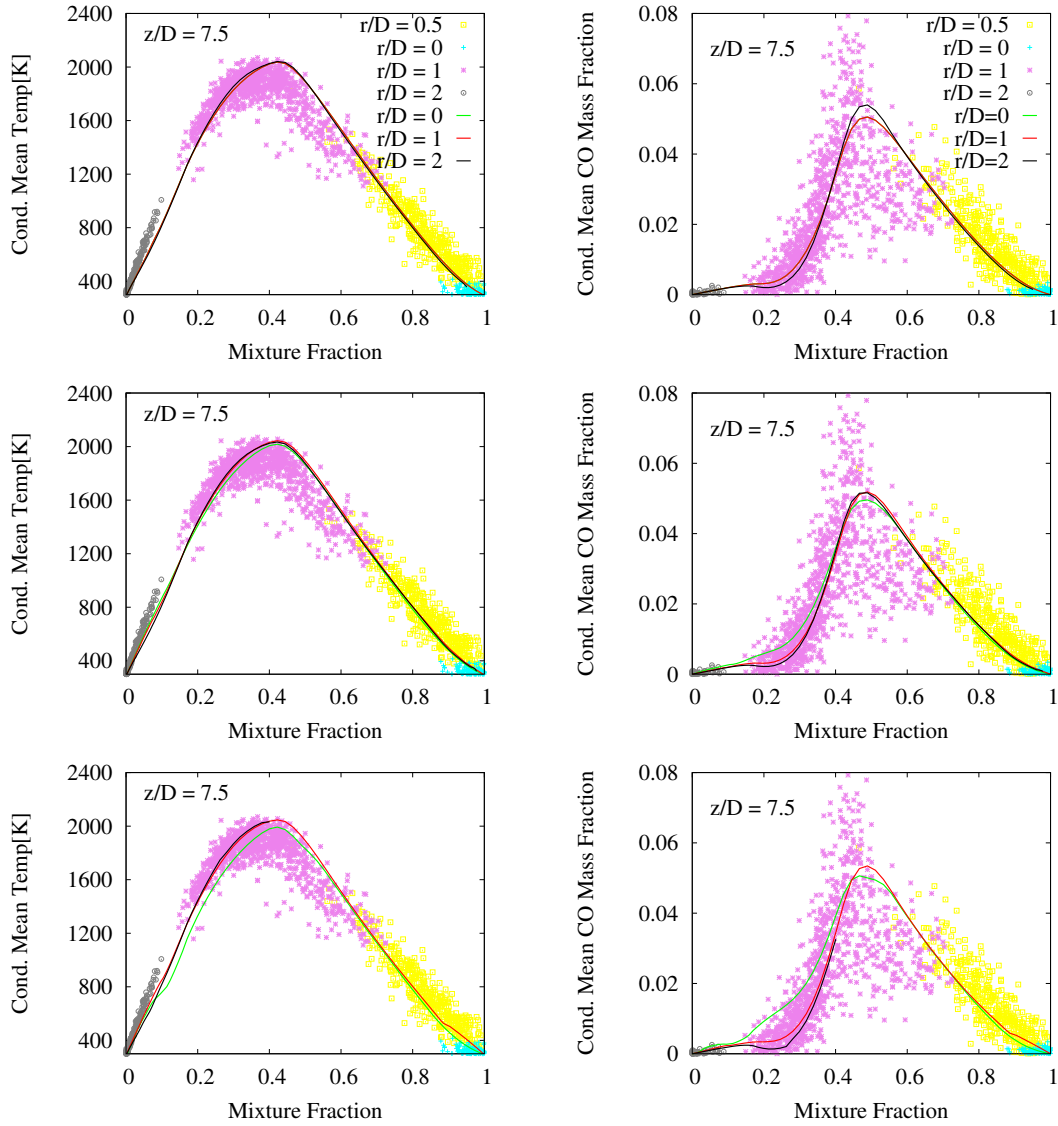


Figure 6.24: Conditional profiles of mean temperature and CO at $z/D = 7.5$ for Flame D. The symbols are experimental data in scatter plots [4], while the lines in the first, second and third rows represent the results of LES-CMC from the different CMC grid resolutions of $4 \times 4 \times 80$, $8 \times 8 \times 80$ and $16 \times 16 \times 80$, respectively (Table 6.5).

It can be observed from Fig. 6.24 that the predictions of res-1 ($4 \times 4 \times 80$ CMC cells) at positions $r/D = 0$ and 1 are similar since the green lines are behind the red lines and thus only the red and black lines can be detected. This occurrence can be clearly seen in CO (top right of Fig. 6.24). The reason for these identical predictions is that the simulation results come from the same CMC cell which captures both positions ($r/D =$

0 and 1). Some differences of conditional predictions at each position can be observed in res-2 ($8 \times 8 \times 80$ CMC cells), while the obvious differences of conditional predictions at each position can be found in res-3 ($16 \times 16 \times 80$ CMC cells). It can be concluded from Fig. 6.24 that the small size of CMC cells in res-3 provides better variation of the conditional moment (compared with the experimental data, scatter plots) than the big size of CMC cells, res-1 and res-2. These accurate results in mixture fraction space will lead to accurate results in physical space. Inexistent values of conditionally mean temperature, where $\widetilde{T}_\eta^* < 291$ K, of res-3 (the third row) at $r/D = 2$ in the range of $\eta \geq 0.40$ are an effect of a small CMC cell which comprises few LES cells. Inside these small CMC cells, the values in some mixture fraction bins might be small and thus the FDF values whose shape are presumed by $\widetilde{\xi}$ and $\widetilde{\xi''^2_{sgs}}$ can be small values in some regions of the mixture fraction space. As a result, the statistical predictions which are computed by using these small FDF values as a weighting factor will be inexistence at the same regions. The same reason can be explained for the value of conditionally mean CO of res-3 at the same position.

Another possibility to observe the effects of different CMC grid resolutions is to consider the predictions with the measurement in physical space; therefore, statistics of radial distributions of unconditionally filtered reactive scalars are considered in the next section.

6.5.3.2 Unconditionally Filtered Reactive Scalars

The mean temperature and CO predictions in radial distributions are shown in Fig. 6.25 which display the same tendency as the conditional scalar predictions in Fig. 6.24. It can be seen from position $z/D = 3$ that res-2 and res-3 perform better than res-1 since there is an under-prediction of the temperature for res-1 around $r/D = 0.7 - 0.9$. A possible reason may relate to the size of CMC cell which the big size of CMC cell may predict inaccurately in which a high level of mixture fraction gradient occurs. Predictions of res-3 can capture the highest value of CO where r/D is around 0.8 at position $z/D = 7.5$. Moreover, predictions from res-3 ($16 \times 16 \times 80$ for CMC cells) are closer to the experiments than the others at position $z/D = 15$ which show a better advantage of small CMC cells in this resolution. However, res-3 requires 60% more computational time than res-2. Based on the computational time and predictions from all CMC resolutions, the appropriate resolution may be taken as res-2 ($8 \times 8 \times 80$ for CMC cells).

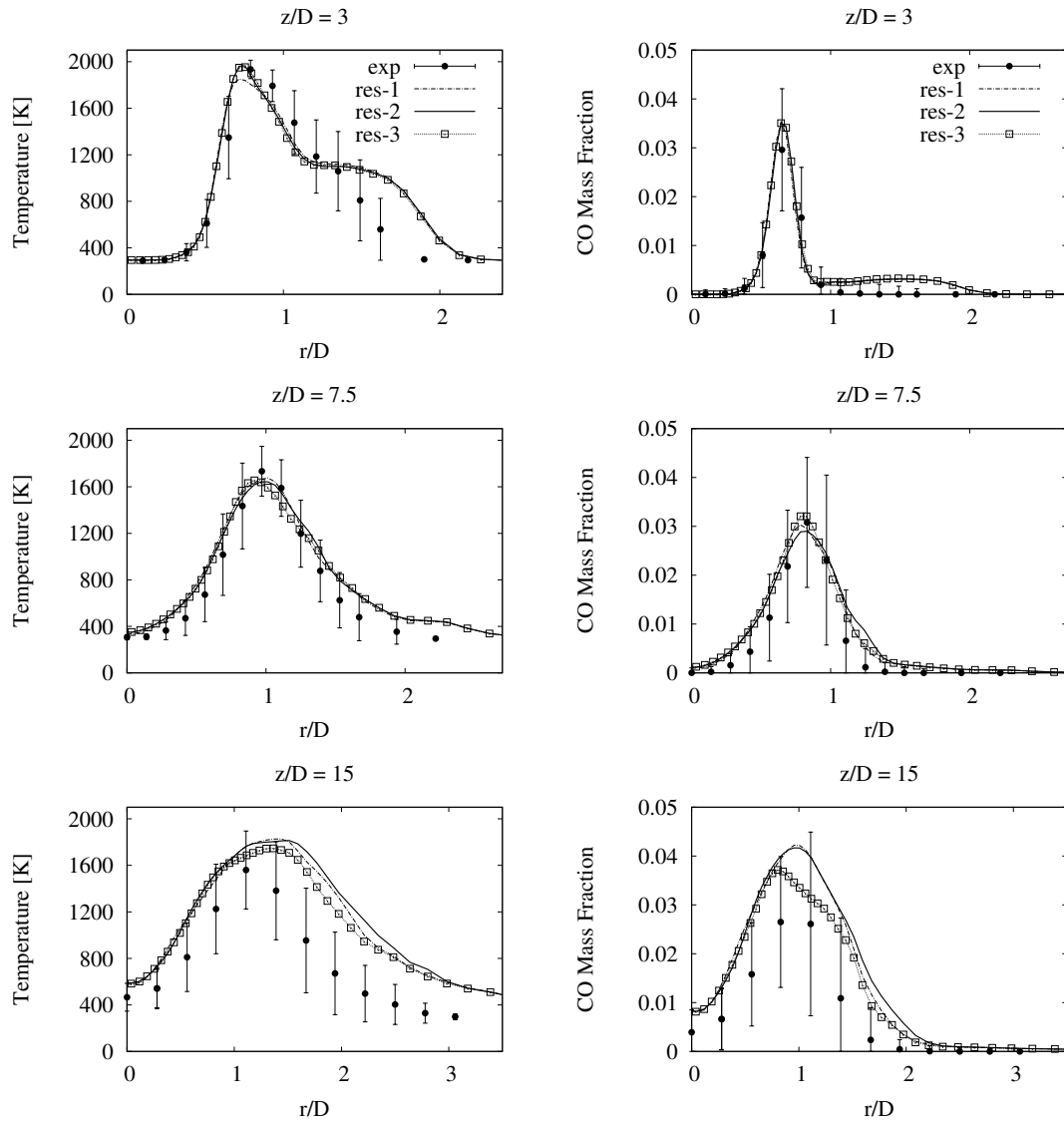


Figure 6.25: Radial profiles of mean temperature and CO for Flame D. Circles are experimental data [4], while the solid, dashed and square-dotted lines represent the results of LES-CMC from the different CMC grid resolutions (Table 6.5).

6.6 Results of Sandia Flame E

Following the previous study of Flame D, the appropriate parameters of the flow and mixing fields (results from section 6.5.1) are applied to Flame E studies. These are the Schmidt number, $Sc = 0.7$, the turbulent Schmidt number, $Sc_t = 0.4$ and the constant for the sub-grid scale variance of mixture fraction, $C_\xi = 0.2$. However, the variances in the turbulent inflow generator for Flame E require a new adjustment, such that the mixture fraction and the axial mean velocity of the simulations agree well with experiments in the same manner as Flame D. As described in section 6.4.1, this adjustment is performed to reduce the high level of turbulence which may come from using the measured velocity profiles at $z/D = 0.14$ as experimental inlet data for the inflow generator. Consequently, the inflow velocity variance levels are reduced to $\frac{1}{3}u'u'$, $\frac{1}{3}v'v'$ and $\frac{1}{3}w'w'$ of the measurements.

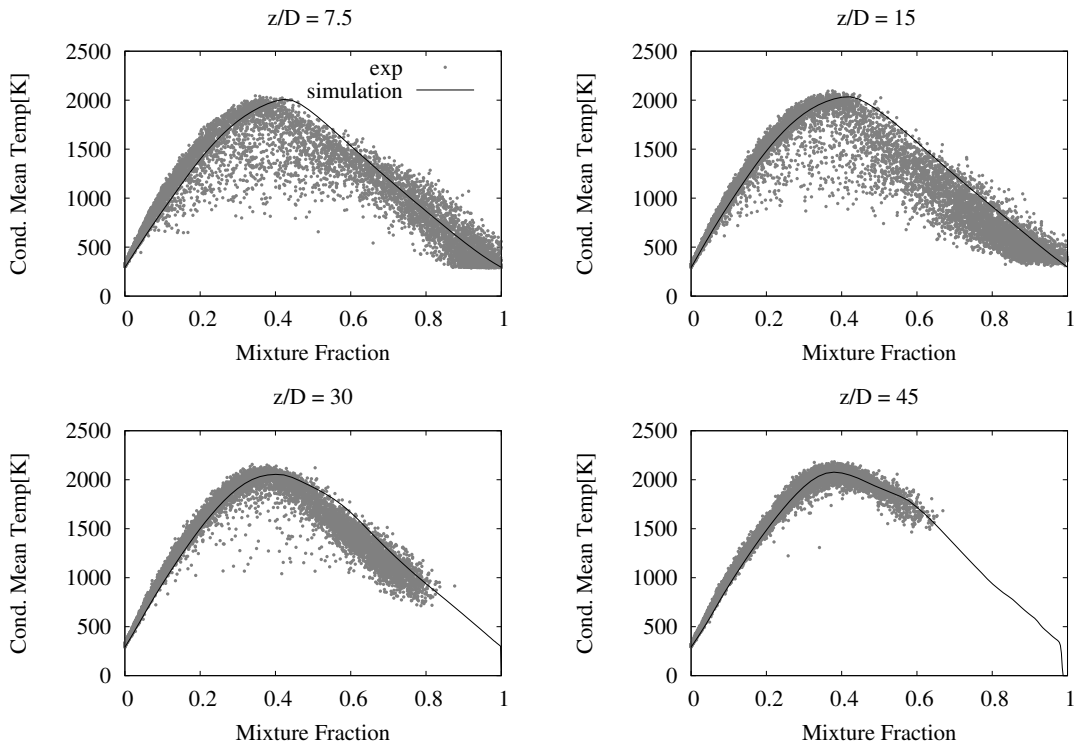


Figure 6.26: Conditional profiles of temperature (see section 4.5.2) for Flame E. Symbols are experimental scatter plots [4], while the solid lines represent the averaged mean temperature results of LES-CMC in reference case of combustion model (Table 6.4).

The consideration of interesting positions of experimental data is determined by

Fig. 6.26, which are simulation results of reference case (case-1: conservative form with a flux approximation based on LES cells at CMC faces) compared with experimental scatter plots. In this figure, the upstream region ($z/D \leq 15$) is of great interest, since the effects of turbulence-chemistry interactions are intensive in these locations. The scatter plots of the experiment of Flame E show the relation of turbulence-chemistry interactions. These can be observed by the fluctuation of temperature which is produced by the turbulence. Therefore, in the upstream region $z/D \leq 15$, there is strong turbulence (high scalar dissipation rates) which leads to locally extinguished samples with a low temperature (increased scatter). On the other hand, at downstream positions, $z/D \geq 30$, less turbulence-chemistry interaction can be observed, as indicated by a reduced scatter and more samples near the conditionally averaged mean temperature. Therefore, the interesting positions for comparison with the experiments in this work are $z/D = 3, 7.5$ and 15 , respectively.

The parametric studies for Flame E will be performed in the next section to investigate the effects of different combustion model parameters and CMC grid resolutions.

6.6.1 Parametric Studies of Combustion Model

The parametric studies of a combustion model contain four main parts. The first part is composed of flow and mixing field predictions which are performed by a reference case (Table 6.4). Preliminary studies of the combustion model are carried out as a second part. Subsequently, conditional predictions of different case studies are investigated and validated with experiments. Finally, unconditional predictions in physical space are discussed.

6.6.1.1 Flow and Mixing Field

In this section, the overview of the flow and mixing field of Sandia Flame E is based on the reference case (case-1 in Table 6.4: the conservative CMC combined with flux approximation based on LES cells at CMC faces and $8 \times 8 \times 80$ CMC grid resolution). Following the recirculation problem in Flame D which occurs in the narrow domain (see section 6.5.2.1), the solution using the wider domain (Table 6.2) is adopted and employed for the calculations of Flame E.

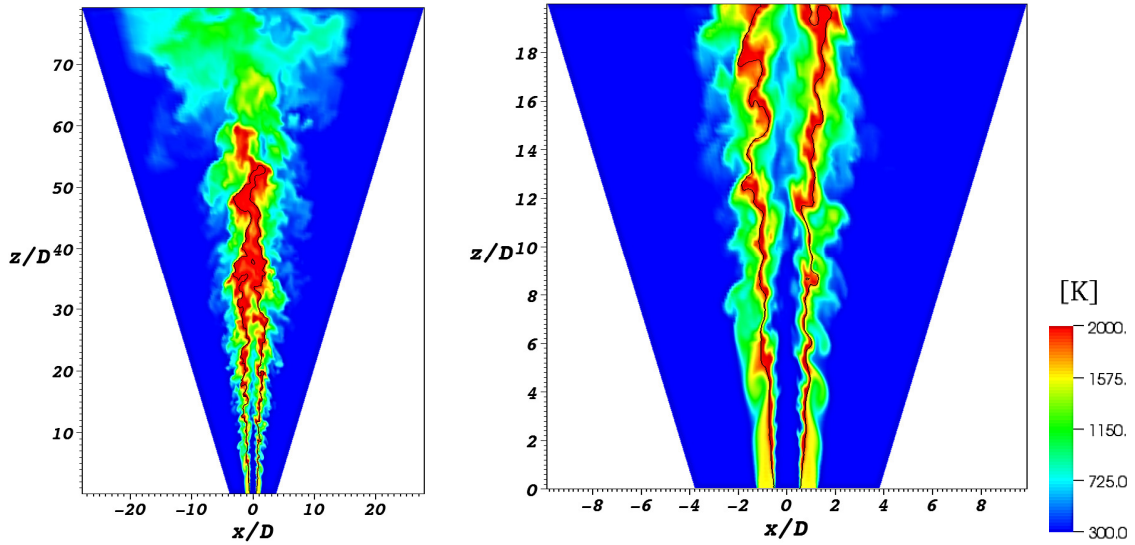


Figure 6.27: Snapshots of the temperature field in the total computational domain (left) and in the upstream region (right) for Sandia Flame E. The iso-contour of stoichiometric mixture fraction is represented by the black lines.

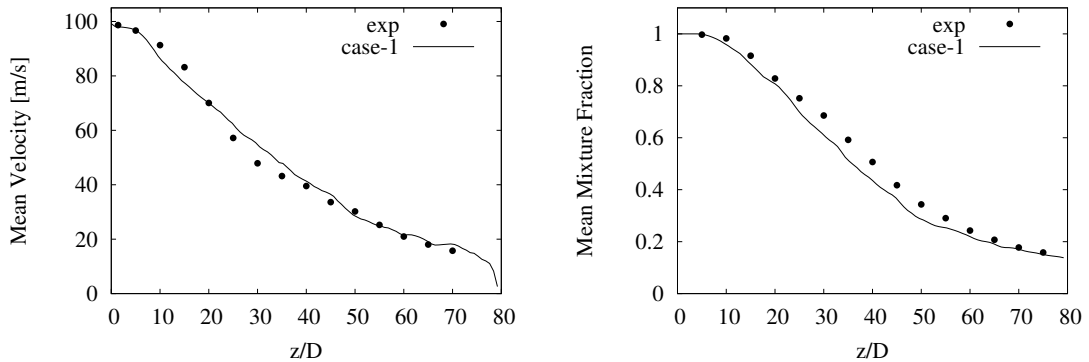


Figure 6.28: Axial profiles of mean axial velocity and mixture fraction along the centerline for Flame E. Symbols denote experimental data [88, 4], while the solid lines represent the mean results of LES-CMC (reference case of Table 6.4).

The instantaneous temperature field along the entire computational domain (left) and a zoom into the upstream region (right) at the centre plane of Sandia Flame E are shown in Fig. 6.27. The black lines indicate the isoline of the stoichiometric mixture fraction. The extinction pockets, which should occur along the isoline of stoichiometric mixture fraction, cannot be detected in the above mentioned simulation. The temperature contour

corresponds to the predictions of conditional scalar which will be discussed in detail within subsection 6.6.1.3.

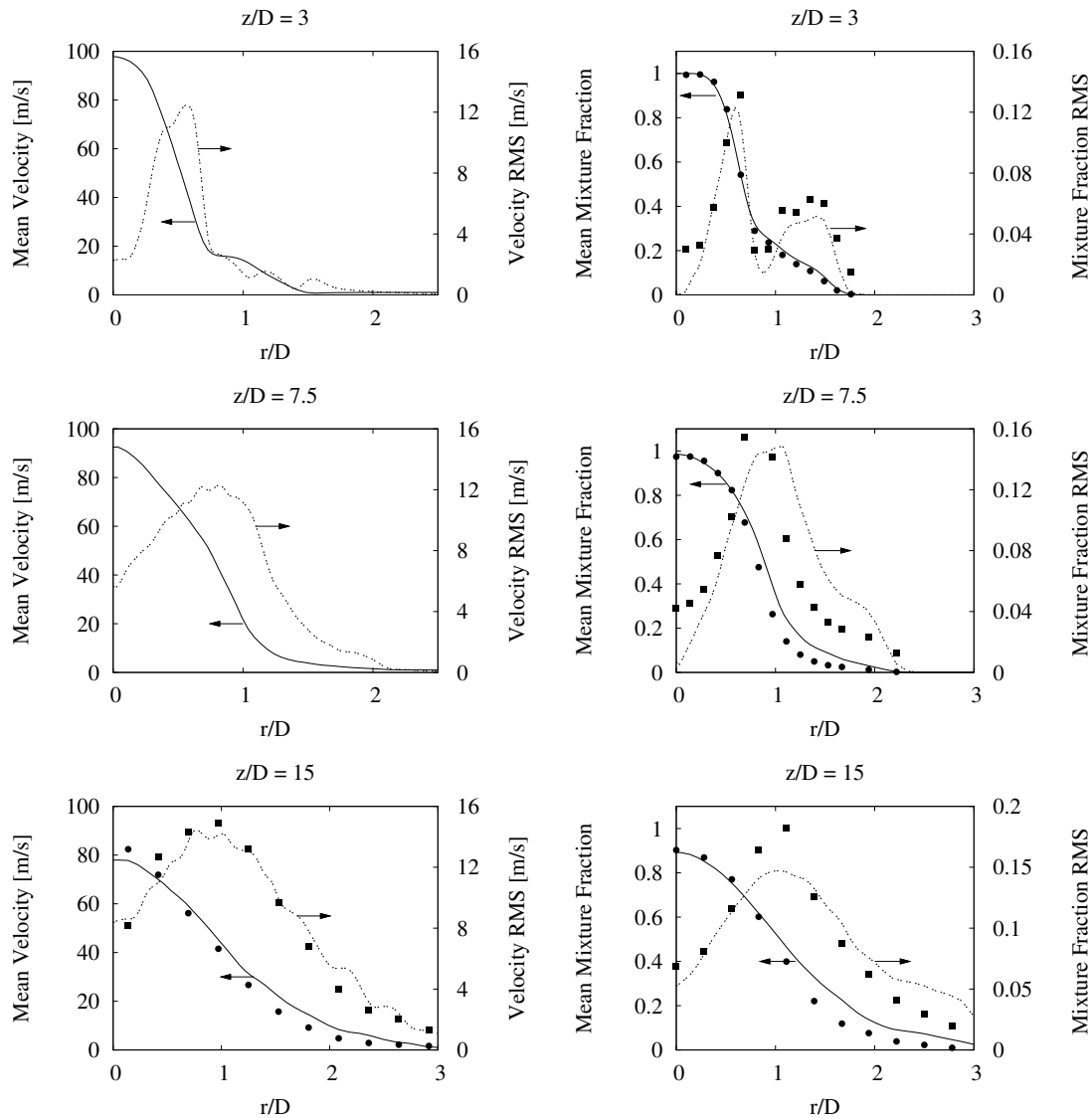


Figure 6.29: Radial profiles of mean and RMS axial velocity and mixture fraction at three downstream locations for Flame E. Symbols denote experimental values [88, 4], while the solid and dotted lines represent the mean and RMS results of LES-CMC (reference case of Table 6.4).

Axial distributions of mean axial velocity and mixture fraction are shown in Fig. 6.28 and agree well with experiments. Radial distributions of mean and RMS of axial velocity and mixture fraction are shown in Fig. 6.29. The radial velocity profiles at $z/D = 15$ are only compared with the experiment since there is no measurement available for the flow

field at positions $z/D = 3$ and 7.5 . Both mean and RMS of velocity in Fig. 6.29 show that the jet spreading is generally captured well. Even though small over-predictions at position $z/D = 7.5$, and under-predictions at position $z/D = 15$ of mixture fraction RMS are observed in Fig. 6.29, the present predictions provide a good basis for the parametric studies of the combustion model.

6.6.1.2 Preliminary Studies

In Flame E, five cases of parametric studies of the combustion model (as presented in Table 6.4) are examined. These cases vary only in the numerical methods (or models) of CMC model, while the fluid properties and the CMC grid resolution ($8 \times 8 \times 80$) remain the same. Since the flux investigation procedures in this section are the same as in Flame D (detailed in section 6.5.2.2), a brief explanation of these procedures is provided in this section.

Due to the investigations of Flame D (section 6.5.2.2), a leading direction (z -direction) which indicates most effects of convection on every scalar mass fraction is investigated in preliminary studies for Flame E. In the first step, all case studies are allowed to run only one time step from the same iteration to ensure that flow solutions are correlated. The comparisons of instantaneous predictions of CH_4 fluxes at different axial and radial positions are shown in Figs. 6.30 and 6.31. Since the differences of the convective fluxes between each case in Fig. 6.31 are more obvious than in Fig. 6.30, the radial positions are used to investigate the effects of different implementations of the convective flux for the other species. It should be noted that a consideration of the FDF is necessary since it is applied to transfer the values from mixture fraction space to physical space, Eq. (4.45). If there is a high convection for low FDF values in the mixture fraction space, only low effects of convection will be observed in physical space. For instance, the appearances of case-3 and case-4 (Fig. 6.31) around $\eta < 0.2$ at position $r/D = 1$ and $z/D = 7.5$ are hardly detected in physical space because FDF values in these regions are close to zero. Subsequently, the convective flux comparisons are investigated for other species (e.g. OH, CH_2O , CO, H_2O , etc.) to decide the cases which have different convective flux predictions to each other. Furthermore, the flux investigation at another starting point, initial time step, is performed to have the time-independent simulation results.

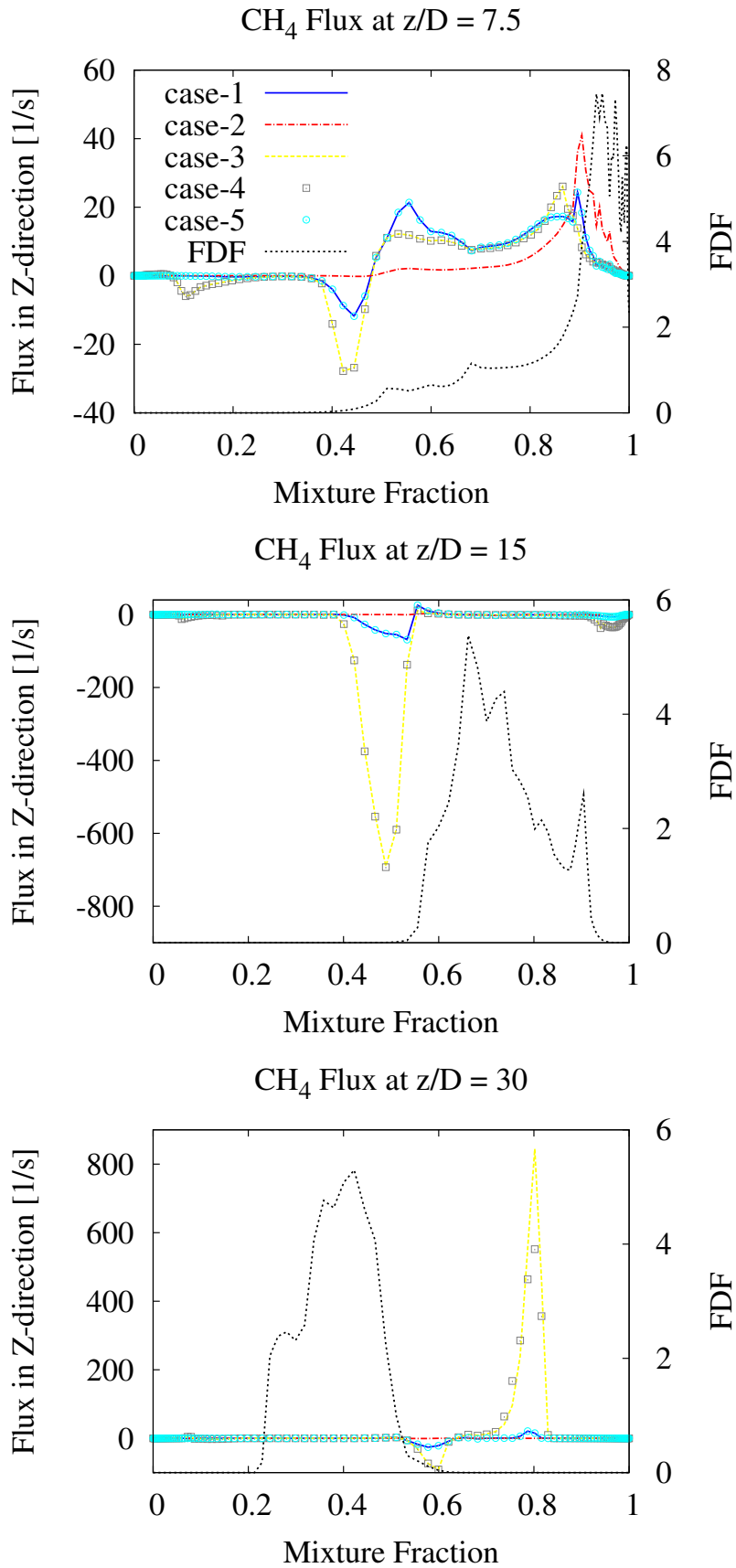


Figure 6.30: Convective fluxes of CH₄ in z -direction for a time step at three different axial positions with the same radial position, $r/D = 0$, for Flame E.

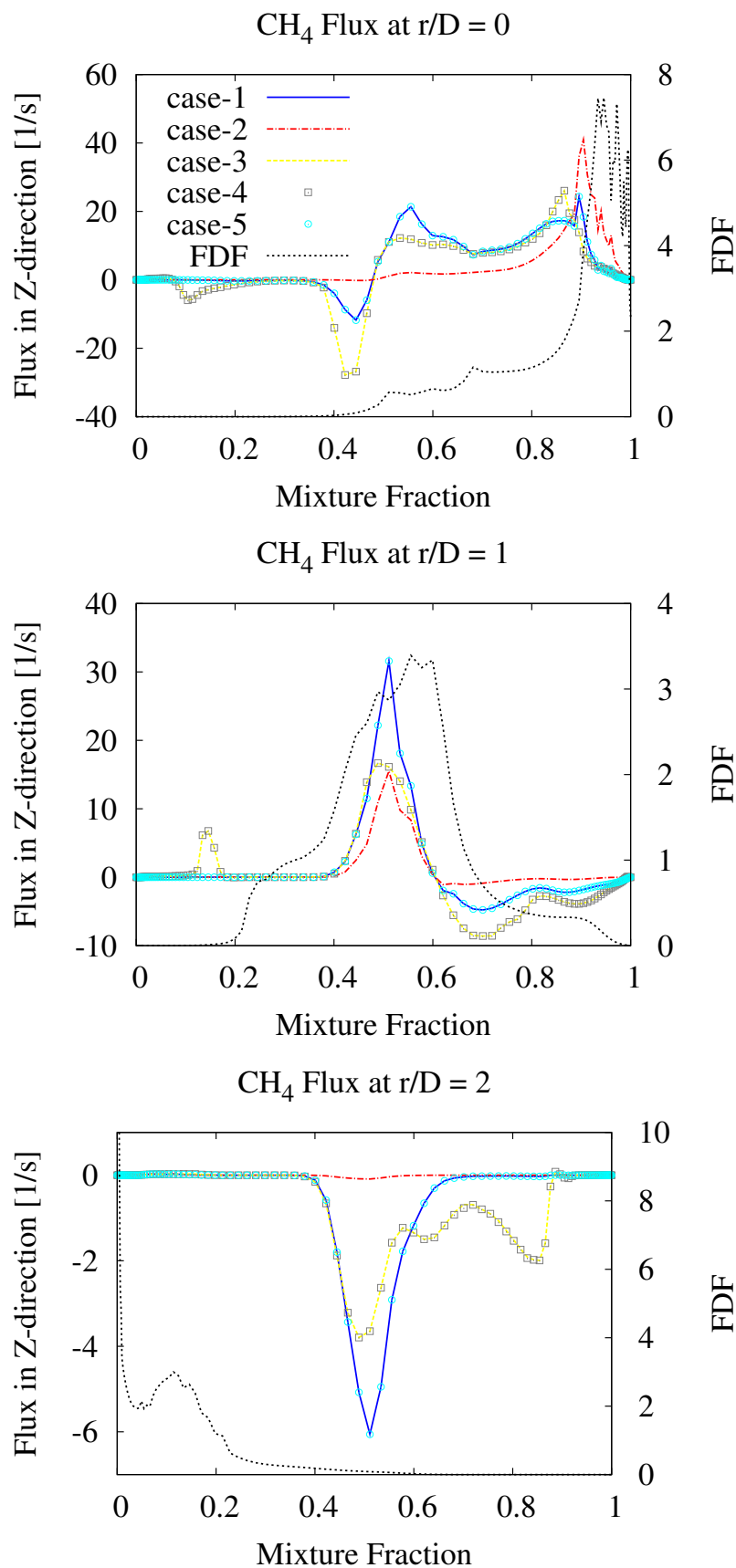


Figure 6.31: Convective fluxes of CH₄ in z-direction for a time step at three different radial positions with the same axial position, $z/D = 7.5$, for Flame E.

The results from the convective flux investigations of many species and of another starting point show similar trends as in Fig. 6.31. It can be concluded from this figure that the flux predictions of case-1, case-2 and case-3 are different and thus the conditional temperature and species mass fraction predictions from these cases will differ from each other. The reason of the similar flux predictions between case-1 vs. case-5 and case-3 vs. case-4 is explained by the low effects of different D_η^* models, which are the modelling for the sub-grid scale conditional flux of convection, on the whole convective term (see Eq. (6.2)).

In the next section, the statistical results of three cases (case-1, case-2 and case-3) are sampled for 14 *ms* (over 30,000 time steps) to investigate the different effects of the combustion model parameters and to validate by comparison with the experiment. Note that the reference time t_{ref} (already discussed in section 6.5.2.2) of Sandia Flame E is 7.74 *ms*. Compared with t_{ref} , the physical time for statistics is enough to collect the fluid particle travelling from inlet to outlet of the whole domain.

6.6.1.3 Conditionally Filtered Reactive Scalars

The effects of any parameter in the combustion model with turbulence-chemistry interaction can be analyzed first by considering the conditionally averaged reactive scalars. Regarding the convective flux analysis in the preliminary studies, case-1, case-2 and case-3 are investigated in this section. Following the discussion in section 6.5.2.3, results of an SLFM solution are used as initial values for the conditional species. Since all statistics of conditional measurements are available only as cross-sectional averages, the conditional simulation results are validated with this kind of measurements at three different positions.

It should be considered that case-1 is the conservative CMC implementation with a flux approximation based on LES cells at the CMC faces, case-2 is the non-conservative CMC implementation with the same flux approximation as case-1, and case-3 is the conservative CMC with a flux approximation based on CMC cell centres.

Figure 6.32 presents a comparison of the conditionally averaged scalar dissipation with experiments [36] for different combustion model parameters at four positions. As in Flame D, over-predictions of scalar dissipation occur at $z/D = 7.5$. However, the simulation values at position $z/D = 15$ correspond well with the measurements. Differences of conditional averages of mean scalar dissipation between three cases originate from a vari-

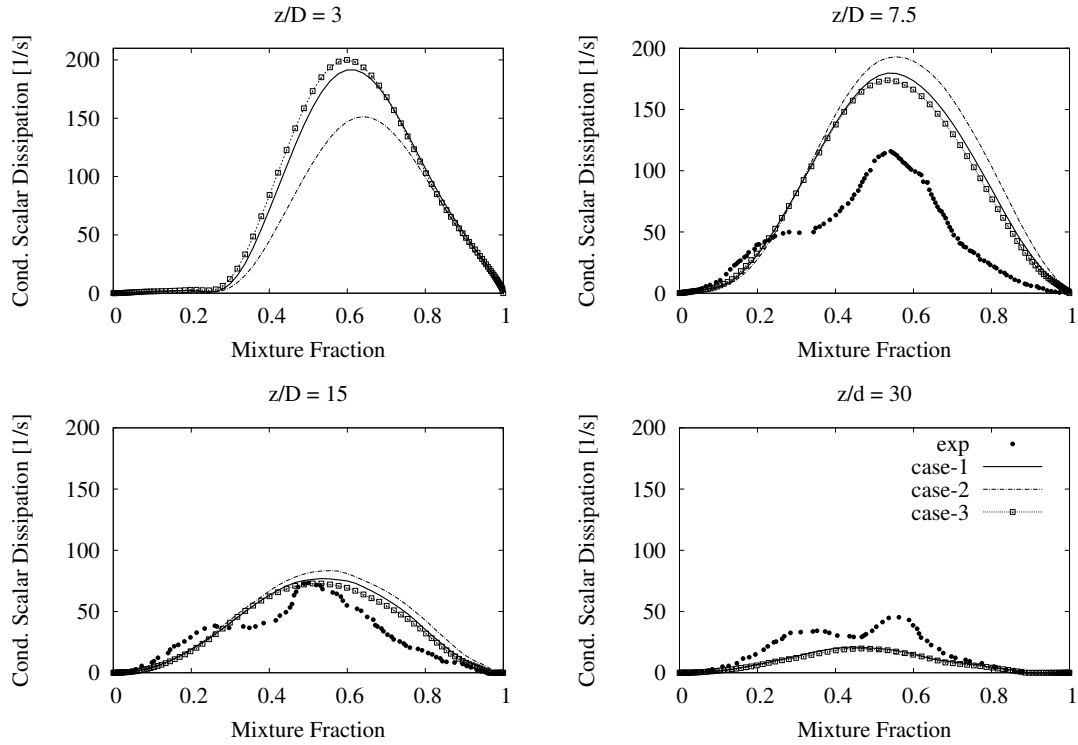


Figure 6.32: Conditional averages of mean scalar dissipation in mixture fraction space at four downstream locations for Flame E. Circles are 3-D experimental data [36], while the solid, dashed and square-dotted lines represent the results of LES-CMC in different cases of combustion model (Table 6.4).

ation of instantaneous convective fluxes which results in different species mass fraction, temperature and updated density profiles. Since the scalar dissipation rate is calculated based on the mixture fraction gradient (Eq. (3.35)), the scalar dissipation rate of each case for the same LES cell is different. As a result, differences of averaged conditional scalar dissipations are observed and we may conclude that the calculations of the convective flux have a large influence on the CMC solutions (at $z/D = 3$ and 7.5 in Fig. 6.32).

Predictions of conditional mean temperature and the conditional mean mass fraction of reactive species (CO, CH₄ and H₂) are shown in Figures 6.33 and 6.34. These species are chosen as a representative of intermediates, products and fuel. In these figures, error bars indicate the conditional RMS and are only plotted to illustrate the conditional turbulent fluctuations of each scalar.

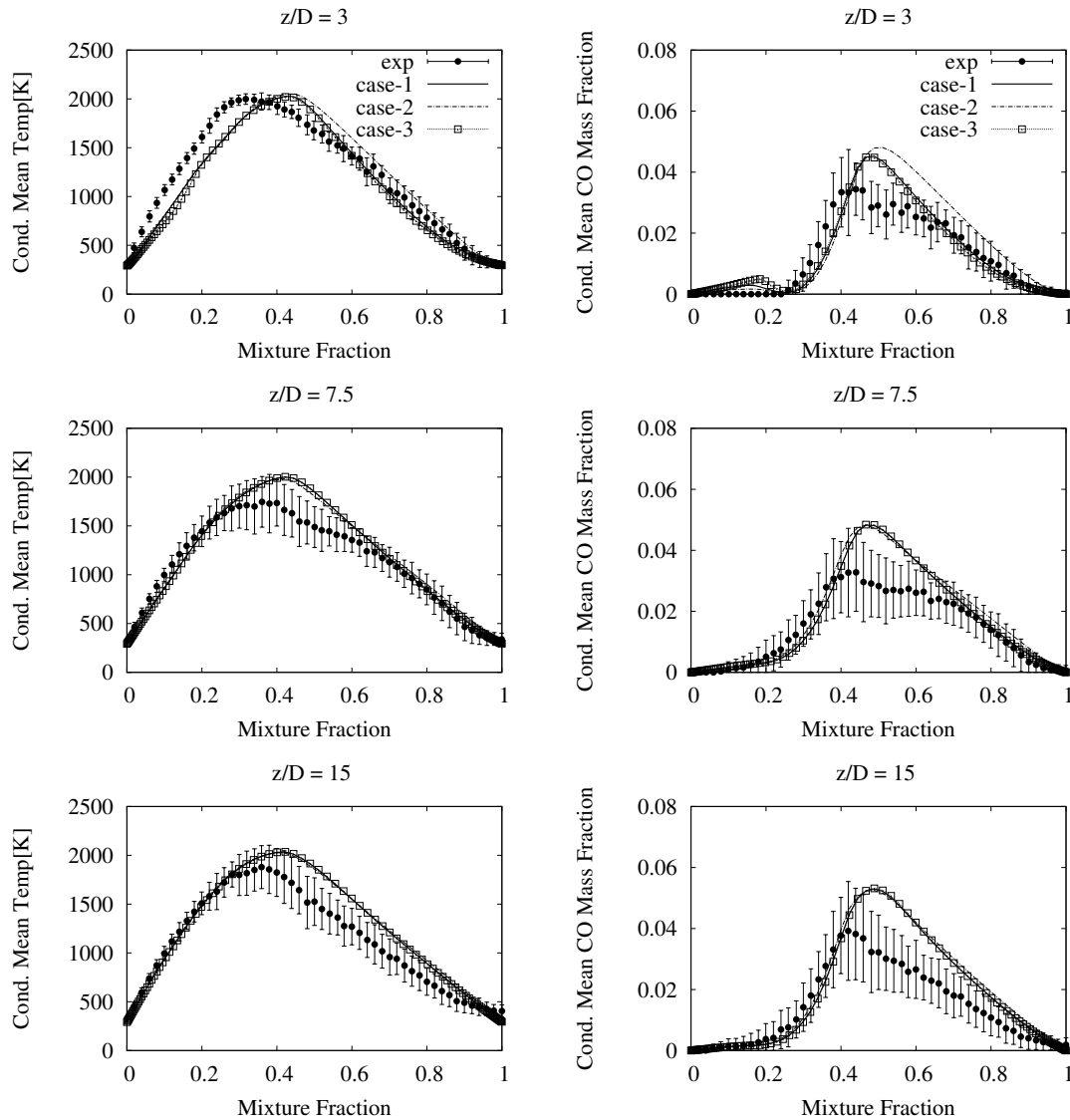


Figure 6.33: Conditional profiles of cross-sectionally averaged temperature and CO at three different downstream positions in mixture fraction space for Flame E. Circles are experimental data [4], while the solid, dashed and square-dotted lines represent the results of LES-CMC in different cases in combustion model (Table 6.4).

As already seen for Flame D, case-1 and case-3 are similar for all results (the reason was already discussed in section 6.5.2.3). The differences between case-1 and case-2 can be detected in a range of $\eta > 0.4$ at position $z/D = 3$ which indicate that case-1 is superior to case-2. The reason of different predictions has been already discussed in the previous test case (section 6.5.2.3) that the two CMC formulations have the most significant differences in the convective fluxes on the rich side of mixture fraction space. This fact can be observed

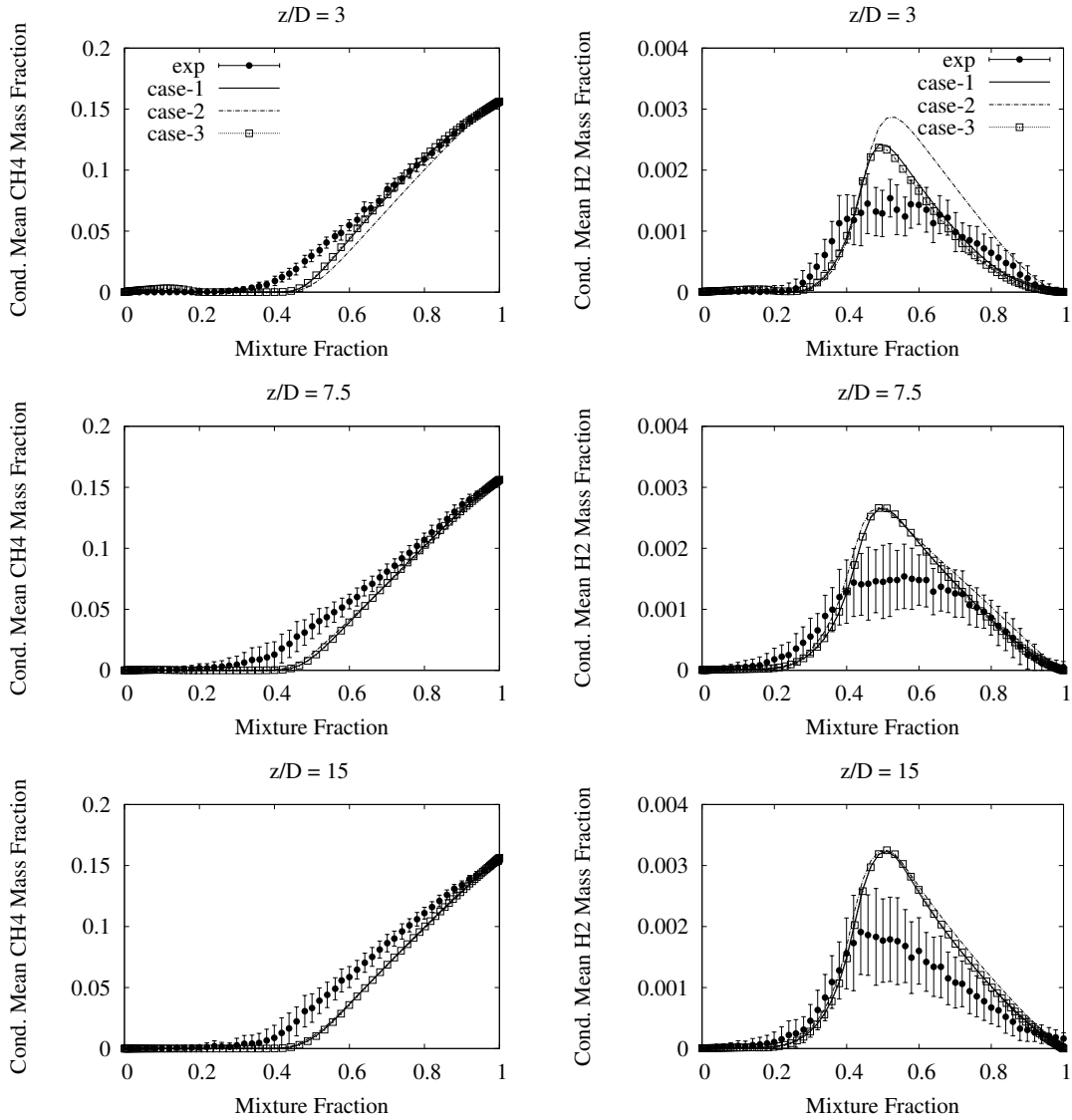


Figure 6.34: Conditional profiles of cross-sectionally averaged CH_4 and H_2 at three different downstream positions in mixture fraction space for Flame E. Circles are experimental data [4], while the solid, dashed and square-dotted lines represent the results of LES-CMC in different cases in combustion model (Table 6.4).

in Fig. 6.35 which shows the conditional predictions and FDF of two different CMC cells at $z/D = 3$.

Under-predictions of conditional temperature distribution for all cases on the lean side ($\eta < 0.35$) at $z/D = 3$ (clearly seen in Fig. 6.33) may result from the initial conditions of large CMC cell over jet and pilot regions. The initial conditions of the CMC part are obtained from the SLFM solution (as previously discussed in section 6.5.2.3). If an

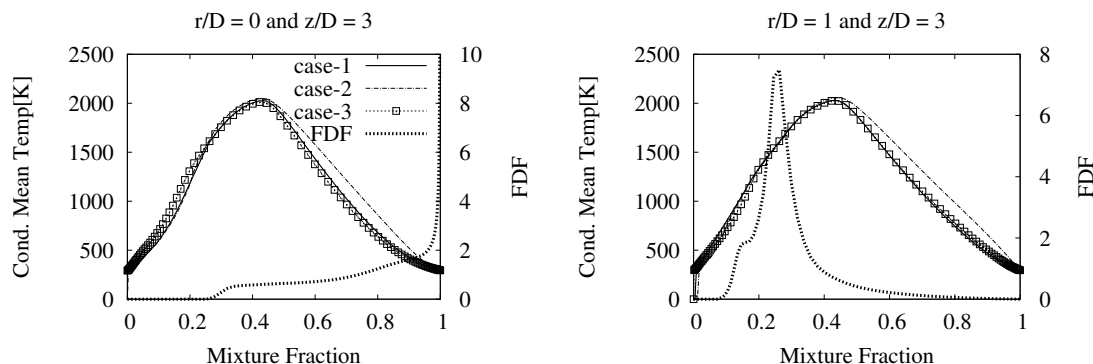


Figure 6.35: Conditional profiles of mean temperature at two different radial positions of $z/D = 3$ in mixture fraction space for Flame E. The solid, dashed and square-dotted lines represent the results of LES-CMC in different cases and FDF (reference case) in combustion model (Table 6.4).

improper initialization for CMC in the upstream region is defined, some effects are still there because of the costly nature of LES, runtime will be only for decisecond for the simulation. Additionally, a peak of the conditional temperature prediction which does not correspond to the experiments at the same position ($z/D = 3$) shows that single conditional reaction source terms might not be accurate since there is an evidence that double conditional reaction source terms can predict the correct peak-position and reduce over-predictions in conditional scalar distributions [50]. Note that the double conditioning is a method which uses two conditioning variables, e.g. mixture fraction and sensible enthalpy. This method is applied for flames where large fluctuations around a conditional mean occur. The new conditioning should reduce the fluctuations if there is a strong dependency of the reactive species on this second conditioning variable [23].

Over-predictions of conditional mean temperature and intermediate products in Figs. 6.33 and 6.34 are observed in the extinction zone (e.g. $0.35 \leq \eta \leq 0.6$ at $z/D = 7.5$ and $\eta \geq 0.30$ at $z/D = 15$ for temperature). The extinction zone can be detected by the lower values of any conditional scalar in the measurements for Flame E compared with the same scalar for Flame D at the same position. Both Figs. 6.33 and 6.34 indicate that all cases do not capture local extinction regions. These results might imply that the first-order closure of CMC with a single conditioning variable has some difficulties to simulate a flame which has extinction and re-ignition. Previous research [51] shows that the reaction source terms should have a larger influence on these phenomena with respect

to the turbulence-chemistry interaction; therefore, the conditional reaction source terms may require further adjustment.

6.6.1.4 Unconditionally Filtered Reactive Scalars

The conditional scalars can be transferred to unconditional scalars by using an FDF table (discussed in section 4.5) with the consideration of mixture fraction and subgrid-scale variance of mixture fraction. This transformation procedure is performed to observe the effects of each case in physical space.

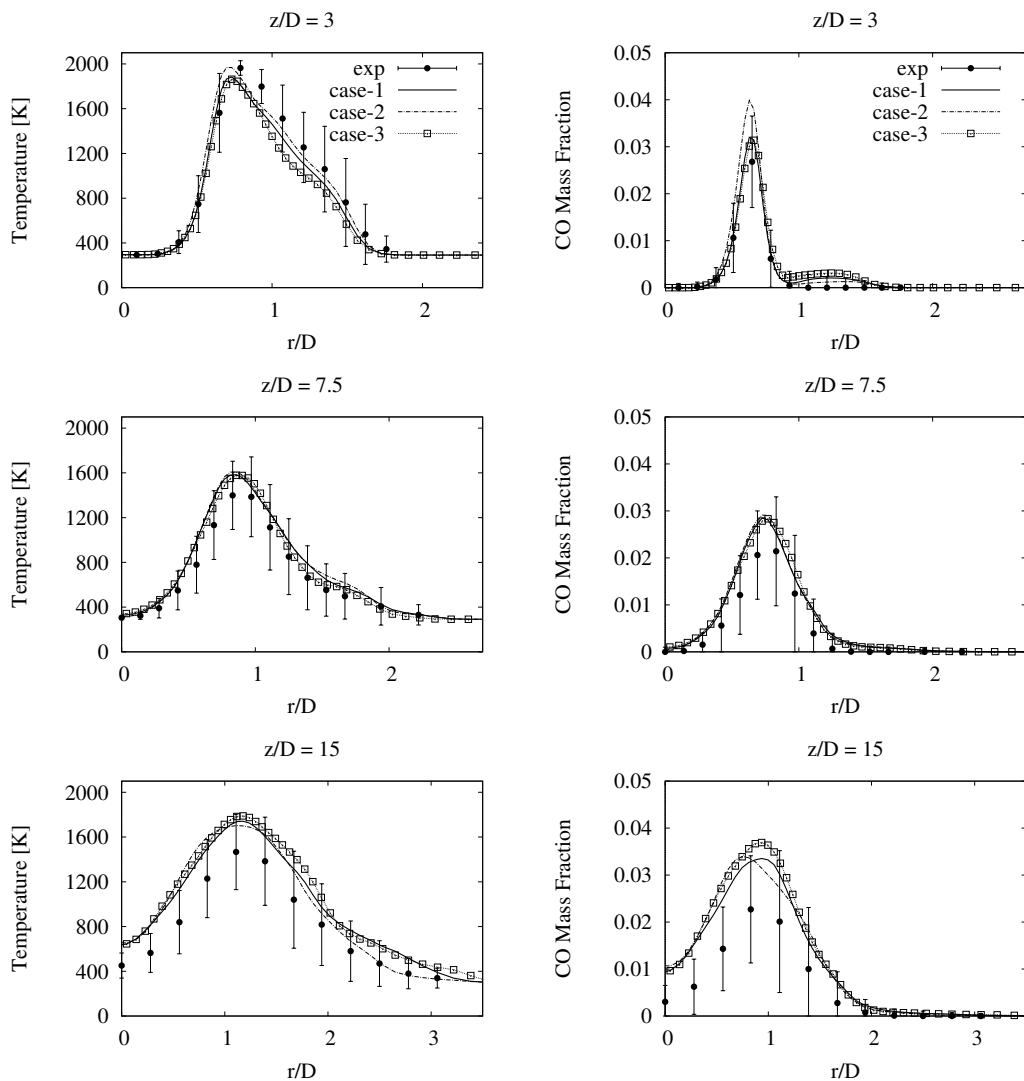


Figure 6.36: Radial profiles of mean temperature and CO for Flame E. Circles are experimental data [4], while the solid, dashed and square-dotted lines represent the results of LES-CMC in different cases in combustion model (Table 6.4).

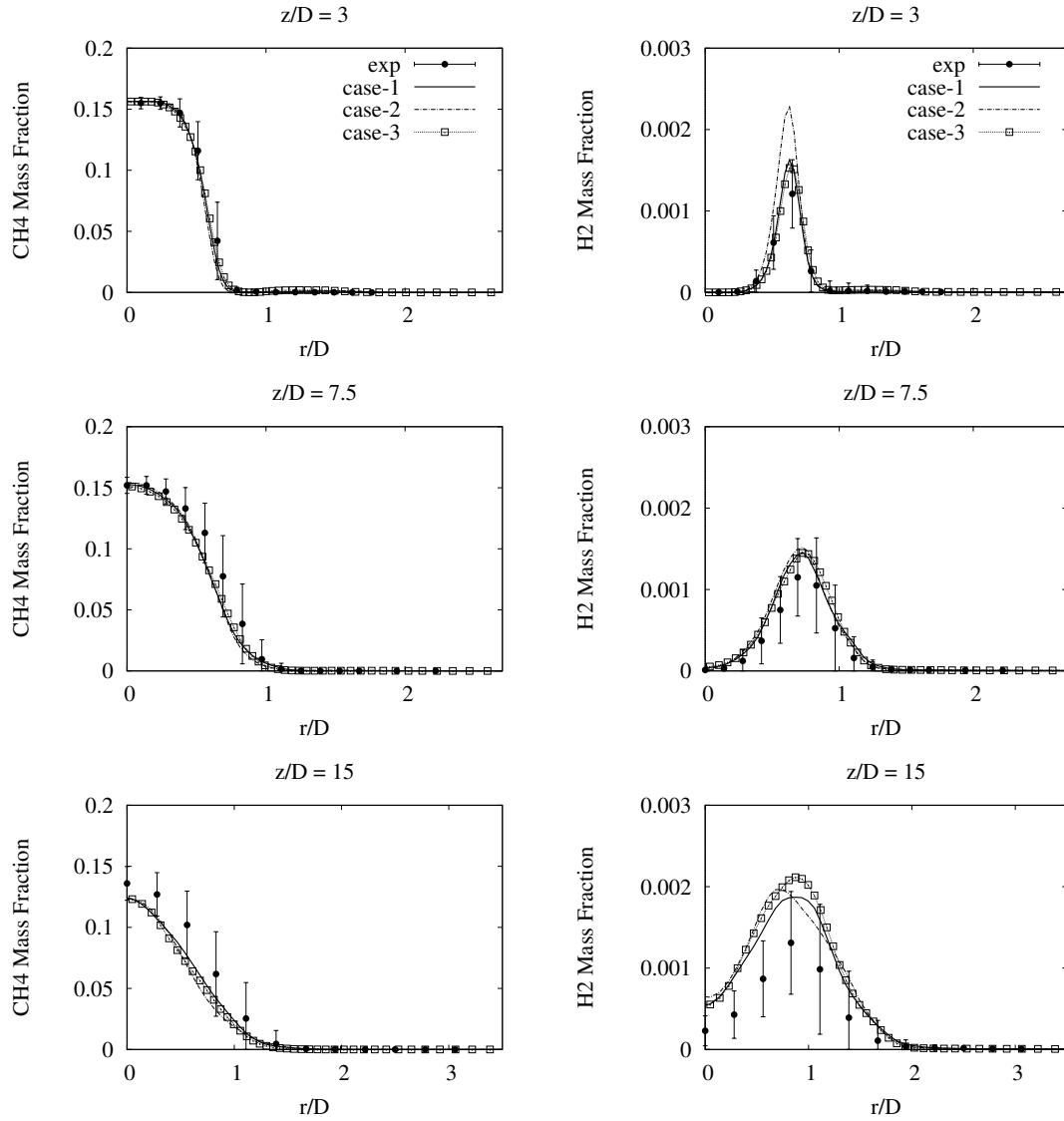


Figure 6.37: Radial profiles of mean CH_4 and H_2 for Flame E. Circles are experimental data [4], while the solid, dashed and square-dotted lines represent the results of LES-CMC in different cases in combustion model (Table 6.4).

Radial distributions of mean temperature, CO, CH_4 and H_2 are shown in Figs. 6.36 and 6.37. The lean and rich sides can be defined by using radial profiles of mean mixture fraction (Fig. 6.38). The region where the mixture fraction value is higher than the stoichiometric value ($\eta_{st} = 0.35$) is considered to be on the rich side, while the region where the mixture fraction value is lower than stoichiometric is considered to be on the lean side. An example of lean and rich sides can be seen by considering the position $z/D = 3$. For $r/D \leq 0.8$ the mixture is rich, while for $r/D > 0.8$ the mixture is lean.

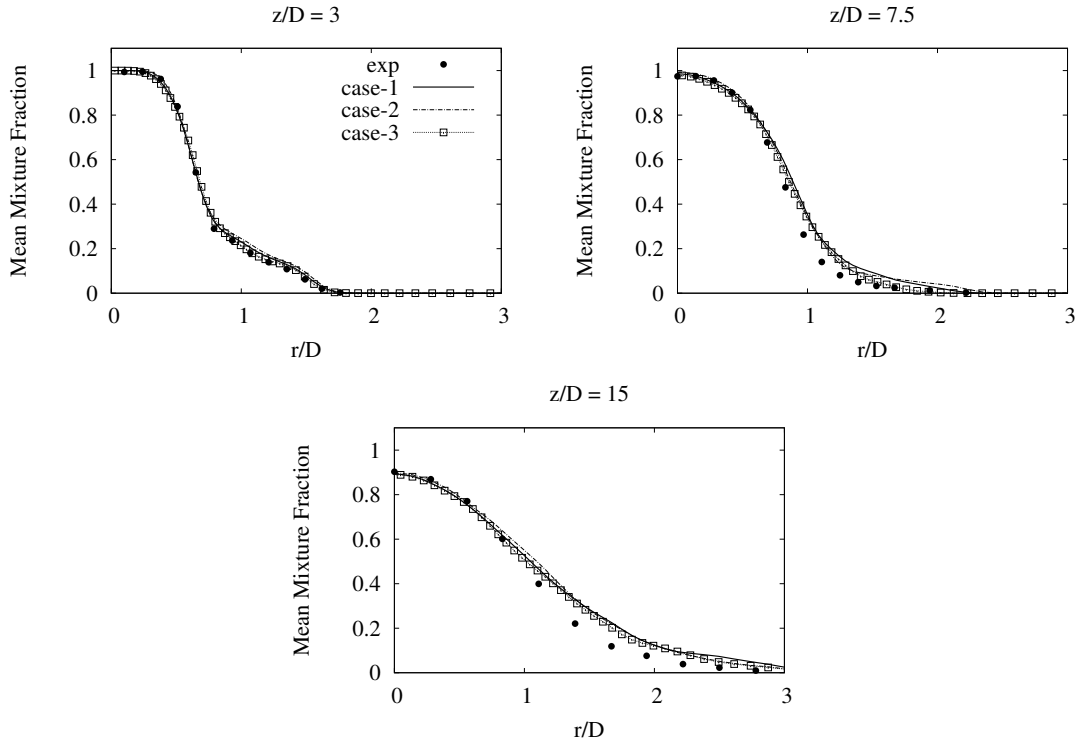


Figure 6.38: Radial profiles of mean mixture fraction for Flame E. Circles are experimental data [4], while the solid, dashed and square-dotted lines represent the results of LES-CMC in different cases in combustion model (Table 6.4).

In general, the unconditional profiles have the same tendency as the conditional profiles. Small under-predictions of the mean temperature at position $z/D = 3$ where $r/D > 0.8$ of three cases from Fig. 6.36 correspond to the under-predictions on the lean side ($\eta < 0.35$) as seen in the conditional profiles (Fig. 6.33), while the different predictions between case-1 and case-2 or between case-1 and case-3 at this position should come from slight variations of the mixture fraction profile (at $z/D = 3$ and $r/D > 0.8$) between both cases.

Over-predictions of radial distributions of temperature, CO and H_2 at position $z/D = 7.5$ relate to the over-predictions of the conditional scalar which cannot capture extinction and re-ignition. However, only small over-predictions can be detected in the unconditional results compared with the conditional results. This may be due to the low values of the presumed FDF (see Fig. 6.39) where the differences between the conditional results and the experiments occur. Consequently, the unconditional values have small variations compared with experiments after performing a convolution with the FDF. The different predictions

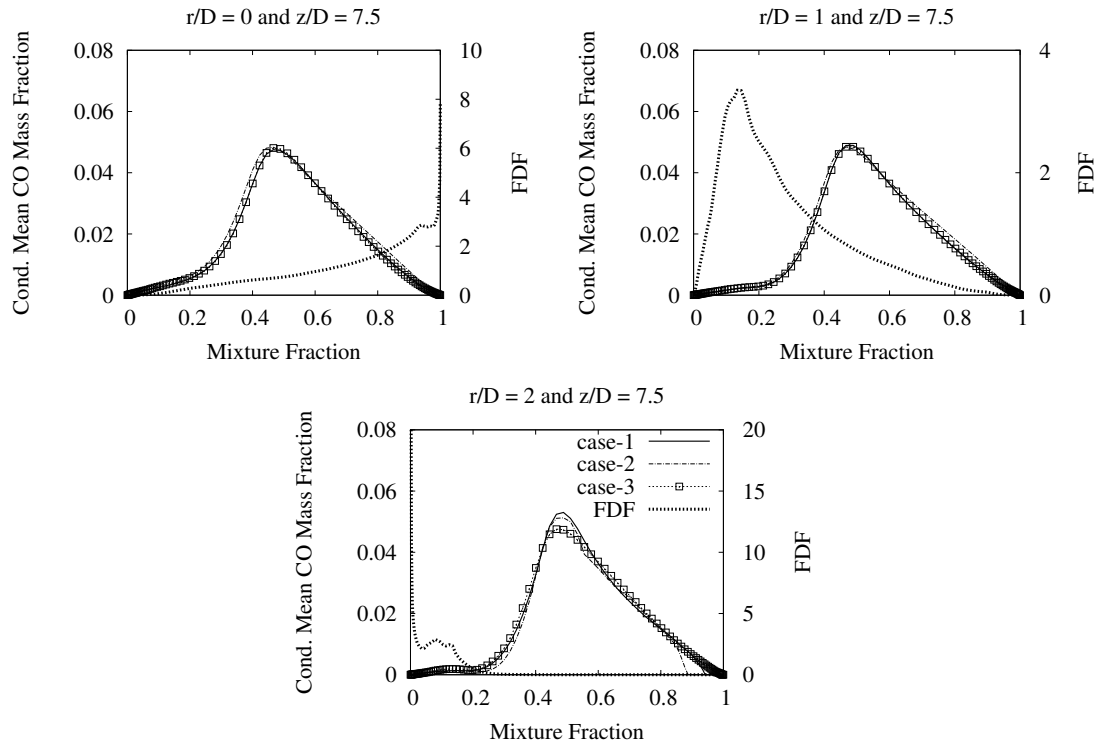


Figure 6.39: Conditional profiles of averaged CO at three different radial positions of $z/D = 7.5$ in mixture fraction space for Flame E. The solid, dashed and square-dotted lines represent the results of LES-CMC in different cases and FDF (reference case) in combustion model (Table 6.4).

of CO and H_2 between case-1 and case-3 at position $z/D = 7.5$ where $0.8 < r/D < 1.0$ may be attributed to the slight discrepancies of both mixture fraction profiles.

Considering the conditional temperature profiles (Fig. 6.33) and the mixture fraction profile (Fig. 6.38) at $z/D = 15$, over-predictions of unconditional temperature (Fig. 6.36) around $r/D < 1.5$ at $z/D = 15$ of three scalars follow the same trend as conditional predictions. However, over-predictions around $r/D > 1.5$ should relate to small over-prediction of mixture profiles at the same position.

6.6.2 Parametric Study of CMC Grid Resolution

Similarly as in Flame D, the study of the effect of CMC grid resolution is performed for Flame E. The three different CMC grid resolutions are $4 \times 4 \times 80$, $8 \times 8 \times 80$ and $16 \times 16 \times 80$ (res-1, res-2 and res-3 respectively, Table 6.5), while the same parameters for the flow and mixing fields and the combustion model (variance-2, S_{c2} , $S_{c_{i,1}}$, $C_{\xi,1}$, CMC-1, flux-1 and $D_{\eta,2}^*$) are used for all cases.

6.6.2.1 Conditionally Filtered Reactive Scalars

The conditional mean temperature and mass fraction of CO are shown at $z/D = 7.5$ in Fig. 6.40. The explanation for the interesting position ($z/D = 7.5$) can be found in section 6.5.3.1. Colours of lines and symbols in Fig. 6.40 denote different radial positions, where green, red and black lines are positions $r/D = 0, 1$ and 2 , respectively.

The conditional predictions at position $z/D = 7.5$ (Fig. 6.40) indicate that the predictions of res-1 ($4 \times 4 \times 80$) are identical at all radial positions since the predictions of each radial position come from the same CMC cell. Some differences of the conditional predictions of each radial position are observed in res-2 ($8 \times 8 \times 80$) and they are obvious in res-3 ($16 \times 16 \times 80$) because these predictions come from different CMC cells. Because of the small sizes of the CMC cells in res-3, each CMC cell can be located at a more precise position needed for comparison with the experiment. Consequently, the predictions from each CMC cell of res-3 should be closer to the mean values of the scatter plots at the respective radial position. It should be noted that the nonexistent value which occurs in res-2 and res-3 at $r/D = 2$ and $\eta > 0.90$ is an artefact of the averaging procedure for zero probability which can be observed in a small CMC cell containing few LES cells. For small CMC cells, the values in some mixture fraction bins might be small or zero. Consequently, the FDF values, which are presumed by $\tilde{\xi}$ and $\widetilde{\xi''^2_{sgs}}$ can be small or zero in some regions of the mixture fraction space. To calculate the relevant statistics, FDF values are used as a weighting factor. Therefore, if FDF values are small or zero, the statistics do not exist in the same regions.

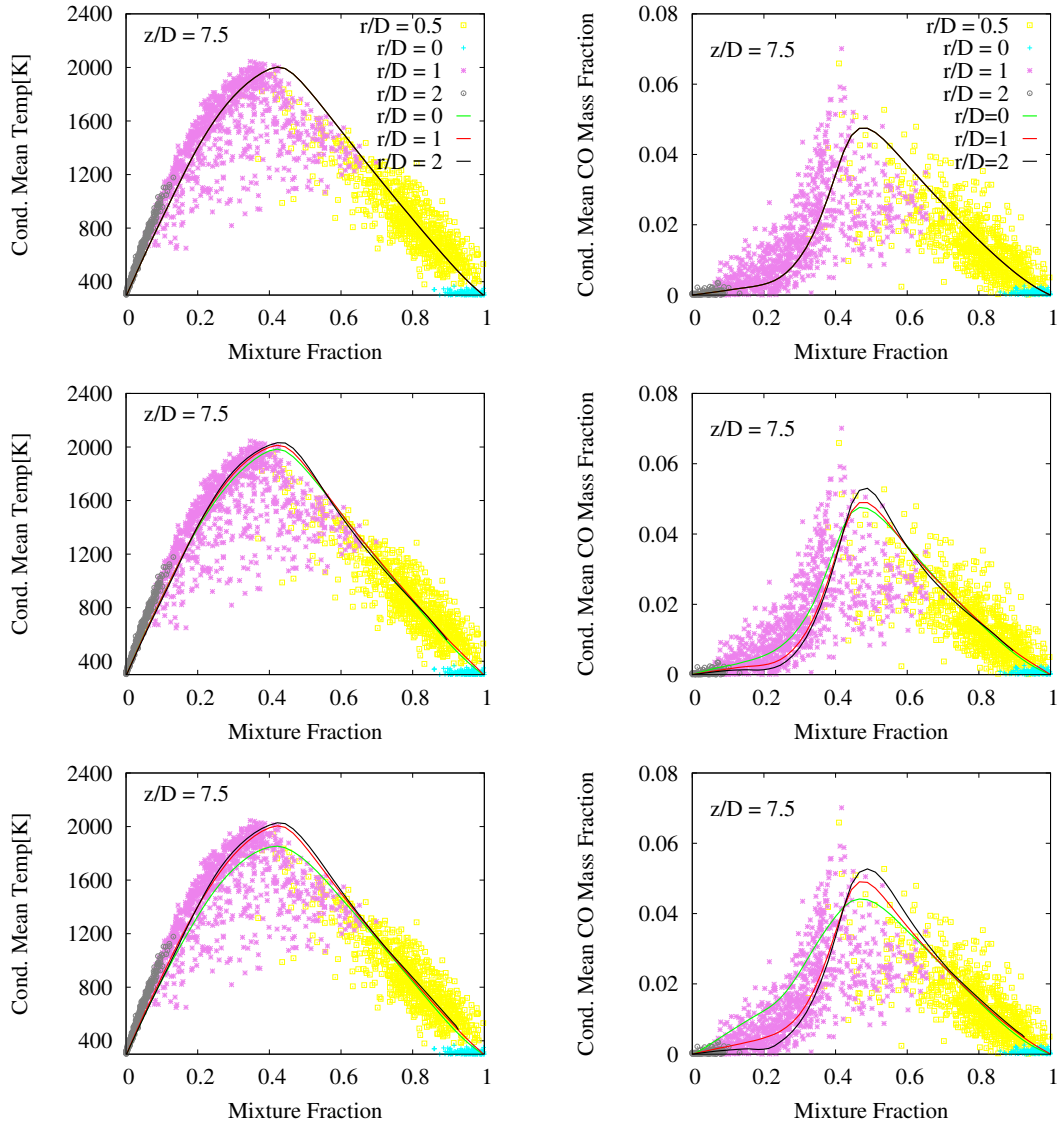


Figure 6.40: Conditional profiles of mean temperature and CO at $z/D = 7.5$ for Flame E. The symbols are experimental data in scatter plots [4], while the lines in the first, second and third rows represent the results of LES-CMC from the different CMC grid resolutions of $4 \times 4 \times 80$, $8 \times 8 \times 80$ and $16 \times 16 \times 80$, respectively (Table 6.5).

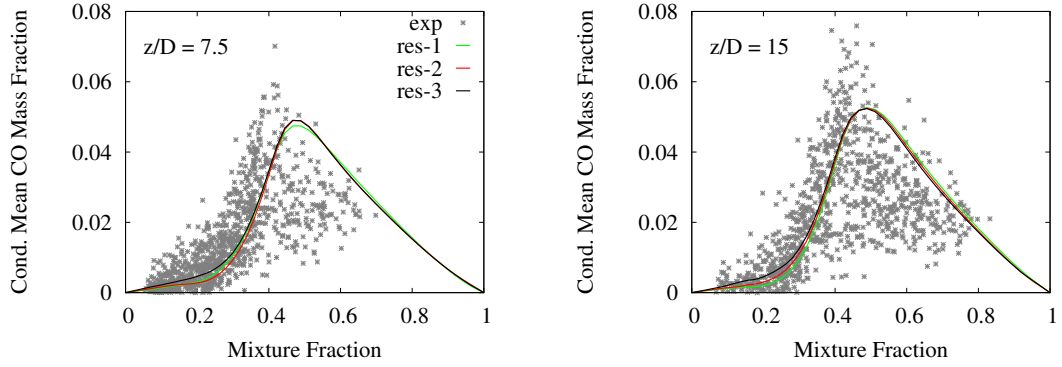


Figure 6.41: Conditional profiles of mean CO at $r/D = 1$ for Flame E. Symbols are experimental data in scatter plots [4], while the green, red and black lines represent the results of LES-CMC from the different CMC grid resolutions (Table 6.5).

In order to compare the accuracy, conditional profiles of mean CO for the three resolutions at position $r/D = 1$ at $z/D = 7.5$ and 15 are shown in Fig. 6.41. It can be observed that the predictions of res-3 are slightly closer to the mean values of scatter plots than the predictions of the other resolutions. Due to more precise predictions of res-3 in both Figs. 6.40 and 6.41, it may be implied that a small size of CMC cells (high resolution) should have a possibility to create more accurate predictions for each radial distribution.

6.6.2.2 Unconditionally Filtered Reactive Scalars

Radial profiles of the mean temperature and CO for different CMC grid resolutions are shown in Fig. 6.42. Normally, the unconditional predictions are outcomes of conditional predictions in physical space. Therefore, the unconditional values should follow the trend of the conditional values as in Flame D (section 6.5.3.2) where it can be seen that res-3 is superior to res-2 and res-1. The reason that over-predictions of res-3 are higher than of the other resolutions should relate to the small differences of mixture fraction profiles among the three resolutions which can be observed in Fig. 6.43.

Regarding the issue of extinction and re-ignition, predictions of unconditional scalars show that all resolutions have some difficulties to capture these phenomena. These effects are observed as over-predictions of temperature around $0.5 < r/D < 2$ at $z/D = 7.5$ and $r/D < 2$ at $z/D = 15$. Due to the high gradient in radial positions of velocity in Flame

$E \left(\frac{1}{2} \left(\frac{\partial \tilde{u}_i}{\partial x_j} + \frac{\partial \tilde{u}_j}{\partial x_i} \right) = \tilde{S}_{ij} \right)$, fluctuations of mixture fraction in a CMC cell become large and they do not correspond to the fluctuations of any species, even though a high CMC resolution is used. Therefore, using only the first-order CMC with single conditioning might not be enough to predict these phenomena.

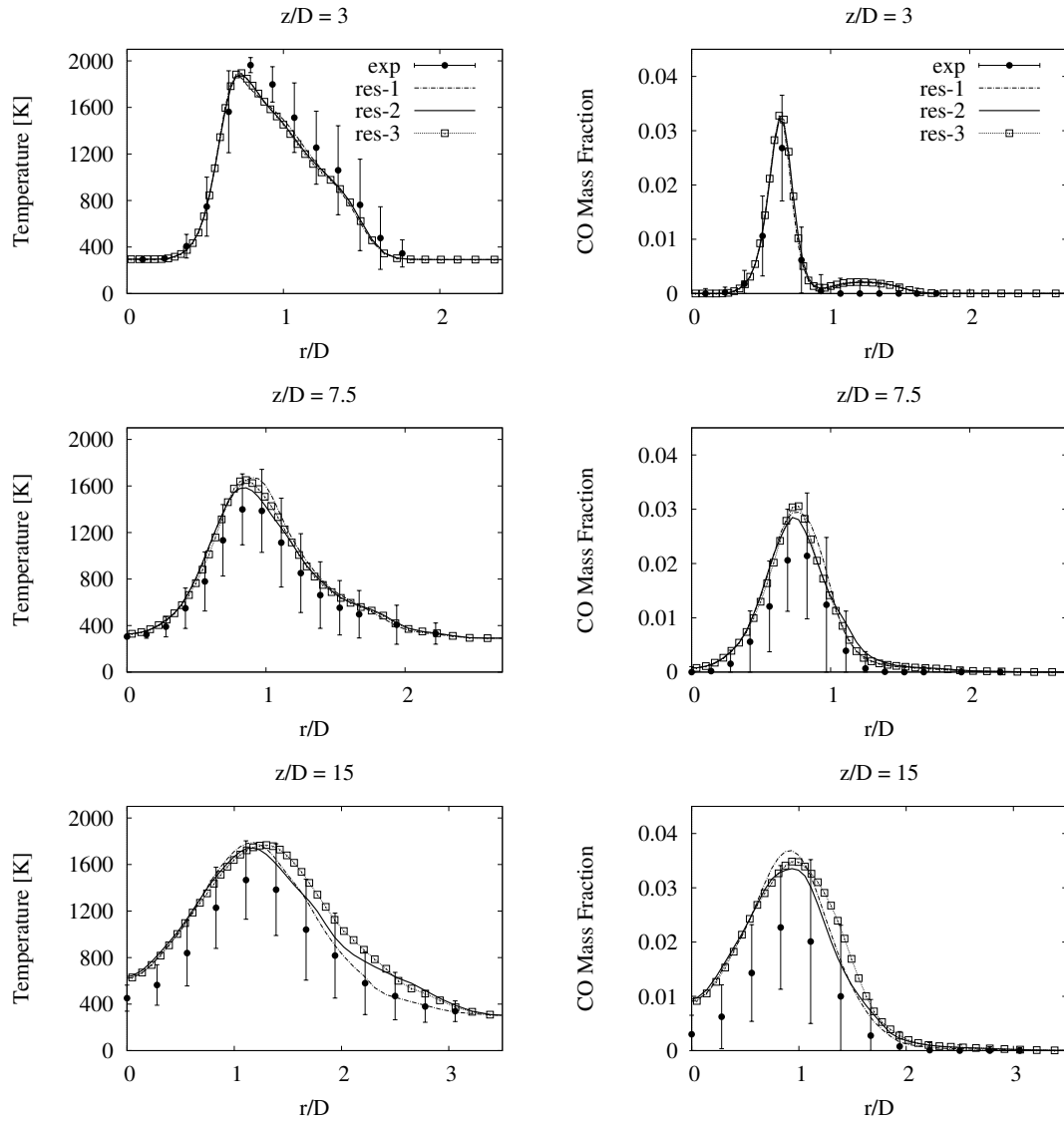


Figure 6.42: Radial profiles of mean temperature and CO for Flame E. Circles are experimental data [4], while the solid, dashed and square-dotted lines represent the results of LES-CMC from the different CMC grid resolutions (Table 6.5).

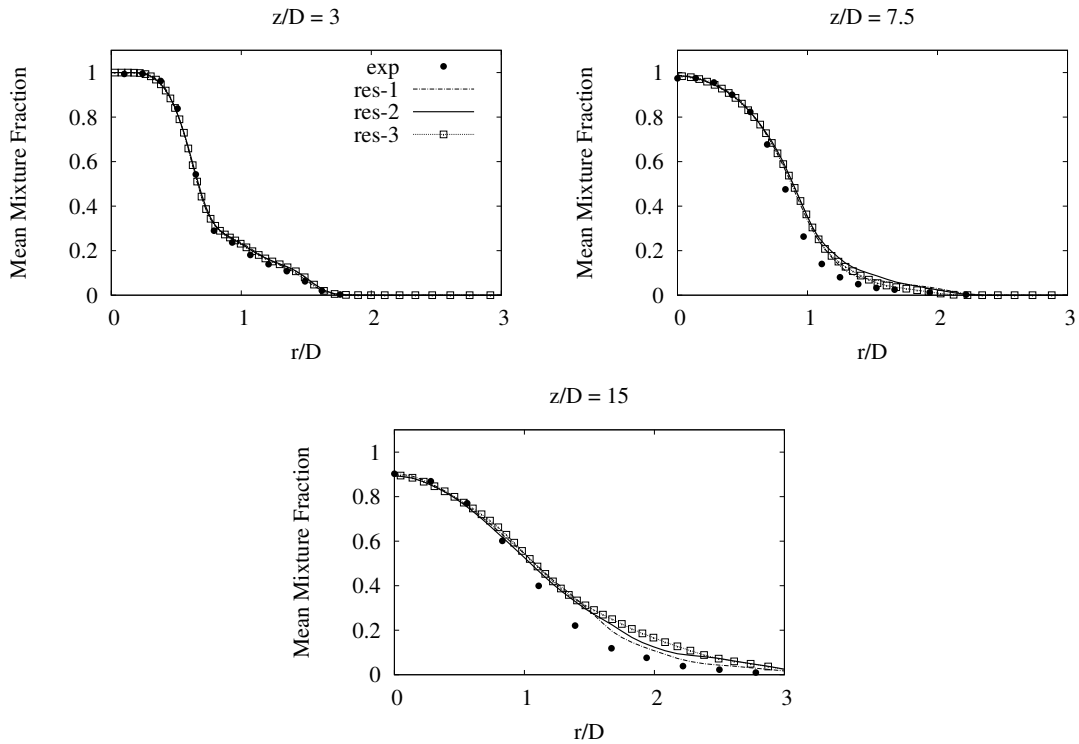


Figure 6.43: Radial profiles of mean mixture fraction for Flame E. Circles are experimental data [4], while the solid, dashed and square-dotted lines illustrate the results of LES-CMC in different cases in the different CMC grid resolutions (Table 6.5).

6.7 Results of Sandia Flame F

Having a higher level of extinction than Flames D and E, Flame F is notoriously difficult to model [50]. As in Flame E, the same parameters of the flow and mixing fields from section 6.5.1 ($Sc = 0.7$, $Sc_t = 0.4$ and $C_\xi = 0.2$) are adopted from the studies of Flame D to be applied to the computation of Flame F. However, the velocity variance in the turbulent inflow generator is re-examined in order to obtain a better agreement with the experiment for the flow and mixing fields. It should be noted that an adjustment is carried out to reduce the high level of turbulence which may occur when using the measured velocities at $z/D = 0.14$ as experimental inlet data for the inflow generator. An inflow variance level of $2/9$ of the measured variances (at $z/D = 0.14$) was found to yield reasonable jet break-up behaviour. Parametric studies of the CMC combustion model and CMC resolution are discussed in the next section.

6.7.1 Parametric Studies of Combustion Model

As shown in Table 6.4, five case studies with different numerical methods (or models) are carried out to demonstrate the effects of each numerical aspect. The structure of the parametric studies is composed of four primary parts. In the first part, an overview of the flow and mixing fields is performed by a reference case (case-1). In the second part, preliminary studies are investigated to define the relevant cases that have the possibility to produce different results. Statistical predictions of the conditional scalars of these cases are investigated and discussed in the third part. The final part presents the statistical predictions in physical space which are shown and analyzed.

6.7.1.1 Flow and Mixing Field

The computational domain for Flame F is adjusted to be wider (details in Table 6.2) so that the recirculation problem as described in Flame D can be avoided (section 6.5.2.1). Using case-1 for predictions, the instantaneous temperature field along the entire computational domain (left) and a zoom into the upstream region (right) at the centre plane of Sandia Flame F are shown in Fig. 6.44. The black lines indicate the isoline of the stoichiometric mixture fraction.

The figure of the upstream regions corroborates the fact that a high turbulence level has developed early on, since an inflow generator has been implemented. However, the high levels of extinction, which are supposed to be found along the isoline of stoichiometric mixture fraction, cannot be seen in the simulation. Details of predictions of extinction and re-ignition phenomena are directly related to predictions of conditional scalars which will be discussed in subsection 6.7.1.3.

The axial variations of mixture fraction and of axial velocity are illustrated in Fig. 6.45 where an agreement with experiments can be observed. The inconsistency between velocity and mixture fraction may come from the inconsistency of the experiments which are done by two groups (i.e. [4] for the species measurements and [88] for the velocity measurements.)

Predictions of radial distributions of mean and RMS of axial velocity are shown in the left column of Fig. 6.46, while predictions of radial distributions of mean and RMS of mixture fraction are illustrated in the right column of the same figure. Generally, predictions agree well with the experiments and the jet spreading is captured well. Small over-predictions of mean and RMS of both axial velocity and mixture fraction are observed

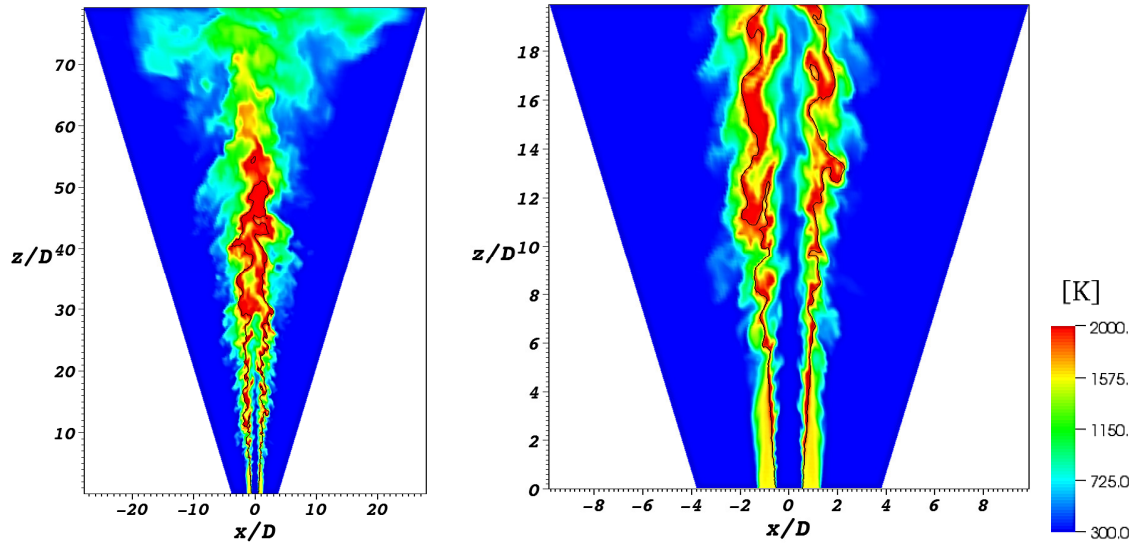


Figure 6.44: Snapshots of the temperature field in the total computational domain (left) and in the upstream region (right) for Sandia Flame F. The iso-contour of stoichiometric mixture fraction is represented by the black lines.

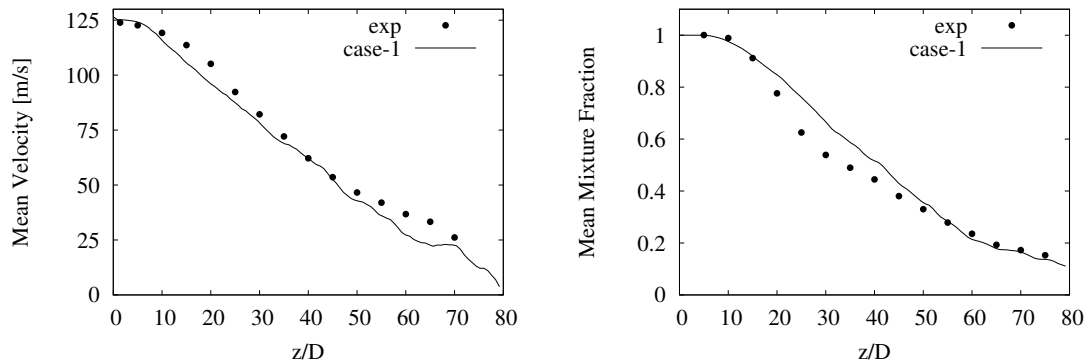


Figure 6.45: Axial profiles of mean axial velocity and mixture fraction along the centerline for Flame F. Symbols denote experimental data, while the solid lines represent the mean results of LES-CMC (reference case of Table 6.4).

at position $z/D = 15$. However, the present predictions can be a good basis for the parametric studies of the combustion model.

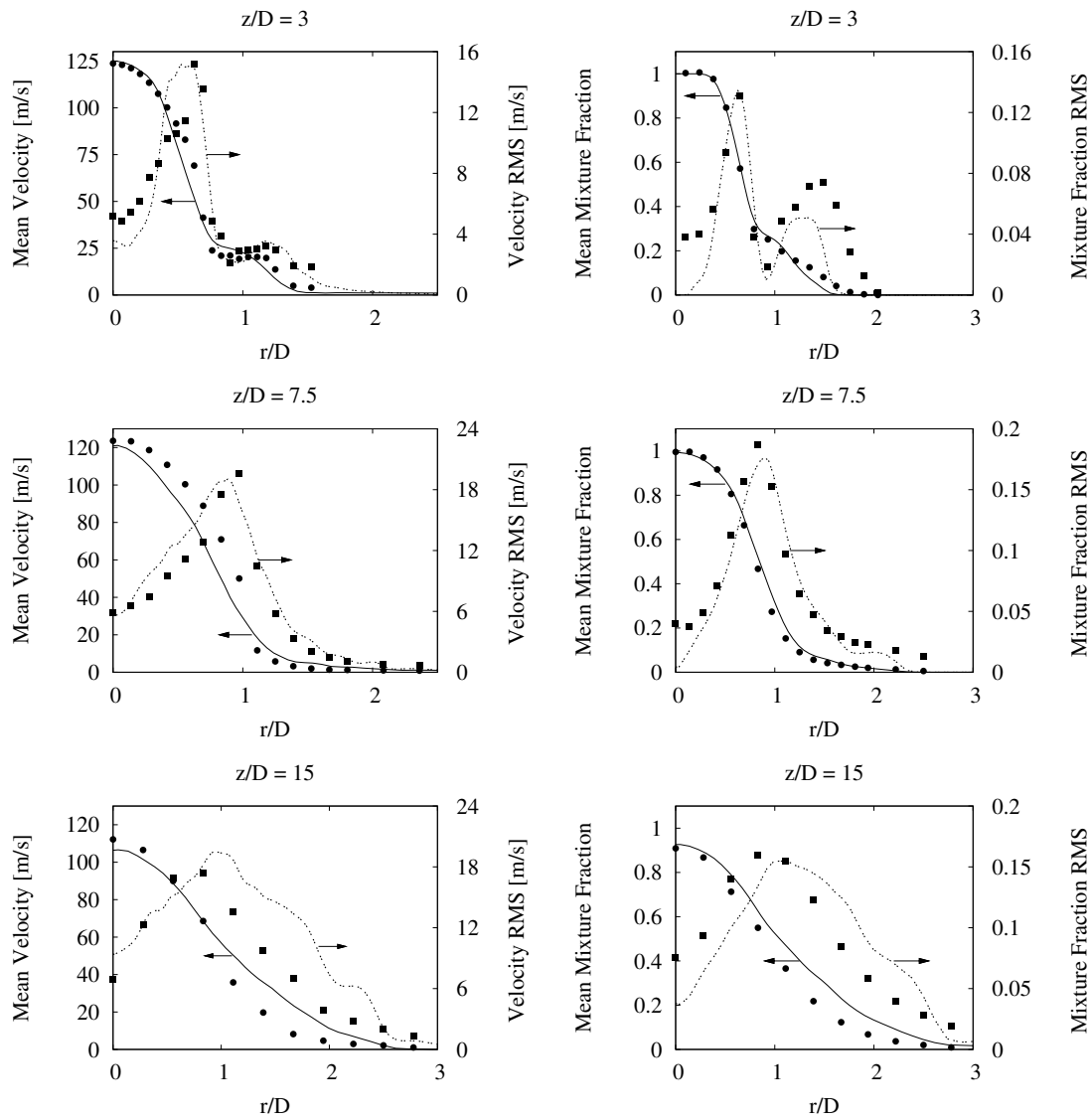


Figure 6.46: Radial profiles of mean and RMS axial velocity and mixture fraction at three downstream locations for Flame F. Symbols denote experimental values [88, 4], while the solid and dotted lines illustrate the mean and RMS results of LES-CMC (reference case of Table 6.4).

6.7.1.2 Preliminary Studies

Based on the same procedures as for Flames D and E, five different cases for the CMC model implementation (which are summarized in Table 6.4) are performed for the convective flux investigations as preliminary studies. Since the details of the investigation procedures are already discussed in section 6.5.2.2, these procedures will be only briefly explained in this section.

Following the investigations of Sandia Flame D (section 6.5.2.2), the z -direction is selected as the leading direction because it indicates most effects of convection on every scalar mass fraction. Since similar results of the convective flux comparison between each direction can be found in all flames of the Sandia Flame series, the z -direction is chosen for consideration within the preliminary studies for Flame F. To ensure that flow solutions are correlated with the same LES simulation results, all case studies are allowed to run only one time step from the same iteration in the first procedure. A comparison of convective fluxes in z -direction between different axial and radial positions (in all five cases) is required to choose appropriate positions to analyze the fluxes. It is observed from the instantaneous CH_4 convective fluxes in Figs. 6.47 and 6.48 that the axial positions show larger differences of fluxes than the radial positions. Therefore, the axial positions are chosen for further investigations. Note that the FDF values are necessary for all considerations because they are used to transfer the effects of the convective values from the mixture fraction space to the physical space. If the FDF values are low, for example, as shown in Fig. 6.48 in the range of $\eta > 0.05$ at $r/D = 2$, the effects of the convective flux in physical space become small or can disappear if the FDF is zero. Subsequently, the convective fluxes at different axial positions are investigated for other species. Furthermore, to have time-independent relations of convective fluxes from each case study, an investigation of convective flux predictions of various cases is required for another initial time step.

Following the same trend as seen in Fig. 6.47, all results of convective flux investigations show that only the predictions of case-1, case-2 and case-3 are different and thus the differences of conditional temperature and species predictions will be detected in these cases. The predictions between case-1 vs. case-5 and case-3 vs. case-4 are identical. The reason for the similar flux prediction is due to the low influences of different D_η^* models on the convective term.

In the next section, the simulation results of case-1, case-2 and case-3 will be collected

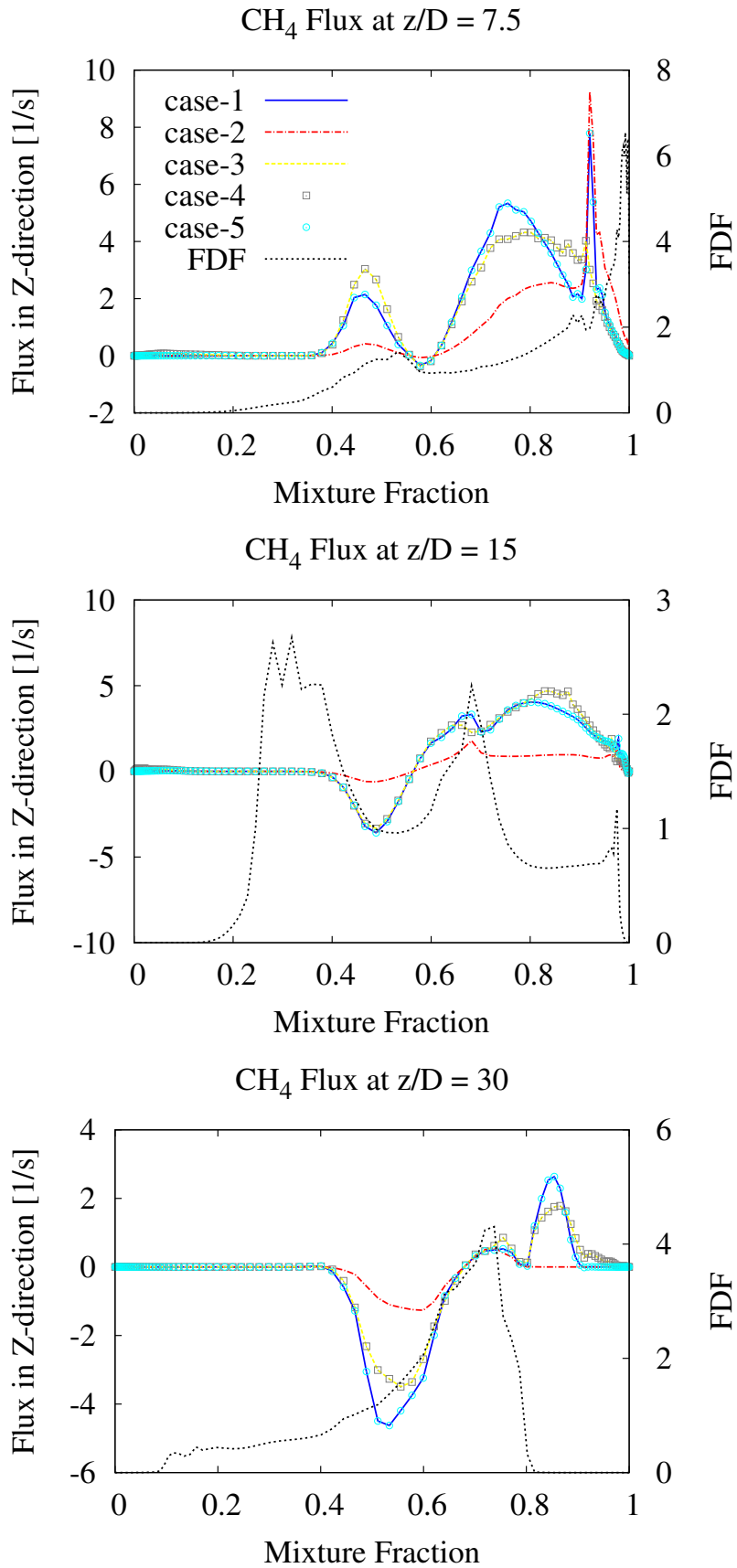


Figure 6.47: Convective fluxes of CH₄ in z -direction for a time step at three different axial positions with the same radial position, $r/D = 0$, for Flame F.

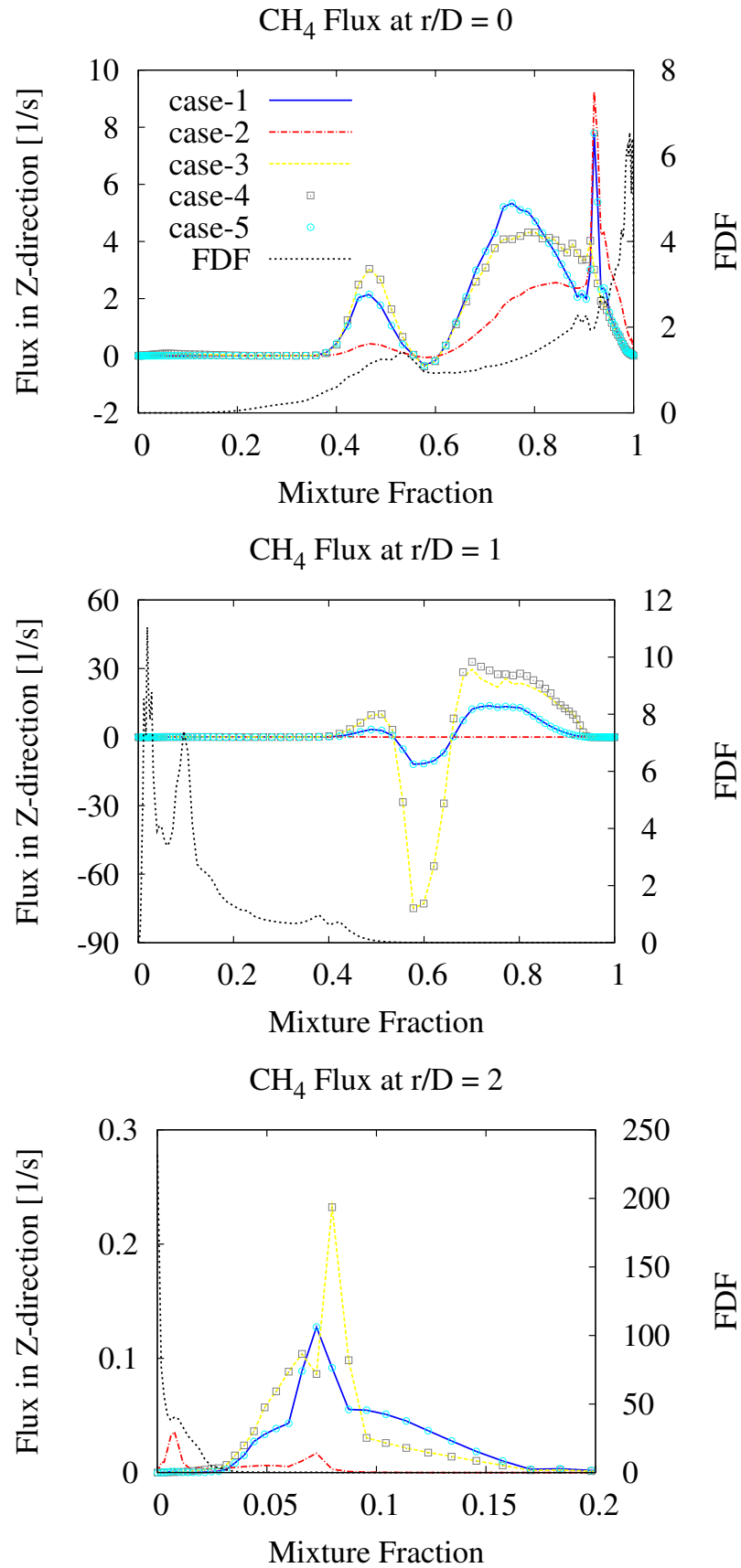


Figure 6.48: Convective fluxes of CH₄ in z-direction for a time step at three different radial positions with the same axial position, $z/D = 7.5$, for Flame F.

for 10.3 *ms* (over 30,000 time steps) for statistical scalar predictions in order to analyze the consequence of these cases in the combustion model. Note that the reference time t_{ref} (as discussed in section 6.5.2.2) of Sandia Flame F is 5.81 *ms*. Compared with t_{ref} , the physical time (10.3 *ms*) is enough to collect statistics of the fluid particle travelling from inlet to outlet of the computational domain for the flame.

6.7.1.3 Conditionally Filtered Reactive Scalars

For the CMC model, the direct performance of any numerical method can be assessed in mixture fraction space. It should be noted that all statistics of conditional measurements are available only as cross-sectional averages, and thus, the conditional simulation results are validated with this kind of measurements at interesting positions. As in Flame D (section 6.5.2.3), results of an SLFM solution are used as initial values for the conditional species. Owing to the preliminary studies of convective fluxes (section 6.7.1.2), investigations of three different cases (case-1, case-2 and case-3 from Table 6.4) are performed for statistical predictions.

The comparisons of the conditional averaged scalar dissipation for three different implementations of the combustion model are illustrated in Fig. 6.49. Note that there is no 3D measurement data for Flame F by Karpetis and Barlow [36]. However, being compared with Flames D and E (Figs. 6.17 and 6.32, respectively) for the same cross section, Flame F has higher conditional averages of mean scalar dissipation than both other flames due to high turbulence from the high shear rates. This means the resolved strain rate, which causes the gradient of velocities ($\frac{1}{2} \left(\frac{\partial \tilde{u}_i}{\partial x_j} + \frac{\partial \tilde{u}_j}{\partial x_i} \right) = \widetilde{S_{ij}}$) is high and hence, an expected increase in scalar dissipation [36]. A reason for different values of scalar dissipation in each case is due to a variation of the instantaneous convective fluxes, which is already discussed in detail for Flames D (section 6.5.2.3) and E (section 6.6.1.3).

Predictions of conditional mean temperature, mass fractions of CO, CH₄ and H₂ are illustrated in Figs. 6.50 and 6.51. Conditional RMS values are indicated by error bars which are only plotted to illustrate the conditional turbulent fluctuations of each scalar. Three species are chosen as representatives of intermediates, products and fuel. The trend of product predictions can be estimated from temperature predictions. Over-predictions of conditional temperature at positions $z/D = 7.5$ and 15 (left column of Fig. 6.50) relate to the under-predictions of CH₄ (left column of Fig. 6.51), while CO and H₂ (right column

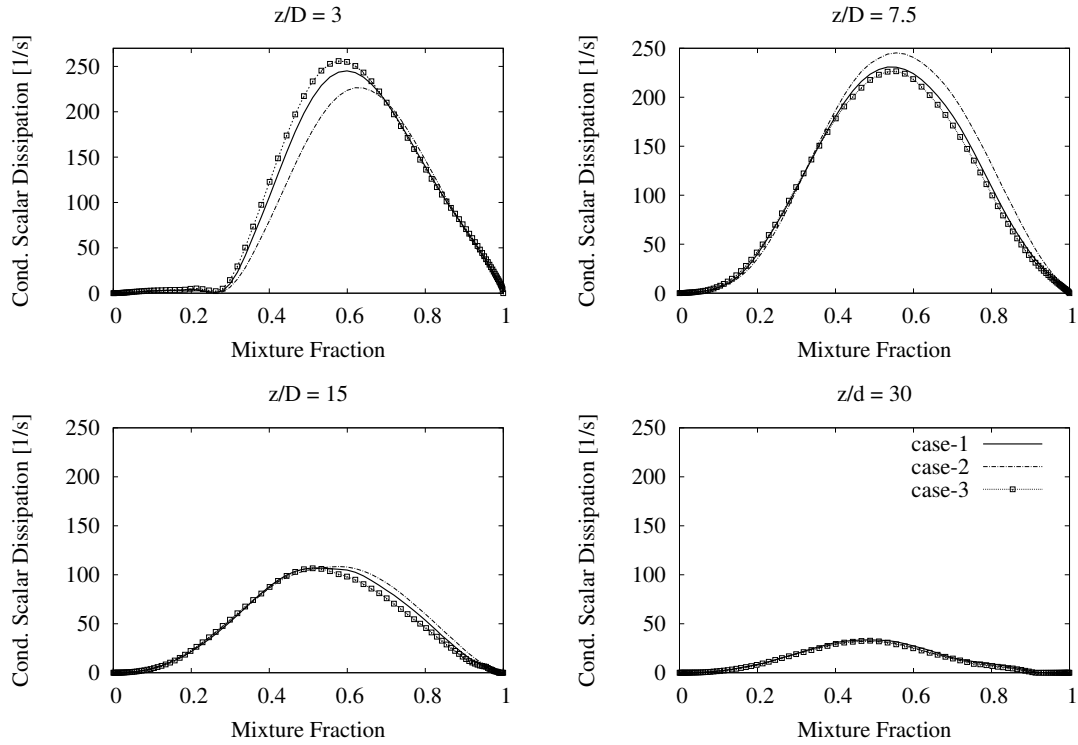


Figure 6.49: Conditional averages of mean scalar dissipation in mixture fraction space at four downstream locations for Flame F. Solid, dashed and square-dotted lines represent the results of LES-CMC in different cases of combustion model (Table 6.4).

of Figs. 6.50 and 6.51) are over-predicted.

Under-predictions of conditional mean temperature around $\eta < 0.35$ at position $z/D = 3$ (Fig. 6.50) may relate to the influences of initialization of CMC on the upstream locations. The determination of conditional temperature predictions on the rich side at $z/D = 3$ seems unclear because there is no experimental data over the mixture fraction field between 0.33 and 0.70. The reason for absent measurements at this position is due to the influences of hydrocarbon fluorescence interferences on the CO-Raman measurement, and thus it creates errors in the conditional means in the region of high interference on the rich side ($\eta > 0.35$) [4]. Differences of predictions from each case on the rich side at position $z/D = 3$ have already occurred in the previous test cases (details can be found in section 6.5.2.3). The reason behind the differences of the predictions is a variation of the convective fluxes on the rich side of each CMC cell which are created from different case studies.

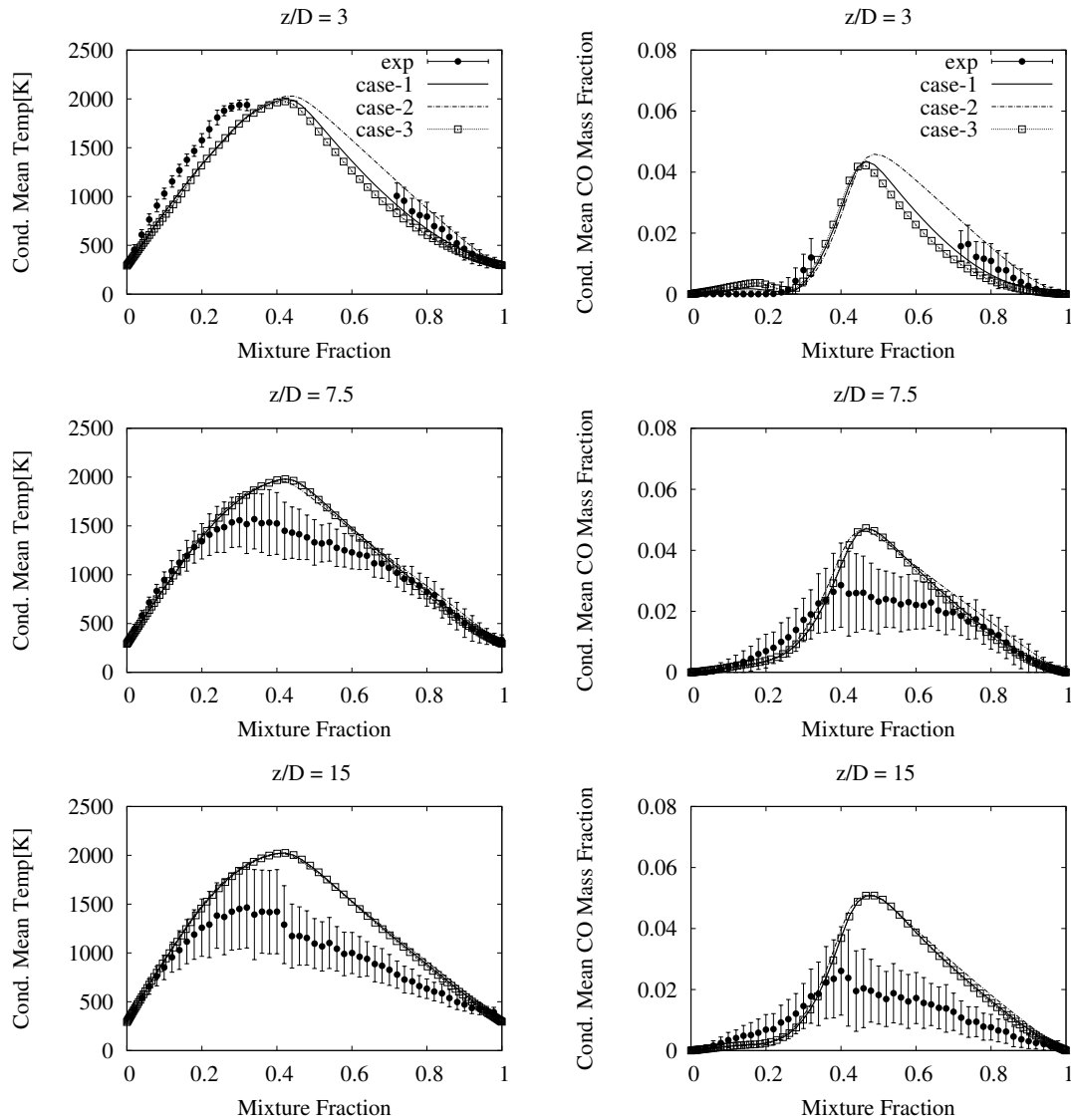


Figure 6.50: Conditional profiles of cross-sectionally averaged temperature and CO at three different downstream positions in mixture fraction space for Flame F. Circles are experimental data [4], while the solid, dashed and square-dotted lines illustrate the results of LES-CMC in different cases in combustion model (Table 6.4).

From Figs. 6.50 and 6.51, it can be observed that results from case-1 agree with the relevant experiments slightly better than case-3. The reason for the similar predictions can be attributed to low FDF values where the predictions are different in each CMC cell at the same cross section. Consequently, the averaged predictions (by weighting with the FDF) for a cross section are similar. More details can be found in section 6.5.2.3. Predictions of CO and H_2 at positions $z/D = 7.5$ and 15 show that case-1 is slightly closer to the

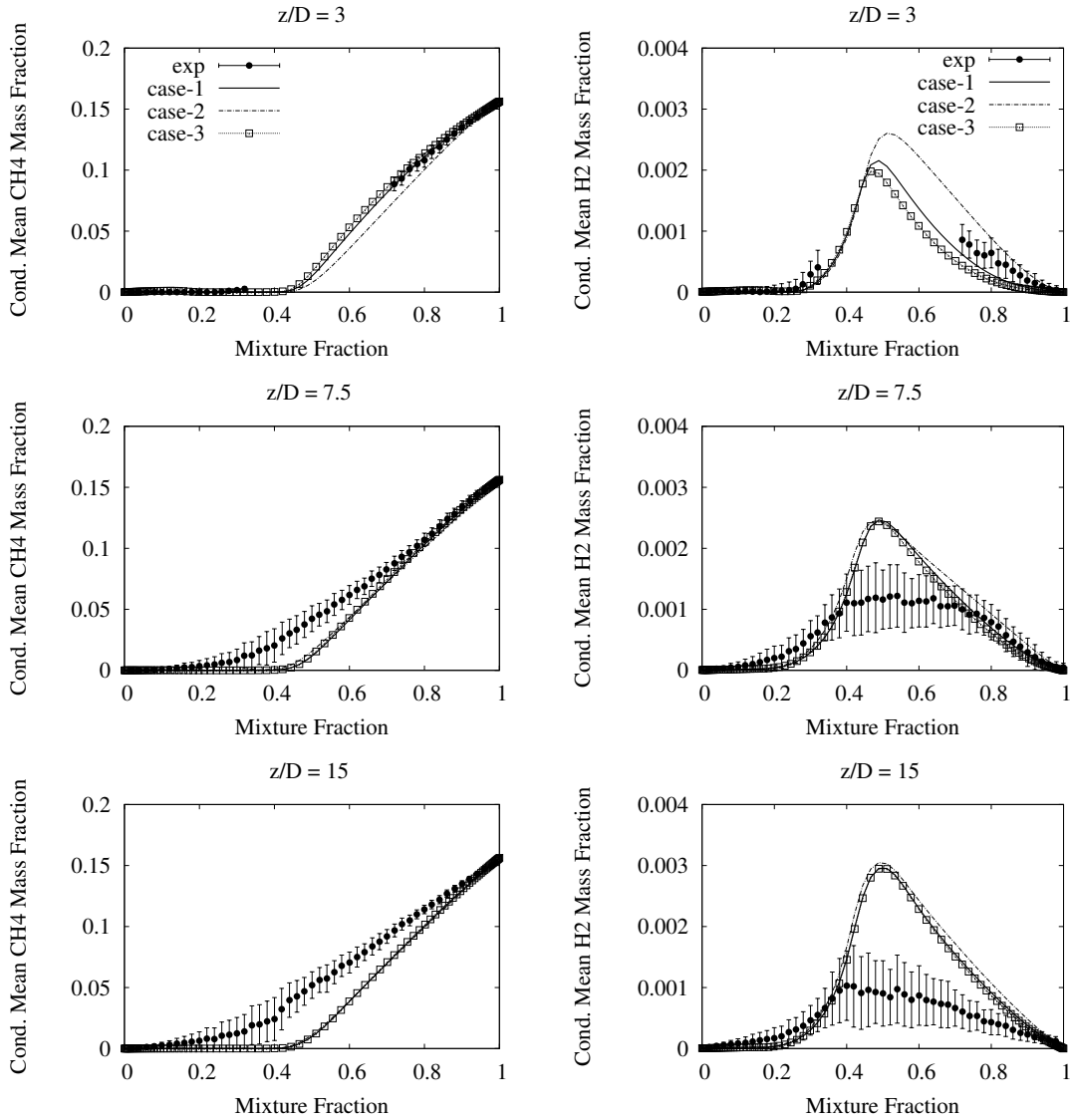


Figure 6.51: Conditional profiles of cross-sectionally averaged CH_4 and H_2 at three different downstream positions in mixture fraction space for Flame F. Circles are experimental data [4], while the solid, dashed and square-dotted lines represent the results of LES-CMC in different cases in combustion model (Table 6.4).

measurements than case-2. However, none of the cases can predict the extinction and re-ignition phenomena (where over-predictions can be observed for conditional temperature between $0.2 < \eta < 0.7$ at $z/D = 7.5$ and between $\eta > 0.15$ at $z/D = 15$) due to the same reason as in Flame E (discussed in section 6.6.1.3).

6.7.1.4 Unconditionally Filtered Reactive Scalars

Besides conditional scalars in mixture fraction space, predictions of three different implementations of the combustion model can be validated in physical space using unconditional scalars. The transformation between conditional values and unconditional values is performed by convolution with the FDF.

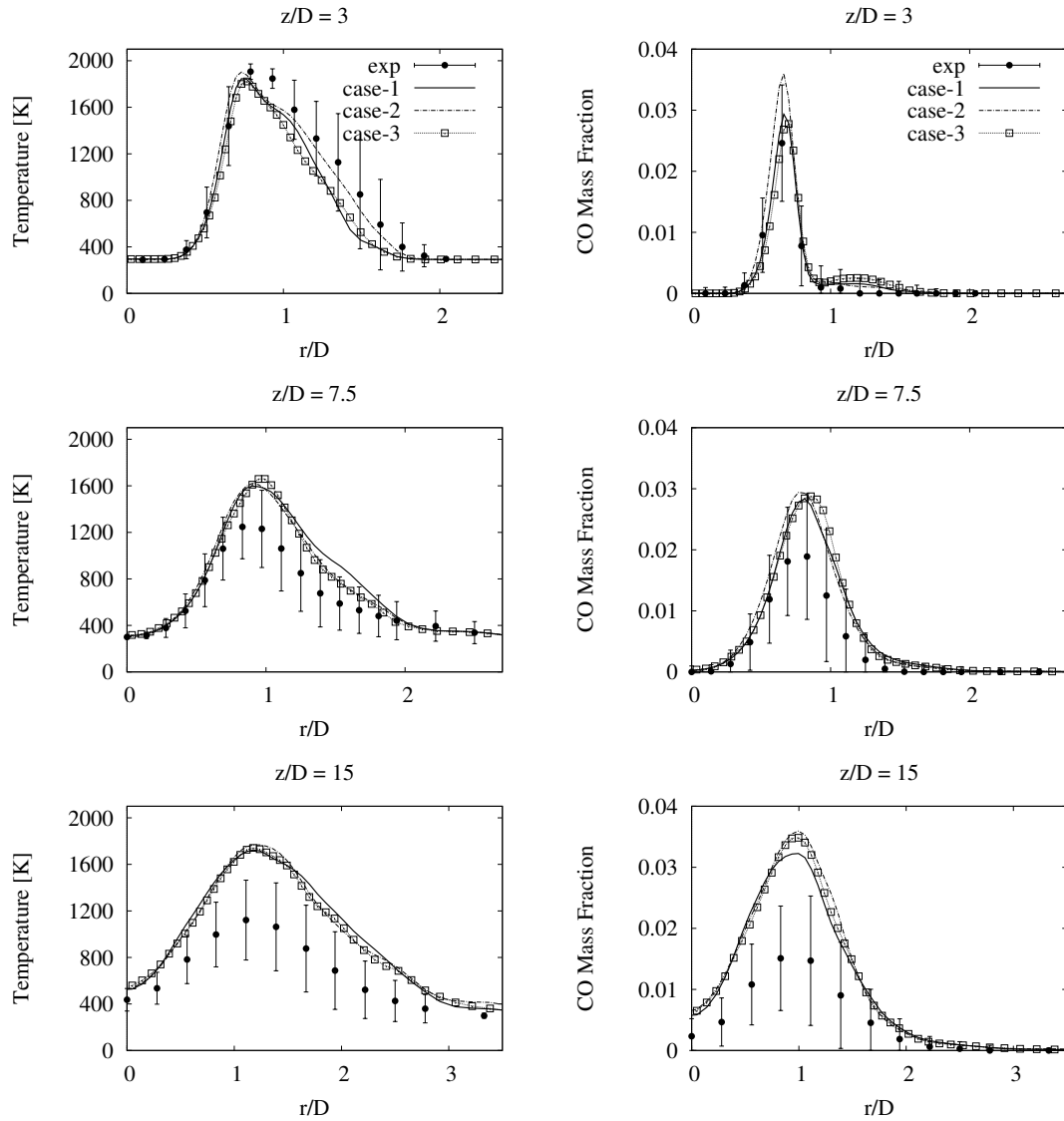


Figure 6.52: Radial profiles of mean temperature and CO for Flame F. Circles are experimental data [4], while the solid, dashed and square-dotted lines represent the results of LES-CMC in different cases in combustion model (Table 6.4).

Figures 6.52 and 6.53 compare the predictions between three cases for radial distri-

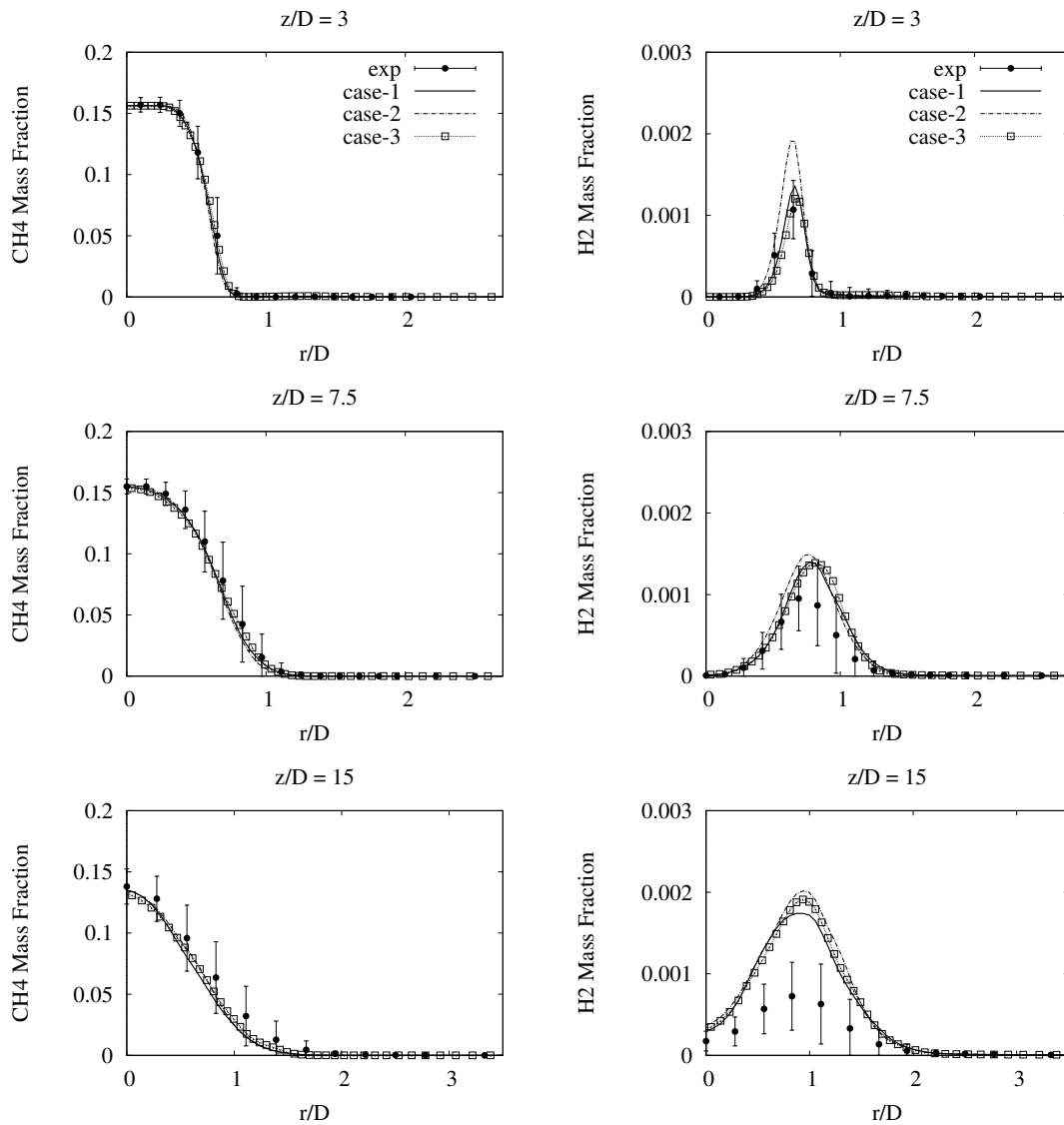


Figure 6.53: Radial profiles of mean CH_4 and H_2 for Flame F. Circles are experimental data [4], while the solid, dashed and square-dotted lines represent the results of LES-CMC in different cases in combustion model (Table 6.4).

butions of mean temperature and some reactive species (CH_4 , CO and H_2). Generally, the unconditionally filtered scalars follow the tendency of the conditionally filtered scalars which demonstrate that case-1 comes closer to experimental results when compared with case-2 and case-3. However, some disagreements between unconditional predictions and conditional predictions can be attributed to the discrepancy of the mixture fraction profiles. A discussion of using mixture fraction profiles for a consideration of rich and lean regions can be found in section 6.6.1.4. Following the trend of conditional predictions,

over-predictions of mean temperature at positions $z/D = 7.5$ and 15 are a consequence of the present first-order CMC formulation not capturing local extinction in Flame F which leads to the under-predictions of mean CH_4 and the over-predictions of CO and H_2 .

6.7.2 Parametric Study of CMC Grid Resolution

Following the same procedure as for Flames D and E, three different CMC grid resolutions are investigated for Flame F. Applying the same parameters for flow, mixing field and combustion model (detailed in Table 6.5), the resolutions of $4 \times 4 \times 80$, $8 \times 8 \times 80$ and $16 \times 16 \times 80$ CMC cells are defined as res-1, res-2 and res-3, respectively. The structure of this section is composed of two main parts. Conditional predictions of filtered reactive scalars are described in the first part since they show the direct effects of combustion model. Unconditionally filtered reactive scalars are reported in the second part which demonstrates the predictions in physical space.

6.7.2.1 Conditionally Filtered Reactive Scalars

Figure 6.54 shows predictions of the conditional mean temperature and CO at position $z/D = 7.5$. Since predictions at position $z/D = 15$ follow the trend of predictions at position $z/D = 7.5$, they will not be shown in this section. The different colours of lines and symbols in Fig. 6.54 illustrate different radial positions, where green, red and black lines are the positions $r/D = 0, 1$ and 2, respectively.

A variation of conditional predictions in different radial positions can be simply detected in Fig. 6.54. As for Flame E (section 6.6.2.1), it can be observed that predictions of res-1 at $r/D = 0, 1$ and 2 are the same because all positions are captured by the same CMC cell (owing to the big size of CMC cells). On the other hand, different predictions at any radial position are produced by res-2 and res-3 due to the small size of CMC cells (high resolutions). These facts can be observed by considering colours of the lines for all resolutions in Fig. 6.54. Moreover, res-2 and res-3 seem to capture the measured conditional mean especially in the mixing zone (at position $r/D = 1$) slightly better than res-1. Note that the inexistent values which occur in res-2 and res-3 at $r/D = 2$ and $\eta > 0.90$ are an effect of a small CMC cell which comprises few LES cells (detailed in sections 6.5.3.1 and 6.6.2.1).

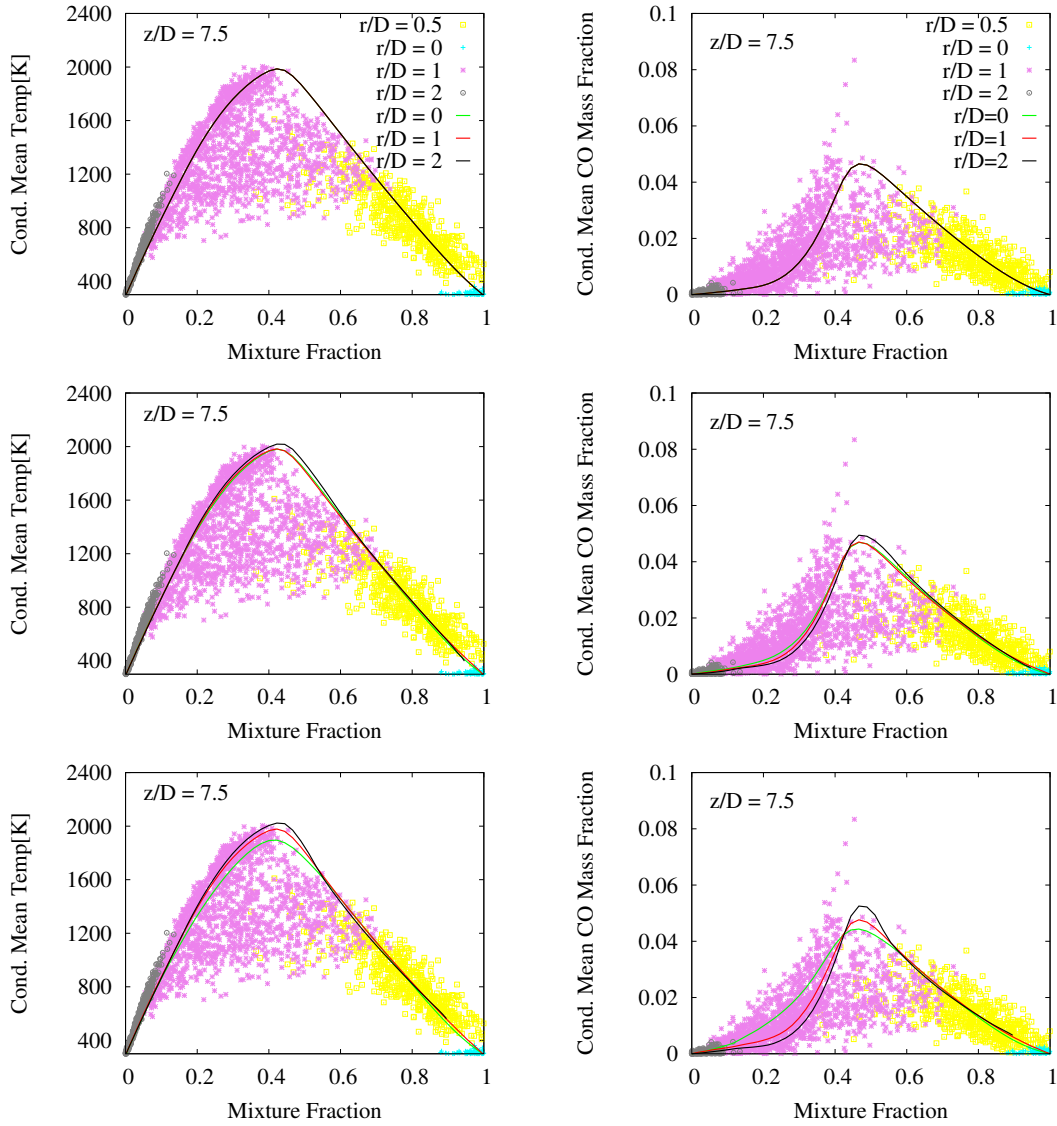


Figure 6.54: Conditional profiles of mean temperature and CO at $z/D = 7.5$ for Flame F. The symbols are experimental data in scatter plots [4], while the lines in the first, second and third rows represent the results of LES-CMC from the different CMC grid resolutions of $4 \times 4 \times 80$, $8 \times 8 \times 80$ and $16 \times 16 \times 80$, respectively (Table 6.5).

The comparisons of the performance between three resolutions are shown for the conditional profiles of mean CO in Fig. 6.55 for $r/D = 1$ at $z/D = 7.5$ and 15. It can be found that the predictions of res-3 ($16 \times 16 \times 80$) appear slightly closer to the mean values of the scatter plots than res-2 and res-1. Another possibility to observe the effects of different CMC grid resolutions is to validate the predictions by the measurements in

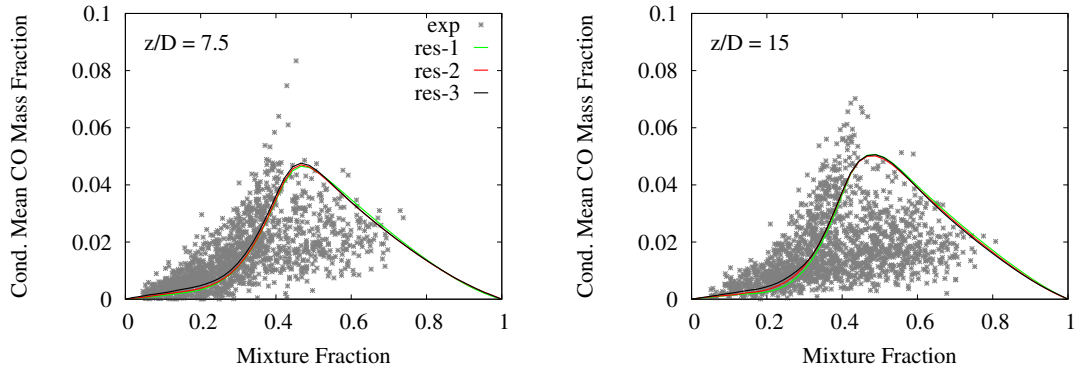


Figure 6.55: Conditional profiles of mean CO at $r/D = 1$ for Flame F. Symbols are experimental data in scatter plots [4], while the green, red and black lines represent the results of LES-CMC from the different CMC grid resolutions (Table 6.5).

physical space. Therefore, unconditional predictions are required to be discussed in the next section.

6.7.2.2 Unconditionally Filtered Reactive Scalars

Radial distributions of the mean temperature and CO for different positions are shown in Fig. 6.56. Following the same tendency as the conditional prediction, the unconditional mean temperature and CO show that res-3 predicts slightly better than res-2 and res-1 which can be easily detected at position $z/D = 15$. However, the predictions at positions $z/D = 7.5$ and 15, where high levels of extinction and re-ignition occur, demonstrate that increasing the number of the CMC cell resolution does not fulfill the performance in order to simulate these phenomena as it was also found in Flame E.

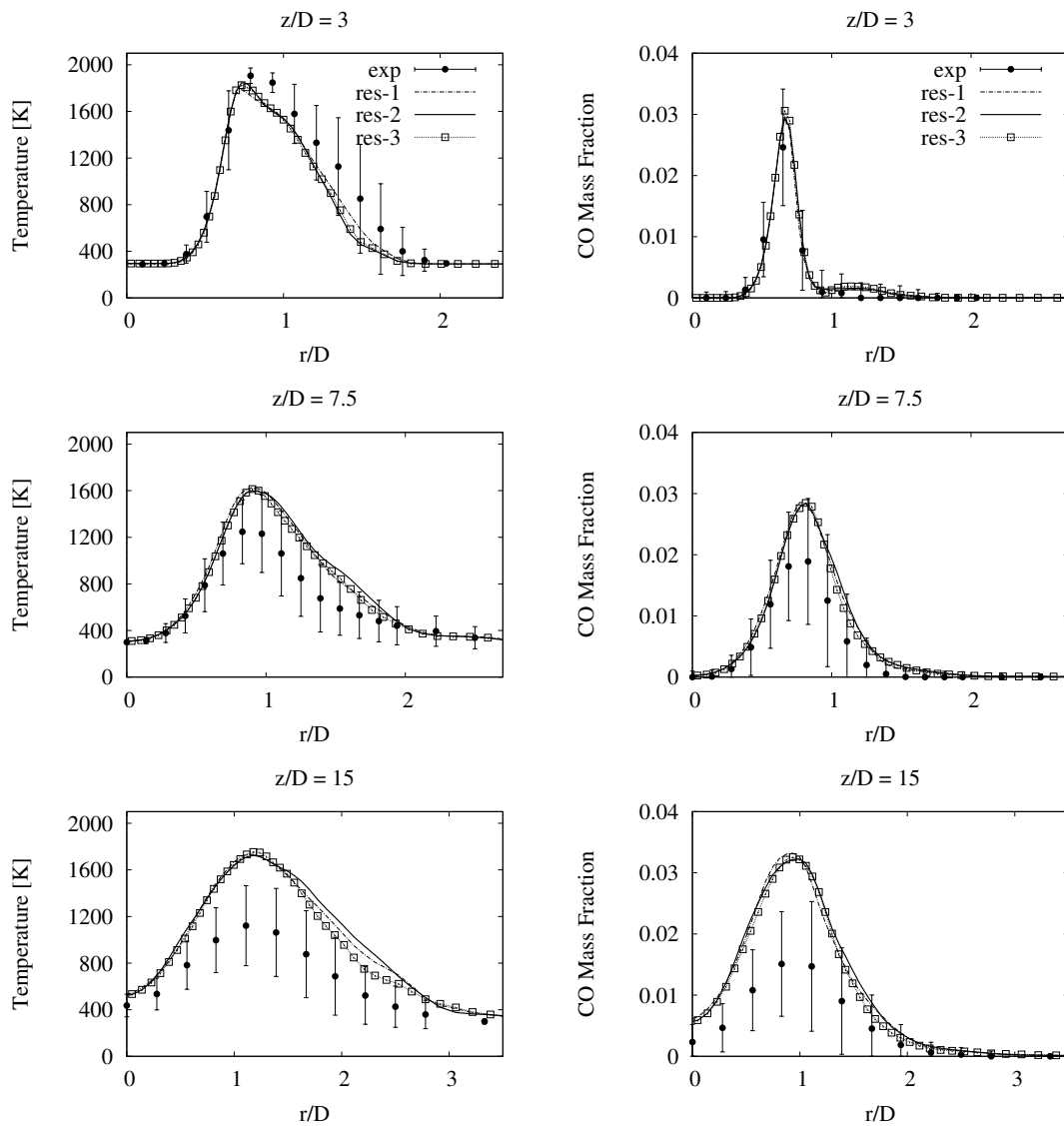


Figure 6.56: Radial profiles of mean temperature and CO for Flame F. Circles are experimental data [4], while the solid, dashed and square-dotted lines represent the results of LES-CMC from the different CMC grid resolutions (Table 6.5).

6.8 Summary

Contained within this chapter, parametric studies of LES-CMC are carried out for the Sandia Flame series. The parameter studies comprised investigations of flow and mixing field, variants of the CMC combustion model parameters and CMC grid resolution.

Flame D is used to investigate the influence of various flow and mixing field parameters on the simulation results. These parameters, which are $Sc = 0.7$, $Sc_t = 0.4$ and $C_\xi = 0.2$, are used for further studies of Flame D, as well as for Flames E and F. Values of velocity variance for the inflow generator, however, depend on the physical inflow of each flame. It should be noted that an adjustment of the velocity variances is carried out to reduce the high level of turbulence which may come from using the measurements of velocities at $z/D = 0.14$ as experimental inlet data for the inflow generator. Suitable inflow variances for Flames D, E and F are found to be $\frac{2}{3}$, $\frac{1}{3}$ and $\frac{2}{9}$ of the measured variances at $z/D = 0.14$ of these flames, respectively.

Parameter studies of different variants of the CMC combustion model are carried out to find the most suitable model as well as to examine the abilities of each case for predicting extinction and re-ignition phenomena. Initial studies of the CMC fluxes have reported that the effect of turbulent diffusivity modelling is negligible. However, a comparison of CMC models, which vary the CMC formulation (conservative vs. non-conservative), reveals considerable differences. Moreover, some slight differences between two methods of the CMC convective flux approximation (cell face vs. cell centre based) are detected. Therefore, three dominant cases which differ in both numerical aspects are investigated for further studies. Conditional profiles of cross-sectionally averaged scalars compared with the measurements show that the conservative CMC formulation with computing convective fluxes based on LES cells located at the CMC cell faces (case-1) is similar to the one with computing convective fluxes based on CMC cell centres (case-3). This can be explained by the low FDF values where the differences of predictions occur in a CMC cell. Consequently, the conditionally averaged predictions with FDF weighting create the similar results over a cross section. Generally, both conditional and unconditional predictions reveal that case-1 can capture better mean measurements than case-2 (the non-conservative formulation using the same flux approximation). This is because the variation of FDF weighting ($\frac{\gamma_{face}^*}{\gamma_P^*}$) in convective flux calculation for different directions of

case-1 allows the predictions to be more accurate. However, an inaccuracy of unconditional predictions can occur due to the inaccuracy of mixture fraction profiles. Regarding the ability to predict extinction and re-ignition, Flames E and F are used as test cases since Flame E exhibits strong local extinction which increases close to blow-off for Flame F. The results from conditional scalar predictions for Flames E and F indicate that the current first-order CMC formulation has some difficulties in predicting these phenomena.

Three different CMC grid resolutions ($4 \times 4 \times 80$, $8 \times 8 \times 80$ and $16 \times 16 \times 80$) are examined in order to find the appropriate number of CMC cells for each Sandia Flame. Due to the computational cost with efficient performance, the reasonable resolution for Flame D is $8 \times 8 \times 80$ CMC cell. A consideration of extinction and re-ignition in Flames E and F indicates that the best predictions are found when the CMC grid resolution is increased to $16 \times 16 \times 80$. However, these predictions do still not capture the extinction and re-ignition phenomena.

CHAPTER 7

Conclusions and Future Work

7.1 Overview

This research concerns LES simulations of non-premixed turbulent flames. The simulations have been carried out using a first-order conservative formulation of the conditional moment closure (CMC) model for combustion and large eddy simulation (LES) for turbulent flow. The objective of this work is to investigate the sensitivity of the results to variants of the CMC combustion model (especially for two CMC formulations, the conservative and the non-conservative forms) as well as to the CMC grid resolution. Three test cases of non-premixed jet flames (Sandia Flames D, E and F) were investigated. Due to increasing Reynolds numbers in the Sandia flame series, the scalar dissipation rate increases from Flame D to Flame F and thus a higher level of extinction and re-ignition is found in Flames E and F, respectively.

7.2 Conclusions

The CMC model was first coupled with the LES methodology by Navarro *et al.* [68] and there have been some studies using the LES-CMC method in recent years. However, only a non-conservative CMC formulation has been applied so far and it may predict inaccurate results in CMC cells which have large temporal variations of the mixture fraction field. A lack of an FDF-weighting function in the convective term in non-conservative CMC is believed to be the main reason for inaccurate predictions. Hence, LES combined with the

conservative CMC formulation was validated and investigated in this research.

Based on the finite volume method, the CMC model was implemented in conservative formulation which considers the ratios of the presumed FDFs of the boundaries and the centre of the CMC cells. These ratios influence the convective fluxes in each direction. Consequently, a quick response of the conditionally filtered reactive scalars to turbulent fluctuations occurs by including these FDF ratios in the convective fluxes. Each CMC cell contains many LES cells and thus the FDF-volume averaging is required to transfer information between the two different grids (LES and CMC). The solution of the LES flow field is passed to the CMC solver to allow the computation of the temperature and reacting scalars, while information on density and viscosity is passed from the CMC solver back to the flow field solver.

Parameter sensitivity studies of the flow and mixing field using Flame D as a reference case were performed to establish a set of valid parameters for the simulation of the whole flame series, Sandia Flame D, E and F. The studies found that $Sc = 0.7$, $Sc_t = 0.4$ and setting the subgrid-scale variance modelling constant C_ξ to 0.2 yields good agreement with experiments. A sensitivity analysis of the results indicated that inflow velocity variance levels corresponding to $\frac{2}{3}$, $\frac{1}{3}$ and $\frac{2}{9}$ of the measured variances at $z/D = 0.14$ were suitable inflow conditions for Flames D, E and F, respectively.

Preliminary studies of variants of the CMC combustion model have been investigated in order to define dominant numerical aspects (or models) which influence statistical predictions for further studies. Instantaneous correlations between diffusion, reaction and the convective fluxes of a reference case were presented. The convective flux in z -direction was chosen as being representative for all next steps because of the highest value of the convective flux in this direction among the three directions. Since all numerical aspects directly influence the convective term, the instantaneous convective flux performances from five case studies were presented. Subsequently, the analyses of relations between numerical aspects and results were reported. The dominant aspects were the CMC formulations and different flux approximation methods. Both aspects were implemented in three case studies as the conservative CMC formulation with computing convective fluxes based on LES cells located at the CMC cell faces, the non-conservative formulation with computing convective fluxes based on LES cells located at the CMC cell faces and the conservative CMC formulation with computing convective fluxes based on CMC cell centres. Since

these three cases showed the different convective fluxes, they were investigated further for statistical predictions.

The investigation of the sensitivity of the conditional mean predictions indicated that the conservative CMC is superior to the non-conservative CMC because the FDF-weighted convective fluxes made the predictions more accurate as proved by comparing with conditional measurements. However, there were small differences in unconditional mean predictions. This may be due to the low FDF values where the differences of conditional results between both CMC formulations have been predicted. Consequently, the slight differences in unconditionally filtered values were produced after performing a convolution with the FDF. Details in the comparisons of the flux approximation methods affirmed that computing the fluxes based on the LES cells located at the CMC faces could predict similar conditional mean scalar predictions as an approximation based on the CMC cell centres. This may be due to the low FDF values in the range of mixture fraction bins where the predictions from both flux approximation methods were different in each CMC cell. As a result, averages over a cross section using FDF weighting produced similar predictions.

The parametric study of CMC grid resolution was investigated for three CMC resolutions. Using the same LES resolution, the different CMC grid resolutions were $4 \times 4 \times 80$, $8 \times 8 \times 80$ and $16 \times 16 \times 80$. The investigation of the sensitivity of the results to different CMC grid resolutions showed that the resolution of $16 \times 16 \times 80$ yields better agreement with experiments than the others. However, the resolution of $8 \times 8 \times 80$ was reasonable considering both the accuracy and computational cost. Therefore, the CMC resolution of $8 \times 8 \times 80$ was recommended as an appropriate resolution for the Sandia Flame series.

Regarding the issue of extinction and re-ignition, the results of Flames E and F showed that the current CMC model has some difficulties in predicting these phenomena. Increasing CMC grid resolution has improved predictions; however, this requires more accurate and advanced modelling of the conditional reaction source terms in order to obtain better results for these high Re flames.

7.3 Suggestions for Future Work

Some inaccuracies and limitations of applying LES combined with a conservative CMC formulation were discovered in this research. For example, the first-order CMC can predict Sandia Flame D effectively, while it has some difficulties in predicting Flames E and F.

The first-order CMC exhibited known difficulties to predict the extinction and re-ignition phenomena which result from fluctuations of scalar dissipation. For low Reynolds number flames (as Flame D), the fluctuations of scalar dissipation in the CMC cells remain small, and so the properties in mixture fraction space can be predicted effectively by only considering the mean quantities. However, high Reynolds number flames (as Flames E and F) generate high fluctuations of scalar dissipation. As a result, using only the conditional mean scalar dissipation might not be enough to predict extinction and re-ignition. Second-order closure which has already been used for predictions of the Sandia Flames [42] may be a better solution. However, there are some difficulties to extend the second-order closure from three-step to a multi-step chemistry which would be more realistic. Another possibility is doubly conditioned CMC which was introduced by Cha *et al.* [15]. Here, scalar dissipation was used as a second conditioning variable since large values of scalar dissipation create extinction which further develops to flame quenching. However, using doubly conditioned CMC based on mixture fraction and scalar dissipation in [15] has shown high fluctuations around this doubly conditional mean, which required further adjustments. Moreover, Cha *et al.*'s results show that only extinction can be predicted well but the re-ignition was predicted too early. Reasons are not only a lack of correlation between scalar dissipation and re-ignition conditions, but there is also no consideration of chemical time scales of the flames [23]. Therefore, another suitable second conditioning variable was required. Following Bilger [9], double conditioning on mixture fraction and sensible enthalpy has been proved by Kronenburg and Kostka [50] that using sensible enthalpy as a second conditioning variable only for the reaction source terms and solving for the conditional variance (fluctuation of sensible enthalpy in mixture fraction space) equation can predict local extinction and re-ignition. Therefore, double conditioning of the reaction source terms and using the conditional variance equation seem to be a good solution since they directly solve the problem of inaccuracy in the conditional reaction source term and can be used with multi-step chemistry. However, such modelling so far

has only been attempted for the non-conservative CMC formulation and future research in this field should extend it to conservative CMC.

Furthermore, in order to show the improved performance of the conservative CMC formulation, some more complex flames, such as bluff-body and lifted flames, are recommended as future study cases for LES-CMC modelling development and validation to demonstrate the full predictive capability of the conservative CMC.

Appendix A

Derivation of CMC Conservative Form

Two equations are required to derive the CMC transport equation with the joint PDF method by Klimenko and Bilger [47]. Both equations are applied for both conservative and non-conservative filtered species transport equations. According to the complete derivation of Navarro *et al.* [68], the first equation is the FDF transport equation, given as

$$\frac{\partial(\bar{\rho}_\eta \tilde{P}(\eta))}{\partial t} + \nabla \cdot (\bar{\rho}_\eta \tilde{\mathbf{v}}_\eta \tilde{P}(\eta)) = -\frac{\partial^2 \bar{\rho}_\eta \tilde{N}_\eta \tilde{P}(\eta)}{\partial \eta^2} - \frac{\partial}{\partial \eta} \left(\nabla \cdot \bar{\rho}_\eta (\widetilde{D\nabla\xi})_\eta \tilde{P}(\eta) \right), \quad (\text{A.1})$$

where \mathbf{v} denotes the velocity field (u, v, w) . In reacting flows, since Lewis numbers of all species are often assumed to be one, the conditional scalar transport equation can be derived for LES which reads

$$\frac{\partial(\bar{\rho}_\eta \tilde{\Phi}_\eta \tilde{P}(\eta))}{\partial t} + \nabla \cdot (\bar{\rho}_\eta (\widetilde{\mathbf{v}\Phi})_\eta \tilde{P}(\eta)) = \tilde{S}_\Phi \tilde{P}(\eta) + \nabla \cdot \mathbf{f}_D + \frac{\partial \tilde{\mathbf{J}}_\Phi}{\partial \eta}, \quad (\text{A.2})$$

where Φ is any scalar. The conditionally filtered flux in conserved scalar space, $\tilde{\mathbf{J}}_\Phi$, is expressed as

$$\tilde{\mathbf{J}}_\Phi = 2\bar{\rho}_\eta (\widetilde{D\nabla\xi\nabla\Phi})_\eta \tilde{P}(\eta) - \frac{\partial}{\partial \eta} [\bar{\rho}_\eta (\widetilde{N\Phi})_\eta \tilde{P}(\eta)], \quad (\text{A.3})$$

and a molecular diffusion flux, \mathbf{f}_D , is

$$\mathbf{f}_D = \bar{\rho}_\eta \tilde{P}(\eta) (\widetilde{D\nabla\Phi})_\eta - \frac{\partial}{\partial\eta} [\bar{\rho}_\eta \tilde{P}(\eta) (\widetilde{D\nabla\xi\Phi})_\eta]. \quad (\text{A.4})$$

The term $\tilde{\mathbf{J}}_\Phi$ is modelled from using primary closure hypothesis [47], which is justified in the LES context. The diffusion in conserved scalar space is assumed to be of Brownian nature, which corresponds with conventional CMC (RANS-CMC) [47]. Following Klimenko and Bilger [47], the term $\tilde{\mathbf{J}}_\Phi$ is expressed in the form of a linear diffusion approximation as

$$\tilde{\mathbf{J}}_\Phi = A \tilde{\Phi}_\eta + B \frac{\partial \tilde{\Phi}_\eta}{\partial \eta}, \quad (\text{A.5})$$

where the drift coefficient A and the diffusion coefficient B must preserve linear properties of turbulent scalar transport and they are thus independent of $\tilde{\Phi}_\eta$. Assuming the linear profile $\Phi = a + b\xi$, where a and b depend on the initial and boundary conditions, the conditional filtering reads $\tilde{\Phi}_\eta = a + b\eta$. Replacing the value of this $\tilde{\Phi}_\eta$ in Eqs. (A.3) and (A.5) with the knowledge of the identities that $(D\nabla\xi\widetilde{\nabla[a + b\xi]})_\eta = b\tilde{N}_\eta$ and $(N[a + b\xi])_\eta = \tilde{N}_\eta[a + b\eta]$, the parameters A and B are

$$A = -\frac{\partial}{\partial\eta} (\bar{\rho}_\eta \tilde{N}_\eta \tilde{P}(\eta)), \quad (\text{A.6})$$

and

$$B = \bar{\rho}_\eta \tilde{N}_\eta \tilde{P}(\eta). \quad (\text{A.7})$$

As the coefficients A and B are independent of Φ in the primary closure hypothesis and these value thus are valid for any field of $\tilde{\Phi}_\eta$. Finally the conditional scalar transport equation can be derived which reads

$$\begin{aligned} \frac{\partial(\bar{\rho}_\eta \tilde{\Phi}_\eta \tilde{P}(\eta))}{\partial t} + \nabla \cdot (\bar{\rho}_\eta (\mathbf{v}\tilde{\Phi})_\eta \tilde{P}(\eta)) &= \tilde{S}_{\Phi_\eta} \tilde{P}(\eta) + \nabla \cdot (\bar{\rho}_\eta \tilde{P}(\eta) (\widetilde{D\nabla\Phi})_\eta) \\ - \nabla \cdot \left[\frac{\partial}{\partial\eta} \left(\bar{\rho}_\eta \tilde{P}(\eta) (\widetilde{D\nabla\xi\Phi})_\eta \right) \right] &+ \bar{\rho}_\eta \tilde{N}_\eta \tilde{P}(\eta) \frac{\partial^2 \tilde{\Phi}_\eta}{\partial \eta^2} - \frac{\partial^2 \bar{\rho}_\eta \tilde{N}_\eta \tilde{P}(\eta)}{\partial \eta^2} \tilde{\Phi}_\eta. \end{aligned} \quad (\text{A.8})$$

As suggested by Clearly [16], the conservative LES-CMC scalar transport equation is

received by substituting the multiplication of Eq. (A.1) by $\tilde{\Phi}_\eta$ into Eq. (A.8). Following this procedure, the multiplication of Eq. (A.1) by $\tilde{\Phi}_\eta$ becomes

$$\tilde{\Phi}_\eta \frac{\partial(\bar{\rho}_\eta \tilde{P}(\eta))}{\partial t} + \tilde{\Phi}_\eta \nabla \cdot (\bar{\rho}_\eta \tilde{\mathbf{v}}_\eta \tilde{P}(\eta)) = -\tilde{\Phi}_\eta \frac{\partial^2 \bar{\rho}_\eta \tilde{N}_\eta \tilde{P}(\eta)}{\partial \eta^2} - \tilde{\Phi}_\eta \frac{\partial}{\partial \eta} \left(\nabla \cdot \bar{\rho}_\eta (\widetilde{D\nabla\xi})_\eta \tilde{P}(\eta) \right). \quad (\text{A.9})$$

Using $\gamma = \bar{\rho}_\eta \tilde{P}(\eta)$, Eq. (A.9) is rewritten as

$$\begin{aligned} \tilde{\Phi}_\eta \frac{\partial \gamma}{\partial t} + \tilde{\Phi}_\eta \nabla \cdot (\gamma \tilde{\mathbf{v}}_\eta) &= -\tilde{\Phi}_\eta \frac{\partial^2 \gamma \tilde{N}_\eta}{\partial \eta^2} - \tilde{\Phi}_\eta \frac{\partial}{\partial \eta} \left(\nabla \cdot \gamma (\widetilde{D\nabla\xi})_\eta \right), \\ \frac{\partial(\gamma \tilde{\Phi}_\eta)}{\partial t} - \gamma \frac{\partial \tilde{\Phi}_\eta}{\partial t} + \tilde{\Phi}_\eta \nabla \cdot (\gamma \tilde{\mathbf{v}}_\eta) &= -\tilde{\Phi}_\eta \frac{\partial^2 \gamma \tilde{N}_\eta}{\partial \eta^2} - \tilde{\Phi}_\eta \frac{\partial}{\partial \eta} \left(\nabla \cdot \gamma (\widetilde{D\nabla\xi})_\eta \right). \end{aligned} \quad (\text{A.10})$$

Eq. (A.8) can be reexpressed using $\gamma = \bar{\rho}_\eta \tilde{P}(\eta)$ as

$$\begin{aligned} \frac{\partial(\gamma \tilde{\Phi}_\eta)}{\partial t} + \nabla \cdot (\gamma (\widetilde{\mathbf{v}\Phi})_\eta) &= \tilde{S}_{\Phi\eta} \tilde{P}(\eta) + \nabla \cdot (\gamma (\widetilde{D\nabla\Phi})_\eta) - \nabla \cdot \left[\frac{\partial}{\partial \eta} \left(\gamma (\widetilde{D\nabla\xi\Phi})_\eta \right) \right] \\ &\quad + \gamma \tilde{N}_\eta \frac{\partial^2 \tilde{\Phi}_\eta}{\partial \eta^2} - \tilde{\Phi}_\eta \frac{\partial^2(\gamma \tilde{N}_\eta)}{\partial \eta^2}. \end{aligned} \quad (\text{A.11})$$

By replacing Eq. (A.10) into Eq. (A.11), the result reads

$$\begin{aligned} \gamma \frac{\partial \tilde{\Phi}_\eta}{\partial t} - \tilde{\Phi}_\eta \nabla \cdot (\gamma \tilde{\mathbf{v}}_\eta) &- \tilde{\Phi}_\eta \frac{\partial}{\partial \eta} \left(\nabla \cdot \gamma (\widetilde{D\nabla\xi})_\eta \right) + \nabla \cdot (\gamma (\widetilde{\mathbf{v}\Phi})_\eta) \\ &= \tilde{S}_{\Phi\eta} \tilde{P}(\eta) + \nabla \cdot (\gamma (\widetilde{D\nabla\Phi})_\eta) - \nabla \cdot \left[\frac{\partial}{\partial \eta} \left(\gamma (\widetilde{D\nabla\xi\Phi})_\eta \right) \right] + \gamma \tilde{N}_\eta \frac{\partial^2 \tilde{\Phi}_\eta}{\partial \eta^2}, \\ \gamma \frac{\partial \tilde{\Phi}_\eta}{\partial t} - \tilde{\Phi}_\eta \nabla \cdot (\gamma \tilde{\mathbf{v}}_\eta) &+ \nabla \cdot (\gamma (\widetilde{\mathbf{v}\Phi})_\eta) \\ &= \tilde{S}_{\Phi\eta} \tilde{P}(\eta) + \nabla \cdot (\gamma (\widetilde{D\nabla\Phi})_\eta) - \nabla \cdot \left[\frac{\partial}{\partial \eta} \left(\gamma (\widetilde{D\nabla\xi\Phi})_\eta \right) \right] \\ &+ \tilde{\Phi}_\eta \frac{\partial}{\partial \eta} \left(\nabla \cdot \gamma (\widetilde{D\nabla\xi})_\eta \right) + \gamma \tilde{N}_\eta \frac{\partial^2 \tilde{\Phi}_\eta}{\partial \eta^2}, \end{aligned} \quad (\text{A.12})$$

where the second term on the RHS is the diffusion of the conditionally filtered scalar in physical space. Since this term scales with Re^{-1} , it is assumed to be small compared to other terms at high Re . Without any direct physical interpretation, the third and fourth contributions on the RHS show the interaction between physical and conditional scales. Both contributions scale with $Re^{1/2}N^{1/2}$ and thus they will be zero at high Re . Moreover they are smaller than the dissipation term in scalar space [68]. For high Reynolds number, these three contributions are neglected. Eq. (A.12) can then be rewritten as

$$\gamma \frac{\partial \tilde{\Phi}_\eta}{\partial t} + \nabla \cdot (\gamma \widetilde{(\mathbf{v}\Phi)_\eta}) = \tilde{S}_{\Phi_\eta} \tilde{P}(\eta) + \gamma \tilde{N}_\eta \frac{\partial^2 \tilde{\Phi}_\eta}{\partial \eta^2} + \tilde{\Phi}_\eta \nabla \cdot (\gamma \tilde{\mathbf{v}}_\eta). \quad (\text{A.13})$$

The second term on the LHS denotes the correlation of the conditional fluctuations of the velocity field and scalar, which are non-linear. Therefore an unknown term called the subgrid scale scalar flux, e_Φ , is required for this unclosed quantity, which is given as

$$\gamma e_\Phi = -\nabla \cdot [\gamma (\widetilde{(\mathbf{v}\Phi)_\eta} - \tilde{\mathbf{v}}_\eta \tilde{\Phi}_\eta)]. \quad (\text{A.14})$$

Replacing Eq. (A.14) into Eq. (A.13), the conservative LES-CMC equation becomes

$$\gamma \frac{\partial \tilde{\Phi}_\eta}{\partial t} + \nabla \cdot \gamma (\tilde{\mathbf{v}}_\eta \tilde{\Phi}_\eta) = \tilde{S}_{\Phi_\eta} \tilde{P}(\eta) + \gamma \tilde{N}_\eta \frac{\partial^2 \tilde{\Phi}_\eta}{\partial \eta^2} + \tilde{\Phi}_\eta \nabla \cdot (\gamma \tilde{\mathbf{v}}_\eta) + \gamma e_\Phi. \quad (\text{A.15})$$

For the species transport equation, the scalar Φ is the mass fraction, the source term S_{Φ_η} is the conditional reaction source term of species α . $S_{\Phi_\eta} = \rho_\eta w_{\alpha,\eta}$, and Q_α denotes the conditionally filtered mass fraction where, $Q_\alpha \equiv \tilde{\Phi}_\eta$. The conditionally filtered reactive species transport equations in conservative form is written as

$$\gamma \frac{\partial Q_\alpha}{\partial t} + \frac{\partial}{\partial x_j} (\gamma \tilde{u}_{j,\eta} Q_\alpha) = \gamma \tilde{w}_{\alpha,\eta} + \gamma \tilde{N}_\eta \frac{\partial^2 Q_\alpha}{\partial \eta^2} + Q_\alpha \frac{\partial}{\partial x_j} (\gamma \tilde{u}_{j,\eta}) + \gamma e_y. \quad (\text{A.16})$$

Appendix B

Details of Pressure Correction

The relation of pressure and velocity fields is described in this chapter. In this work, a SIMPLE algorithm [70], which stands for Semi-Implicit Method for Pressure-Linked Equations, is applied as a pressure correction method (to adapt momentum and velocities such that continuity is ensured) in this work. The numerical integration of the semidiscrete equation is governed by a predictor-corrector approach. Both predictor and corrector parts rely on a second order Crank-Nicolson time integration method. The details can be shown as follows.

The pressure-split momentum equation is required for this method first. This can be performed by splitting the pressure field of the momentum equation into a thermodynamic pressure field and the pressure perturbation ($p = p_0 + \Delta p$), which can be written as

$$\frac{\partial}{\partial t}(\rho u_i) + \frac{\partial}{\partial x_j}(\rho u_i u_j) = \frac{\partial \tau_{ij}}{\partial x_j} - \frac{\partial p_0}{\partial x_i} - \frac{\partial \Delta p}{\partial x_i} + \rho g_i. \quad (\text{B.1})$$

Equation (B.1) can be rewritten in temporal discretization form as

$$\frac{(\rho \mathbf{u})^{n+1} - (\rho \mathbf{u})^n}{\Delta t} = \mathbf{R} - \frac{\partial \Delta p}{\partial x_i}, \quad (\text{B.2})$$

where \mathbf{u} is the velocity field, Δt denotes the time-step size, while n and $n + 1$ are the time-level index. Since p_0 is constant for incompressible fluid, the variance \mathbf{R} is given as

$$\mathbf{R} = -\frac{\partial}{\partial x_j}(\rho u_i u_j) + \frac{\partial \tau_{ij}}{\partial x_j} + \rho g_i. \quad (\text{B.3})$$

Equation (B.2) can be separated into two equations, which are given as

$$\frac{(\rho\mathbf{u})^* - (\rho\mathbf{u})^n}{\Delta t} = \mathbf{R}, \quad (\text{B.4})$$

$$\frac{(\rho\mathbf{u})^{n+1} - (\rho\mathbf{u})^*}{\Delta t} = -\frac{\partial\Delta p}{\partial x_i}. \quad (\text{B.5})$$

Here, * denotes the intermediate time-level index. Since the Crank-Nicolson method is used for time discretization, the pressure-split momentum equation (Eq. (B.4)) of the predictor part reads

$$\frac{\rho^m \hat{\mathbf{u}} - \rho^n \mathbf{u}^n}{\Delta t} = \frac{1}{2}(\mathbf{R}^m + \mathbf{R}^n), \quad (\text{B.6})$$

$$\frac{\rho^m \mathbf{u}^m - \rho^m \hat{\mathbf{u}}}{\Delta t} = -\frac{\partial(\Delta p)^m}{\partial x_i}. \quad (\text{B.7})$$

where $\hat{\mathbf{u}}$ is an intermediate velocity field between time level index n and m .

The intermediate hydrodynamic pressure field, Δp^m , is calculated by inverting the Poisson equation for pressure [95], which is obtained by enforcing continuity equation into momentum equation (Eq. (B.7)). This can be written as

$$\nabla^2(\Delta p)^m = \frac{1}{\Delta t} \left[\nabla \cdot (\rho^m \hat{\mathbf{u}}) + \frac{\partial \rho}{\partial t} \Big| ^m \right]. \quad (\text{B.8})$$

The second term on RHS in Eq. (B.8) can be approximated from the known values ρ^{n+1} and ρ^n

Therefore, the value of $(\Delta p)^m$ can be calculated from Eq. (B.8). Finally the predicted velocity field \mathbf{u}^m is obtained by using the projection step of Eq. (B.7). Then the corrector step follows in the same manner as the predictor step in order to calculate the velocity field having the pressure correction at the next time step, $n + 1$.

Bibliography

- [1] Clean Air: Air Pollution, Asthma, Radon, Lead, Mercury fact sheet, http://www.michigan.gov/documents/CleanAir_PollutionAsthmaRadonLeadMercuryFactShee_154685_7..pdf.
- [2] International workshop on measurement and computation of turbulent nonpremixed flames, <http://www.sandia.gov/tnf/radiation.html>.
- [3] R.S. Barlow and J.H. Frank. Effects of turbulence on species mass fractions in methane/air jet flames. *Proc. Combust. Inst.*, 27:1087, 1998.
- [4] R.S. Barlow and J.H. Frank. Piloted CH₄/ air flames C, D, E, and F - release 2.1. *Technical report, Sandia National Laboratories*, 2007.
- [5] R.S. Barlow and A.N. Karpetis. Scalar length scales and spatial averaging effects in turbulent piloted methane/air jet flames. *Proc. Combust. Inst.*, 30:673–680, 2005.
- [6] G.K. Batchelor. *An Introduction to Fluid Dynamics*. Cambridge University Press, 2000.
- [7] R.W. Bilger. The structure of turbulent nonpremixed flames. *Proc. Combust. Inst.*, 22:475–488, 1989.
- [8] R.W. Bilger. Turbulent diffusion flames. *Ann. Rev. Fluid Mech.*, 21:101–135, 1989.
- [9] R.W. Bilger. *Advanced laser diagnostics: implications of recent results for advanced combustor models*. In: R.S.L. Lee, J.H. Whitelaw, and T.S. Wung (eds.) *Aerothermodynamics in Combustors*. Springer Verlag, Berlin, 1993.
- [10] R.W. Bilger. Conditional moment closure for turbulent reacting flow. *Phys. Fluids A*, 5(2):436–444, 1993.

- [11] N. Branley. *Large Eddy Simulation of a Turbulent Non-premixed Flame*. PhD thesis, Imperial College, UK, 1999.
- [12] N. Branley and W.P. Jones. Large Eddy Simulation of a Turbulent Non-premixed Flame. *Combust. Flame*, 127:1914–1934, 2001.
- [13] S.P. Burke and T.E.W. Schumann. Diffusion Flames. *Proc. Combust. Inst.*, 1:2–11, 1928.
- [14] R.S. Cant and E. Mastorakos. *An Introduction to Turbulent Reacting Flows*. Imperial College Press, 2008.
- [15] C.M. Cha, G. Kosály, and H. Pitsch. Modeling extinction and reignition in turbulent nonpremixed combustion using a doubly-conditional moment closure approach. *Phys. Fluids*, 13:3824–3834, 2001.
- [16] M.J. Cleary. *CMC Modelling of Enclosure Fires*. PhD thesis, University of Sydney, Australia, 2004.
- [17] M.J. Cleary and J.H. Kent, editors. *A numerical method for conditional moment closure*, Melbourne, VIC, December 2003. Australian Symposium on Combustion & the Eighth Australian Flame Days, Monash University.
- [18] P.J. Colucci, F.A. Jaber, P. Givi, and S.B. Pope. Filtered density function for large eddy simulation of turbulent reacting flows. *Phys. Fluids*, 10:499–515, 1998.
- [19] A.W. Cook and J.J. Riley. A subgrid model for equilibrium chemistry in turbulent flows. *Phys. Fluids*, 6:2868–2870, 1994.
- [20] B.B. Dally, R.S. Barlow, A.R. Masri, and G.J. Fiechtner. Instantaneous and mean compositional structure of bluff-body stabilized nonpremixed flames. *Combust. Flame*, 114:119–148, 1998.
- [21] J.W. Deardorff. A numerical study of three-dimensional turbulent channel flow at large Reynolds number. *J. Fluid Mech.*, 41:452–480, 1970.
- [22] F. di Mare. *Large Eddy Simulation of Reacting and Non-reacting Turbulent Flows*. PhD thesis, Imperial College, UK, 2002.

- [23] T. Echehki and E. Mastorakos, editors. *Turbulent Combustion Modeling*. Springer, 2011.
- [24] Energy Information Administration (EIA). International Energy Outlook. "World Energy Demand and Economic Outlook ". 2010.
- [25] M. Fairweather and R.M. Woolley. First-order conditional moment closure modeling of turbulent, nonpremixed methane flames. *Combust. Flame*, 138:3–19, 2004.
- [26] J.H. Ferziger and M. Peric. *Computational Methods for Fluid Dynamics*. Springer, 2002.
- [27] H. Forkel. *Über die Grobstruktursimulation turbulenter Wasserstoff-Diffusionsflammen*. PhD thesis, TU Darmstadt, 1999.
- [28] F. Gao and E.E. ÓBrien. A large-eddy simulation scheme for turbulent reacting flows. *Phys. Fluids*, 5(6):1282–1284, 1993.
- [29] A. Garmory and E. Mastorakos. Capturing localised extinction in Sandia flame F with LES-CMC. *Proc. Combust. Inst.*, 33(1):1673–1680, 2011.
- [30] A. Garmory, E.S. Richardson, and E. Mastorakos. Micromixing effects in a reacting plume by the Stochastic Fields method. *Atmospheric Environment*, 40:1078–1091, 2006.
- [31] M. Germano, U. Piomelli, P. Moin, and W.H. Cabot. A dynamic subgrid-scale eddy viscosity model. *Phys. Fluids A*, 3(7):1760–1765, 1991.
- [32] B. Gustafsson, H.O. Kreiss, and A. Sundstroem. Stability theory of difference approximations for mixed initial boundary value problems. ii. *Mathematics of Computation*, 26(119):649–686, 1972.
- [33] W.P. Jones. *BOFFIN: A Computer Program for Flow and Combustion in Complex Geometries*.
- [34] W.P. Jones, F. di Mare, and A.J. Marquis. *LES-BOFFIN: User's Guide*, 2002.
- [35] W.P. Jones and B.E. Launder. The prediction of laminarization with a two-equation model of turbulence. *International Journal of Heat and Mass Transfer*, 15:301 – 314, 1972.

- [36] A.N. Karpetis and R.S. Barlow. Measurements of flame orientation and scalar dissipation in turbulent partially premixed methane flames. *Proc. Combust. Inst.*, 30:665–672, 2005.
- [37] A. Kempf, F. Flemming, and J. Janicka. Investigation of lengthscales, scalar dissipation, and flame orientation in a piloted diffusion flame by LES. *Proc. Combust. Inst.*, 30:557–565, 2005.
- [38] A. Kempf, H. Forkel, A. Sadiki, J. Janicka, and J. Chen. Large-Eddy Simulation of a Counterflow Configuration with and without Combustion. *Proc. Combust. Inst.*, 28:35–40, 2000.
- [39] J.H. Kent and R.W. Bilger. The prediction of turbulent diffusion flame fields and nitric oxide formation. *Proc. Combust. Inst.*, 16(1):1643–1656, 1976.
- [40] D.S. Kershaw. The incomplete choleskyconjugate gradient method for the iterative solution of systems of linear equations. *Journal of Computational Physics*, 26:43–65, 1978.
- [41] S. Kim and H. Pitsch. Conditional filtering method for large-eddy simulation of turbulent nonpremixed combustion. *Phys. Fluids*, 17:105103, 2005.
- [42] S.H. Kim and K.Y. Huh. Second-order conditional moment closure modeling of turbulent piloted jet diffusion flames. *Combust. Flame*, 138:336–352, 2004.
- [43] S.H. Kim, K.Y. Huh, and T. Liu. Application of the elliptic conditional moment closure model to a two-dimensional nonpremixed methanol bluff-body flame. *Combust. Flame*, 120:75–90, 2000.
- [44] M. Klein, A. Sadiki, and J. Janicka. A digital filter based generation of inflow data for spatially developing direct numerical or large eddy simulations. *Journal of Computational Physics*, 186(2):652–665, 2003.
- [45] A.Y. Klimenko. Multicomponent diffusion of various admixtures in turbulent flow. *Fluid Dynamics*, 25(3):327–334, 1990.
- [46] A.Y. Klimenko. Note on the conditional moment closure in turbulent shear flows. *Phys. Fluids*, 7:446–448, 1995.

- [47] A.Y. Klimenko and R.W. Bilger. Conditional moment closure for turbulent combustion. *Prog. Energ. Combust. Sci.*, 25:595–687, 1999.
- [48] E. Kreyzing. *Advanced Engineering Mathematics*. John Wiley & Sons, INC., 2006.
- [49] A. Kronenburg, R.W. Bilger, and J.H. Kent. Modelling soot and formation in turbulent methane-air jet diffusion flames. *Combust. Flame*, 121:20–40, 2000.
- [50] A. Kronenburg and M. Kostka. Modelling Extinction and Re-ignition in Turbulent Flames. *Combust. Flame*, 143:342–356, 2005.
- [51] A. Kronenburg and A.E. Papoutsakis. Conditional moment closure modeling of extinction and re-ignition in turbulent non-premixed flames. *Proc. Combust. Inst.*, 30:759–766, 2005.
- [52] B. Van Leer. Towards the ultimate conservative difference scheme ii. Monotonicity and conservation combined in a second order scheme. *J. Comput. Phys.*, 14:361–370, 1974.
- [53] A. Leonard. Energy cascade in Large-Eddy Simulations of turbulent fluid flows. *Advances in Geophysics*, 18:235–248, 1974.
- [54] M.J. Lighthill. *Introduction to Fourier Analysis*. Cambridge University Press, Cambridge, 1958.
- [55] D.K. Lilly. The representation of small-scale turbulence in numerical simulation experiments. *Proc. IBM Scientific Computing Symposium on Environmental Sciences*, pages 195–210, 1967.
- [56] D.K. Lilly. A proposed modification of the germano subgrid-scale closure method. *Phys. Fluids A*, 4(3):633–635, 1992.
- [57] T.S. Lund, X. Wu, and K.D. Squires. Generation of Turbulent Inflow Data for Spatially-Developing Boundary Layer Simulations. *Journal of Computational Physics*, 140(2):233–258, 1998.
- [58] B.F. Magnussen and B.H. Hjertager. On mathematical modeling of turbulent combustion with special emphasis on soot formation and combustion. *Proc. Combust. Inst.*, 16, 1976.

- [59] A.J. Marquis and M. Wille. *BOFFIN for parallel Computers*. Imperial College of Science, Technology and Medicine, London, July 2008.
- [60] A.R. Masri, S.B. Pope, and B.B. Dally. PDF computations of a strongly swirling nonpremixed flame stabilised on a new burner. *Proc. Combust. Inst.*, 28:123–132, 2000.
- [61] J.A. Meijerink and H.A. van der Vorst. Guidelines for the usage of incomplete decompositions in solving sets of linear equations as they occur in practical problems. *Journal of Computational Physics*, 44:134–155, 1981.
- [62] M.P. Meyer. *The Application of Detailed and Systematically Reduced Chemistry to Transient Laminar Flames*. PhD thesis, University of London, 2001.
- [63] P. Moin and J. Kim. Numerical investigation of turbulent channel flow. *J. Fluid Mech.*, 118:341–377, 1982.
- [64] R. Mustata, L. Valino, C. Jimenez, W.P. Jones, and S. Bondi. A probability density function Eulerian Monte Carlo field method for large eddy simulations: Application to a turbulent piloted methane/air diffusion flame (Sandia D). *Combust. Flame*, 145:88–104, 2006.
- [65] S. Navarro-Martinez and A. Kronenburg. LES-CMC simulations of a turbulent bluff-body flame. *Proc. Combust. Inst.*, 31:1721–1728, 2007.
- [66] S. Navarro-Martinez and A. Kronenburg. LES-CMC simulations of a turbulent a lifted methane flame. *Proc. Combust. Inst.*, 32:1509–1516, 2009.
- [67] S. Navarro-Martinez and A. Kronenburg. Flame Stabilization Mechanisms in Lifted Flames. *Flow Turb. Combust.*, 87:377–406, 2011.
- [68] S. Navarro-Martinez, A. Kronenburg, and F. di Mare. Conditional Moment Closure for Large Eddy Simulations. *Flow Turb. Combust.*, 75:245–274, 2005.
- [69] S.V. Patankar. *Numerical Heat Transfer and Fluid Flow*. Hemisphere, New York, USA, 1980.

- [70] S.V. Patankar and D.B. Spalding. A calculation procedure for heat, mass and momentum transfer in three dimensional parabolic flows. *International Journal of Heat and Mass Transfer*, 15:1787–1806, 1971.
- [71] M. Peric, R. Kessler, and G. Scheuerer. Comparison of finite-volume numerical methods with staggered and colocated grids. *Computers and Fluids*, 16(4):389–403, 1988.
- [72] N. Peters. Laminar diffusion flamelet models in non-premixed turbulent combustion. *Prog. Energ. Combust. Sci.*, 10:319–339, 1984.
- [73] N. Peters. *Turbulent Combustion*. Cambridge University Press, Cambridge, UK, 2000.
- [74] C.D. Pierce and P. Moin. A dynamic model for subgrid-scale variance and dissipation rate of a conserved scalar. *Phys. Fluids*, 10(12):3041–3044, 1998.
- [75] U. Piomelli. High Reynolds number calculations using the dynamic subgrid-scale stress model. *Phys. Fluids*, 5:1484–1490, 1993.
- [76] U. Piomelli and J. Liu. Large eddy simulation of rotating channel flows using a localized dynamic model. *Phys. Fluids*, 7:839–848, 1995.
- [77] H. Pitsch. Improved pollutants prediction in large-eddy simulation of turbulent non-premixed combustion by considering scalar dissipation rate fluctuations. *Proc. Combust. Inst.*, 29:1971–1978, 2002.
- [78] H. Pitsch. Large-Eddy Simulation of Turbulent combustion. *Ann. Rev. Fluid Mech.*, 38:453–482, 2006.
- [79] H. Pitsch and H. Steiner. Large eddy simulations of a turbulent piloted methane/air diffusion flame (sandia flame D). *Phys. Fluids*, 12(10):2542–2554, 2000.
- [80] T. Poinso and D. Veynante. *Theoretical Numerical Combustion*. Edwards, Philadelphia, USA, 2005.
- [81] S.B. Pope. PDF methods for turbulent reactive flows. *Prog. Energ. Combust. Sci.*, 11:119–192, 1985.

- [82] S.B. Pope. *Turbulent Flows*. Cambridge University Press, Cambridge, UK, 2001.
- [83] V.N. Prasad. *Large Eddy Simulation of partially premixed turbulent combustion*. PhD thesis, Imperial College, London, UK, 2011.
- [84] C.M. Rhie and W.L. Chow. Numerical study of the turbulent flow past an airfoil with trailing edge separation. *AIAA J.*, 21:1525–1532, 1983.
- [85] L.F. Richardson. *Weather Prediction by Numerical Process*. Cambridge University press, Cambridge, UK, 1922.
- [86] M.R. Roomina and R.W. Bilger. Conditional moment closure (CMC) predictions of a turbulent methane-air jet flame. *Combust. Flame*, 125:1176–1195, 2001.
- [87] V. Saxena and S.B. Pope. PDF calculations of major and minor species in a turbulent piloted jet flame. *Proc. Combust. Inst.*, 27:1081–1086, 1998.
- [88] Ch. Schneider, A. Dreizler, J. Janicka, and E.P. Hassel. Flow field measurements of stable and locally extinguishing hydrocarbon-fuelled jet flames. *Combust. Flame*, 135:185–190, 2003.
- [89] U. Schumann. Subgrid scale model for finite difference simulations of turbulent flows in plane channels and annuli. *J. Comput. Phys.*, 10:1049–1051, 1975.
- [90] J. Smagorinsky. General circulation experiments with the primitive equations: I. The basic equations. *Monthly Weather Review*, 91:99–164, 1963.
- [91] O. Souldarda, V. Sabel'nikov, and M. Gorokhovski. Stochastic scalar mixing models accounting for turbulent frequency multiscale fluctuations. *International Journal of Heat and Fluid Flow*, 25:875–883, 2004.
- [92] I. Stanković and B. Merci. Analysis of autoignition of heated hydrogenair mixtures with different detailed reaction mechanisms. *Combust. Theo. Mod.*, 15:409436, 2011.
- [93] I. Stanković and B. Merci. Simulation of hydrogen autoignition in a turbulent coflow of heated air with LES and CMC approach. *Flow Turb. Combust.*, 68:689710, 2011.
- [94] H. Steiner and W.K. Bushe. Large eddy simulation of a turbulent reacting jet with conditional source-term estimation. *Phys. Fluids*, 13:754–768, 2001.

- [95] J.C. Tannehill, D.A. Anderson, and R.H. Pletcher. *Computational Fluid Mechanics and Heat Transfer*. McGraw-Hill, New York, USA, 1984.
- [96] H. Tennekes. Simple Model for the small-scale structure of turbulence. *Phys. Fluids*, 11:669–671, 1968.
- [97] H. Tennekes and J.L. Lumley. *A first Course in Turbulence*. MIT Press, 1972.
- [98] J.F. Thompson, C.W. Mastin, and F.C. Thames. Automatic numerical generation of body-fitted curvilinear coordinate system for field containing any number of arbitrary two-dimensional bodies. *Journal of Computational Physics*, 302:274–302, 1974.
- [99] B. Thornber, R.W. Bilger, A.R. Masri, and E.R. Hawkes. An algorithm for LES of premixed compressible flows using the Conditional Moment Closure model. *Journal of Computational Physics*, 230:76877705, 2011.
- [100] A. Triantafyllidis. *Large Eddy Simulations of Spark Ignition Processes with the CMC Method*. PhD thesis, University of Cambridge, Department of Engineering, 2009.
- [101] A. Triantafyllidis and E. Mastorakos. Implementation issues of the Conditional Moment Closure Model in Large Eddy Simulations. *Flow Turb. Combust.*, 84(3):481–512, 2010.
- [102] A. Triantafyllidis, E. Mastorakos, and R. Eggels. Large Eddy Simulations of forced ignition of a non-premixed bluff-body methane flame with conditional moment closure. *Combust. Flame*, 156:23282345, 2009.
- [103] S.R. Turns. *An Introduction to Combustion*. McGraw-Hill, 2006.
- [104] L. Valino. A Field Monte Carlo Formulation for Calculating the Probability Density Function of a Single Scalar in a Turbulent Flow. *Flow Turb. Combust.*, 60:157–172, 1998.
- [105] H.A. van der Vorst. A Vectorizable Variant of some ICCG Methods. *SIAM Journal on scientific and Statistical Computing*, 3:350–356, 1982.
- [106] H.K. Versteeg and W. Malalasekera. *An Introduction to Computational Fluid Dynamics: The Finite Volume Method*. Pearson Education Limited, 2007.

- [107] A.W. Vreman, B.A. Albrecht, J.A. van Oijen, L.P.H. de Goey, and R.J.M. Bastiaans. Premixed and non-premixed generated manifolds in large-eddy simulation of Sandia flame D and F. *Combust. Flame*, 153:394–416, 2008.
- [108] J. Warnatz, U. Maas, and R.W. Dibble. *Combustion Physical and Chemical Fundamentals Modeling and Simulation, Experiments, Pollutant Formation*. Springer, 2006.
- [109] Wikipedia.org. Beta distribution.
- [110] M. Wille. *Large Eddy Simulation of jets in cross flows*. PhD thesis, Department of Chemical Engineering, Imperial College of Science, Technology and Medicine, London, 1997.

Lebenslauf

Persönliche Daten

Name	Siwaborworn, Papakorn
Geburtsdatum und -ort	16.08.1979, Bangkok
Anschrift	Enzbergerstr. 8 74363 Güglingen

Schulischer Werdegang

Mai 1985 - März 1991	Besuch der Tubthong School in Bangkok, Thailand
Mai 1991 - März 1997	Besuch der Satriwitthaya 2 School in Bangkok, Thailand

Studium

Mai 1997 - Mai 2001	Studium der Umweltschutztechnik an der Chulalongkorn-Universität in Bangkok, Thailand Bachelorarbeit: Eignung der Pelletformen für die Wasserreinigung
----------------------------	--

Januar 2005 - Februar 2007

Studium der WASTE (Umweltschutztechnik als internationales Programm) an der Universität Stuttgart
Masterarbeit: Statistical Simulation of Partially Turbulent Premixed Flames using the EMST Mixing Model

Beruflicher Werdegang

September 2001 - Dezember 2003

Anstellung als Umweltingenieurin bei CMS Engineering & Management Co., Ltd., in Bangkok, Thailand

März 2007 - August 2011

Wissenschaftliche Angestellte am Institut für Technische Verbrennung der Universität Stuttgart,
Leiter: Professor Dr. Andreas Kronenburg